IMPERIAL COLLEGE LONDON

Department of Earth Science and Engineering

Centre for Petroleum Studies

The Grid Dependence of Well Inflow Performance in Reservoir Simulation

By

Shaun Bambridge

A report submitted in partial fulfilment of the requirements for the MSc and/or the DIC

September 2010

DECLARATION OF OWN WORK

I declare that this thesis, *The Grid Dependence of Well Inflow Performance in Reservoir Simulation*, is entirely my own work and where any material could be construed as the work of others, it is fully cited and referenced, and/or with appropriate acknowledgement given.

Signature:

Name of Student: Shaun Bambridge

Name of Supervisor(s): Dr Tara LaForce, Imperial College London
Dr Tony Fitzpatrick, Schlumberger

EXECUTIVE SUMMARY

A simulation well model can be thought of in terms of three main elements – the geological properties (within the wells drainage area), the grid (discretizing the drainage area) and the well connection factors (relating well-flowing to well-block pressures). These factors combine to determine the productivity of the well and the flow and pressure fields that develop around it. A numerical model is intended to be a representation of reality, which provides a predictive capability that will support reservoir management and the decision-maker. Considering the well model, the quality of the numerical representation and thus its predictive power depends upon the suitability of these three factors.

The purpose of this study is to investigate local grid refinement, for several near well models designed to test the grid dependence of inflow performance in reservoir simulation. The principal flow regimes are modelled numerically – radial, spherical, cylindrical, linear and elliptical – using different well types in a homogeneous, isotropic medium saturated with single-phase oil. This ensures that all results are a product of the grid alone.

Well production simulates a pressure transient test and the simulator output is subjected to pressure transient analysis to compare and contrast model parameters under varying gridding schemes. Results are assessed qualitatively, by way of direct comparison to pressure and derivative curves, whereby the development of the flow regimes can be observed and the implication of the grid characteristics on the numerical model identified. Interpretation of simulation model parameters using the pressure data permits a quantitative assessment of accuracy by grid type and the simulator performance vectors allow assessment of computational efficiency. Initial simulations make use of Cartesian grid refinement, but the study is extended to different grid types (i.e. geometric series, radial and unstructured), varying well-versus-grid orientation, sensitivity to aspect ratio and higher-order flux approximation schemes.

The results provide insight to the effect of gridding on the well model parameters – permeability-thickness product, well-bore storage, skin, permeability anisotropy and horizontal well length. Generally speaking, total well productivity is modelled accurately and is relatively insensitive to the grid; however this is not always true where the well model relies on flow converging in three dimensions. In such cases refinement is essential to reproduce the correct behaviour. Well-bore storage exhibits a strong dependence on well-block volume and is therefore sensitive to the grid refinement. Less accuracy is observed for parameters affecting the flow fields about the well – permeability anisotropy and horizontal well length – and a greater dependence on grid type, intensity and extent of the refinement. It is apparent that the expected values are not always honoured by the numerical model, which adversely affects the flow geometry.

This study concludes that;

1. In cases of three-dimensional flow regimes (e.g. limited entry, horizontal wells), local grid refinement is the only way to accurately model well productivity and the geometry of flow in the vicinity of the well.
2. Analysis of the results from this study has shown that significant improvement can be obtained on the accuracy of well-model parameters in numerical simulation through local refinement. Between coarse and refined grids improvements of 1-2% (half the error) can be expected on permeability-thickness product, improvement on the total skin from 0.1 to 2.8 (15-1000% better accuracy), improvements of between 10 and 40% for accuracy of permeability anisotropy and between 8 and 19% for the accuracy of horizontal well half-length. With well-bore storage directly linked to well-block volume, the error can be reduced by several hundred-thousand percent by the introduction of local refinement, which carries real significance to an accurate representation of the near-well flow geometry.
3. Unstructured gridding is by far the most accurate and adaptable in cases of complex well-geometries and adverse well-versus-grid orientations. For arbitrary well and grid geometry it achieves provides a close match to the flow regime behaviours and an overall improvement on Cartesian refinement.
4. Cartesian cell aspect ratio is significant when simulating three-dimensional flow, especially where cell length normal to the well track greatly exceeds that parallel to it. For best results, aspect ratio within the refinement should be kept cubic (or near thereto).
5. 9-point flux schemes do not exhibit any benefit to near-well modelling, but have been observed to double the computational cost. Although an oversight prior performing the simulations in this study, it is thought that 9-point schemes do not readily extend to local grid refinement, which is a theoretical problem that prevents the higher-order scheme being resolved at the interface of coarse grid and local grid.

Finally, with a better understanding of how the grid impacts well inflow for simple well geometries it is possible to apply lessons learned to more realistic (and perhaps more complex) wells and systems, with a view to improving the well model and therefore providing better predictive capability. Respect for the near well flow geometry results in more accurate representation of inflow to the various segments of the well-bore, therefore improving the predictive capability of the well model.

ACKNOWLEDGEMENTS

The author wishes to acknowledge the support of Schlumberger, without whom the provision of financial and technical support, access to the software and infrastructure required to complete this project wouldn't have been possible. Special thanks to Tony Fitzpatrick, David Rowan and Marie-Ann Giddins, of Schlumberger Information Solutions, for their direction, encouragement and critical feedback along the way. Thanks also to Tara LaForce, of Imperial College London, for providing instruction where needed and timely review of this study.

TABLE OF CONTENTS

THIS PAGE LEFT BLANK INTENTIONALLY

Imperial College
London

The Grid Dependence of Well Inflow Performance in Reservoir Simulation

Shaun Bambridge

Dr Tara LaForce, Imperial College London

Dr Tony Fitzpatrick, Schlumberger Information Solutions

Abstract

Local grid refinements are investigated for several near well models designed to test the grid dependence of inflow performance in reservoir simulation. The principal flow regimes are modelled numerically – radial, spherical, cylindrical, linear and elliptical – using different well types produced under transient conditions and the performance is evaluated in terms of accuracy and computational efficiency. Direct comparison is made to the appropriate analytical models and the simulator output is subjected to pressure transient analysis to compare and contrast model parameters under varying gridding schemes. Initial simulations make use of Cartesian grid refinement, but the study is extended to different grid types (i.e. geometric series, radial and unstructured refinement), varying well-versus-grid orientation, sensitivity to aspect ratio and higher-order flux approximation schemes.

The results provide insight to the effect of gridding on the well model parameters – permeability-thickness product, well-bore storage, skin, permeability anisotropy and horizontal well length – whereby it is apparent that the expected values are not always honoured by the numerical model and adversely affect the flow geometry. Finally, the implications of the observed effects are discussed and the lessons learned are used to offer recommendations on gridding for more accurate well performance.

This study concludes that in cases of three-dimensional flow regimes (e.g. limited entry, horizontal wells), local grid refinement is the only way to accurately model well productivity and the geometry of flow in the vicinity of the well. Analysis of the results from this study has shown that significant improvement can be obtained on the accuracy of well-model parameters in numerical simulation through local refinement. Between coarse and refined grids improvements of 1-2% (half the error) can be expected on permeability-thickness product, improvement on the total skin from 0.1 to 2.8 (15-1000% better accuracy), improvements of between 10 and 40% for accuracy of permeability anisotropy and between 8 and 19% for the accuracy of horizontal well half-length. With well-bore storage directly linked to well-block volume, the error can be reduced by several hundred-thousand percent by the introduction of local refinement, which carries real significance to an accurate representation of the near-well flow geometry.

Unstructured gridding is by far the most accurate and adaptable in cases of complex well-geometries and adverse well-versus-grid orientations. For arbitrary well and grid geometry it achieves provides a close match to the flow regime behaviours and an overall improvement on Cartesian refinement.

Introduction

Reservoir simulation is the art (and science) of dynamically modelling porous media (typically of a heterogeneous and anisotropic nature), saturated to varying extents with hydrocarbon fluids. The principle aim of reservoir simulation is to predict future performance of the system and to maximize the recovery of hydrocarbons; to assist the cost effective extraction of an optimum volume of hydrocarbon within an optimum timeframe, where optimum is stated in an economic context. Due to the complexity of this problem it is not possible to determine accurate solutions analytically, but much more reliable to use numerical methods. With modern computers and the existence of advanced commercial software, numerical simulation is now well established as a tool for reservoir management. In fact it is a necessary tool that provides the only real means to evaluate and optimize full field development and production strategies. The output of reservoir simulation impacts management of the asset during the entire field lifecycle, from exploration and appraisal, through operation to abandonment, and it is a key input to the economic forecast.

At the most fundamental level, the calculations performed in reservoir simulation can be thought of in two-parts; firstly, calculation of fluid saturation and pressure distribution in the field, and secondly, well inflow. The former concerns itself with numerical solution of the non-linear partial differential equations - via a system of simultaneous algebraic difference equations - that govern flow in porous media and express the mass balance of the system's fluids. The solution domain, representative of a physical volume, is discretized by allocating to it discrete points that can be connected in various ways to form a network of cells. This gives rise to the various modes of numerical modelling; point discretization, termed *finite difference*, and cell discretization, known as *finite element* (solution variables in each cell are represented by selected functions integrated analytically over the cell volume) or *finite volume* (fluxes through each cell are balanced at its boundaries) (Thompson et al, 1999). Extensive research on this subject has resulted in much literature and significant improvements in this area and is therefore not the concern of this paper.

This research concerns itself, rather, with the topic of near-well modelling and well inflow in reservoir simulation, which is by comparison far more neglected in the literature. This prospect might be considered with some concern given the importance of well modelling to history matching and prediction, both of which are key elements in any reservoir simulation workflow. In reality, many factors contribute to the performance of a well – the geology, fluid properties and PVT behaviour, reservoir boundary conditions, the well completion and tubing efficiency, the operating parameters of the subsurface development and even the network of surface process and transmission facilities. These are the high level factors and there are many more at an ever finer scale, though fortunately most of these are beyond the scope of this work. The focus here is on modelling the continuous subsurface system, which we may delineate from the rest of the system at the well-bore, in particular the zone between the well's sand face (inner boundary) and its drainage radius (outer-boundary) – known as it's drainage area. In the context of this study, the simulation well model can be thought of in terms of three main elements – the geological properties (within the wells drainage area), the grid (discretizing the drainage area) and the well connection factors (relating well-flowing to well-block pressures).

The objective is to investigate the impact of the grid, local to the well, on the simulator's ability to accurately capture near-well flow and pressure fields. The principal flow-regimes are studied – radial, spherical, cylindrical, linear and elliptical – by way of simple, standard well models – vertical (fully and partially penetrating) and horizontal – in a homogeneous, isotropic system. Use is made of analytic pressure transient models to assess the near-well numerical model – for their ability to characterise the flow regimes, and, where the system model is known with certainty, to accurately quantify the model parameters. This analysis is primarily performed with Cartesian grids and local grid refinement (LGR), but is extended to several sensitivities; grid type, well-versus-grid orientation, cell aspect ratio and higher-flux calculation schemes. In addition to Cartesian refinement, the study makes use of geometric series, radial and unstructured LGR, whereby unstructured gridding takes the form of localised 2.5-D perpendicular bisector (PEBI) grids constructed using 2-D PEBI grids in the horizontal plane projected vertically along coordinate lines. The type, level and extent of the grid refinement, along with the flux calculation scheme, have implications to both the accuracy and computational cost of the well model and these are quantified.

With a better understanding of how the grid impacts well inflow for simple models it is possible to apply lessons learned to more realistic (and perhaps more complex) wells and systems, with a view to improving the well model and therefore providing better predictive capability. Respect for the near well flow geometry results in more accurate representation of inflow to the various segments of the well-bore, therefore improving the predictive capability of the well model.

Literature Review

Several elements of the petroleum engineering literature are relevant to this study. The first is gridding for reservoir simulation, in particular local grid refinement, which allows for more accurate spatial definition of the well flowing pressure profile as it extends away from the well-bore. Likewise the flow field in the vicinity of the well as it develops according to the dominant flow regime. Secondly, well connection as a way of relating bottomhole pressure in the well to the pressure of the grid-block(s) into which it is connected. In terms of modelling wells in reservoir simulation, some of the most significant works have come from the area of well connection factor. These elements are looked at in some detail and the relevant literature summarised here and in Appendix A.

Gridding. Numerical simulation necessitates discretization of the solution domain, resulting in a grid (or mesh) to encompass it. These grids are typically classified into two main categories – structured or unstructured – where the main difference is the structuring (or ordering) of the data. Structured grids have a data structure that is naturally ordered by their geometry and can be logically thought of in terms of orthogonal *i, j, k* identifiers. Unstructured grid points cannot be represented in such a manner and additional information is needed - namely a connectivity matrix (Thompson et al, 1999). Reservoir simulation has historically favoured structured grids; Cartesian and curvilinear block-centred or corner point grids, which are less computationally expensive. The additional cost of unstructured grids may be justified, however, when the solution domain is of considerable geometrical complexity, or involves complex flow-field features, and thus their comparative flexibility can help improve the solution accuracy.

Gridding is an important consideration in any numerical study, but particularly so around wells, geological features or where it is necessary to capture steep fluid saturation gradients. Typically the grid is refined near a feature of interest to better represent the movement of fluid and the propagation of pressure in that localized zone. Historically, grid refinements were extended across the entire grid, but in their modern form, are truly local.

Local grid refinement was introduced to finite difference type reservoir simulation by von Rosenberg (1982) and Heinemann et al. (1983). In the first instance, local grid refinement was Cartesian. Later, Pedrosa and Aziz (1985) proposed a hybrid grid method making use of a radial grid in the well regions and a rectangular grid elsewhere. This method was seen to improve the near-well model but was limited by the fact that the well had to be at the centre of the Cartesian grid cells and required an approximate method for handling the transition from radial to Cartesian grid blocks. Fung et al. (1993) extended the idea of cylindrical refinement to the control-volume-finite-element (CVFE) method originally introduced to reservoir simulation by Forsythe (1989). This offered the benefit of radial grids, a greater geometric flexibility and the elimination of discretization errors at the local-to-coarse grid interface. Unstructured gridding was introduced to reservoir simulation by Heinemann et al. (1989), who made use of 2-D and 2.5-D PEBI grids to demonstrate their improved accuracy and flexibility over Cartesian grids and 9-point flux schemes for reservoir flooding patterns under adverse grid-orientation and mobility ratios. Heinemann also demonstrated the accuracy of the radial flow representation using PEBI grids. This work was later followed by that of Consonni et al. (1993) and Palagi and Aziz (1994), who applied unstructured gridding as local refinements for coning and water flood studies, respectively.

To give a detailed description of the geometry, generation, benefits and limitations of each grid type is not the purpose of this review, but is better left to the vast array of literature on the topic of gridding in reservoir simulation. A small, but pertinent cross-section of that literature is referenced here. Likewise, local grid refinement as a method for improved well-modelling has found varied uses and specialised applications, reflected again by abundant reference to it in the petroleum literature, but it is not practical to honour even a fraction of that literature here. It is sufficient to say, however, that local grid refinement has proven essential to accurate near-well modelling where flow converges, pressure gradients steepen and saturation profiles change rapidly.

Well to Grid Connection. For radial grid about cylindrical well-bore the well model is trivial, since it quite simply obeys the radial form of Darcy's law with cell pressure, p_o, taken at a distance from the well-bore, r, equal to the distance of the adjacent cell node from the inner cell boundary (i.e. the well-bore) according to the following relationship;

$$p_o - p_{wf} = \frac{141.2 qB\mu}{kh} \ln\left(\frac{r}{r_w}\right) \quad (1)$$

The problem of connecting a well into grid-blocks of non-circular dimension was solved during the late 1970s and early 1980s. The challenge in connecting a well into a square or rectangular grid was that of relating well pressure to grid-block pressure. Typically the grid-block is much larger in size and volume than the well itself, by one or several orders of magnitude, and by the very nature of numerical simulation, block pressure and fluid saturations are instantaneously averaged across the block volume at each time-step. This strongly impacts the well model.

The first noteworthy treatment of this in the literature is the work of van Poollen et al. (1968), whom made use the radial form of Darcy's Law for steady-state flow, as given be Equation (1). They postulated that the calculated pressure of a well is the pressure of the node (grid block) in which it is located; therefore the pressure should be compared with the average pressure in that portion of the reservoir represented by the node. On this basis, they approximated well-flowing pressure as the average pressure in a circle of an equivalent area to that of the well-block, by integration of Equation (1) over the area of a circle, and thus the well-model took the form;

$$p - p_{wf} = \frac{141.2 qB\mu}{kh} \left(\ln\left(\frac{r_b}{r_w}\right) - \frac{1}{2} \right) \quad (2)$$

The work of van Poollen et al. was later superseded by that of Peaceman (1977) and Peaceman (1983), the results of which are still current in reservoir simulation today. In the first of these papers, Peaceman further explored the idea of van Poollen et al. for square grid-blocks and noted that while it was appropriate for the majority of a numerical model to regard the material balance accumulation term, $\Delta p_{i,j}/\Delta t$, as the change in average pressure of the block (i, j) and therefore associate $p_{i,j}$ with the average pressure of the block, this was not the proper interpretation of pressure in blocks containing wells. Peaceman subsequently introduced the concept of pressure equivalent radius (also known as the Peaceman radius), r_o, as a way of relating well and block pressure. He defined this as the radius at which the steady-state flowing pressure for the actual well is equal to the numerically calculated pressure for the well-block after which he expressed Equation (1) as follows;

$$p_o - p_{wf} = \frac{141.2 qB\mu}{kh} \ln\left(\frac{r_o}{r_w}\right) \quad (3)$$

Through mathematical derivation, confirmed by numerical experiments, Peaceman showed in the second of these papers that for an anisotropic medium discretized by rectangular grid-blocks of arbitrary dimension, the general form of the pressure equivalent radius is;

$$r_o = \frac{0.28\left[DX^2\sqrt{k_y/k_x} + DY^2\sqrt{k_x/k_y}\right]^{1/2}}{\sqrt[4]{k_y/k_x} + \sqrt[4]{k_x/k_y}} \quad (4)$$

In a later paper Peaceman (1993) discussed some of the assumptions underlying his previous work – namely uniform grid spacing, uniform permeability, well isolation and the planar flow idealisation (neglecting three-dimensional effects) – and some of the implications of these when pressure equivalent radius is applied to wells close to boundaries or in stratified reservoirs. His discussion focussed on horizontal wells, which will commonly suffer the adverse affects of these assumptions. It was demonstrated, for some cases where the given assumptions don't hold, that alternative methods of calculating the pressure equivalent radius are required.

Nonetheless, it is apparent that for the most part, well connections factors are still calculated in modern software using the Peaceman radius applied in three-dimensions. The three-part Peaceman equation (Schlumberger Information Solutions, 2010, a) evaluates equivalent radius in each dimension – r_{ox} , r_{oy} and r_{oz} – and similarly for permeability-thickness product – kh_x, kh_y and kh_z – and transmissibility constant – T_x, T_y and T_z – for each segment of the well-bore as it passes through successive grid-blocks. Subsequently, the well model retains the same basic form given in Equation (3), but with the addition of damage skin, S, and rearranged in terms of r_o according to the following definition;

$$r_o = r_{w.}e^{\left[\left(kh/141.2T\right)-S\right]} \quad (5)$$

Here T and kh are given by the vector combination of their component parts in each dimension and in Equation (6), below, the component Peaceman radii are calculated as per Equation (4), which is an expression of r_{ox}, but with grid block dimensions and permeability ratios exchanged appropriately for the plane of interest;

$$T = \sqrt{\frac{kh_x}{141.2\left(\ln\left(r_{ox}/r_w\right)+S\right)} + \frac{kh_y}{141.2\left(\ln\left(r_{oy}/r_w\right)+S\right)} + \frac{kh_z}{141.2\left(\ln\left(r_{oz}/r_w\right)+S\right)}} \quad (6)$$

$$kh = \sqrt{kh_x + kh_y + kh_z} \quad (7)$$

For the unstructured grids used in this study, a similar yet not identical method is used to determine the well connection factor. The well model remains unchanged, as given by Equation (5), but the method, as outlined by Gunasekera et al. (1997), can be used for calculating the well connection for 2.5D grids with cells aligned along the track of horizontal wells (as is applicable in our case). The approach resolves the well track into two components; one which is horizontal along the well track, and the other vertical. Peaceman's well connection for both these components is then added vectorially to obtain the overall connection factor, T. Thus, if we let the direction along the well track on the x-y plane be l, normal to the well track in the x-y plane be n and vertically be v, the well connection factor is then expressed according to the following set of equations;

$$T = \sqrt{T_l^2 + T_v^2} \quad (8)$$

$$T_l = \frac{\sqrt{k_l k_v}\,h_l}{141.2\left(\ln\left(r_l/r_w\right)+S\right)} \quad (9)$$

$$T_v = \frac{k_l h_v}{141.2\left(\ln\left(r_v/r_w\right)+S\right)} \quad (10)$$

$$r_l = \frac{0.28\left[D_n^{\,2}\sqrt{k_v/k_l} + D_v^{\,2}\sqrt{k_l/k_v}\right]^{1/2}}{\sqrt[4]{k_v/k_l} + \sqrt[4]{k_l/k_v}} \quad (11)$$

$$r_v = 0.14\sqrt{D_l^{\,2} + D_n^{\,2}} \quad (12)$$

$$h_l = \sqrt{h_x^{\,2} + h_y^{\,2}} \quad (13)$$

$$h_v = h_z \quad (14)$$

It is important to note that the permeability tensor used in all well models must be adjusted for the net-to-gross ratio.

Methodology

Model Construction. The models used for investigation of the flow regimes, involve several elements – grid, well, rock and fluid properties – each of which is described here in basic detail. Since the primary concern of this study is the grid itself, the characteristics of the model are designed to minimise the effects of everything else and to ensure that observed effects are indeed attributable to the grid only.

Coarse grid. The representation of the reservoir system was designed to be sufficiently large so as to behave as an infinite system. This means that the pressure transient does not encounter any outer boundaries and that system pressure depletion due to production is negligible. It would have been possible to maintain system pressure, by way of injection, however this was not considered necessary since the methodology used is not sensitive to well inflow being transient, pseudo-steady-state or steady-state and the introduction of an injection pattern would have made the simulations more computationally expensive.

Two grids were used for numerical simulation of the flow regimes (Model-1 and Model-2), differing only in their layering to ensure that well placement was through the centre of the grid block regardless of well direction – vertical or horizontal. The introduction of Model-2 was for the horizontal wells, as an odd number of layers (each with equal dimension) was required to ensure that the well travelled along the mid-point of the reservoir and intersected the mid-point of the associated cells.

Both models were built using a simple corner-point Cartesian grid with vertical pillars. All cell angles are orthogonal and the grid is aligned along the principal *x*, *y* and *z* axes. In any given direction, cell dimensions are constant. The grid is designed in such a way that one vertical column of cells is perfectly cubic in its dimension – 200 feet each way. A summary of the grid characteristics is given in Appendix B (Table B-1) while an illustration of the grid is provided by Figure 1.

Grid coordinate system. The grid uses a null coordinate system, meaning that all points in the grid are referenced to the upper south-west corner (0,0,0). The coordinate system therefore increases to the east in the *i*-direction, to the north in the *j*-direction and decreases downward (i.e. becomes increasingly negative) in the *k*-direction.

Wells. The use of several different well models was required; in the first instance, vertical fully penetrating, vertical partially penetrating and horizontal. These well models can be considered ideal. Their trajectories travel exactly along the appropriate principal axes (*z*-axis for vertical wells and *x*-axis for horizontal wells) and they intersect the centre of the grid blocks through which they pass. Areal placement of the wells is at the centre of the field, and similarly for horizontal wells, along the vertical mid-point of the reservoir. This was supposed to be the best case for modelling well inflow. Figure 1 illustrates for the vertical well cases. A similar illustration of the horizontal well is included in Appendix B (Figure B-1). The details of the well completion properties are also provided in Appendix B (Table B-2).

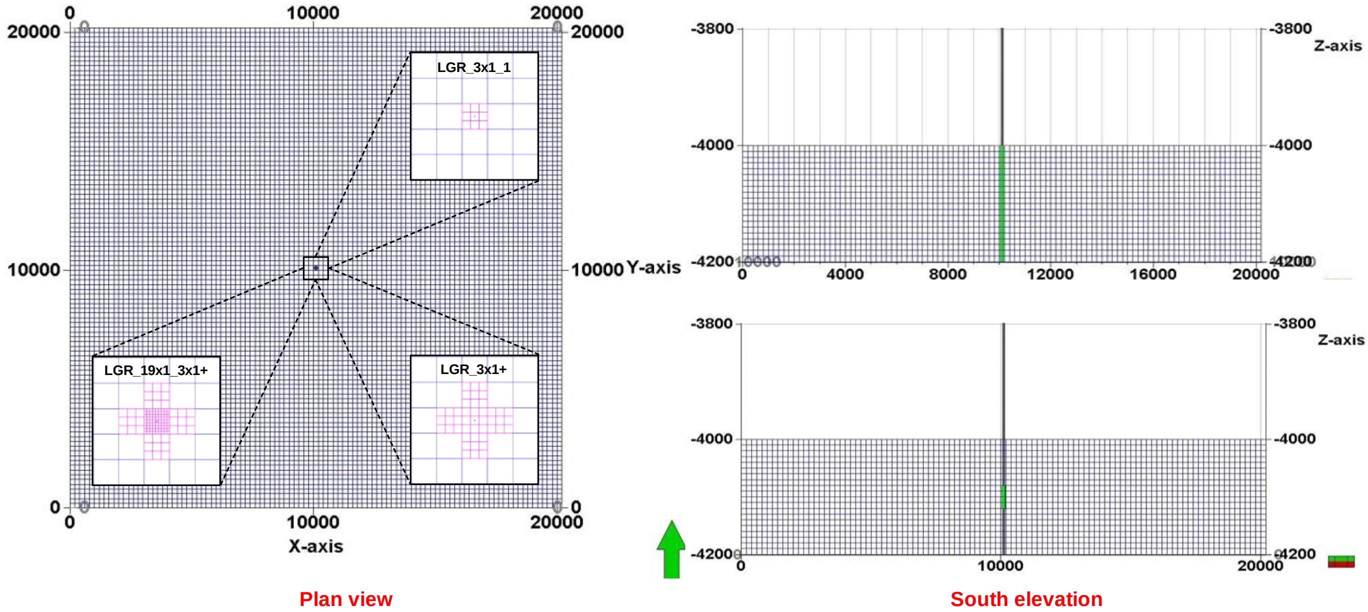

Figure 1: The location of well and completion within the grid for both fully penetrating (top right) and partially penetrating (bottom right) vertical wells. Some example LGR are shown by explosion of the near-well grid (inset at left).

More realistic well trajectories were investigated through sensitivity runs on relative orientation of well-versus-grid. Although remaining simplistic, the deviated trajectories were intended to build understanding in a systematic way as to how simulated well inflow is affected by changes to the well-grid symmetry. Appropriate illustrations and the details of the well completion properties are provided in Appendix B (Figure B-2 and Table B-3). The grid position remained fixed throughout the sensitivity study, aligned as usual along the principal axes, and the configuration of wells for the test cases was chosen based on an apparent dip in the *x*-*z* plane and rotation of the grid in the *x*-*y* plane. Apparent dip has been used to express the relative orientation of well-verses-grid in the *x-z* plane, and similarly, apparent rotation for the orientation of well-versus-grid in the *x-y* plane. Due to symmetry, only grid rotations of between 0º and 45º were included and it was only thought necessary to test an apparent dip of 0º, 90º and one value in between, chosen as 30º, to obtain an understanding of the effect.

Fine grids. Investigation of the gridding effect on well inflow involved the incorporation of numerous local grid refinements (LGR) about the wells. This was done systematically, by first observing the coarse grid simulation results, before those of local grids with varying level and lateral extent of refinement. The fine grid cell dimensions were kept cubic (or near there to), for initial simulations. Comparison of local grid type (i.e. Cartesian, radial, unstructured and geometric series) and varied Cartesian cell aspect ratio was investigated through sensitivity study on those parameters. Figure 1 offers some illustration of the gridding of LGR to wells, while the full catalogue of LGR is available in Appendix D. Grid type sensitivity was evaluated according to the matrix of test cases given in Appendix B (Table B-8), likewise for aspect ratio sensitivity (Table B-6).

Rock properties. The system was modelled as homogenous and isotropic – to reduce complexity and ensure that results obtained would not be affected by variation in system properties. It would pose a problem to correctly reconcile average porosity and permeability within the drainage area and this would inhibit comparisons to analytical models, which reflect an average porosity and permeability within the radius of investigation. Net-to-gross throughout the reservoir is taken as unity. The reservoir system rock properties are tabulated in Appendix B (Table B-4).

The oil-water relative permeabilities were built using Corey functions, as were the gas-oil relative permeabilities, but since water was immobile and there was no free gas in the simulations, description of them is not relevant to this discussion. For the given fluid saturations (see *Initialisation*, below) k_{ro} was 0.7 while k_{rg} and k_{rw} were 0.0.

Fluid properties. The system was modelled using black oil at pressures sufficiently higher than the saturation pressure (bubble point) of the fluid, to ensure single phase flow at all points in the reservoir, including the near-well bore zone and inside the well-bore itself. The choice of single phase fluid was necessary to more easily discern the impact of the grid without the added complexity of multi-phase flow effects. A summary of the fluid properties, as used for comparisons to analytical pressure transient models, is tabulated in Appendix B (Table B-5)

Initialisation. The model was initialised by equilibration, such that the entire reservoir interval was oil bearing without the presence of oil-water or gas-oil contacts. The system fluid saturations – S_o = 0.8 and S_w = 0.2 – are constant throughout, with water rendered immobile by a critical water saturation (S_{wc}) of 0.24. The reservoir pressure datum is at 4100 feet and the system is normally pressured with an initial pressure at datum of 1618 psia.

Flow Regime Modelling. There are several flow regimes which impact near-well flow. These include well-bore storage, radial, linear, spherical, cylindrical and elliptical flow. These regimes are present whenever flow converges on the well, though they may be distorted in real cases where the affect of reservoir geology and well geometry on flow fields and pressure propagation is complex. Analytical models describing these flow regimes are often idealised to consider the reservoir as a homogeneous and isotropic medium, with properties that are constant or uniform throughout. More complex models are able to account for heterogeneities and anisotropy, but still in a rather simplistic fashion by comparison to reality. These models describe the reservoir in terms of its average properties.

Largely, we can attribute the limitations of such models to the complex mathematics describing flow in porous media. Analytical solutions of the partial differential equations that govern flow require some simplifying assumptions. Nonetheless, analytic solutions often work well and bring great value to the petroleum engineer for the information they distil from the reservoir. Even so, how to make best use of this information is an area of continued application and learning, and it is that which we hope to contribute through this research.

In essence, we refer here to pressure transient modelling, when the well is subjected to a rate change and the pressure disturbance (or signal) created has not yet felt the effects of any closed boundaries or pressure support. It is during this period of time that the flow regimes can be analysed by way of derivative (or log-log) and specialised (or semi-log) analyses. Making use of such analyses for pressure data output by the simulator, it has been possible to investigate inflow performance, dependent upon gridding and well connection factor, for how well the expected flow regimes are reproduced.

A brief outline of the analysis methodology and the flow regime descriptions is provided here. To support the explanation the relevant equations for the derivative and specialized analyses are provided in Appendix C.

Pressure transient analysis. Short-term production histories were simulated in order that pressure transient analyses could be performed. The production history involved a twelve hour static period to check the simulation had initialised correctly, followed by a twenty-four hour flow period (drawdown) at a rate of 1500 stock tank barrels per day (STBD), and subsequent shut-in (build-up) with varying duration selected to ensure that all relevant flow regimes had sufficient time to fully develop and be recognised in the pressure derivative. All analyses were carried out using the build-up pressure data.

Pressure derivative. Analysis of the pressure derivative has the distinct advantage of clear flow regime identification. Both pressure (Δp) and derivative ($\Delta p'$) are plotted against elapsed time since the beginning of the build-up (Δt) on a log-log scale. In order to emphasise the radial flow regime, where pressure change is a linear function of the logarithm of time, the derivative is taken with respect to the logarithm of time. Then, by using the natural logarithm, the derivative can be expressed as the normal time derivative, multiplied by the superposition time function (Bourdet, 2002). Note here that since this is an analysis of the build-up following first drawdown, although the derivative is plotted against elapsed time (Δt), it is generated with respect to the relevant superposition time (determined from the rate history).

The model parameters are then determined from a pressure and time matching process in dimensionless space using a set of independent variables appropriate to the model (Gringarten et al, 1979). In this case, the raw data was plotted, as above, and matched with a type-curve (i.e. solution curve) also plotted on log-log axes in terms of dimensionless pressure (p_D) and dimensionless time group (t_D/C_D), defined in Appendix C. The dimensionless well condition group (C_De^{2S}) completes the match.

By overlaying curves and selecting a match point to obtain Δp corresponding to p_D (the pressure match), Δt corresponding to t_D/C_D (the time match) and the curve corresponding to a C_De^{2S} label, the model parameters can be determined. This process is performed automatically in the software (see *Software*, below).

Specialized plots. Each individual flow regime exhibits a characteristic pressure behaviour that is in some way a function of time. The time function varies with the mathematical description of the flow regime and it is on this basis that we may obtain a specialized plot specific to it. For a given flow regime and its corresponding plot, the specialized analysis results in a straight line from which we may obtain the relevant parameters. Specialized analysis is only accurate where the relevant flow regime (i.e. straight line) can be clearly identified on the appropriate plot and for this reason it is often unreliable. A consistent analysis will yield the same parameter values as those from the derivative analysis, within an acceptable level of tolerance. Again, the process is automated in the software.

Well-bore storage. At the beginning of a flow period, following a rate change, the measured surface flow rate is an artefact of fluid compressibility (and/or changing liquid level). It is not representative of flow from the reservoir and is generally not of particular interest to the reservoir engineer during simulation. It appears, however, as a straight line of unit slope on a log-log plot, assessed from the time match, and a straight line with slope m_{WBS} tangent to the Δp versus Δt curve at the origin in Cartesian space (Bourdet, 2002).

Fully penetrating vertical well. Radial flow modelling was carried out with well VERT_FP, described in Appendix B. Radial flow can be discerned from a log-log plot as the derivative stabilization. The level of the stabilization is inversely proportional to the mobility term (k_hh/μ) which can therefore be quantified from the pressure match. The concept of derivative stabilization during radial flow is illustrated in Figure 2.

Specialized analysis for radial flow is performed using the Horner Method (Horner, 1951), a semi-log technique that plots pressure against the log of Horner time enabling determination of permeability-thickness product from the slope, m_H, of the straight-line section, and total skin from extrapolation of the same straight-line to $\Delta p(\Delta t = 1hr)$.

Partially penetrating vertical well. Simulation of well VERT_PP, described in Appendix B, allowed modelling of the spherical flow regime. Spherical flow occurs due to convergence of flow to a zone of limited entry where the connection of well-bore to formation occurs across only a fraction of the reservoir thickness. Strictly speaking, a well with limited entry has three characteristic flow regimes; (a) radial flow across the open interval with stabilization at k_hh_w, although this flow regime is often masked by well-bore storage and skin, (b) spherical flow with Δp proportional to $1/\sqrt{\Delta t}$ and negative half-unit slope straight line on the log-log plot, and, (c) radial flow over the entire reservoir thickness, as described previously, with stabilization at k_hh and total skin S_t (Bourdet, 2002). For illustration, these flow regimes are indicated in Figure 3.

Due to non-uniqueness of the solution with varying k_v/k_h, z_w/h and h_w/h there is no type curve set for spherical flow. Instead, matching of the derivative curve at the negative unit slope straight line yields the k_v/k_h ratio. Logically, decreasing k_v/k_h displaces the spherical flow regime toward late times. Well-bore storage is determined from the time match, permeability-thickness product from the pressure match, and with k_v/k_h determined from the spherical flow regime, h_w can then be discerned from the first radial flow stabilization, if present (and assuming interval thickness is known).

Specialized analysis of spherical flow plots Δp against $1/\sqrt{\Delta t}$ and the spherical permeability (k_s) can be determined from the slope, m_{SPH}, of the straight line section (Bourdet, 2002).The Horner Method can be used to evaluate permeability-thickness product and the total skin, as before, using the pressure points corresponding to the late time radial flow regime.

Horizontal well. Flow converges to a horizontal well according to three characteristic flow regimes; (a) cylindrical flow in the vertical plane about the longitudinal axis of the well with stabilization $2L\sqrt{(k_vk_h)}/\mu$, (b) a linear flow after the upper and lower limits of the interval are reached during which Δp is proportional to $\sqrt{\Delta t}$ and the derivative exhibits a half-unit slope straight line on the log-log plot, and, (c) an elliptical flow in the horizontal plane that corresponds to infinite behaviour in the reservoir, thus stabilization, k_hh/μ, and total skin, S_t (Bourdet, 2002). Figure 4 illustrates.

Due to the complex behaviour of horizontal wells, namely the interplay of k_v/k_h, L/h, and z_w/h, the solution is non-unique and no type curves are available. Variation of k_v/k_h shifts the level of the cylindrical flow stabilization; the ratio L/h also affects the level of the cylindrical flow stabilisation as well as the timing of the transition to linear flow. Likewise, variation of z_w/h affects the transition from cylindrical to linear flow. Again, well-bore storage is determined from the time match and permeability-thickness product from the pressure match during derivative analysis. The intermediate time linear flow is used to estimate L by fitting the solution curve to the derivative half-unit slope straight line. Finally, with k_hh and L known, the cylindrical flow stabilization yields the permeability anisotropy, k_v/k_h.

Specialized analysis of the cylindrical and elliptical flow regimes plots Δp versus log Δt, yielding two characteristic straight lines. The slope, m_{CF}, of the cylindrical flow straight line provides the product of well half-length and the geometric average of permeability in the vertical plane (Bourdet, 2002). This will allow us to determine k_v/k_h. Similarly the slope, m_{EF}, of the elliptical flow regime provides the product of horizontal permeability and interval thickness as well as the total skin (Bourdet, 2002). Provided the half-unit slope straight line characterising linear flow is clearly established in the derivative, the corresponding pressure points can be analysed on a plot of Δp against $\sqrt{\Delta t}$ where the slope, m_{LF}, of the straight line provides the product of horizontal permeability and the square of well half-length. Making use of the permeability determined previously we may then obtain the well half-length (Bourdet, 2002).

Software. This study involved the use of several commercial software – for model construction, numerical simulation and for the pressure transient analyses. Model construction was performed in Petrel version 2010.1 (Schlumberger Information Solutions, 2010, b), which was the pre-processor for the majority of simulations. For the grid type sensitivity cases, however, radial and geometric series refinements had to be manually built in the ECLIPSE deck. Unstructured grid generation utilized a development version of the same software, Petrel version 2011.1 beta.

Numerical simulations were performed in ECLIPSE 100 version 2010.2 (Schlumberger Information Solutions, 2010, c), with the exception of unstructured grid simulation, where it was necessary to use Intersect version 2011.1 beta (Schlumberger Information Solutions, 2010, d). All transient analyses of simulated pressure data were carried using Saphir, in Ecrin version 4.12 (KAPPA Engineering, 2010).

Results

The presentation of results is aided by graphical illustration, however due to the large number of simulations and subsequent quantity of plots produced, it was necessary to leave most to Appendix. Moreover, while in some cases the figures here may lack resolution, the reader is referred to Appendix E, where the full set of results are reproduced in an improved format.

The LGR referenced in the figures follow a set naming convention for the purpose of identification. Generally the first term indicates the type of refinement (e.g. LGR for Cartesian refinement). The second term defines the level of the refinement – areal (x,y) by vertical (z) subdivisions of the coarse grid block. The last term defines the areal extent of the refinement in the x-y plane or its lateral extension in terms of coarse grid blocks. Vertically, all LGR extend fully through the interval modelled. In some cases (e.g. for other grid types and gradual refinements) the naming convention is modified slightly and other terms may appear. The full catalogue of LGR is provided in Appendix D.

Flow Regimes. For varied Cartesian LGR the simulation pressure results are presented in terms of the real pressure history, in addition to the log-log plot of pressure and derivative. The analytic solution is plotted for the purpose of comparison and a brief qualitative discussion is provided with particular focus on the model parameters. Some numerical effects are also evident in the data during middle and late times, occurring as the pressure transient propagates away from the well and encounters the increased elemental volumes of larger grid-blocks. These effects appear as low amplitude oscillations, but can be ignored.

Fully penetrating vertical well. The results of modelling radial flow for a fully penetrating vertical well are shown in Figure 2. As demonstrated, there are three parameters defining inflow behaviour of this type of well and flow regime in a homogeneous, isotropic medium – well-bore storage, skin and permeability-thickness product.

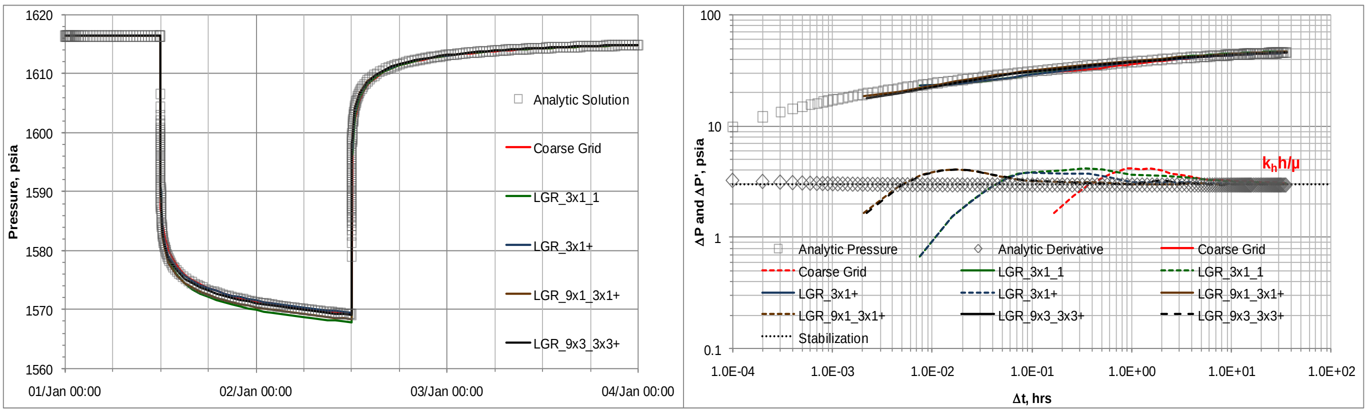

Figure 2: Comparison of simulated and analytic pressure history (left) and diagnostic plot (right) for fully penetrating vertical well modelled by Cartesian grid refinements. Solid lines in the diagnostic plot represent pressure, while dashed lines represent the derivative.

Notice firstly that the well-bore storage term appears to decrease and the radial flow regime is reached more quickly as the level of refinement increases. This is indicated by the shift of derivate to the left and the flattening against the radial flow stabilization. The well-storage term converges toward the analytical value, as the well-blocks become smaller. In analytical terms, the well-bore storage reflects the volume of the well-bore. In simulation, it appears to maintain some relation to the volume of the well-block(s) themselves.

Second, we observe from all derivative stabilizations that the permeability-thickness product is accurately modelled by simulation. It does not appear sensitive to the level or extent of the grid refinement. In fact, even the coarse grid obtains a good match with the analytical solution. It is clear that all simulations converge to the correct mobility ratio, $k_h h/\mu$, shown in Figure 2 by the radial flow stabilization of the derivative.

Thirdly, skin also appears to be well matched and does not appear to be significantly sensitive to the grid refinement. Given that the permeability-thickness product is accurate, the history plot in Figure 2 indicates an additional pressure drop due to skin of less than 2-psia at the point of shut-in for all cases.

Partially penetrating vertical well. By contrast, the results of modelling spherical flow with a limited entry vertical well are shown in Figure 3. Here, in addition to well-bore storage, permeability-thickness product and skin, the well inflow can only be fully described by consideration of the length and position of the perforated interval within the pay zone and the permeability anisotropy. With respect to permeability-thickness product we observe similar behaviour to the radial flow case.

As expected, well-bore storage exhibits the same behaviour too and with an increased level of refinement and a reduced well-bore storage term, we observe more of the early time spherical flow regime. This demonstrates how well (or not) the spherical inflow is modelled, dependent upon the grid, since larger blocks show less resolution in flow geometry.

What we notice here, however, is that even for very high levels of Cartesian refinement, which come at great computational cost to the simulator, it is not possible to model the early time radial flow. This flow regime represents the behaviour very near the perforations where flow in the adjacent region becomes orthogonal to the well-bore. There is a convergence toward the first stabilisation of the analytic solution, $k_h h_w/\mu$, but it is not reached even with a very fine grid having cubic grid cells.

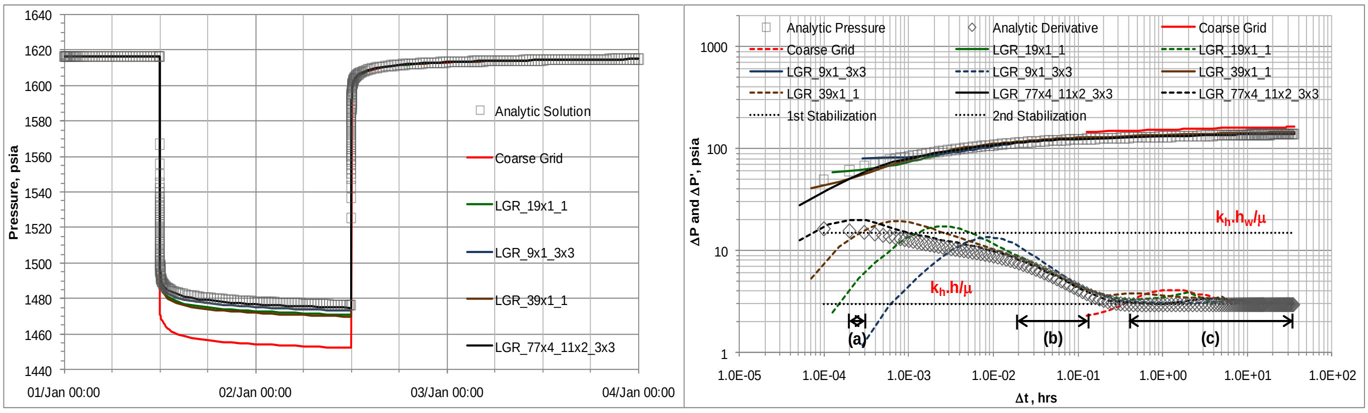

Figure 3: Comparison of simulated and analytic pressure history (left) and diagnostic plot (right) for partially penetrating vertical well modelled by Cartesian grid refinements. Solid lines in the diagnostic plot represent pressure, while dashed lines represent the derivative.

It is logical then, that with the convergence of flow about the well being modified by the grid, the skin term should be affected. This is reflected in the results and is evident in both plots of Figure 3, though more so in the pressure history since log-scales compress the effect on the diagnostic plot. The skin, quantifiable from the extent of separation between pressure and derivative in the diagnostic plot, is shown to be dependent upon both level and extent of the refinement. For example, a 9 areal by 1 vertical refinement, spread over a 3 by 3 column of coarse grid-cells encompassing the well, gives a skin that is reduced greatly in comparison to that of the coarse grid. Meanwhile, the benefit in terms of skin from introducing a 19 areal by 1 vertical refinement in the single column of cells containing the well is also evident. There does however appear to be some law of diminishing returns in terms of skin, as the additional benefit from the further refined LGR appears to be limited. The range of pressure drop due to grid-induced skin, across the test cases, is in the range of 1 to 24-psia at the time of shut-in.

Horizontal Well. The propagation of pressure and convergence of flow about a horizontal well is dependent on numerous parameters. Permeability-thickness product of the pay zone, permeability anisotropy, perforated well length and well position relative to the interval thickness. Together with the well-bore storage and skin terms the analytical model of a horizontal well is then completely described.

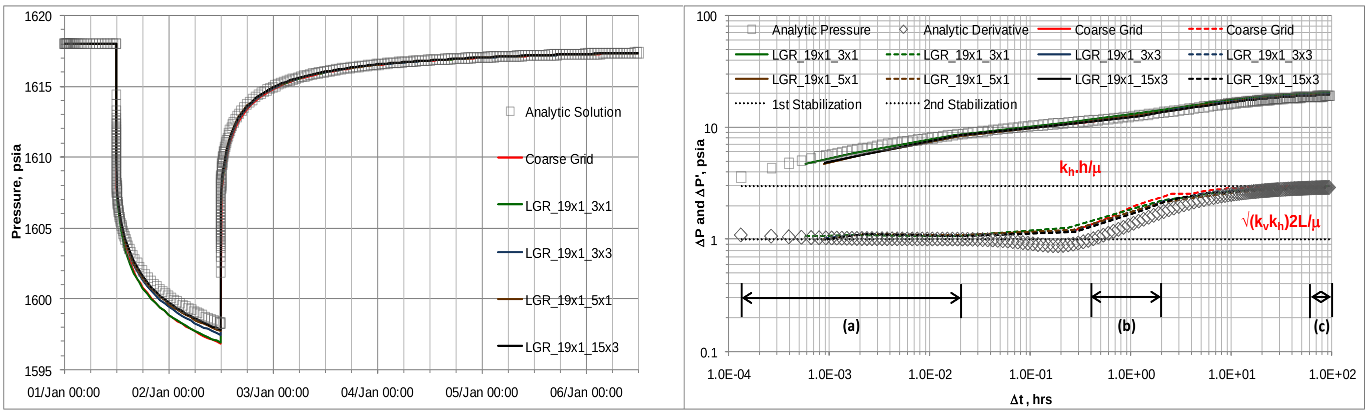

Figure 4: Comparison of simulated and analytic pressure history (left) and diagnostic plot (right) for horizontal well modelled by Cartesian grid refinements. Solid lines in the diagnostic plot represent pressure, while dashed lines represent the derivative.

With reference to Figure 4, it is clear that the simulator accurately and reliably models the permeability-thickness product of the interval, indicated by the convergence of all simulations with the second stabilization, $k_h h/\mu$, regardless of the refinement. The other parameter obtained from the late time elliptical flow regime is total skin, and with skin related pressure drops not exceeding 2-psia at the point of shut-in, we may consider these results relatively insensitive to gridding. Well-bore storage from the simulations follows the same trend seen in the vertical wells.

Observe that the cylindrical flow regime is modelled less accurately. Although visually the results are near to the first stabilisation of the analytic derivative, due to the log scale, the mobility discrepancy is significant and will result in incorrect apparent permeability anisotropy and a distortion of the cylindrical flow field about the well in the numerical model.

By contrast, however, the most significant aspect of the simulated response is the discrepancy between simulator and analytical models during the linear flow regime. Observe that the linear flow regime in the simulations plots to the left of the analytical model. The implication is that the modelled well-length is less than the actual well length. This is surprising since the well connections are correct and we could expect well productivity to be comparable since $k_h h$ and S_t are reproduced with reasonable accuracy.

It follows, that with an erroneous well half-length further error in apparent permeability anisotropy will occur during interpretation. Therefore, due only to the gridding effect, we would expect the horizontal well to be comparable to the analytical (or actual) well in terms of total productivity, but with incorrect flow and pressure fields affecting the inflow. It has been confirmed through simulations of much more refined LGR (i.e. up to 57 areal by 3 vertical subdivisions per coarse cell), given in Appendix E, that further refinement offers no significant improvement in reproducing the correct linear flow regime.

Sensitivity Cases. An array of sensitivity cases were run for relative orientation of well-versus-grid, cell aspect ratio, 9-point versus 5-point flux schemes, and grid-type. Only select results are outlined here, while the remainder are set out in Appendix E.

Well-versus-grid orientation. Even for a modest change in well-versus-grid orientation such as a 30**º** dip in the *x-z* plane and an equivalent rotation in the *x-y* plane we see a definite effect on the inflow performance of the well. This is a much more realistic geometry for a well, which rarely intersects a reservoir (or grid) in a perfectly vertical fashion (i.e. through the centre of a single column of cells). A deviated well such as this has a radial flow adjacent the perforations, aligned in the plane normal to the longitudinal axis of the well-bore. The corresponding early time stabilization (though normally a very short-lived one) is $k_n h/(\mu cos\theta)$, which is affected by the permeability anisotropy. There is then a transitional period as the macroscopic radial flow regime develops and the derivative stabilizes at $k_h h/\mu$. As expected from previous results, this is modelled well with LGR.

The point to note, however, is the gridding induced skin factor. Due to the inclination, the transmissibility in the vicinity of the well-bore is increased, which acts as an apparent negative skin in comparison to the vertical case. This corresponds to a smaller drawdown for the same rate of production. We observe this effect, but with even greater magnitude in the numerical models than in the analytical, and resulting in small grid induced pressure gain of up to 3-psia at the time of shut-in for the cases run.

Of the three cases studied for deviated wells this represents the worst case. In terms of the coarse grids, the effect was slightly less pronounced for a rotation of 0º, but more pronounced for a rotation of 45º. However, with refinement, a better fit for the analytical model was achieved in both cases. Refinement had the greatest benefit for a 45º grid rotation.

Similarly, using the horizontal well models, the well-versus-grid orientation effect was investigated for several test cases. The results for an apparent dip of 90º in the *x-z* plane and rotation of 30º in the *x-y* plane are illustrated in Figure 5. According the trend, behaviour of total system permeability-thickness product and well-bore storage are as expected. It is clear that the capability of the simulator to reproduce the near-well flow is poor, even using local refinement, though the accuracy of the flow regimes in the numerical models does not appear to be particularly sensitive to the level or extent of the refinement.

The linear regime is not well matched, in general, neither the early time cylindrical flow regime, while total system skin is well matched. For this case, a maximum grid induced pressure drop due to skin at the point of shut-in of less than 1-psia.

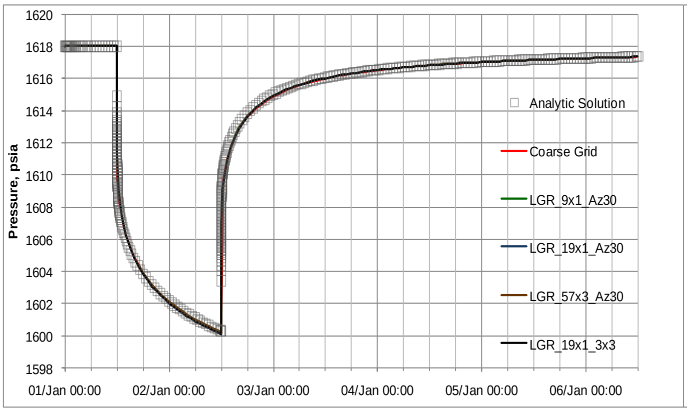

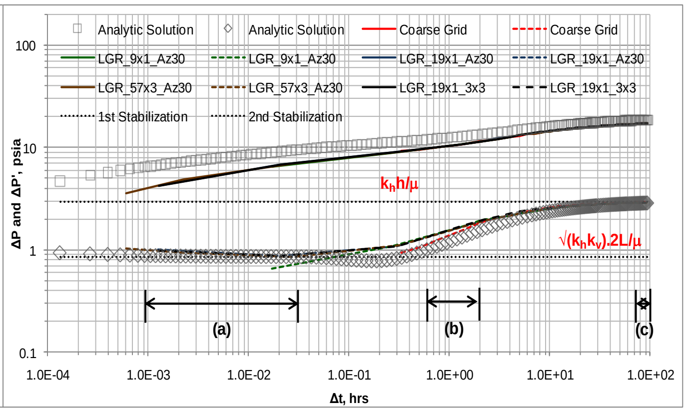

Figure 5: Comparison of simulated and analytic pressure history (left) and diagnostic plot (right) for well-versus-grid orientation case – horizontal well, grid orthogonal to the *k*-direction and rotated 30º in the *x-y* plane. Solid lines in the diagnostic plot represent pressure, while dashed lines represent the derivative.

The implication, as we saw with the initial horizontal well model, is that despite well productivity being a match, the near well flow fields are not well modelled. The inflow performance resembles that of a shorter horizontal well with a distortion in the permeability anisotropy. Note also the discrepancy between simulated and analytic pressure curves during early time in the diagnostic plot, which represents a simulated build-up lagging the analytical and can be taken as further evidence for the modification of the well model due to the grid effect.

For the other test case, set out in Appendix E, the rotation of 45º in the *x-y* plane offers a similar quality of productivity match, but with even more erratic derivative behaviour. Clearly Cartesian grids do not handle adverse grid orientation well.

Cell aspect ratio. The test cases for cell aspect ratio are indicated in Appendix B (Table B-6) and all results are set out in Appendix E. It has been shown that inflow to a fully penetrating vertical well is insensitive to aspect ratio in the *x-y* plane (i.e. *DX/DY*). Numerical experiments run for aspect ratios between 1 and 6.33 exhibit near identical behaviours. Only well-bore storage, as expected, exhibits the normal dependence on well-block volume. No experiments have been conducted for *x-z* or *y-z* plane aspect ratios since flow is horizontal planar and symmetrical, so no anomalous behaviour is expected.

By contrast, the flow regimes about a horizontal well do appear sensitive to cell aspect ratios. Numerical experiments for aspect ratios in the *x-z* plane (i.e. *DX/DZ*) of between 1 and 57 demonstrate that the capability of the simulator to reproduce the correct inflow behaviour deteriorates with increasing aspect ratio – where an aspect ratio of 1 (i.e. cells of cubic dimension) is optimum. At least partially, this is attributable to the well-bore storage effect, but it is also due to modification of the flow-fields about the well due simply to cell geometry. Increasing *x-z* plane aspect ratio compromises first the cylindrical flow about the well bore, followed by the linear flow when increased further. The implication for the model parameters determined from these flow regimes and apparent during the simulations has been discussed previously.

For aspect ratios in the *x-y* plane, numerical experiments were conducted for cases with ratios between 1 and 19 and for their reciprocals (i.e. *DY/DX* as opposed to *DX/DY*). This contrasts not only the affect of aspect ratio in general, but also the alignment of the lengthwise cell dimension parallel and normal to the well. It seems logical that the alignment of refined cells parallel to the well recreates inflow behaviour more accurately. This supposition is supported by the results.

For *x-y* plane aspect ratios of 1 and greater, the results are reasonable and appear insensitive to the grid. The numerical experiments approximate the analytic solution as well as we could expect from previous results. These results represent the effect of cell length parallel to the well. Meanwhile, increased lengthwise cell dimension normal to the well has a similar effect (not identical) on the inflow behaviour to that of increasing *x-z* plane aspect ratio normal to the well, as discussed above.

Flux calculation schemes. By default, the simulator configuration is for 5-point flux calculation. Such an approach considers planar flux into any cell being resultant from an exchange between the cell itself and its four adjacent neighbours based on a finite difference scheme. The total flux for any cell is then the sum of the flux from each of the three planes aligned with the principal axes – *x-y*, *x-z* and *y-z* planes. A 9-point flux calculation is similar, but considers all eight neighbouring cells by including the diagonals. This technique is more computationally expensive but has particular value in water-flood applications where the direction of flood front propagation is out of alignment with the grid (Yanosik and McCracken, 1976).

Since well inflow naturally tends to be planar-radial normal to the well-bore and adjacent the perforations, it was thought that 9-point flux could be used to more accurately model the inflow behaviour, since it would consider the flow diagonally into the well-block and thus be more radial in nature. A comparison between flux schemes was made using a selection of existing test cases, tabulated in Appendix B (Table B-7).

It is evident from the results, however, that they do not comply with expectation. For the vertical well cases (fully and partially penetrating) and the horizontal well case, without exception, the simulated pressure history for 9-point flux plots below that for 5-point flux. An increased discrepancy with the analytical model representing an increase in grid related skin. For the limited number of numerical experiments conducted inspection of the pressure histories indicates that the additional skin related pressure drop at the point of shut-in is between 0.1 and 6-psia. In terms of the pressure derivative and thus the accuracy with which flow regimes and inflow model parameters are reproduced in the simulations, it is apparent that the results are insensitive to flux calculation. The derivatives closely match those of the 5-point flux scheme and there is no evident improvement. All results are presented in Appendix E.

These observations also hold when we introduce the 9-point flux scheme to the horizontal wells from the well-versus-grid orientation cases. These cases, having wells misaligned with the principal axes of the grid, might be expected to show some improvement with the 9-point scheme, but again, they do not. The simulated pressure histories and the derivatives show negligible variation on the 5-point flux experimental values.

It is only the deviated well cases, where the relative orientation of well-versus-grid introduces a negative pseudo-skin that the 9-point flux scheme offers any value; though even here it is minimal. Since the 9-point flux scheme invariably results in a pressure history that plots below that of the corresponding 5-point flux simulation, this often results in a higher pseudo-skin that compensates for the inclination effect and better reproduces the analytic model. However, according the observed behaviour, wherever the 5-point flux result is already accurate, as was the case for HZ_90IN_45AZ, the 9-point flux result will suffer the same increase in pseudo-skin and will therefore diverge from the analytic solution.

Grid type. Thus far, all numerical experiments have involved Cartesian grids and we have observed how grid refinement in the vicinity of the well better reproduces the correct well inflow behaviour. However we have also observed that the fineness of the LGR and its extension away from the well connection are not always sufficient to accurately model the flow geometry. This leads us logically into looking at alternate grid types – to geometric series, radial and unstructured refinements. The matrix of test cases run to compare grid type is given in Appendix B (Table B-8).

Geometric series refinement. Several numerical experiments were designed for the vertical well (both fully and partially penetrating) and horizontal well, making use of Cartesian refinements configured in the *x*, *y* and sometimes *z* dimensions according to a geometric series extending away from the well connections. The intention was to better spatially represent the well-flowing pressure profile and limit the well-block volume to reduce well-bore storage, with fewer overall grid-blocks.

The results, unfortunately, did not entirely conform to expectations. The permeability-thickness product was well modelled in all cases and the flow regimes were generally well represented in the pressure derivative, provided that a sufficient number of refined cells were introduced. The optimum was 11 by 11 areal divisions, with vertical refinement providing some additional benefit. Well-bore storage was accurately modelled due to the minimised well-blocks.

Conversely, total skin was poorly modelled. There was typically an improvement from the coarse grid, except for the fully penetrating vertical well, which exhibits purely planar flow and where we have seen the coarse grid accurately reproduces the pressure history in any case. Yet the geometric series LGR still compared poorly to the analytic models. Comparison to the analytic solution indicated a grid induced pressure loss due to skin at the point of shut-in between 1 and 16-psia for the cases modelled. Furthermore, despite the smaller number of cells, it became clear that the geometric series refinements came at significantly greater computational cost.

Radial refinement. Radial refinements provide a viable alternative for this problem and one which has been successfully applied by others (Pedrosa and Aziz, 1986). When it comes to near-well modelling, we would expect radial grids to better respect the flow geometry and thus better capture the near-well flow regimes. Also, since radial grids do not rely on wells being connected into the grid in the same way as Cartesian grids, simulated well-bore storage should provide good match to the analytical model. There are some limitations to the application of radial LGR – namely that they can only be applied within a single column of cells or within an amalgamation of four adjacent columns, and only with vertical wells. Their application here, was thus simply to the fully and partially penetrating vertical well cases.

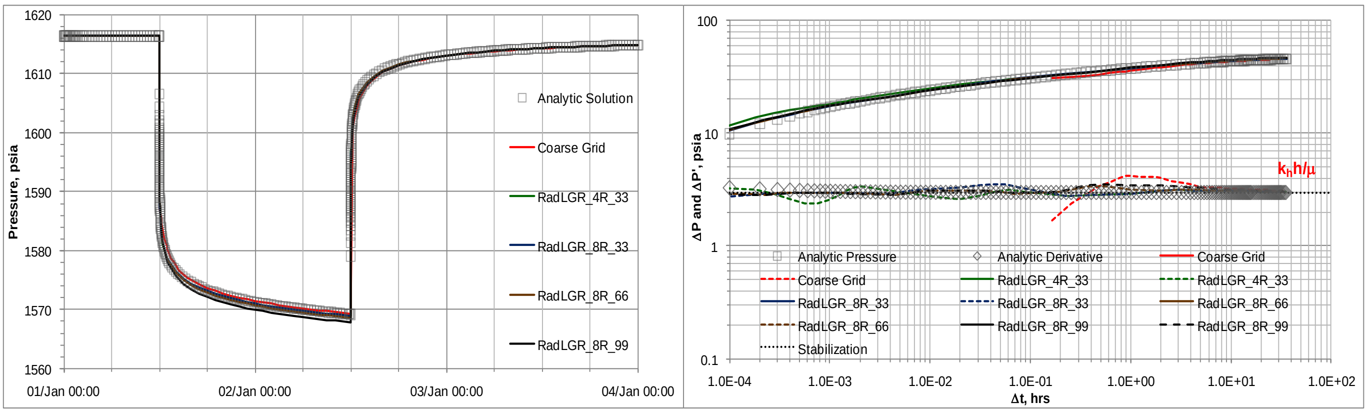

Figure 6: Comparison of simulated and analytic pressure history (left) and diagnostic plot (right) for fully penetrating vertical well modelled by radial grid refinements. Solid lines in the diagnostic plot represent pressure, while dashed lines represent the derivative.

Figure 6 illustrates the results of simulation with radial refinement for fully penetrating vertical well. Results show very good accuracy on all model parameters and thus close approximation to the analytical solution. Well-bore storage, permeability-thickness product, and total skin are all in close agreement. There are some numerical effects of changing grid block volumes as we step out from the well that appear as oscillations in the pressure derivative, but these are to be expected. The oscillations have been minimised by increasing the number of radial divisions from four to eight. The lateral extent of the radial divisions inside the LGR did not appear to have a significant effect, but best results were achieved for LGR with 8 radial divisions extending laterally with an outer radius of 66 feet (or two-thirds of the well block diameter).

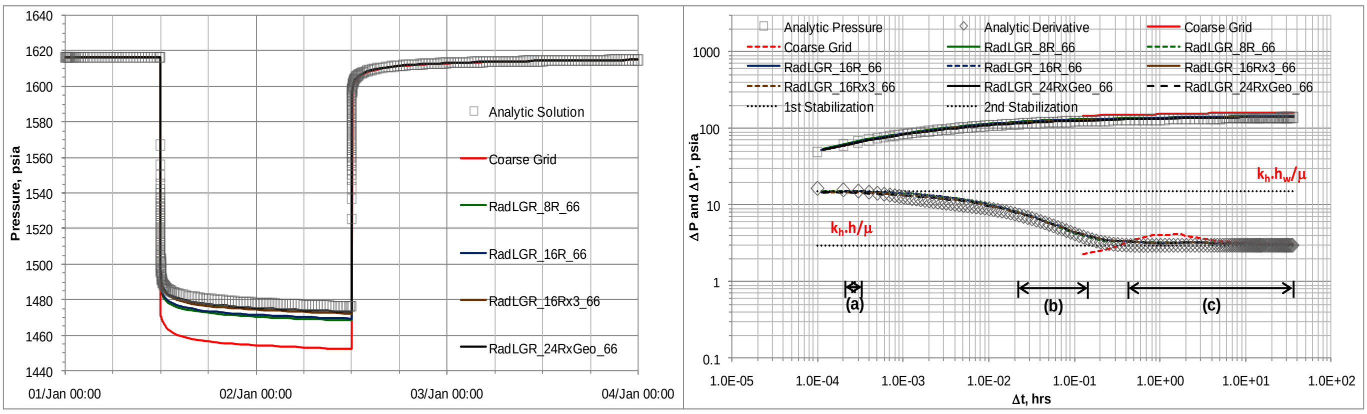

Figure 7: Comparison of simulated and analytic pressure history (left) and diagnostic plot (right) for partially penetrating vertical well modelled by radial grid refinements. Solid lines in the diagnostic plot represent pressure, while dashed lines represent the derivative.

Figure 7 shows results for the partially penetrating vertical well. While requiring additional refinement to correctly model the three-dimensional nature of well inflow, as opposed to planar, the results are equally satisfactory. There is vast improvement with respect to the coarse grid and all model parameters are in close agreement with the analytical solution; total skin being least well matched, but still with a grid related pressure loss due to skin of less than 2-psia at the point of shut-in.

Quite possibly the most impressive aspect of using radial refinement with limited entry well was the ability to reproduce the radial inflow adjacent the perforations, appearing in the derivative during early time and matched with high accuracy to the first stabilization plotted in Figure 7. This represents a vast improvement on Cartesian grids, which even for high levels of refinement have not been able to achieve such detail in matching the correct inflow behaviour. The implication is that the flow and pressure fields are being correctly modelled numerically from the microscopic to the macroscopic level.

As noted, in comparison to the fully penetrating radial flow model, the limited entry case required a more refined LGR for comparative accuracy. This seems reasonable since there are three flow regimes acting in three-dimensions, as opposed to one regime acting in two-dimensions. In terms of efficiency, for both cases presented here, radial LGR required fewer cells but were significantly more computationally expensive.

Unstructured refinement. Although not widely adopted by practicing engineers, unstructured grids have found applications in reservoir simulation due to their ability to better conform to geological features and better reflect the true flow geometry. It is these qualities that we have sought to investigate during this study – from a well modelling perspective, to exploit a grid which can better fit the geometry of well and inflow, much like the radial grid, only adaptive to more complex well geometries. Here we utilize the horizontal well models, set-up with differing well-versus-grid orientations, to investigate unstructured gridding for this application.

If to compare the results in Figure 8 and Figure 9 with the corresponding test cases using Cartesian grid refinement, shown previously in Figure 4 and Figure 5, we note some marked improvement. As we have come to expect, the overall well productivity compares well in all cases with the analytical model, but most significant, are the improvements unstructured gridding provides to modelling the near-well cylindrical and linear flow regimes. Even more impressive, the ability to do so despite changes to the well-versus-grid orientation. This represents a significant improvement on Cartesian grids, reflected in the quality of the pressure and derivative match in the diagnostic plots.

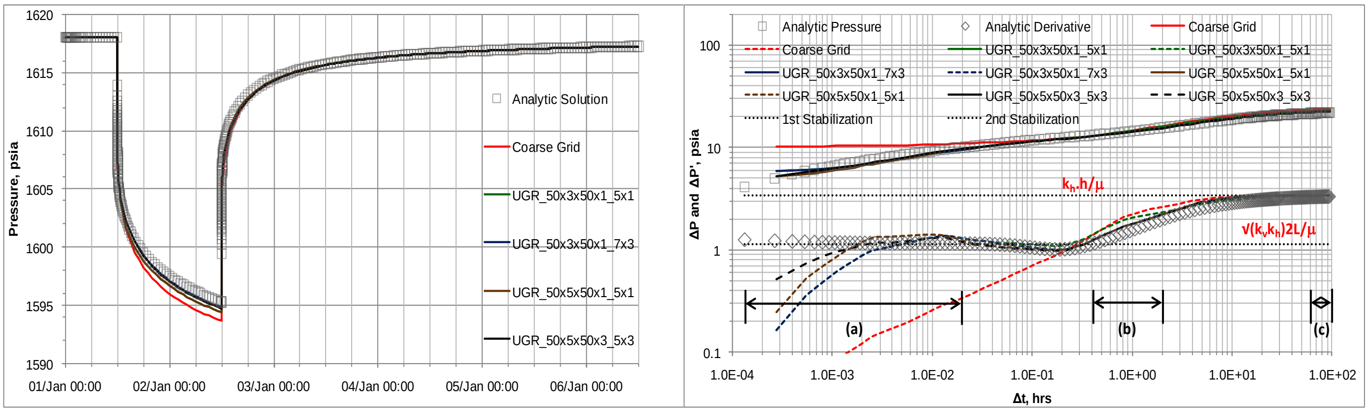

Figure 8: Comparison of simulated and analytic pressure history (left) and diagnostic plot (right) for a horizontal well modelled by unstructured grid refinements. Solid lines in the diagnostic plot represent pressure, while dashed lines represent the derivative.

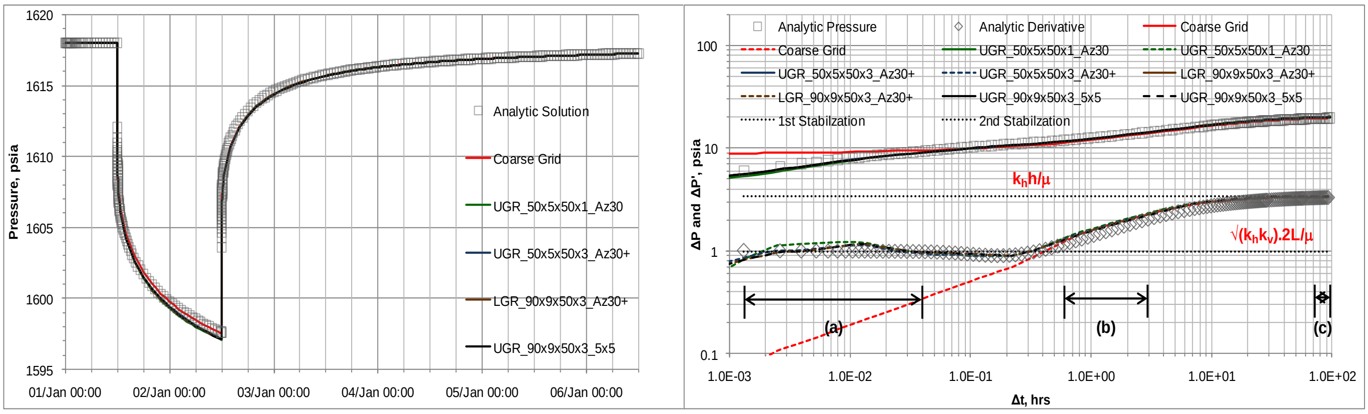

Figure 9: Comparison of simulated and analytic pressure history (left) and diagnostic plot (right) for horizontal well-versus-grid orientation case modelled using unstructured refinement – grid orthogonal to the *k*-direction and rotated 30º in the *x-y* plane. Solid lines in the diagnostic plot represent pressure, while dashed lines represent the derivative.

Analysis

On the basis of the results presented, it seems pertinent to evaluate the gridding performance in terms of accuracy and computational efficiency. To this point we have compared and contrasted results qualitatively, by way of visual comparison to analytic models; however, when comparing experimental data, it is preferable to establish some suitable metrics to allow quantitative comparison. This poses several challenges in our case.

Firstly, in terms of accuracy, comparisons can be made on the basis of the model parameters. However, to do so has meant interpretation of the simulator data using pressure transient analysis. In some cases, the solution is non-unique and therefore the model parameters contain some uncertainty. Fortunately, knowing as we do the exact reservoir and well geometries, we are able to constrain some of the model variables to achieve a more accurate interpretation. Nonetheless, some uncertainty persists and in some models more than others – essentially, the greater the number of parameters, the less unique the solution.

Secondly, to evaluate computational efficiency has involved comparison between different well models and the performance of different simulator software. Solution convergence for different well models occurs at different rates and a suitable metric to universally compare results on the basis of grid-type alone was not found. Instead, results for each well-type were normalised to that of its corresponding coarse grid and grouped by refinement type. Comparisons were made on a per well-type basis. Also, since the alternate simulation software each differs in their solver engine, it would be haphazard to directly compare the results of one with the other. This affects comparison of unstructured gridding with the other grid types.

Accuracy. Many of the simulation results have not been subjected to full pressure transient analysis and have been included for qualitative comparison only. However, a generous cross-section of them – namely those appearing in Figures 2 through Figure 9, some 36 simulated pressure histories – have been interpreted. Each of the individual analyses is provided in Appendix F.

Based on the interpretations, the accuracy of the results may be expressed in terms of root mean squared error. Although it would have been preferable, we were not able to calculate this error from the pressure and derivative curves themselves, since simulated and analytical data was not synchronised. Instead, the error calculation was made using the model parameters determined from the interpretations, in terms of deviation from the analytical model for all analyses of a given well-type. The error values have been grouped by parameter – permeability-thickness product, total skin, permeability anisotropy and horizontal well half-length – and presented graphically in Figure 10. Where there is no visible error value in the figure, either the parameter is not relevant to the given well model, or the grid was not used / assessed. Almost without exception, we observe that local refinement offers a significant improvement on the coarse grid and in general that radial and unstructured refinements perform better than Cartesian – though not in every area.

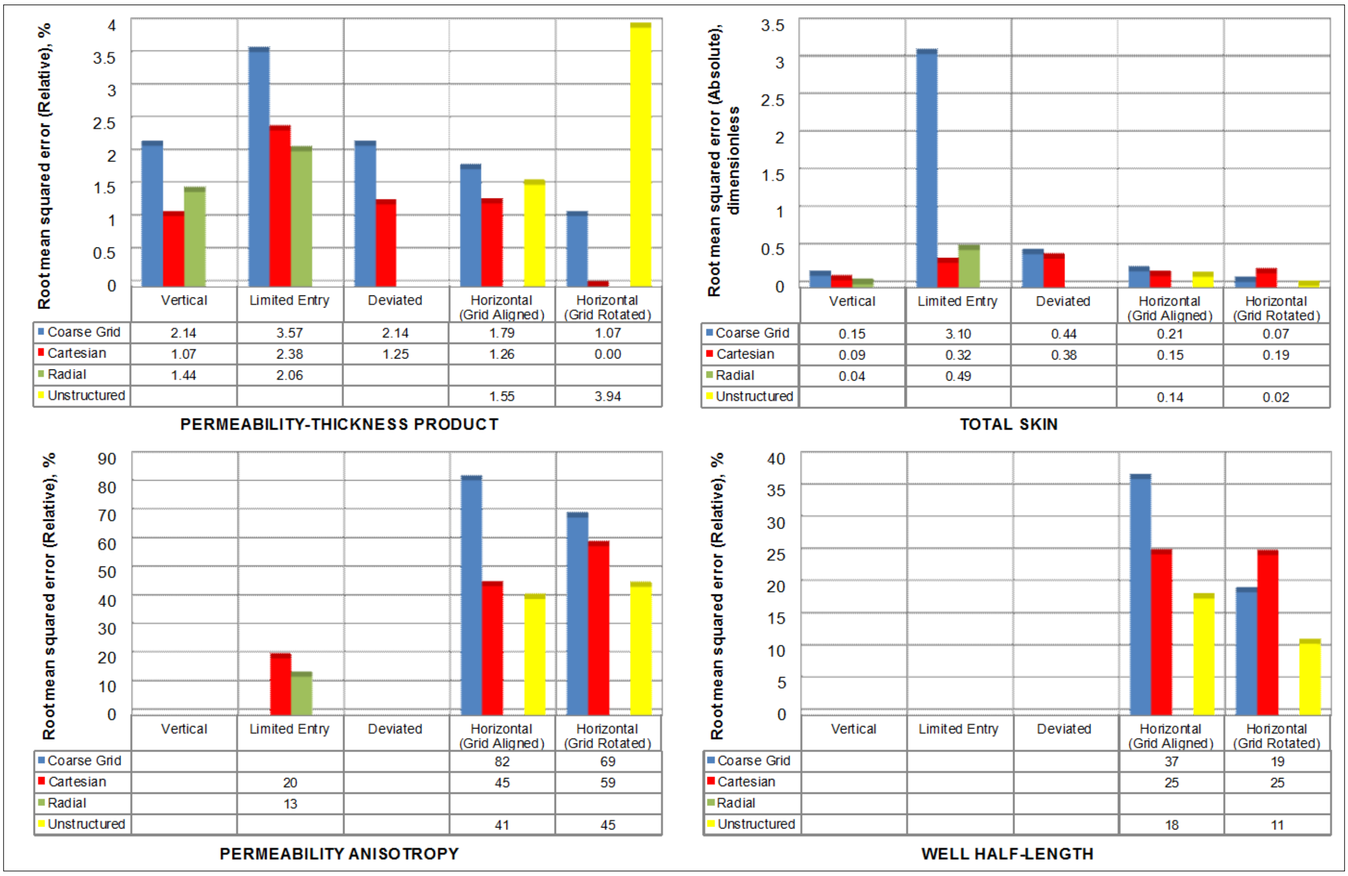

Permeability-thickness product

	Vertical	Limited Entry	Deviated	Horizontal (Grid Aligned)	Horizontal (Grid Rotated)
Coarse Grid	2.14	3.57	2.14	1.79	1.07
Cartesian	1.07	2.38	1.25	1.26	0.00
Radial	1.44	2.06			
Unstructured				1.55	3.94

Total skin

	Vertical	Limited Entry	Deviated	Horizontal (Grid Aligned)	Horizontal (Grid Rotated)
Coarse Grid	0.15	3.10	0.44	0.21	0.07
Cartesian	0.09	0.32	0.38	0.15	0.19
Radial	0.04	0.49			
Unstructured				0.14	0.02

Permeability anisotropy

	Vertical	Limited Entry	Deviated	Horizontal (Grid Aligned)	Horizontal (Grid Rotated)
Coarse Grid				82	69
Cartesian		20		45	59
Radial		13			
Unstructured				41	45

Well half-length

	Vertical	Limited Entry	Deviated	Horizontal (Grid Aligned)	Horizontal (Grid Rotated)
Coarse Grid				37	19
Cartesian				25	25
Radial					
Unstructured				18	11

Figure 10: Summary of gridding performance, by well type, in terms of accuracy on key model parameters referenced to the analytical model and expressed as root mean squared error.

The other model parameter, omitted from Figure 10, is well-bore storage. Its omission from the figure is a consequence of its limited importance on the normal time scales of reservoir simulation. It is true, however, that with the well-bore storage term being closely linked to well-block volume in the numerical well model, it is important that this be minimised to increase the resolution of the near-well flow geometry. All types of local refinement, when configured with well-blocks approaching the well-bore volume, achieve a minimised well-bore storage, but radial grids do so with the greatest effect. Cartesian and unstructured grids suffer a threshold for the reduction of well-block volume since their connection to the grid necessitates the use of a pressure equivalent radius whose dimension must be less than that of the grid-block itself.

It is important that these results are viewed with some degree of caution, since the local refinements tested throughout this study are by no means optimised to match the model parameters as closely as possible, rather designed to test different aspects of local refinement and understand the effect. It is expected that the results and analysis presented here lead to correct conclusions, but in some cases the comparisons may be slightly unfair on one grid or the other, especially where further optimisation is possible.

Computational Efficiency. As simulator performance is complex, it is difficult to pick any clear relationships between grid and cost. As far as this study is concerned, since it involves only single well models, the cost of numerical simulation appears to be primarily dependent upon the number of cells and number of non-neighbour connections, as well as the number of linear and non-linear iterations, which reflect the capability of the simulator to converge. Due to the sheer quantity, it would be inappropriate to list all simulator performance vectors here, thus they have been tabulated, in full, in Appendix H.

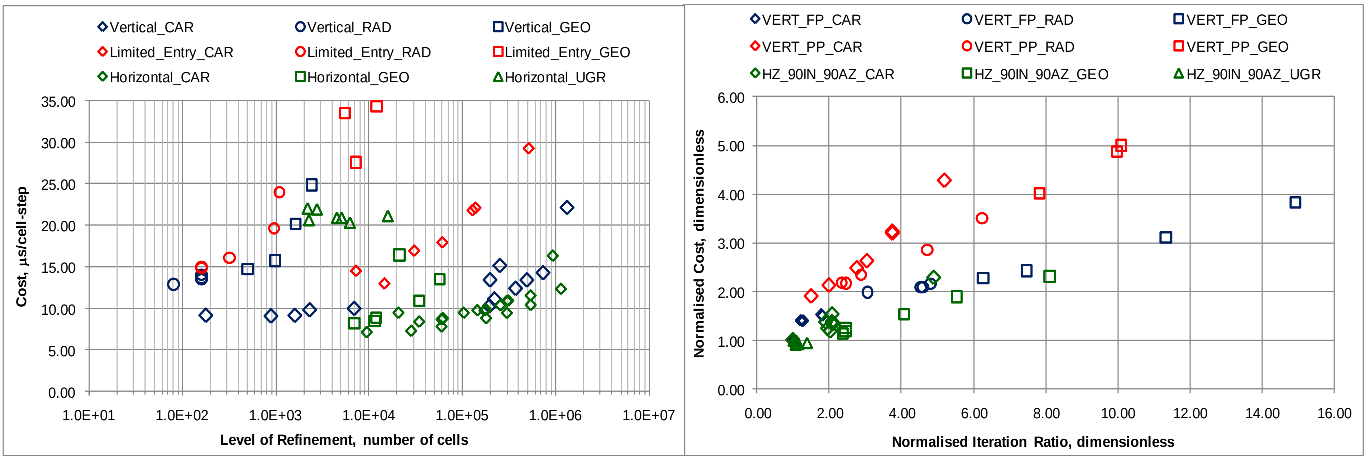

Figure 11: Scatter diagrams for computational cost. Cost versus level of refinement (at left) and normalised cost versus normalised iteration ratio (at right) for vertical and horizontal wells grouped by grid type.

Nonetheless, for the purpose of this discussion, computational efficiency is illustrated in Figure 11, where the relative cost of simulation by well model and grid-type is demonstrated. The figure plots computational cost versus the number of cells in the refinement, and the same cost, normalised for each refinement to the corresponding coarse grid, versus the iteration ratio normalised in the same way. Computational cost is defined as the total CPU time per cell, per time-step. The iteration ratio is defined as the number of linear iterations per non-linear iteration and is intended to reflect the effort required by the simulator to achieve convergence. Only the initial well models are plotted – vertical well (both fully and partially penetrating) and horizontal well – with data grouped by grid type, since for the most part the sensitivity cases exhibit similar behaviour but with slightly different scatter.

Primarily, we observe that the horizontal and fully penetrating vertical wells, modelled by Cartesian grids, follow a similar trend line with cost approximately increasing linearly in proportion to the size of the refinement (remembering that the level of refinement in Figure 11 is plotted on log-scale). The partially penetrating well appears to be more computationally expensive. Quite clearly, we observe the much greater computational cost of the geometric series and radial grids, whose cost increases rapidly as the refinement size is increased. Unstructured grids have a high initial cost, even for the coarse grid, but exhibit little dependence on refinement level since they suffer negligible increase in cost as the number of cells increases. This is probably more a contrast in the software than the grid performance itself.

The plot of normalised parameters is intended to place all grid types along an individual line for each well model, and it does so with moderate success. The partially penetrating vertical well exhibits somewhat anomalous behaviour. This plot demonstrates that the geometric series refinements, followed by radial, have the most trouble converging. It shows that simulation cost is roughly a linear function of iteration ratio for a given well type, with the partially penetrating well model being the most expensive.

Although not shown in the figure, it was determined that 9-point flux schemes were approximately twice as computationally expensive as the standard 5-point flux scheme for the cases compared.

Discussion

Implications for Reservoir Simulation. We have seen how the attributes of the grid local to the well impact the quality with which numerical models are capable of producing the correct behaviour and assessment of gridding has been made through qualitative and quantitative comparison to the analytical models. It is the implication of these results to practical reservoir simulation that must now be addressed.

Key parameters of any well-model are permeability-thickness product and skin. These parameters determine the overall well productivity and without accuracy on these parameters our well model will be inadequate. Fortunately, the work done previously, by Peaceman and others, has given rise to well connection factors which effectively connect well to grid and for most cases result in the correct well productivity. There are limitations, however, such as the limited entry and horizontal well cases, where the three-dimensional nature of flow affects the accuracy of numerical well productivity – in some cases significantly. Peaceman himself recognised that there were certain assumptions underlying his work and in some cases alternate well models were required.

Productivity is one important element of the well model, but should not overshadow the value of having correct inflow behaviour – correct flow and pressure fields around the well. Productivity index (PI) multipliers are available in the software to correct mismatched productivity due to gridding (and local geology), but these will offer no improvement to the flow regime description in the simulation. Even where the geology is known, it has been shown that the only way to obtain accurate approximation to the flow geometry about a well is through grid refinement.

Certainly the flow in the simulator converges on the well regardless of the grid, but the nature of that convergence is only correct if the grid honours the flow geometry. This has been reflected in discrepancies with the analytic pressure derivates shown in the results and appears as grid induced skin or apparent permeability anisotropy. Incorrect convergence due to poor near-well gridding often places the well model automatically in error. This becomes more significant with increased complexity of the well model.

While certain parameters can be corrected by PI multipliers, others, such as permeability anisotropy and horizontal well-length cannot. Assuming completion details and geology are known (or honour some geostatistical upscaling technique) and were fixed during model construction, these parameters should not be modified to correct their apparent exaggeration by the grid. It is the grid that requires correction. It can be argued that these parameters are the most critical, not to total well productivity, but to the well inflow behaviour, since they have the greatest impact on the geometry of flow about the well. It has been clearly demonstrated that a grid which honours the flow geometry achieves much more accurate inflow performance – the results for radial grids about vertical wells and unstructured grids about horizontal wells provide ideal examples.

The implication of honouring (or not) the flow regime about a well may not be so apparent in single-phase simulations such as these, but the value will certainly be recognised when modelling real cases. For example, to history match multi-phase rates from a horizontal well with true three-dimensional flow geometry, located near an oil-water or gas water contact, may prove problematic. It will become all the more difficult if the modelled flow geometry represents a well just two thirds the length with an apparent permeability anisotropy nearly twice the actual value – as was the case with our coarse grid simulation of a horizontal well. It is important for the modeller to understand the significance of gridding around the well or else these effects may not be immediately obvious. Application of PI multipliers may have some value to the history match problem at hand, but will certainly not improve the predictive capability of the well-model as reservoir conditions change.

Honouring the flow geometry about wells through gridding might also find key application to the simulation of multi-lateral wells. Here, flow geometry is complex, wells are highly deviated and there will almost certainly be misalignment of well and grid for at least one lateral, if not all. Furthermore, the inflow to each well segment (or lateral) will likely be affected by some or all of the others. This study has shown that even with intensive local Cartesian refinement about relatively simple wells, the flow regime definition and apparent model parameters can be inaccurate, a situation that can be improved through the use of unstructured gridding. The expectation is that this will be exaggerated significantly in multi-lateral wells.

Based on some key observations of this work – primarily the importance of grid geometry near wells, the detrimental effect of adverse well-versus-grid orientation and unfavourable cell aspect ratios, the limited application of radial refinement and the ineffectiveness of 9-point flux schemes to improving simulated well inflow performance – the overwhelming perception is of the value in unstructured gridding near wells to offer the most versatility and most accurately simulate inflow performance.

Recommendations for Further Research. How to use pressure transient analysis to refine real grids with real well geometries and in real reservoir models is an area worthy of further effort. Such an idea, while not exactly a new one, is not a part of conventional reservoir simulation work-flows and perhaps not intuitive to the reservoir engineering community at large, but could offer value to the well model. The challenge would be reconciling the real geology first, before optimising the grid. The availability of well test data could help, or perhaps well test simulations using sector models taken from the geostatistical realizations could be used (or both), but clearly further research would be required to determine if there is any value in such an approach.

When conducting a pressure transient analysis for simulated data from a fully penetrating well it has been observed that the well-blocks act somewhat like a finite conductivity fracture, with fracture half-length equal to the half-width of the cell (e.g. $x_f = 0.5DX$) and the fracture width equivalent to the other areal dimension of the cell (e.g. $w_f = DY$). The conductivity then is equivalent to the well connection factor. This enables very good match to the pressure and derivative on diagnostic plot and makes some sense since the passage of fluids from well-block to well is no longer one of flow in porous media, but a little like linear flow inside a finite conductivity fracture controlled by the well connection factor (instead of fracture conductivity). There may be no useful meaning in this, but it is worth some further thought.

Furthermore, it may be possible to determine some correlations for the correction of grid induced pseudo-skin by way of PI multipliers, which would require a carefully designed set of experiments catering to that objective, and finally, investigation of the gridding effect with some more realistic examples of well geometry, reservoir geology and/or multi-phase fluids is expected to yield interesting results that might also lead to new workflows for gridding to wells for real applications.

Conclusions

1. In cases of three-dimensional flow regimes (e.g. limited entry, horizontal wells), local grid refinement is the only way to accurately model well productivity and the geometry of flow in the vicinity of the well.
2. Analysis of the results from this study has shown that significant improvement can be obtained on the accuracy of well-model parameters in numerical simulation through local refinement. Between coarse and refined grids improvements of 1-2% (half the error) can be expected on permeability-thickness product, improvement on the total skin from 0.1 to 2.8 (15-1000% better accuracy), improvements of between 10 and 40% for accuracy of permeability anisotropy and between 8 and 19% for the accuracy of horizontal well half-length. With well-bore storage directly linked to well-block volume, the error can be reduced by several hundred-thousand percent by the introduction of local refinement, which carries real significance to an accurate representation of the near-well flow geometry.
3. Unstructured gridding is by far the most accurate and adaptable in cases of complex well-geometries and adverse well-versus-grid orientations. For arbitrary well and grid geometry it provides a close match to the flow regime behaviours and an overall improvement on Cartesian refinement.
4. Cartesian cell aspect ratio is significant when simulating three-dimensional flow, especially where cell length normal to the well track greatly exceeds that parallel to it. For best results, aspect ratio within the refinement should be kept cubic (or near thereto).
5. 9-point flux schemes do not exhibit any benefit to near-well modelling, but have been observed to double the computational cost. Although an oversight prior performing the simulations in this study, it is thought that 9-point schemes do not readily extend to local grid refinement, which is a theoretical problem that prevents the higher-order scheme being resolved at the interface of the coarse grid and local grid.

Nomenclature

B = oil formation volume factor, rbbl/stb
c_t = total compressibility, psi^{-1}
C_D = dimensionless storage, dimensionless
D_l = grid block dimension in l-direction, ft
D_n = grid block dimension in n-direction, ft
D_v = grid block dimension in v-direction, ft
DX = grid block dimension in i-direction, ft
DY = grid block dimension in j-direction, ft
DZ = grid block dimension in k-direction, ft
h_l = horizontal plane distance along well-bore, ft
h_v = vertical plane distance along well-bore, ft
h_w = perforated interval length, ft
h_x = i-component distance along well-bore, ft
h_y = j-component distance along well-bore, ft
h_z = k-component distance along well-bore, ft
h = net pay zone thickness, ft
i,j,k = unit vectors for Cartesian coordinate system
k_h = horizontal permeability, mD
k_l = l-component horizontal permeability, mD
k_n = permeability normal to the well-bore, mD
k_{rw} = gas relative permeability, dimensionless
k_{ro} = oil relative permeability, dimensionless
k_{rw} = water relative permeability, dimensionless
k_s = spherical permeability, mD
k_v = vertical permeability, mD
k_x = permeability in the i-direction, mD
k_y = permeability in the j-direction, mD
k_z = permeability in the k-direction, mD
k = permeability, mD
kh_x = i-component permeability thickness product, mD-ft
m_{SPH} = slope Horner straight line, psi-√hr
m_{WBS} = slope well-bore storage straight line, psi/hr
p_o = well-block pressure, psia
p_{wf} = well flowing pressure, psia
p_D = dimensionless pressure, dimensionless
p = average reservoir pressure, psia
q = oil production rate, stb/d
r_b = well-block equivalent radius, ft
r_l = pressure equivalent radius for n-v plane, ft
r_o = pressure equivalent radius, ft
r_{ox} = pressure equivalent radius for y-z plane, ft
r_{oy} = pressure equivalent radius for x-z plane, ft
r_{oz} = pressure equivalent radius for x-y plane, ft
r_{oz} = pressure equivalent radius for x-y plane, ft
r_v = pressure equivalent radius for l-n plane, ft
r_w = well bore radius, ft
r = radius at a given point of interest, ft
S_o = oil saturation, dimensionless
S_t = total skin, dimensionless
S_w = water saturation, dimensionless
S_{wc} = critical water saturation, dimensionless
S = damage skin, dimensionless
t_D = dimensionless time, dimensionless
T_l = l-component transmissibility, mD-ft
T_v = v-component transmissibility, mD-ft
T_x = i-component transmissibility, mD-ft
T_y = j-component transmissibility, mD-ft
T_z = k-component transmissibility, mD-ft
T = total transmissibility, mD-ft
w_f = fracture width, ft

kh_y = j-component permeability thickness product, mD-ft
kh_z = k-component permeability thickness product, mD-ft
l,n,v = unit vectors for unstructured grid system
$\Delta p_{i,j}$ = grid-block incremental pressure change, psia
L = well half-length, ft
m_{CF} = slope cylindrical flow straight line, psi/cycle
Δp = build-up pressure, psia
$\Delta p'$ = build-up pressure derivative, psia
x_f = fracture half-length, ft
x,y,z = Cartesian axes
z_w = distance base pay-zone to perf. mid-point, ft
Δt = time-step increment, hrs
θ = well inclination, degrees
μ = oil viscosity, cp
ϕ = porosity, dimensionless

References

1. Bourdet, D. 2002. *Well Test Analysis: The Use of Advanced Interpretation Models*. Amsterdam: Elsevier Science B.V.
2. Consonni, P., Thiele, M.R., Palagi, C.L., and Aziz, K. 1993. Flexible Gridding Techniques for Coning Studies in Vertical and Horizontal Wells. SPE Paper 25563 presented at the SPE Middle East Oil Technical Conference and Exhibition, Bahrain, 3-6 April.
3. ECLIPSE Simulation Software. 2010, c. Schlumberger, http://www.slb.com/services/software/reseng/blackoil.aspx
4. Forsyth, P.A. 1989. A Control-Volume, Finite-Element Method for Local Mesh Refinement in Thermal Reservoir Simulation. Paper SPE 18415 presented at the SPE Symposium on Reservoir Simulation, Houston, Texas, 6-8 February.
5. Fung, S.K., Buchanan, L., and Sharma, R. 1993. Hybrid-CVFE Method for Flexible Grid Reservoir Simulation. SPE Paper 25266 presented at SPE Symposium on Reservoir Simulation, New Orleans, Louisiana, 28 February – 3 March
6. Gringarten, A.C., Bourdet, D.P., Landel, P.A., and Kniazeff, V.J. 1979. A Comparison Between Different Skin and Wellbore Storage Type Curves for Early-Time Transient Analysis. SPE Paper 8205 presented at the 54th Annual Fall Meeting, Las Vegas, Nevada 23-26 Sepetember.
7. Gunasekera, D., Cox, J., and Lindsey, P. 1997. The Generation and Application of k-Orthogonal Grid Systems. Paper SPE 37998 presented at the 14th SPE Symposium on Reservoir Simulation, Dallas, Texas, 8-11 June.
8. Heinemann, Z.E. and von Hantelmann, G.V. 1983. Using Local Grid Refinement in a Multiple Application Reservoir Simulator. SPE Paper 12255 presented at the Reservoir Simulation Symposium, San Francisco, California, 15-18 November.
9. Heinemann, Z.E., Brand, C.W., Munka, M., and Chen, Y.M. 1989. Modelling Reservoir Geometry with Irregular Grids. SPE Paper 18412, SPE Symposium on Reservoir Simulation, Houston, Texas, 6-8 February.
10. Horner, D.R. 1951. Pressure Build-Up in Wells. Proc. Third World Petroleum Congress, Leiden, 503-22
11. ECLIPSE Simulation Software. 2010, c. Schlumberger, http://www.slb.com/services/software/reseng/blackoil.aspx
12. Intersect Software. 2010, d. Schlumberger. http://www.slb.com/services/software/reseng/intersect.aspx
13. Palagi, C.L. and Aziz, K. 1994. Use of Voronoi Grid in Reservoir Simulation. SPE Advanced Technology Series **2** (2): 69-75; SPE 22889.
14. Peaceman, D.W. 1977. Interpretation of Well-Block Pressures in Numerical Reservoir Simulation. SPE Paper 6983 presented at the SPE-AIME 52nd Annual Fall Technical Conference and Exhibition, Denver, 9-12 October.
15. Peaceman, D.W. 1983. Interpretation of Well-Block Pressures in Numerical Reservoir Simulation With Nonsquare Grid Blocks and Anisotropic Permeability. SPE Paper 10528 presented at the 1982 SPE Symposium on Reservoir Simulation, New Orleans, Louisiana, 31 January – 3 March.
16. Peaceman, D.W. 1993. Representation of a Horizontal Well in Numerical Reservoir Simulation. SPE Advanced Technology Series 1 (1): 7-16; SPE 21217
17. Pedrosa, O.A. Jr and Aziz, K. 1985. Use of a Hybrid Grid in Reservoir Simulation. Paper SPE 13507 presented at the Symposium on Reservoir Simulation, Dallas, Texas, 10-13 February.
18. Petrel Seismic to Simulation Software. 2010, b. Schlumberger, http://www.slb.com/en/services/software/geo/petrel.aspx
19. Saphir Software. 2010. KAPPA Engineering, http://www.kappaeng.com/software.aspx?f=XMLSoftDoc&n=SAP&soft=SAP
20. Schlumberger. 2010, a. ECLIPSE Schedule Manual, 275-277.
21. Thompson, J.F., Soni, B.K., and Weatherill, N.P, ed.1999. *Handbook of Grid Generation*, Preface. Washington, D.C: CRC Press
22. van Poollen, H.K. and Breitenback, E.A.1968. Treatment of Individual Wells and Grid in Reservoir Modeling. Paper SPE 2022 presented at the SPE Symposium on Numerical Simulation of Reservoir Performance, Dallas, Texas, 22-23 April.
23. von Rosenberg, D.U. 1982. Local Mesh Refinement for Finite Difference Methods. Paper SPE 10974 presented at the 57th Annual Fall Technical Conference and Exhibition, New Orleans, Louisiana, 26-29 September.
24. Yanosik, J.L. and McCracken, T.A. 1976. A Nine-Point Finite Difference Simulator for Realistic Prediction of Adverse Mobility Ratio Displacements. SPE Paper 5734 presented at the SPE-AIME Fourth Symposium of Numerical Simulation of Reservoir Performance, Los Angeles, California, 19-20 February.

-

Appendix A: Critical Literature Review

Summary

SPE Paper No.	Year	Title	Author(s)	Contribution
2022	1968	Treatment of Individual Wells and Grid in Reservoir Modeling	van Poollen, H.K. and Breitenback, E.A	First significant attempt to relate well to grid-block pressures in reservoir simulation.
6983	1977	Interpretation of Well-Block Pressures in Numerical Reservoir Simulation	Peaceman, D.W.	Developed the first accurate interpretation of well-block pressures in reservoir simulation for square grid-blocks in isotropic medium.
10974	1982	Local Mesh Refinement for Finite Difference Methods	von Rosenberg, D.U.	Introdcued local grid refinements to Cartesian finite difference simulation that were truly local to the well, unlike previous refinements which extended to the boundaries of the grid
12255	1983	Using Local Grid Refinement in a Multiple Application Reservoir Simulator	Heinemann, Z.E. and von Hantelmann, G.V.	Another early introduction of local grid refinement to finite difference type numerical reservoir simulation
10528	1983	Interpretation of Well-Block Pressures in Numerical Reservoir Simulation With Nonsquare Grid Blocks and Anisotropic Permability	Peaceman, D.W.	Determined the general form of the well-connection factor for rectangular grid-blocks and anisotropic medium
13507	1985	Use of a Hybrid Grid in Reservoir Simulation	Pedrosa, O.A. Jr and Aziz, K.	Introduced radial local grid refinements into a finite difference Cartesian grid to improve near-well modelling
18412	1989	Modelling Reservoir Geometry with Irregular Grids.	Heinemann, Z.E., Brand, C.W., Munka, M., and Chen, Y.M.	Introduced unstructured gridding to reservoir simulation
18412	1991	Modelling Reservoir Geometry with Irregular Grids	Z.E. Heinemann, C.W. Brand, M. Munka, and Y.M Chen	First to use perpendicular bisector (PEBI) grids to describe reservoir geometry. Made use of full and anisotropic but symmetric permeability tensors. These are known as k-orthogonal grids, or generalized PEBI (GPEBI)
25563	1993	Flexible Gridding Techniques for Coning Studies in Vertical and Horizontal Wells	Consonni, P., Thiele, M.R., Palagi, C.L., and Aziz, K.	An early practicle application of unstructured gridding to well-modelling for water coning study.
25266	1993	Hybrid-CVFE Method for Flexible Grid Reservoir Simulation	L.S.K Fung, L. Buchanan, and R. Sharma	First application of radial near-well gridding with CVFE method reservoir simulators
22889	1994	Use of Voronoi Grid in Reservoir Simulation	C.L. Palagi and K. Aziz	First to describe a method of implementing Voronoi grids for field scale simulations
37998	1997	The Generation and Applicaton of k-Orthogonal Grid Systems	D. Gunasekera, J. Cox, and P. Lindsey	The process of generating good k-orthogonal PEBI and composite tetrahedral grids applicable to a wide class of reservoir simulation problems.

Table A-1: Milestones in the development of near-well modelling techniques in reservoir simulation.

SPE 6893 (1978)

Paper Title: Interpretation of Well-Block Pressures in Numerical Reservoir Simulation

Author(s): Peaceman, D.W.

Contribution to knowledge: A work of key importance to the understanding on the connection of wells to grid-blocks in numerical reservoir simulators. The paper advanced the concept of pressure-equivalent radius, and its derivation, respecting radial inflow in the vicinity of the well, but also accounting grid-block dimensions.

Furthermore, the paper provided showed how build-up test data can be used for the purpose of history matching well-block pressures.

Objective of the paper: To determine a correction to the recognized problem that well-block pressure modelled through numerical simulation does not match the bottom-hole flowing pressure of the well. This was an issue not well addressed by the literature of the time.

Methodology used:

1. Defined pressure equivalent radius, r_o, as the distance at which steady-state flowing pressure of the well is equal to the numerically calculated pressure for the well-block, such that $q = \frac{2\pi kh}{\mu} \frac{p_o - p_{wf}}{\ln\left(r_o/r_w\right)}$

2. According the given equation, provides numerical evaluation of r_o determined from a straight-line of slope ½ π plotted through a pressure term, $(p_{i,j} - p_o)kh/q\mu$, calculated using the numerical solution of grid block pressures, versus the logarithm of distance from the well, up to 6 Δx. This method determines r_o from the intercept of the straight-line with $p_{i,j} - p_o = 0$, as $r_o = 0.2\ \Delta x$, where Δx is the cell side length.

3. Provides mathematical proof using a finite-difference-type flux calculation describing flow into the well-block as the sum of influx from its four orthogonal neighbours. This gives the approximate result that $r_o = 0.208\ \Delta x$. Approximate because it assumes the pressure of the neighbouring cells lie exactly on the straight line, when they actually lies very near it, but not exactly on it.

4. Provides exact calculation of r_o from a numerical steady-state pressure distribution between injector and producer together with a corresponding analytical model for a repeated five-spot pattern given by Muskat (1934). As the number of intermediate grid blocks increases, the value of r_o converges to 0.1982 Δx.

5. Demonstrates that the pressure equivalent radius, derived for steady-state radial flow, can also be derived, by similar means, with the same result for transient conditions.

Conclusion reached:

1. Well block flowing pressure, $p_o = p(r_o) = p(0.2\Delta x)$ which can be related to the well-flowing pressure using the conventional steady-state radial inflow equation.

2. Build-up pressures should be measured at a time equal to $67.5\emptyset\mu c_t \Delta x^2/k$ for history matching with simulator well-block pressures.

Comments:

SPE 7697 (1981)

Paper Title: Representing Wells in Numerical Reservoir Simulation: Part 1 - Theory

Author(s): Williamson, A.S; Chappelear, J.E.

Contribution to knowledge: This paper offers several perspectives on the limitations of existing methods of well representation in reservoir simulation and provides improved methods for application of analytical source functions as well representations. Also describes attempts to decouple the well bore with grid-block and better model flowing pressure in terms of the lift profile dependencies.

Objective of the paper: To extend the theoretical basis of the source representation of wells in numerical simulation and to give a number of useful applications for the basic method. Moreover, to elaborate several areas of limitation with existing well modelling techniques in reservoir and stimulate further research (or publication thereof) on the topic.

Methodology used:

1. An analytic solution is constructed with a given well bottomhole flowing pressure and with pressures which coincide with the nodal pressures of surrounding adjacent grid blocks. This equation is similar in form to previous derivations, but includes a matrix term of geometrical terms obtained by fitting an analytic expression for the local pressure distribution near the well to the pressures in the four nodes in blocks adjacent to the well block.

2. Extending this theory to two or wells in a single well block, the paper describes two methods of handling such problems; either (a) by replacing the multiple wells with a single pseudo-well or (b) a more rigorous treatment of each individual well using a source term for each individual well, specification of the interference between wells and a source term for the well-block itself.

3. It is further shown how local heterogeneities such as permeability or net thickness variation between grid-blocks and also near-well damage (i.e. skin) can be included into the given source function.

4. Similar to Peaceman (1978), the paper describes non-steady transient pressure / flow behaviour (i.e. step-type change) which does not compromise the use of source functions to represent the well, however goes on to define continuous changes to well and local nodal pressures for which steady-flow assumptions are unlikely to yield acceptable results until the pressure transients have migrated through the region of the well encompassed by the well grid-block. For the latter case a perturbation analysis is performed to quantify the ratio of transient to steady well flow contributions.

5. The paper further describes a methodology for the calculation of sand-face pressure gradient.

Conclusion reached:

1. The pressure boundary conditions on a well surface can be represented in a manner suitable for inclusion in a reservoir simulator.

2. Saturation boundary conditions have usually been included in well models in a very approximate manner.

3. A well boundary can be approximated by sources of a particular form.

Comments:

SPE 9770 (1981)

Paper Title: Representing Wells in Numerical Reservoir Simulation: Part 2 - Implementation

Author(s): Chappelear, J.E; Williamson, A.S.

Contribution to knowledge: While not contributing any new theoretical material, it elaborates on the theory presented in the earlier supplementary paper (Part 1, SPE 7697) by the same authors; discusses the implementation of the well model into numerical simulator.

Objective of the paper: To detail numerical aspects of well model implementation in the reservoir simulator, with particular treatment of black-oil, compositional and thermal well models. In addition, and like Part 1, to evoke further research / publication on the topic of well modelling in reservoir simulation.

Methodology used:

1. The well model is given by $q_p = \frac{2\pi(k.\Delta z)k_{rp}\left(p_{well}+{}^{1}/_{2}\sum_{k'=1}^{k-1} g(\rho_{k'}+\rho_{k'+1})z_{k'}-p_{node}\right)}{\mu_p B_p\left[ln\left({}^{r_e}/_{r_w}\right)-0.9984+S+Dq_g\right]}$, where the terms are essentially according to Darcy's law within square grid blocks and include gravity, as defined in the paper.

2. For reasons pertaining to matching historical production during history matching and honouring rate constraints during prediction, the well model is rate constrained and bottomhole flowing pressure is chosen to honour the constraints.

3. The well model is incorporated for an IMPES-type simulator as follows:

    a. Everything in the well model is evaluated at the beginning of the time-step to determine the well constraint;

    b. Node and well flowing pressures are determined at the new time-step, keeping the constraint fixed;

    c. Gravity heads and productivity indices for each completion interval are computed using grid-block values and are not recomputed within the given time-step;

    d. The well is rate constrained if productivity index is larger than the imposed rate constraints, else it is pressure constrained. In either case a well rate is allocated and used to compute p_{well}

    e. Material balance equations are then solved, the well model is recalled to calculate p_{well} and the process is repeated iteratively until material balance errors are within a pre-specified tolerance.

Conclusion reached:

A wide variety of constraints and conditions was found valuable in representing well behaviour in reservoir simulations.

Comments:

The paper also raises questions for further work, pertaining to how one might measure / check the well model (e.g. against analytic solutions, by comparison of solutions given in different grid-types, experiments or theoretical investigations.

SPE 10528 (1983)

Paper Title: Interpretation of Well-Block Pressures in Numerical Reservoir Simulation with Nonsquare Grid Blocks and Anisotropic Permeability

Author(s): Peaceman, D.W.

Contribution to knowledge: A definitive treatment of well connection factor still widely adopted today; determined the general relationship for bottomhole pressure (BHP) and well-block pressure (WBP) to account for cell aspect ratio and permeability anisotropy, both in terms of planar radial flow.

Objective of the paper: To investigate the effect of nonsquare grid ($\Delta x \neq \Delta y$), or aspect ratio (α) and anisotropic permeability ($k_x \neq k_y$) on the pressure equivalent radius (r_o) of the well-block.

Methodology used:

1. A similar analytic derivation can be made for nonsquare grid-blocks as that in Peaceman's earlier work on square grid-blocks (Peaceman, 1978), suggesting a quotient $\frac{r_o}{\Delta x} = exp\left(\frac{\ln(\alpha)-\pi\alpha}{1+\alpha^2}\right)$
2. Numerical experiments were performed using a repeated five spot pattern for various aspect ratios and grid refinements. Due to symmetry, only ¼ of the pattern needed to be considered. The domain was discretised into M x N dimensions in the i- and j-directions and the results of the simulations used to determine the equivalent well-block radii according to Muskat's (1937) relationship for pressure drop between injector and producer.

   $\frac{r_o}{\Delta x} = \sqrt{2}M.exp\left[-0.6174 - \frac{\pi kh}{q\mu}\left(p_{M,N} - p_{o,o}\right)\right]$ and $\frac{r_o}{\Delta y} = \sqrt{2}N.exp\left[-0.6174 - \frac{\pi kh}{q\mu}\left(p_{M,N} - p_{o,o}\right)\right]$
3. The several theories are tested by plotting aspect ratio versus the relevant quotients;
   a. WBP as the areal average of a circle with the same area as that of the well-block (van Poollen et al, 1968) is disproven since the quotient $r_o/(\Delta x\Delta y)^{½}$ does not equal the constant of integration, as his theory suggests;
   b. Extrapolated values of $r_o/\Delta x$ determined from numerical experiments are divided by the analytic quotient determined as per Peaceman's earlier work (see 1 above). Failure of this ratio to remain constant with varying aspect ratio is proof enough to invalidate it;
   c. According to the reasoning given in the paper, it is supposed that the correct quotient should be the ratio of r_o to the diagonal of the grid block, $r_o /(\Delta x^2 + \Delta y^2)^{½}$, and this is indeed demonstrated concluding that $r_o = 0.14(\Delta x^2 + \Delta y^2)^{½}$.
4. Finally, using the differential equation for steady-state pressure $k_x\frac{\delta^2 p}{\delta x^2} + k_y\frac{\delta^2 p}{\delta x^2} = 0$ and making a change of variables $u = x.(k_y/k_x)^{¼}$ and $v = y.(k_x/k_y)^{¼}$ to convert to Laplace's equation, a derivation was performed to arrive at a general equation for r_o in anisotropic media.

Conclusion reached: In general, WBP can be related to BHP as follows, $p_o - p_{wf} = \frac{qu}{2\pi\sqrt{k_x k_y}h} ln\left(\frac{r_o}{r_w}\right)$, where $r_o = \frac{0.28\left[\Delta x^2\sqrt{k_y/k_x}+\Delta y^2\sqrt{k_x/k_y}\right]^{1/2}}{\sqrt[4]{k_y/k_x}+\sqrt[4]{k_x/k_y}}$, which holds for nonsquare grid and anisotropic media.

SPE 11759 (1985)

Paper Title: The Proper Interpretation of Field-Determined Buildup Pressure and Skin Values for Simulator Use

Author(s): Odeh, A.S.

Contribution to knowledge: First to recognise the fundamental difference between field determined and numerical simulator skin values, and to determine a correction factor to allow the reconciliation between them. Extended the idea first proposed by Peaceman (1978), for the special case of two-dimensional flow and square grid blocks, to the general case of three-dimensional flow and nonsquare grid-blocks, whereby real well pressure build-up data can be compared with numerically generated well-block pressure.

Objective of the paper: There are essentially two objectives of the paper:

1. To consider the necessity to scale skin field determined skin parameters to give an acceptable match between real pressure drop due to skin and the model-calculated value.

2. To determine an equation that gives the build-up time, Δt, when the well pressure becomes equal to the cell pressure after accounting for both three-dimensional flow and the well completion.

Methodology used:

1. The physical elements of skin are stated and mathematically defined. In this case, the elements are damage skin, termed s_A, located in a narrow region of altered permeability close to the well-bore, and restricted entry skin s_R, resulting from the convergence of flow to partially penetrating completions.

2. The radial flow equation describing flow close to the well-bore, and used by the simulator, is defined to demonstrate that s_R is accounted for inherently, but that s_A is not.

3. A scaling factor is developed that corrects the skin factor used in the simulator inflow equation, based on the well connection kh being equivalent to $\Sigma\Delta k_i\Delta z_i$ of the well-blocks, while the real value is the average kh of the drainage area.

4. A derivation is offered for the case where production time, t, is much greater than build-up time, Δt, and therefore a build-up time can be determined when the simulator well-block pressure equals the actual build-up pressure for use in history matching. This idea follows from Peaceman (1978) but extends the special case in Peaceman's paper to the general case.

Conclusion reached:

1. The simulator inflow equation, with corrected skin, is $q_i = \frac{7.08\times10^{-3} k_i \Delta z_i \Delta p_i}{B\mu\left[ln\left({}^{r_o}/_{r_w}\right)+\frac{\sum_{i=1}^{hp}\Delta z_i k_i}{\overline{kh}} s_A\right]}$

2. The shut-in pressure of an actual well will equal the well-block pressure after a shut-in time, $\Delta t = \left[\left({}^{r_o}/_{r_w}\right)^2\right]^{\overline{kh}/\sum_{i=1}^{hp}\Delta z_i k_i} \left(\frac{1687 r_w{}^2 \emptyset \mu c_t}{\bar{k}}\right) e^{-2s_R}$

Comments: The paper does not offer any numerical tests or proofs of the theoretical statements presented but they appear to be sound.

SPE 18412 (1991)

Paper Title: Modelling Reservoir Geometry with Irregular Grids

Author(s): Heinemann, Z.E; Brand, C.W; Munka, M; Chen, Y.M.

Contribution to knowledge: Irregular (unstructured) grid block systems for simulation of complicated reservoirs are proposed, making use of perpendicular bisector (PEBI) grids and a finite-volume method for discretization of multi-phase flow equations.

An evaluation of irregular grid performance is demonstrated through several numerical examples complete with comparison to Cartesian grids;

1. PEBI grids have as good (or better) performance with respect to grid-orientation effect as the nine-point Cartesian grid up to mobility ratios of at least 50

2. Computational efficiency (i.e. CPU time per grid-block) is approximately the same for both PEBI and Cartesian grid, but the same simulation can be achieved with fewer PEBI grid-blocks

3. PEBI grids can perfectly represent analytical solutions to radial flow performance around wells

Objective of the paper: To demonstrate the flexibility of PEBI grids in reservoir simulation and to compare the performance of PEBI grids with traditional grids based on Cartesian coordinate systems.

Methodology used:

6. Finite-volume discretization of the multi-phase flow equations using an integral approach similar to that described by Pedrosa and Aziz (1986) and Ngheim (1988)

7. Spatial discretization using a PEBI grid satisfying the conditions of Delaunay triangulation. The 2D PEBI grid was constructed in an areal sense only and projected vertically through the model layers.

Conclusion reached:

3. PEBI grids offer a higher flexibility to represent the reservoir geometry since the location of grid-points can be chosen freely

4. PEBI grids are well suited to calculating radial flow and well performance as they can be constructed with higher cell density around wells and with a smooth transition to the coarse-grid region

5. The grid-orientation effect is lower for PEBI grids than for five-point Cartesian grid, but slightly higher than that for the nine-point Cartesian scheme.

Comments:

The approach used for finite-volume discretization of the differential equations accounts for anisotropy by way of a permeability tensor which is symmetric and orthogonal to block surfaces. This is known as k-orthogonal PEBI gridding.

SPE 25563 (1993)

Paper Title: Flexible Gridding Techniques for Coning Studies in Vertical and Horizontal Wells

Author(s): Consonni, P; Thiele, M.R; Palagi, C.L; Aziz, K.

Contribution to knowledge: Nothing significant; the paper appears to use a globally unstructured grid complete with Cartesian or radial local refinements around wells. As such, the framing of the problem thus results in a discussion centred on the local refinements, which are not unstructured and thus say nothing conclusive on the topic of interest.

Objective of the paper: To investigate the applicability of flexible gridding - in particular hybrid grids with local mesh refinements - for the modelling of water coning in vertical and horizontal wells within both homogeneous and heterogeneous systems.

Methodology used:

A neat systematic methodology was used, outlined as follows;

1. Simple sector geometry including a single producer and single injector was established

2. System fine grid simulation using average petrophysical properties generated as reference case

3. Vertical layering on coarse grid optimised to reproduce coning break-through times between fine and coarse grids

4. Various local mesh refinements introduced to the coarse grid in the vicinity of the producer in attempts to reproduce the water-cut curves (both break-through and shape) between fine and course grids

5. Diagonal coarse grid introduced (with and without local mesh refinements) in an attempt to reproduce the water-cut curves between fine and course grids.

This procedure was repeated for homogeneous and heterogeneous systems involving vertical and horizontal wells.

Conclusion reached:

1. For vertical wells the refinement itself is more important than its geometry provided that there are enough points around the wells. Heterogeneity requires that a larger area be defined

2. For horizontal wells the Voronoi grid becomes particularly useful as it avoids orientation problems by aligning the refinement along the well

3. When heterogeneities are considered, the dominant feature to resolve remains the upscaling of petrophysical properties, irrespective of the type of grid used

Comments: It provides interesting perspectives on the value of hybrid grids (i.e. those using both structured and unstructured elements) to water-coning and/or water breakthrough modelling and on the challenges of upscaling reservoir properties from the structured fine grid to an unstructured course grid.

SPE 25266 (1994)

Paper Title: Hybrid-CVFE Method for Flexible-Grid Reservoir Simulation

Author(s): Fung, S.K; Buchanan, L; Sharma, R.

Contribution to knowledge: Demonstrates the flexibility, accuracy and efficiency of hybrid gridding techniques by coupling control volume finite element (CVFE) unstructured gridding with local radial and curvilinear refinements around wells.

Objective of the paper: To combine the benefits of curvilinear cylindrical or elliptical grids, which accurately model near-well regions, with those of CVFE grids to represent the reservoir region, which offer greater geometric flexibility and lower grid orientation effects.

The objective was to improve on existing hybrid-Cartesian methods available at the time, by allowing more freedom in selecting the size and location of local refinements, previously constrained by rectangular grid cells, while eliminating the approximate method of handling the transition between regular and cylindrical grids.

Methodology used:

1. The numerical formulation follows the CVFE discretization by the method of weighted residuals, as described by Finlayson in 1972.

2. The CVFE grid is generated using an automated triangulation routine. A smoothing technique, as proposed by Cavendish in 1974, is then applied to perturb the triangulation so that elements are closer to equilateral triangles. The Delaunay criterion is then checked by using a swap-test algorithm, after Cline and Renka, 1984.

3. The local curvilinear grid refinement is achieved by eliminating a sufficient number of triangular CVFE elements where the cylindrical grid is positioned. Transmissibilities inside the cylindrical grid are calculated by the finite difference approach. Transmissibilities at the interface of local curvilinear and global CVFE grids are determined by considering radial flow between adjacent nodes.

4. The model was validated against analytical solutions to two test cases; single well in a cylindrical reservoir using the pressure distribution obtained from van Everdingen and Hurst (1977), and, three wells producing at different rates within a rectangular reservoir using the method of images.

5. A number of numerical examples were performed to compare the performance of different grid arrangements.

Conclusion reached: There are several advantages of the hybrid-CVFE method; greater geometrical flexibility, enhanced treatment of near-well processes, minimised grid distortion effects at the transition, continuity of pressure derivatives at the hybrid grid interface, and a sound level of accuracy and computational efficiency.

Comments: The full permeability tensor for transmissibility calculations is included on the CVFE surface

SPE 27998 (1994)

Paper Title: Interactive Generation of Irregular Simulation Grids and It's Practical Applications

Author(s): Heinemann, Z.E.

Contribution to knowledge: Nothing significant; the paper does not develop or test any new ideas, but rather discusses several new concepts and tools in reservoir simulation and how they might be used in practice.

Objective of the paper: To make several new tools in reservoir simulation practical for everyday use; PEBI and Median grids with the use of the Control Volume Method, modelling of non-vertical faults, windowing technique, dual time-stepping, vertical and horizontal well models.

Methodology used: The paper describes, from a high level, a method for automated and interactive grid generation.

Conclusion reached: Not applicable

Comments: This is a useful and informative paper for the practising engineer working in the field of reservoir simulation, but not one which contributes much relevant material for this review.

SPE 22889 (1994)

Paper Title: Use of Voronoi Grid in Reservoir Simulation

Author(s): Palagi, C.L; Aziz, K

Contribution to knowledge: Primarily, this paper develops a method of implementing Voronoi grids in reservoir simulation, and a means of assigning petrophysical properties to the grid independent of the location of known data. It also extends the applicability of existing well models.

Objective of the paper: To describe a practical gridding technique for the use of Voronoi grids in reservoir simulation; including the generation of grid blocks, the assignment of physical properties and the treatment of wells.

Methodology used:

1. The grid is constructed in a modular fashion through use or user-selected modules of easy to handle geometry. These modules provide a variety of grid options. Grid modules can be located translated, scaled and rotated on a horizontal plane, within the domain, to model particular features that are later connected to each other (or the background grid) using Voronoi blocks. A 3D geometry is achieved by projecting the gridding vertically through the model layers.

2. Discretization of the flow equations in the Voronoi blocks follows the method proposed by Heinrich in 1987. The discretization of flow equations elsewhere uses a control volume finite difference (CVFD) scheme.

3. Assignment of physical properties to each block and its connections is determined using interpolation of known "property-points" which are independent of the grid itself. Interpolation is based on the method proposed by Isaaks and Srivastava in 1989 and involves subdivision of each Voronoi block into internal triangles.

4. The well models follow work published by Peaceman in 1978, and Abou-Kassem and Aziz in 1985.

Conclusion reached:

1. The combination of several modules in a single physical domain allows a good representation of vertical and horizontal wells and major geological features.

2. The specification of physical properties at locations that are independent of grid-points provides a practical way to simulate field-scale problems with irregular grids.

Comments: The paper also investigates grid orientation effects, concluding that hybrid-Cartesian and hybrid-hexagonal grids are less sensitive to grid orientation than purely hexagonal or nine-point Cartesian grids, due primarily to their ability to incorporate cylindrical modules to represent radial flow around wells.

Although not explicit in the paper, it is not thought that the treatment of permeability used here honours the full tensor formulation for handling truly isotropic problems.

SPE 37028 (1996)

<u>Paper Title:</u> Development and Applications of a Three-Dimensional Voronoi-Based Flexible Grid Black Oil Reservoir Simulator

<u>Author(s):</u> Kuwauchi, Y; Abbaszadeh, M; Shirakawa, S; Yamazaki, N.

<u>Contribution to knowledge:</u> This paper applies similar methods as those previously discussed by Palagi and Aziz to develop a reservoir simulator using Voronoi based gridding, but demonstrates far more rigour in the selection of an appropriate methodology. It offers rigorous assessment of gridding techniques, discretization methods and provides simulator validation through more complex reservoir examples not previously treated in the literature.

<u>Objective of the paper:</u> To present a methodology for the development and application of a black-oil reservoir simulator based on the Voronoi flexible gridding scheme and control volume finite element (CVFE) method for discretization of the flow equations. To verify simulator performance, using analytical solutions, in the context of difficult reservoir problems.

<u>Methodology used:</u>

1. The two-dimensional Voronoi (PEBI) grid is used in the horizontal plane and stacked vertically. Its selection is based on flexibility, accuracy and practicality. Similar to Palagi and Aziz (1994) a system of background and sub-grids is adopted, supporting the use of both cylindrical and Cartesian grids combined using Voronoi transitions.

2. Discretization of the flexible grid is implemented using the CVFE method, which is demonstrated to have higher accuracy (i.e. pressure gradient with second-order accuracy).

3. Physical parameters are defined on the Voronoi points. They are assigned to the background grid and values are calculated by linear interpolation on the Voronoi points. Sub-grids enable manual modification.

4. Verification was performed by comparison with analytical models; line source solution after Hurst, finite conductivity fracture near a producing well according to Abbaszadeh and Cinco-Ley (1995), horizontal well intersecting random fractures as described by Guo et al (1994), and, Tracer flow in a reservoir containing fracture barrier after Sato and Abbaszadeh (1994).

5. Further application to other reservoir engineering problems is defined by way of the flexible Voronoi gridding; namely, infill wells, multilaterals, random faults, and geostatistical heterogeneity.

<u>Conclusion reached:</u>

1. Flexible gridding of Voronoi is most suited to representing reservoir geological features

2. CVFE methods are most suitable for upstream weighted mobility calculations

3. The described Voronoi simulator can be reliably applied to well test simulation and recovery performance prediction in complex reservoirs

<u>Comments:</u>

SPE 37998 (1997)

Paper Title: The Generation and Application of K-Orthogonal Grid Systems

Author(s): Gunasekera, D; Cox, J; and Lindsey, P.

Contribution to knowledge: The definition and generation of composite tetrahedral grids, the process of generating good K-orthogonal PEBI and composite tetrahedral grids, algorithms for computing volumes, transmissibilities, well connections and cell renumbering for general K-orthogonal grids.

Objective of the paper: To develop a robust unstructured grid generation technique, which provides alternative to earlier methods proposed by Heinemann, Aavatsmark and Durlofsky, so as to overcome some of their respective drawbacks. In particular, the drawbacks were; poor handling of layers with contrasting permeability by Voronoi grids, cell boundary overlap in highly anisotropic systems in Voronoi grids, and the high number of cells in triangular grids.

Methodology used:

1. Discretization by way of a fully implicit control volume formulation to determine the flow terms. This scheme is applicable to any grid that satisfies the K-orthogonality condition.

2. K-orthogonal grid generation by scaling - the physical domain is transformed into a computational domain in which orthogonality corresponds to K-orthogonality in the physical domain, points are triangulated in the computational space prior transformation back to the physical domain. The transformation is applied by scaling the z-coordinate of the model using horizontal and vertical permeabilities. Triangles (or tetrahedra) are aggregated in computational space to reduce the overall number of cells in the model.

3. Grid generation follows a systematic process involving (a) point distribution according to the global grid type and local grid style suited to modelling system features, (b) triangulation (or tetrahedralization) involving a Delaunay tessellation and a incremental point insertion method proposed by Bowyer in 1981, and, (c) Cell generation and triangle aggregation.

4. Cell property generation, grid smoothing, deviated coordinate lines well connection factors and cell renumbering algorithms are subsequently described.

5. Validation step is performed using several simulations compared to analytical models.

Conclusion reached:

1. The unstructured gridding technique developed produces K-orthogonal grids applicable to a wide class of reservoir simulation problems.

2. The two-point transmissibility formula, other cell property calculations and well connection factor calculations are derived for general unstructured grids.

3. The deviation from K-orthogonality reported on a cell basis could be used to identify regions for local application of multi-point flux approximation schemes (MPFA).

Comments:

SPE 37999 (1997)

Paper Title: A Control Volume Scheme for Flexible Grids in Reservoir Simulation

Author(s): Verma, S; and Aziz, K.

Contribution to knowledge: A new finite-difference approach that can be applied to existing flexible grid types to reduce the number of cells required for complex reservoir simulation. First to attempt grid alignment along streamlines.

Objective of the paper: To present a method capable of modelling full, anisotropic and asymmetric permeability tensors and permeability heterogeneity, to overcome the limitations of Cartesian and locally orthogonal Voronoi or k-orthogonal PEBI grids.

Methodology used:

1. Flow equations according to the Method proposed by Lake in 1989, valid for multi-component, multi-phase systems, derived from mass conservation and Darcy Law fundamentals.

2. The numerical method applies to grids (triangulations/tetrahedralizations) obeying the Voronoi criterion, but allows permeability to vary inside the element by breaking it down into a sub-set of control volumes about each vertex within which properties are constant. The discretization scheme maintains flux continuity across grid block faces inside each tetrahedron and potential continuity at a specific point on each interface.

3. Interblock transmissibility (i.e. between tetrahedra) is based upon the same principles as those used for Cartesian grids. Intrablock transmissibilities (i.e. between the six faces connecting the four internal control volumes about the vertices of each tetrahedron) result in six flow terms inside each tetrahedron. A face potential is introduced at each interface, which when combined with potentials at the nodes can be used to estimate velocities at the interface, and in turn, the velocities to estimate the flux.

4. Control volume finite element (CVFE), boundary adapting grids (BAG) are used in two numerical examples; (a) coning in a horizontal well, and (b) aligning grid along streamlines.

5. Several numerical examples were performed comparing results of fine grid simulation with ECLIPSE (reference case) with those of FLEX (the developed simulator); water coning in a horizontal well, and, grid aligned along streamlines.

Conclusion reached: Flexible grids can be exploited to significantly reduce the number of blocks required for complex reservoir simulation problems.

Comments: Not sure that the numerical cases and their respective results, demonstrated well the objective of the paper, which was to model full anisotropic and heterogeneous systems that improves the results of Voronoi or k-orthogonal PEBI grids, since no relevant comparisons were made.

SPE 76783 (2002)

Paper Title: PEBI Grid Selection for Numerical Simulation of Transient Tests

Author(s): Escobar, F.H; Tiab, D.

Contribution to knowledge: Provides an investigation of the applicability of various PEBI grid types to model pressure transient behaviour of different well types

Objective of the paper: To establish and recommend the use of specific PEBI grid types – hexagonal, elliptical, rectangular, circular and variable – for the simulation of transient pressure behaviour in vertical wells, vertical hydraulically fractured wells and horizontal wells.

Methodology used:

1. For each of the selected well types a number of simulations were performed using the different PEBI grid geometries and the results compared to analytical solutions. The arithmetic error was used to quantify the discrepancy between numerical and analytical results.

2. Analytical models were provided by Cinco-Ley (1976) for vertical fractured well and by Goode and Thambynayagam (1987) for horizontal wells. No reference is given to the analytical model used for undamaged vertical well, nor vertical well with damage skin and well-bore storage.

Conclusion reached:

1. For unfractured vertical wells, the circular and variable PEBI grids provide best results with fewer grid-points. The application of circular PEBI grids can be extended to vertical wells having well-bore storage and skin

2. For fractured vertical wells, the elliptical PEBI grid provided the best results for fracture conductivities > 1. All PEBI grid simulation was unreliable for fracture conductivities < 1. Elliptical PEBI grids were able to reliably handle non-orthogonal fracture systems that are rotated in any direction on the Cartesian plane.

3. All PEBI grid geometries provide good results for horizontal wells at any angle, with the elliptical grid being deemed most suitable.

Comments: This paper appears to be basic and trivial, but nonetheless does provide some useful recommendations to the practicing reservoir engineer involved in reservoir simulation.

SPE 79684 (2003)

Paper Title: Locally Stream-Line-Pressure-Potential-Based PEBI (SPP-PEBI) Grids

Author(s): Mlacnik, M.J; Harrer, A. W; Heinemann, Z.E.

Contribution to knowledge: A successful procedure to generate and handle 2.5D PEBI grids based on streamlines and pressure potentials using the windowing technique

Objective of the paper: To present the first step to a general applicable procedure that allows to dynamically integrate streamline -pressure-potential-based grids into full field models.

Methodology used:

1. Fully implicit solution for the full model is calculated, but inner blocks of the windows, represented by fine scale Cartesian grids, are solved for pressure only. Saturations and mole fractions are not updated, but this step provides the boundary influx for the windows and the pressure distribution that allows to determine the grid points of a streamline - pressure potential grid.

2. Based on the point distribution a new set of window grids are constructed using the PEBI algorithm, which is subsequently solved for the same overall time-step using the boundary flux determined during the first step.

3. The method makes use of local time-steps, modified as required, to ensure convergence of the window solutions.

4. Quality check is performed following convergence of the last local time-step by ensuring both implicit and explicit boundary fluxes of all components are within a specified tolerance across the window boundary blocks.

Conclusion reached:

1. A successful procedure to generate and handle 2.5D PEBI grids based on streamlines and pressure potentials has been presented.

2. SPP-PEBI grids can be generated and exchanged during a simulation run using the windowing technique.

3. SPP-PEBI grids can handle displacement problems at adverse mobility ratio with less CPU time and higher accuracy than 5 or 9-point stencils for small scale examples.

4. Calculated results can be improved in full-field simulations.

Comments: Results obtained from SPP-PEBI grids could probably be further improved by smoothing algorithms and appropriate upscaling techniques.

SPE 84373 (2003)

Paper Title: Use of PEBI Grids for a Heavily Faulted Reservoir in the Gulf of Mexico

Author(s): Melichar, H; Reingruber, A.J; Shotts, D.R; Dobbs, W.C.

Contribution to knowledge: The application of PEBI gridding techniques to full-field reservoir simulation and comparison with structured Cartesian or corner-point grids for the same application; introduced a technique to interface PEBI grid fault connections with standard reservoir simulators – piecewise orthogonalization.

Objective of the paper: To compare different gridding techniques and determine gridding efficiency within the context of a complex (highly faulted) full-field reservoir simulation aimed at development well optimisation and where revised reservoir descriptions are available frequently via drilling updates.

Methodology used:

1. Three different simulation models were built for the subject reservoir system; a rectangular grid that uses stair-step approach to model faults, a curvilinear grid that follows the main bounding faults, and a PEBI grid.

2. The PEBI grid utilises unstructured grid patches to model structural features and wells interfaced with the rectangular point-distributed grid. The goal was to keep the node distribution regular and to model geological features by adaptation of block faces without shifting centre points. Individual patches are connected to the main grid by non-neighbour connections and are handled efficiently by the conventional simulator. Underlying main grid blocks were set inactive wherever a patch has been introduced.

3. Fault modelling is achieved through a new technique which enables the interfacing of PEBI grid fault connections by piecewise orthogonalization of fault block faces in the direction of the adjoining block-pair connections. Once a set of communicating block pairs is given the piecewise orthogonalization of corresponding faces was processed.

Conclusion reached:

1. The unstructured PEBI gridding technique was successfully combined with a conventional reservoir simulator based on structured gridding through the use of grid patches.

2. Simulation using PEBI grids was considerably more practical that similar models based on Cartesian or curvilinear grids. The flexible aspects of the PEBI grid allowed accurate and rapid gridding of the complex structural reservoir system, the computational and dynamic flow model was improved and run times were shorter.

Comments: All gridding alternatives investigated offered similar results in terms of pressure decline, production rates and recoveries, but it was the flexibility, user-friendliness and computational efficiency of the PEBI grid that set it apart in this real-world example.

SPE 79685 (2003)

Paper Title: Use of PEBI Grids for Complex Advanced Process Simulators

Author(s): Skoreyko, F; Sammon, P.H; and, Melichar, H.

Contribution to knowledge: Successfully demonstrated that PEBI gridding techniques could be applied for complex thermal processes, namely steam assisted gravity drainage (SAGD), in a full-field setting.

Objective of the paper: To extend previous work with PEBI grids in the simulation of relatively simple processes and investigate PEBI-based gridding for a complex thermal process (SAGD) in a full-field setting, by way of comparing several metrics – computing time and accuracy – between PEBI grids and a conventional corner-point grid with local refinement.

Methodology used:

1. Simulation was of a large, heavy oil field produced under SAGD using nine horizontal well pairs.

2. Two simulation cases were developed; a corner-point grid model with local refinements (the reference case) which had 241000 cells and a PEBI-grid model which had 129000 cells.

3. The PEBI-grid generation technology was based on the work of Heinemann in 1994, which used Cartesian gridding wherever reasonable with local refinements near wells and structural features that are interfaced to the background grid by way of PEBI grid transitions.

4. The discretization method is related to the control volume finite element (CVFE) technique, after Forsyth (1989).

5. Single well-pair cases were run prior the full-field SAGD simulations to determine the largest grid cell sizes in the vicinity of the horizontal wells required to accurately model the SAGD process.

Conclusion reached:

1. The added flexibility of PEBI gridding allowed for better alignment near horizontal wells

2. Through PEBI-gridding it was possible to halve the number of cells in the model, while still maintaining the required definition and grid resolution at the points of interest

3. The ILU-based sparse matrix solver was shown to be capable of computing in an unstructured grid environment

4. PEBI-based gridding can be used efficiently to model complex processes in a full-field setting. In this case, these grids demonstrably improved accuracy and improved run-time by 32% over the conventional corner-point model.

Comments:

Appendix B: Model Construction

Grid

	NX	NY	NZ	DX	DY	DZ	Grid Cells	Depth (top)	Depth (bottom)	Bulk Volume
	#	#	#	ft	ft	ft	#	ft	ft	MMbbl
Model-1	101	101	20	200	200	10	204020	4000	4200	14535
Model-2	101	101	19	200	200	10.53	193819	4000	4200	14535

Table B-1: Summary of grid properties and dimensions for the two models used in simulation.

Initial Well Models

	Well Name	VERT_FP	VERT_PP	HZ_90IN_90AZ
	Well Type	vertical (fully penetrating)	vertical (partially penetrating)	horizontal
Casing Diameter	inch	7	7	7
Casing Setting Depth	ft MD (TVD)	4250 (4250)	4250 (4250)	7350 (4100)
Top Perforation	ft MD (TVD)	4000 (4000)	4080 (4080)	6718.8 (4100)
Bottom Perforation	ft MD (TVD)	4200 (4200)	4120 (4120)	7318.8 (4100)
Perforation Length	ft	200	40	600
Well Reference Depth	ft MD (TVD)	4095 (4095)	4095 (4095)	4100 (4100)
Completion Skin	-	0	0	0

Table B-2: Summary of well and completion properties for initial simulations

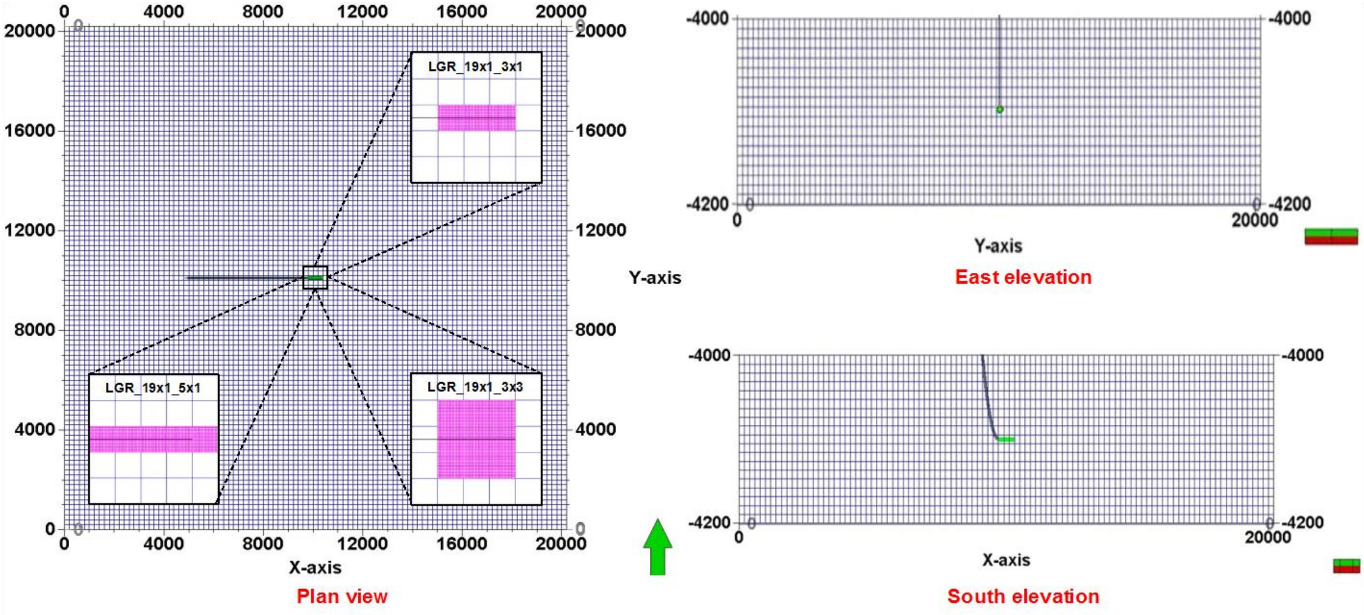

Figure B-1: The location of well and completion within the grid for the horizontal well. Some example LGR are shown by explosion of the near-well grid (inset at left).

Well-Versus-Grid Orientation Well Models

	Well Name	W_30IN_90AZ	W_34IN_60AZ	W_39IN_45AZ	HZ_90IN_90AZ	HZ_90IN_60AZ	HZ_90IN_45AZ
	Well Type	deviated (fully penetrating)	deviated (fully penetrating)	deviated (fully penetrating)	horizontal	horizontal	horizontal
Casing Diameter	inch	7	7	7	7	7	7
Casing Setting Depth	ft MD (TVD)	4250 (4216.5)	4250 (4208)	4300 (4236)	7350 (4100)	7450 (4100)	7600 (4100)
Top Perforation	ft MD (TVD)	4000 (4000)	4000 (4000)	4000 (4000)	6718.8 (4100)	6718.8 (4100)	6718.8 (4100)
Bottom Perforation	ft MD (TVD)	4230.9 (4200)	4240.4 (4200)	4258.4 (4200)	7318.8 (4100)	7411.6 (4100)	7567.3 (4100)
Perforation Length	ft	230.9	240.4	258.4	600	692.8	848.5
Well Reference Depth	ft TVD	4095	4095	4095	4100	4100	4100
Completion Skin	-	0	0	0	0	0	0
Apparent Dip	degree	30	30	30	90	90	90
Apparent Rotation	degree	0	30	45	0	30	45
Well Inclination	degree	30	34	39	90	90	90
Well Azimuth	degree	90	60	45	90	60	45

Table B-3: Summary of well and completion properties for the well-versus-grid orientation sensitivity runs.

Inclination and azimuth are used in the conventional sense, to represent true deviation of the well-bore with respect to the vertical and horizontal. Inclination is defined relative to the vertical, while azimuth is defined relative to the direction north. Apparent dip has been used to express the relative orientation of well-verses-grid in the x-z plane, and similarly, apparent rotation for the orientation of well-versus-grid in the x-y plane.

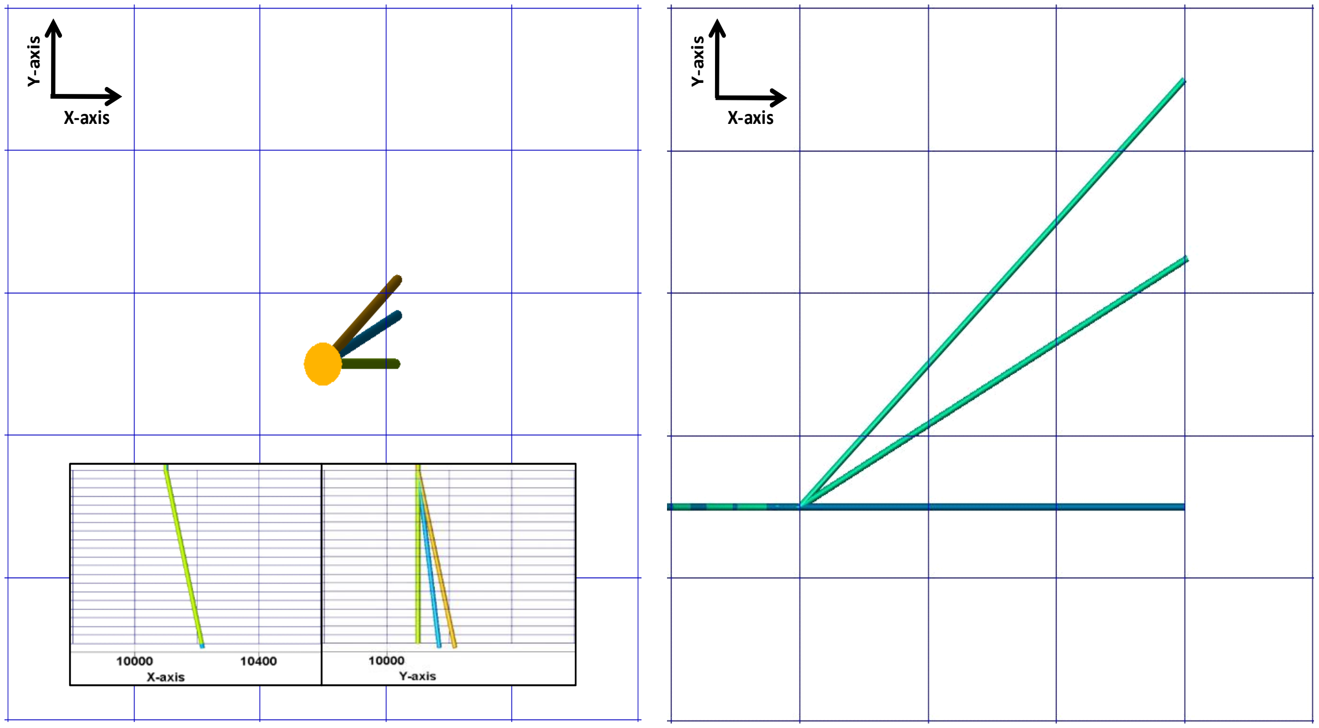

Figure B-2: Plan view of the well configuration for well-versus-grid orientation sensitivity runs each with apparent grid rotations of 0°, 30° and 45°; deviated vertical wells (superimposed at left) complete with south elevation (left inset) and east elevation (right inset), and horizontal wells (superimposed at right).

Rock Properties

ϕ	-	0.2
k_x	mD	200
k_y	mD	200
k_z	mD	200
c_f	psi^{-1}	$1x10^{-5}$

Table B-4: Summary of reservoir rock properties used to define the porous media in the simulations.

Fluid Properties

	Density (ρ_w)	Viscosity (μ)	Compressibility	Volume Factor
	lbm/ft^3	cp	psi^{-1}	rbbl/sbbl
Oil	52.06	0.688	$1.03x10^{-5}$	1.144
Water	63.7	0.396	$2.84x10^{-6}$	1.015
Gas	0.051	0.016	$6.32x10^{-4}$	0.01

Table B-5: Average fluid properties representative of the model used in simulation and for comparison with analytic solutions.

Viscosity and volume factors are representative of an average reservoir condition interpolated from the simulator input data, whereas density represents a stock-tank condition. Hydrocarbon compressibility values have been determined from the formation volume factors input to the simulator and represent an average reservoir condition.

Aspect Ratio Sensitivity Cases

	ASPECT RATIO				
	DX/DY (DY=DZ)				
VERT_FP	1	2.11	3.8	6.33	
	DX/DZ (DX=DY)				
HZ_90IN_90AZ	1	2.11	6.33	19	57
	DX/DY (DY=DZ)				
HZ_90IN_90AZ	0.053	0.158	1	6.3	19

Table B-6: Summary of test cases used for sensitivity on Cartesian grid aspect ratio

9-Point Versus 5-Point Flux Sensitivity Cases

	TEST CASES	
	1	2
VERT_FP	Coarse	LGR_3x1_1
VERT_PP	Coarse	LGR_19x1_1
W_30IN_90AZ	Coarse	LGR_39x2_2x1
W_34IN_60AZ	Coarse	LGR_39x2_2x1
W_39IN_45AZ	Coarse	LGR_39x2_2xD
HZ_90IN_90AZ	LGR_19x1_3x3	LGR_19x1_5x1
HZ_90IN_60AZ	Coarse	LGR_19x1_3x3
HZ_90IN_45AZ	Coarse	LGR_19x1_Track

Table B-7: Summary of test cases used for comparison of 9-point with 5-point flux schemes.

Grid Type Sensitivity Cases

	WELL NAME							
	VERT_FP	VERT_PP	W_30IN_90AZ	W_34IN_60AZ	W_39IN_45AZ	HZ_90IN_90AZ	HZ_90IN_60AZ	HZ_90IN_45AZ
Cartesian LGR	X	X	X	X	X	X	X	X
Radial LGR	X	X						
Geometric Series LGR	X	X				X		
Unstructured LGR						X	X	X

Table B-8: Summary of test cases used for sensitivity on grid type

Appendix C: Formulae for Pressure Transient Analyses

Derivative Analysis

Equation (C-1) defines the superposition time function for build-up analysis. Equations (C-2) to (C-4) outline the functions to be plotted.

$$f(t) = \frac{t_p \Delta t}{t_p + \Delta t} \quad \text{(C-1)}$$

$$\Delta t = t - t_p \quad \text{(C-2)}$$

$$\Delta p = p(\Delta t) - p(\Delta t = 0) \quad \text{(C-3)}$$

$$\Delta p' = \frac{dp}{d\ln[f(t)]} = \frac{dp}{d\ln\left(\frac{t_p \Delta t}{t_p + \Delta t}\right)} = \frac{t_p + \Delta t}{t_p}\Delta t \frac{dp}{dt} \quad \text{(C-4)}$$

Dimensionless pressure for pressure match;

$$p_D = \frac{kh}{141.2qB\mu}\Delta p \quad \text{(C-5)}$$

Dimensionless time group for time match;

$$\frac{t_D}{C_D} = 0.000295\frac{kh}{\mu}\frac{\Delta t}{C} \quad \text{(C-6)}$$

Dimensionless well condition group for curve match;

$$C_D e^{2S} = \frac{0.8936C}{\phi c_t h r_w^2} e^{2S} \quad \text{(C-7)}$$

Specialized Analyses

For each flow regime, the formulae used to determine the relevant parameters from the specialised analyses are given by Equations (C-8) through (C-16)

Well-bore storage;

$$C = \frac{qB}{24m_{WBS}} \quad \text{(C-8)}$$

Radial flow (Horner Analysis);

$$kh = 162.6\frac{qB\mu}{m_H} \quad \text{(C-9)}$$

$$S_t = 1.151\left(\frac{\Delta p_{1hr}}{m} - \log\frac{k}{\phi\mu c_t r_w^2} + \log\frac{t_p + 1}{t_p} + 3.23\right) \quad \text{(C-10)}$$

Spherical flow for a vertically centred zone of limited entry;

$$k_s = \left(2452.9 qB\mu \frac{\sqrt{\phi\mu c_t}}{m_{SPH}} \right)^{2/3} \quad \text{(C-11)}$$

$$k_s = \sqrt[3]{k_x k_y k_z} \quad \text{(C-12)}$$

Cylindrical flow taken from the first straight line on the semi-log analysis of horizontal well;

$$\sqrt{k_v k_h} L = \frac{81.3 qB\mu}{m_{CF}} \quad \text{(C-13)}$$

Elliptical flow taken from the second straight line on a semi-log analysis of horizontal well;

$$k_h h = \frac{162.6 qB\mu}{m_{EF}} \quad \text{(C-14)}$$

$$S_t = 1.151 \left(\frac{\Delta p_{1hr}}{m_{EF}} - \log \frac{k_h}{\phi\mu c_t r_w^2} + 3.23 \right) \quad \text{(C-15)}$$

Linear Flow;

$$k_h L^2 = 16.52 \left(\frac{qB}{m_{LF} h} \right)^2 \frac{\mu}{\phi c_t} \quad \text{(C-16)}$$

Appendix D: LGR Catalogue

The following pages provide illustration of all LGR referenced in the figures of the main body and Appendix E of this report. For each individual LGR the diagrams consist of an areal view (*x*-*y* plane) to illustrate the lateral near-well discretization, and a cross-section through the column of cells containing the well (*x*-*z* plane) to illustrate the vertical near-well discretization. In most illustrations we attempt to show some course grid cells to illustrate the refinement as opposed to the background grid. The LGR are listed in the order that they appear in the figures of Appendix E.

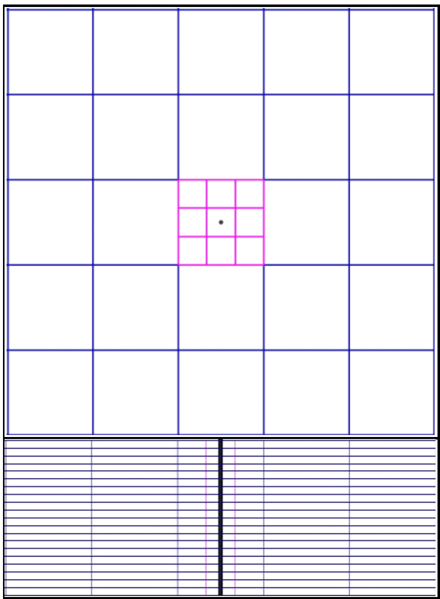

VERT_FP: LGR_3x1_1

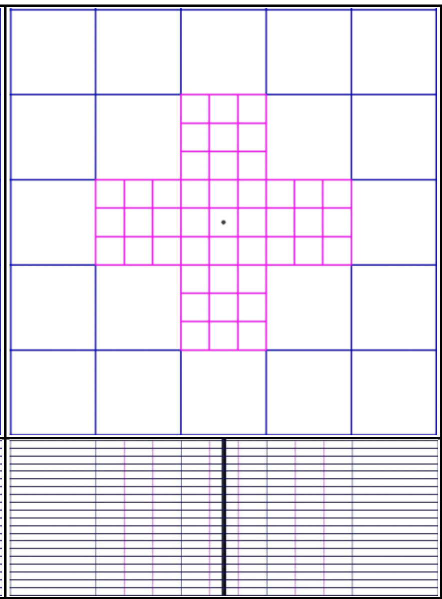

VERT_FP: LGR_3x1+

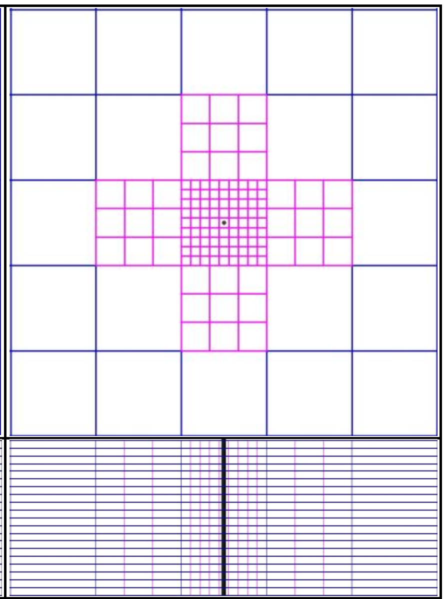

VERT_FP: LGR_9x1_3x1+

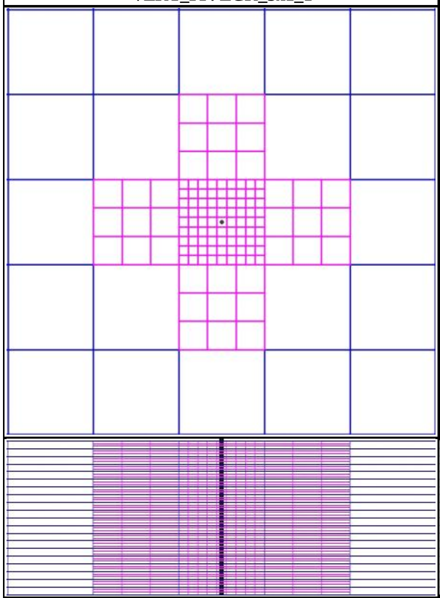

VERT_FP: LGR_9x3_3x3+

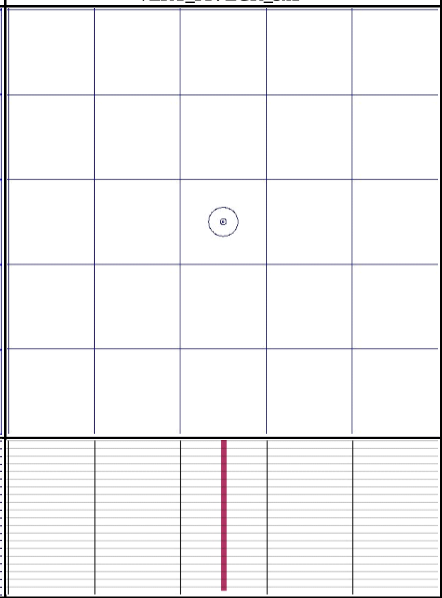

VERT_FP: RadLGR_4R_33

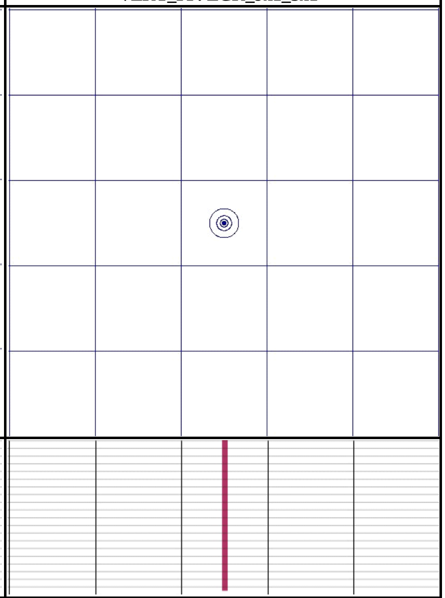

VERT_FP: RadLGR_8R_33

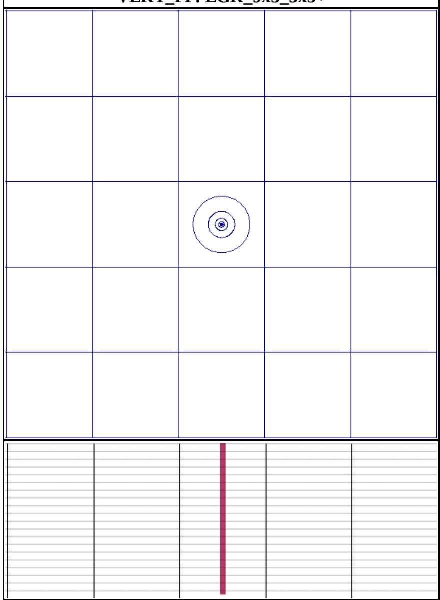

VERT_FP: RadLGR_8R_66

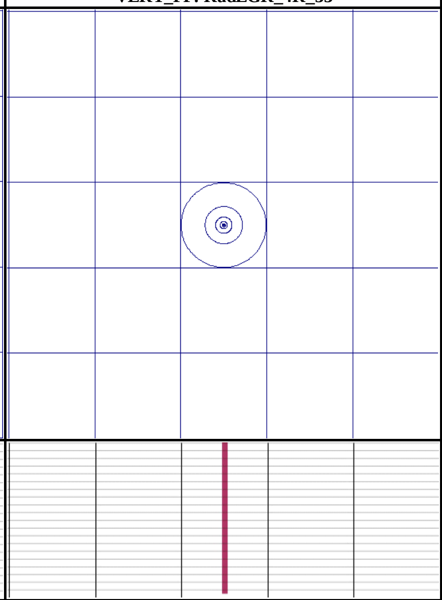

VERT_FP: RadLGR_8R_99

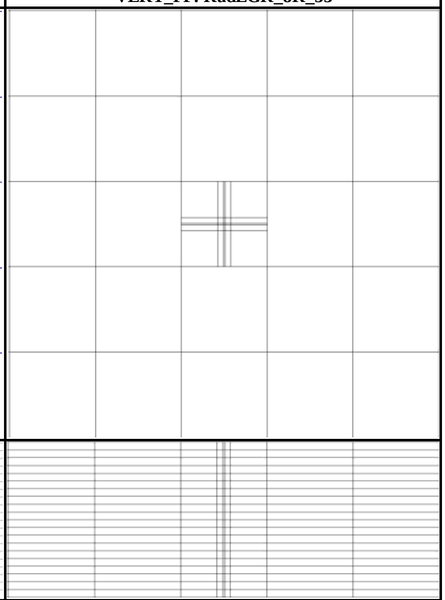

VERT_FP: GeoXY_5x20

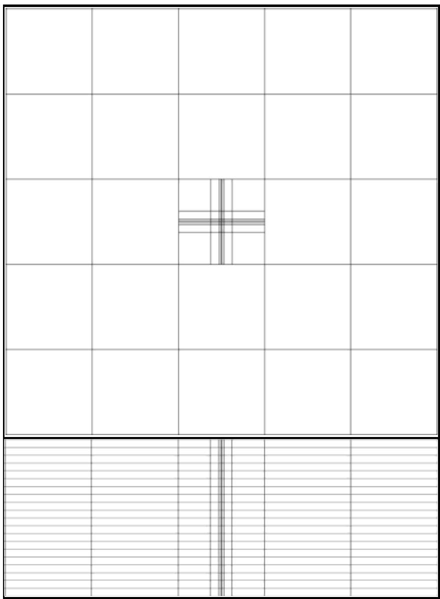

VERT_FP: GeoXY_7x20

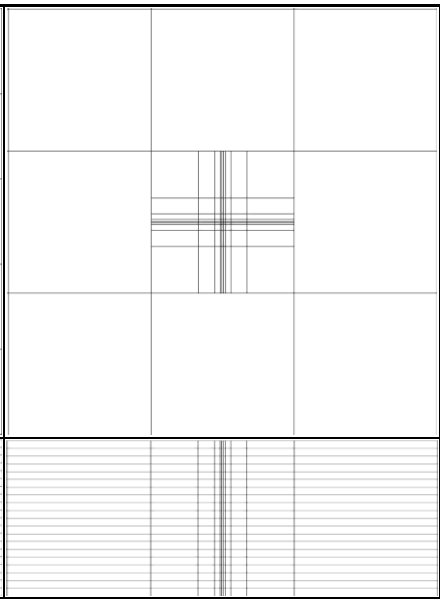

VERT_FP: GeoXY_9x20

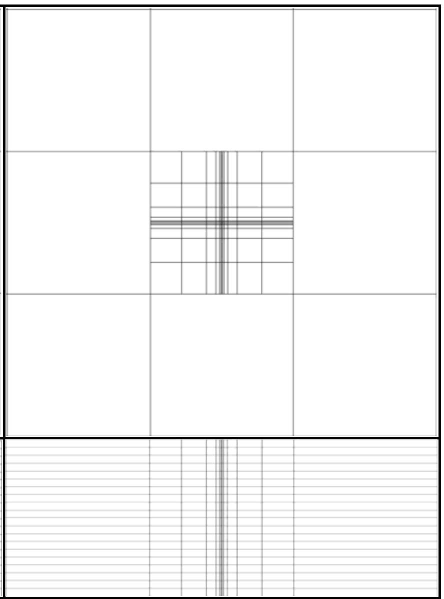

VERT_FP: GeoXY_11x20

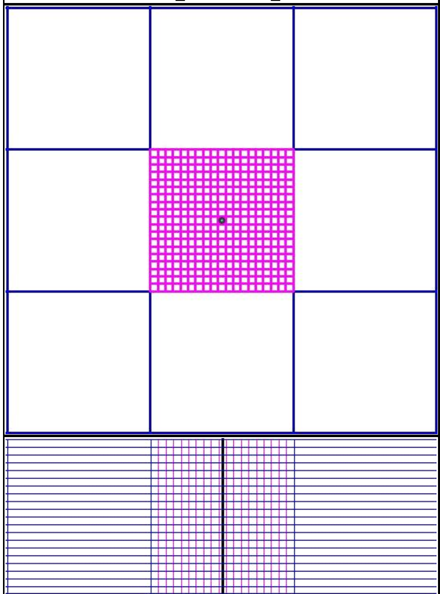

VERT_PP: LGR_19x1_1

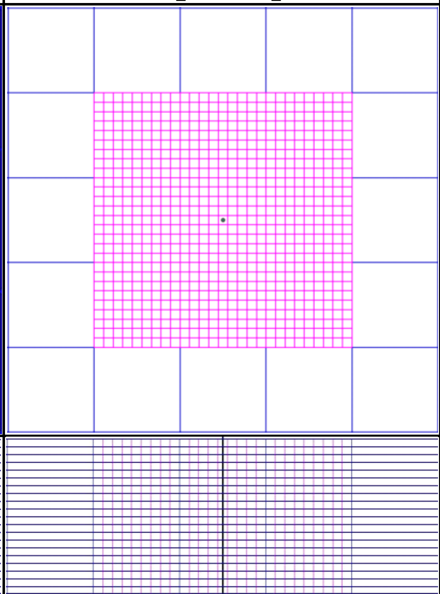

VERT_PP: LGR_9x1_3x3

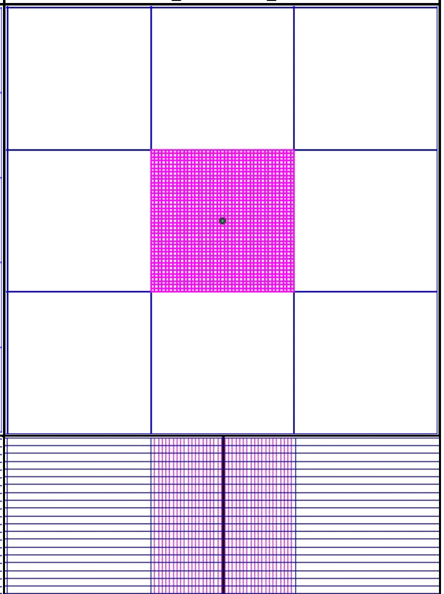

VERT_PP: LGR_39x1_1

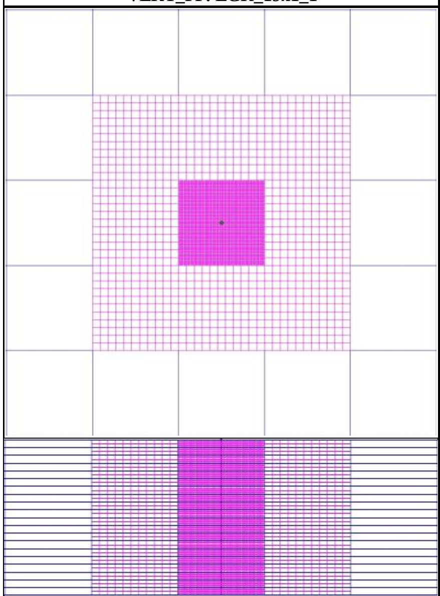

VERT_PP: LGR_77x4_11x2_3x3

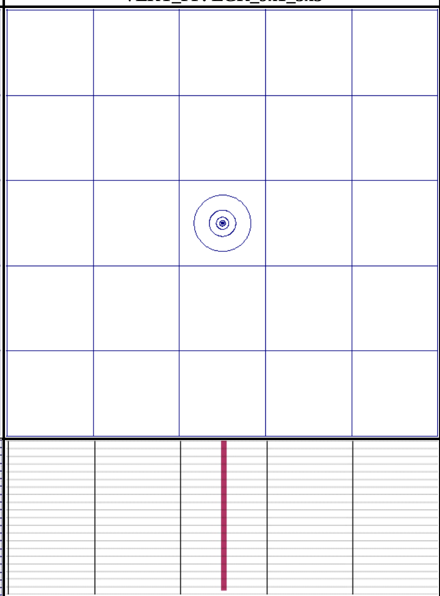

VERT_PP: RadLGR_8R_66

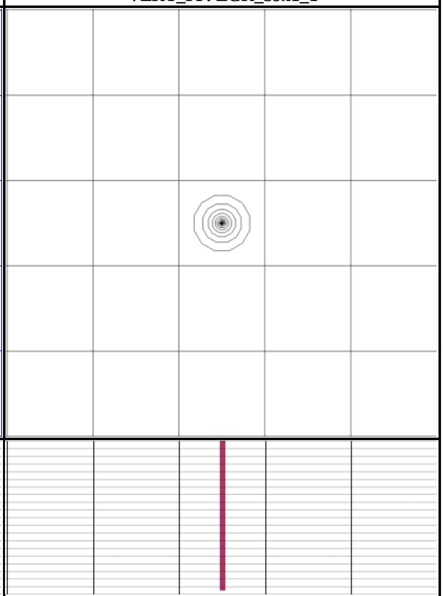

VERT_PP: RadLGR_16R_66

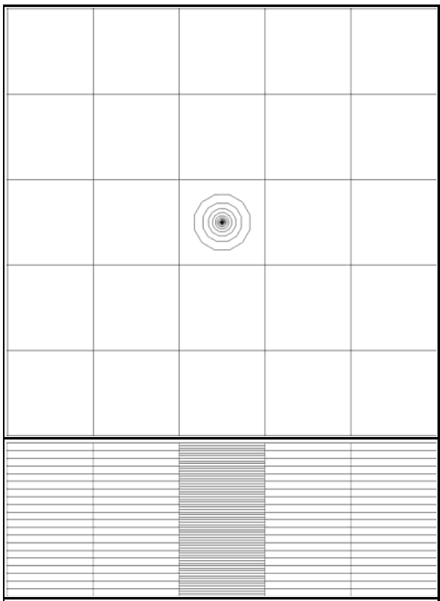

VERT_PP: RadLGR_16Rx3_66

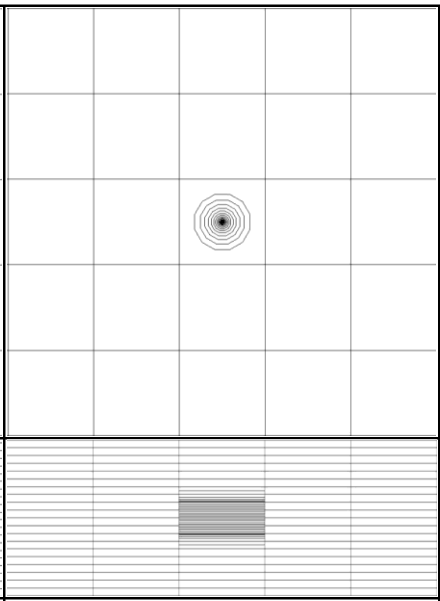

VERT_PP: RadLGR_24RxGeo_66

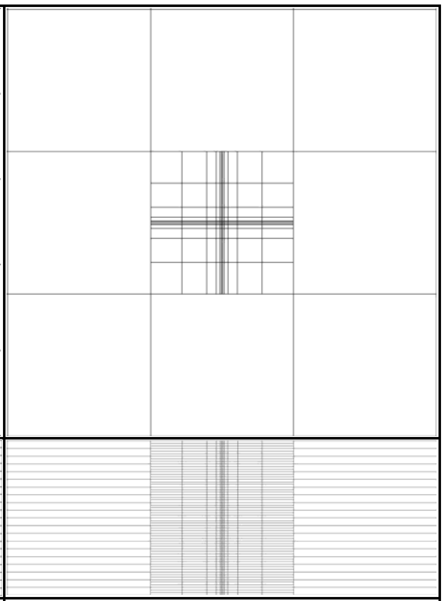

VERT_PP: GeoXY_11x60

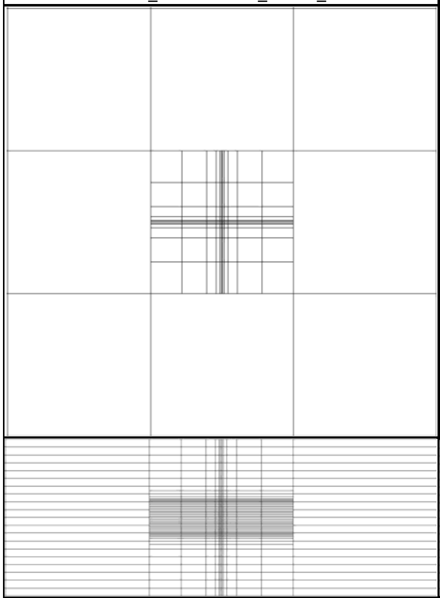

VERT_PP:GeoXYZ_11x46

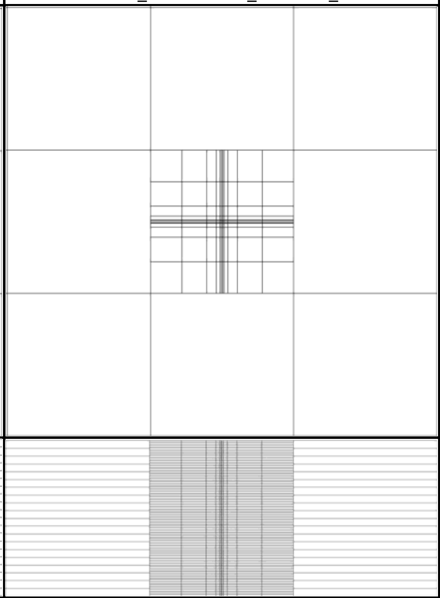

VERT_PP: GeoXY_11x100

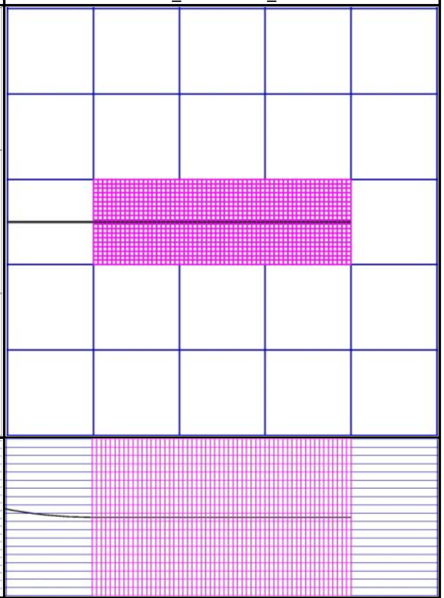

HZ_90IN_90AZ: LGR_19x1_3x1

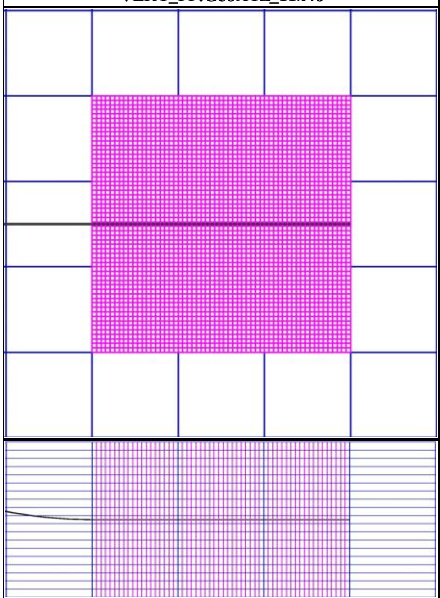

HZ_90IN_90AZ: LGR_19x1_3x3

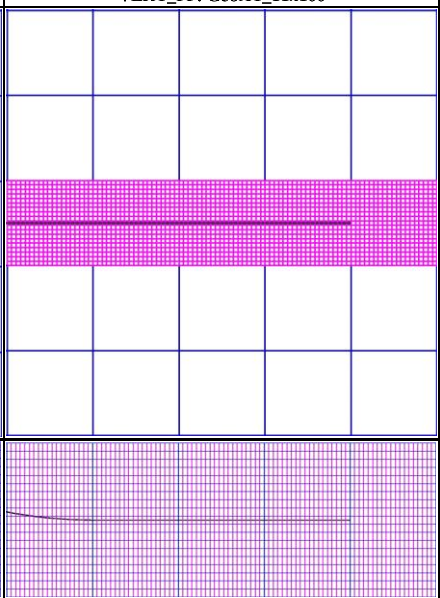

HZ_90IN_90AZ: LGR_19x1_5x1

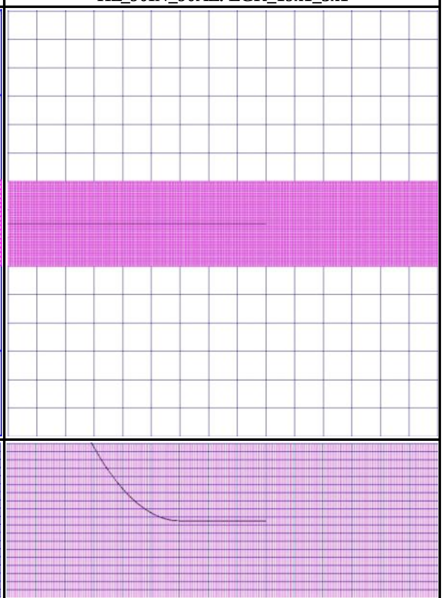

HZ_90IN_90AZ: LGR_19x1_15x3

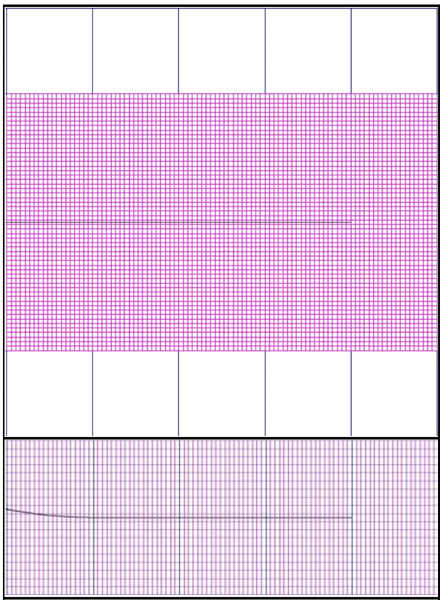

HZ_90IN_90AZ: LGR_19x1_5x3

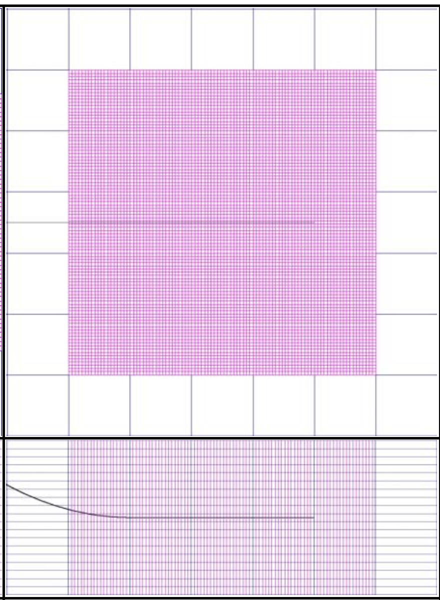

HZ_90IN_90AZ: LGR_19x1_5x5

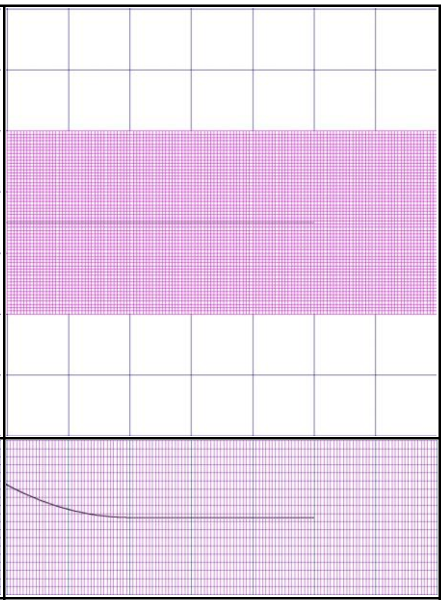

HZ_90IN_90AZ: LGR_19x1_7x3

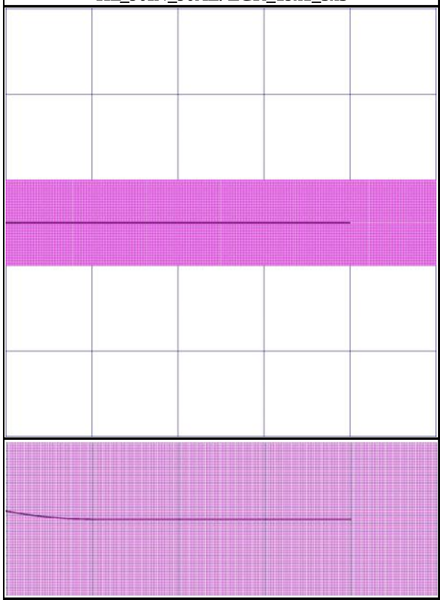

HZ_90IN_90AZ: LGR_57x3_5x1

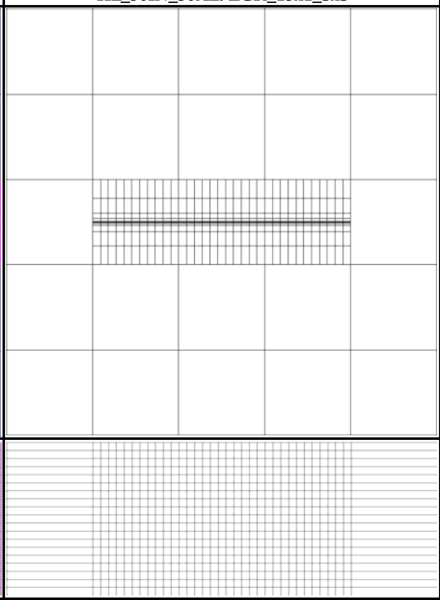

HZ_90IN_90AZ: GeoY_11x1_3x1

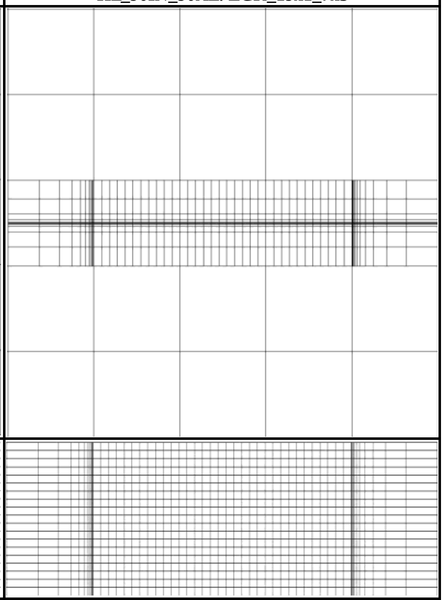

HZ_90IN_90AZ: GeoXY_11x1_5x1

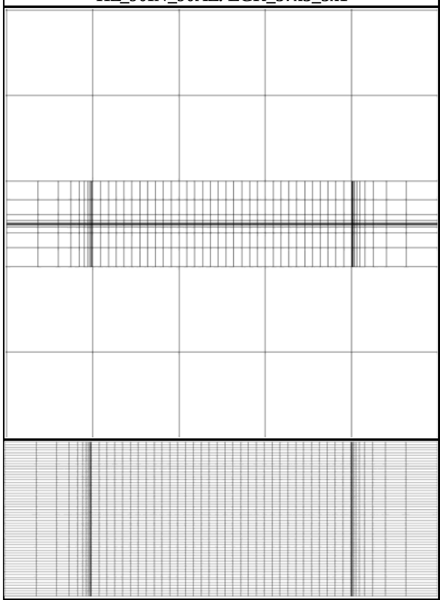

HZ_90IN_90AZ: GeoXY_11x3_5x1

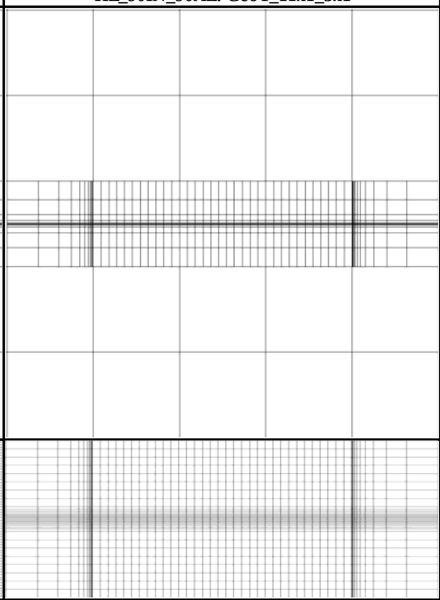

HZ_90IN_90AZ: GeoXYZ_11x36_5x1

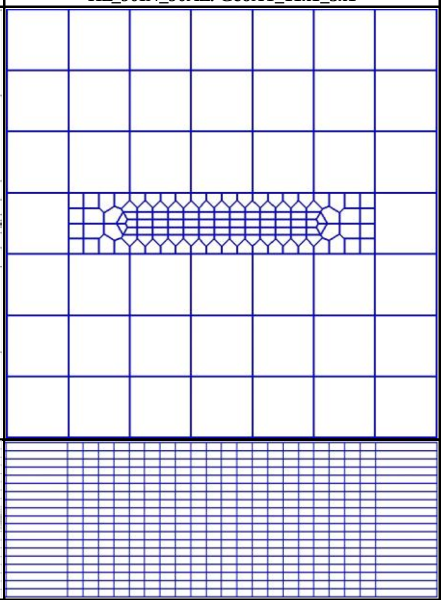

HZ_90IN_90AZ: UGR_50x3x50x1_5x1

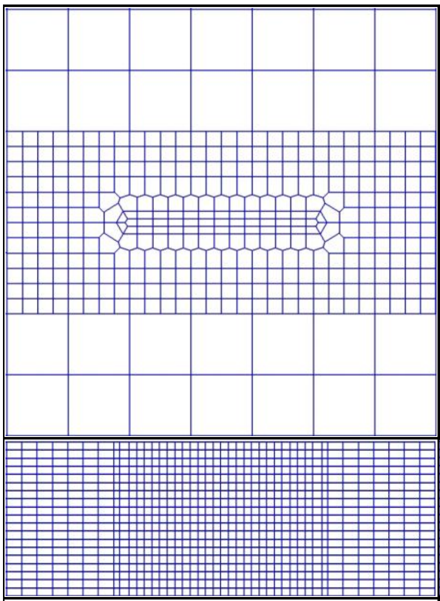

HZ_90IN_90AZ: UGR_50x3x50x1_7x3

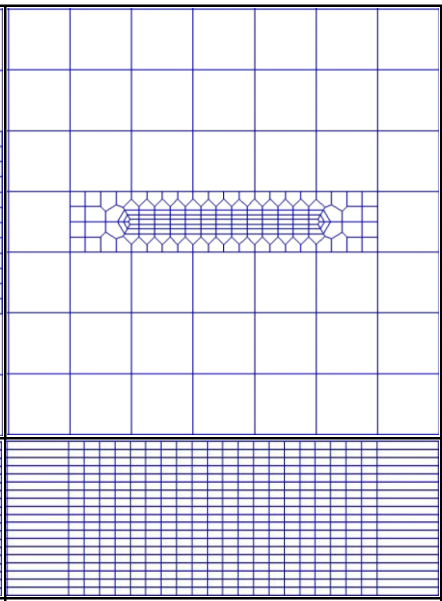

HZ_90IN_90AZ: UGR_50x5x50x1_5x1

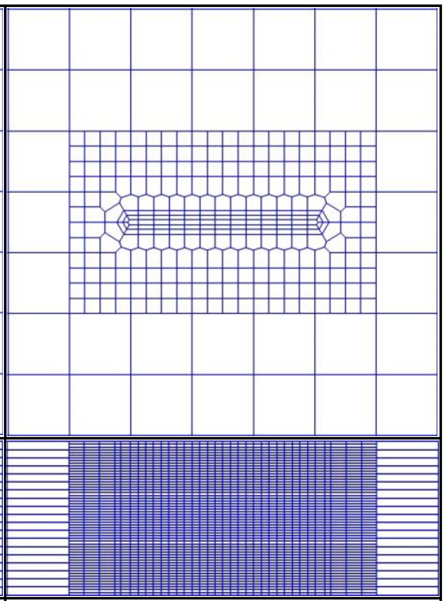

HZ_90IN_90AZ: UGR_50x5x50x3_5x3

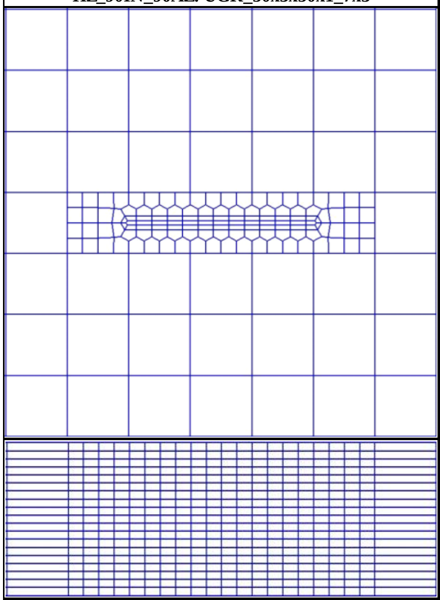

HZ_90IN_90AZ: UGR_30x3x50x1_5x1

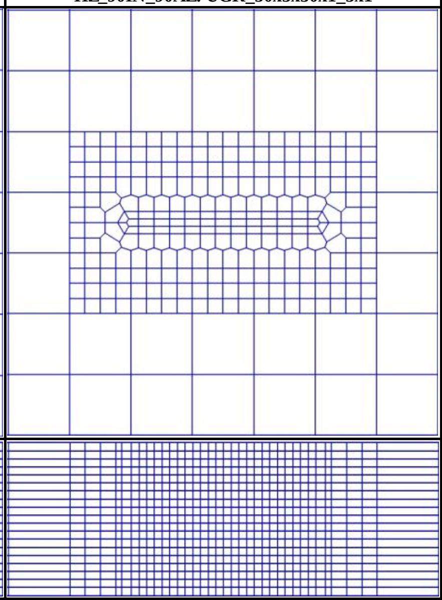

HZ_90IN_90AZ: UGR_50x3x50x1_5x3

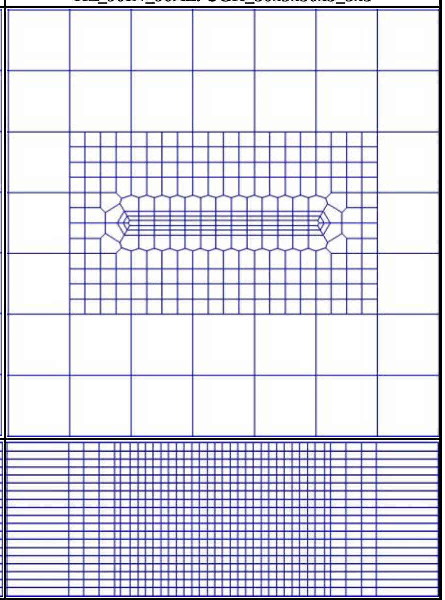

HZ_90IN_90AZ: UGR_50x5x50x1_5x3

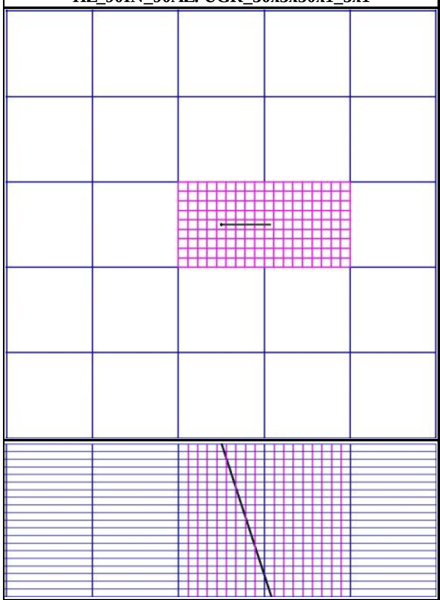

W_30IN_90AZ: LGR_9x1_2x1

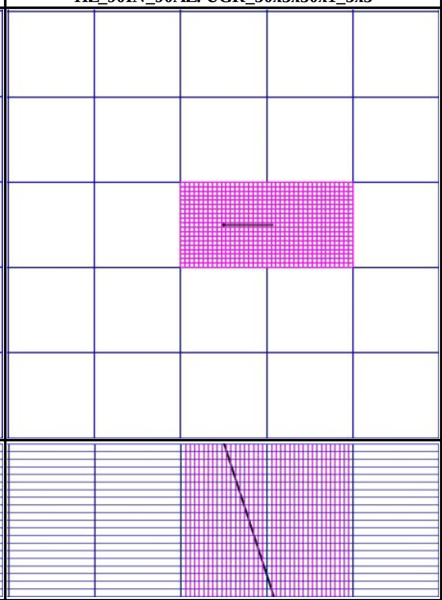

W_30IN_90AZ: LGR_19x1_2x1

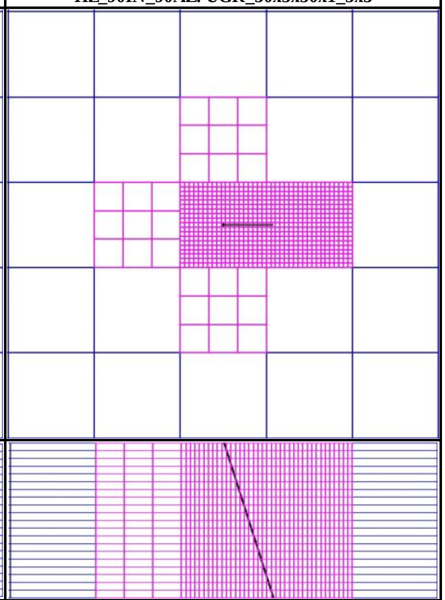

W_30IN_90AZ: LGR_19x1_2x1_3x1+

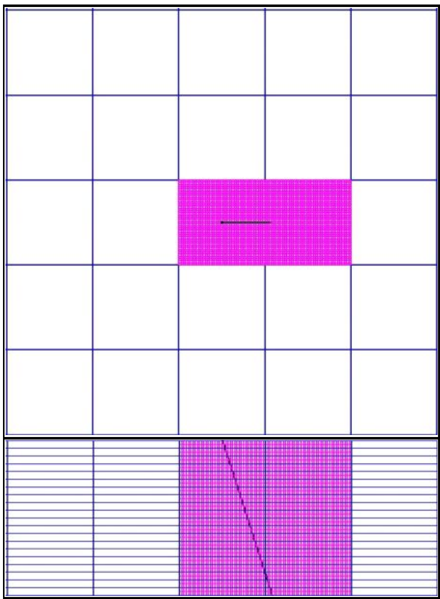

W_30IN_90AZ: LGR_39x2_2x1

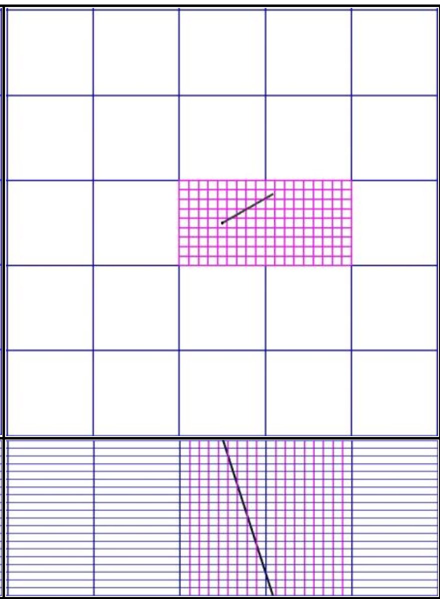

W_34IN_60AZ: LGR_9x1_2x1

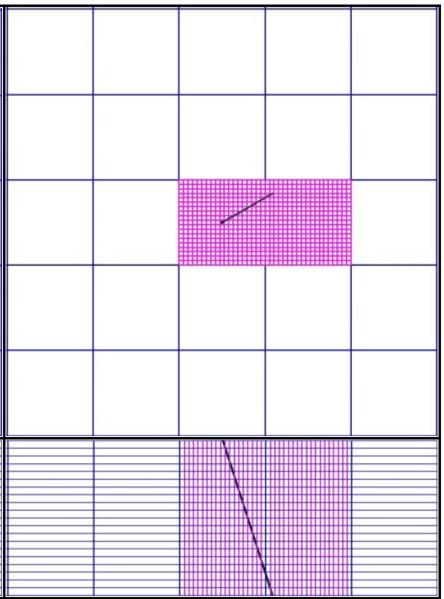

W_34IN_60AZ: LGR_19x1_2x1

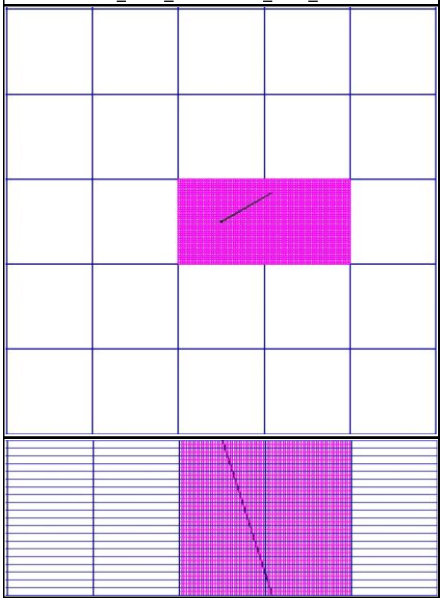

W_34IN_60AZ: LGR_39x2_2x1

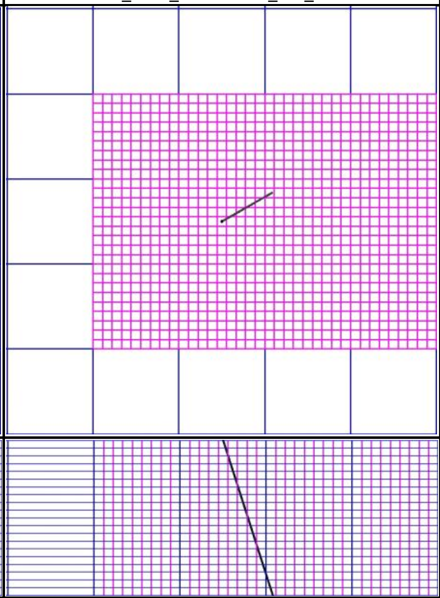

W_34IN_60AZ: LGR_9x1_4x3

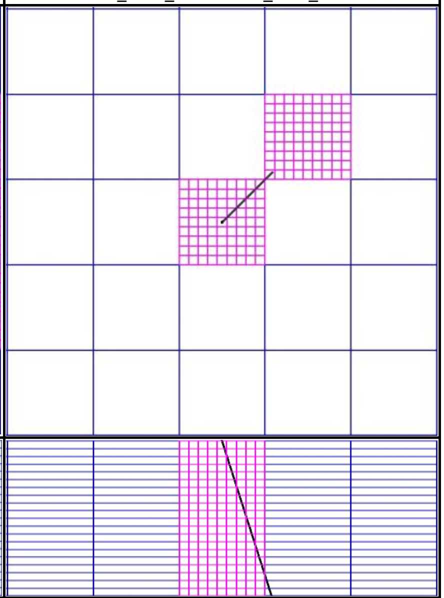

W_39IN_45AZ: LGR_9x1_2xD

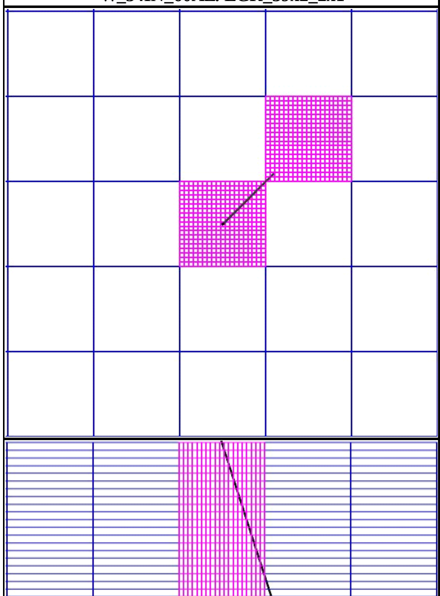

W_39IN_45AZ: LGR_19x1_2xD

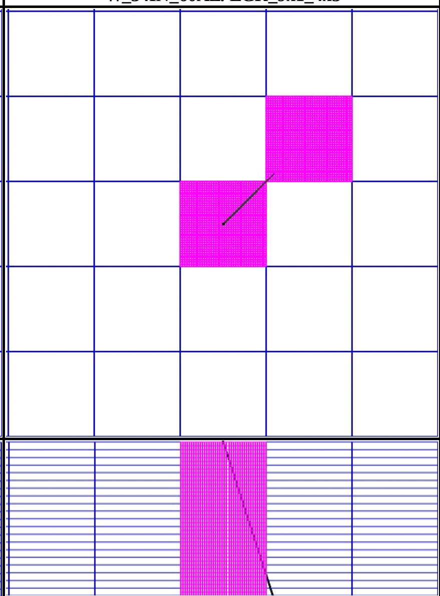

W_39IN_45AZ: LGR_39x2_2xD

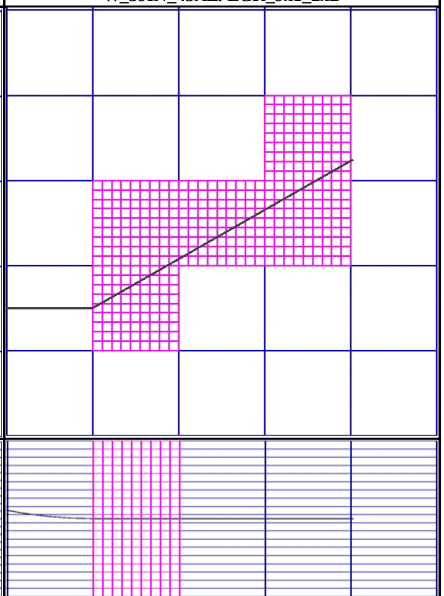

HZ_90IN_60AZ: LGR_9x1_Az30

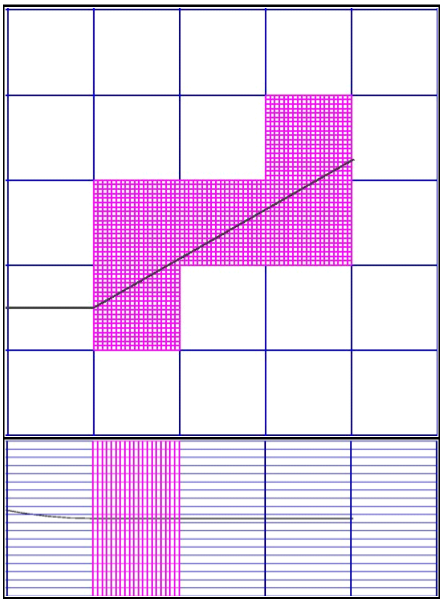

HZ_90IN_60AZ: LGR_19x1_Az30

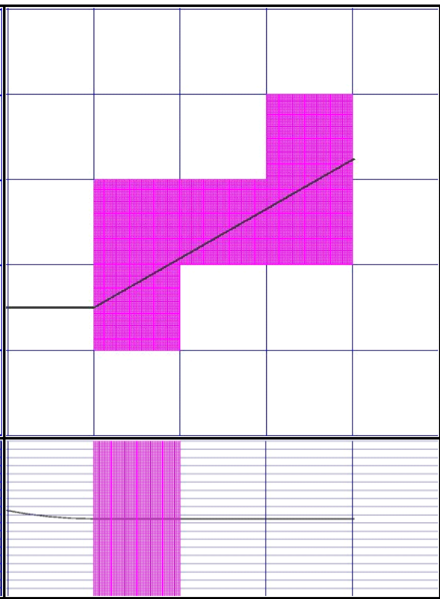

HZ_90IN_60AZ: LGR_57x3_Az30

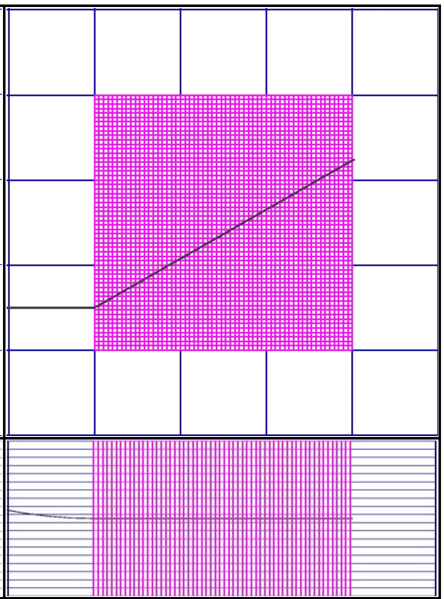

HZ_90IN_60AZ: LGR_19x1_3x3

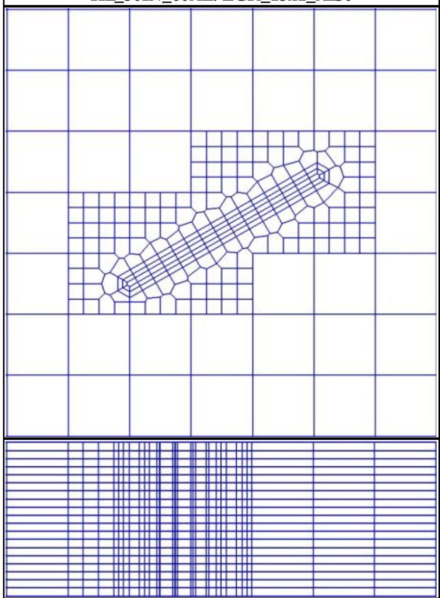

HZ_90IN_60AZ: UGR_50x5x50x1_Az30

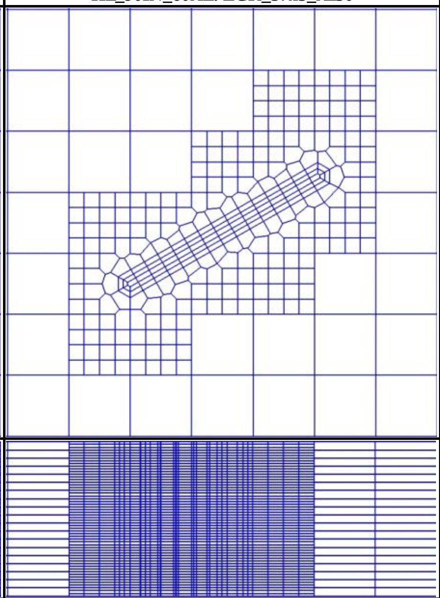

HZ_90IN_60AZ: UGR_50x5x50x3_Az30+

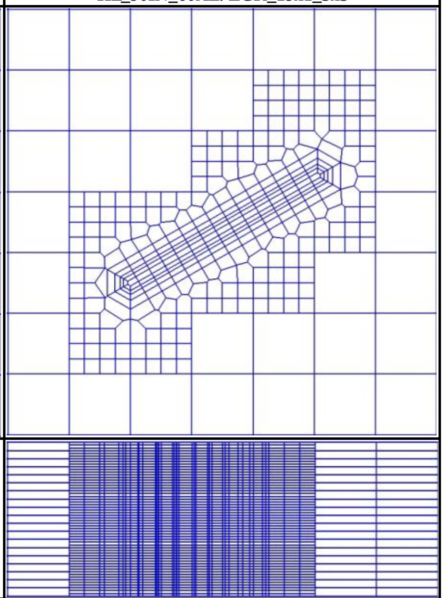

HZ_90IN_60AZ: UGR_90x9x50x3_Az30+

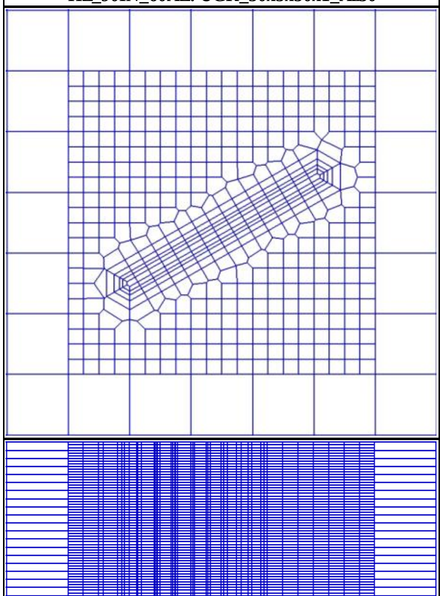

HZ_90IN_60AZ: UGR_90x9x50x3_5x5

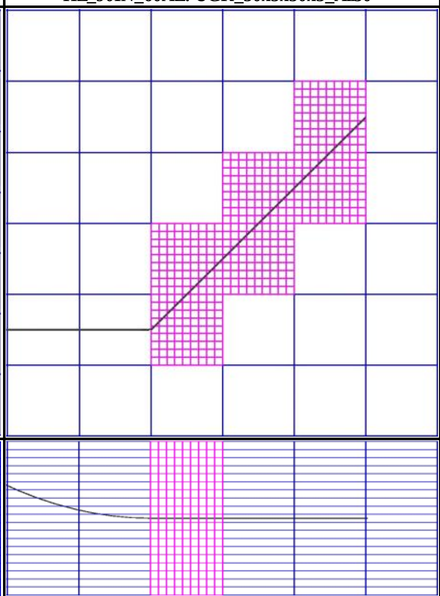

HZ_90IN_45AZ: LGR_9x1_Az45

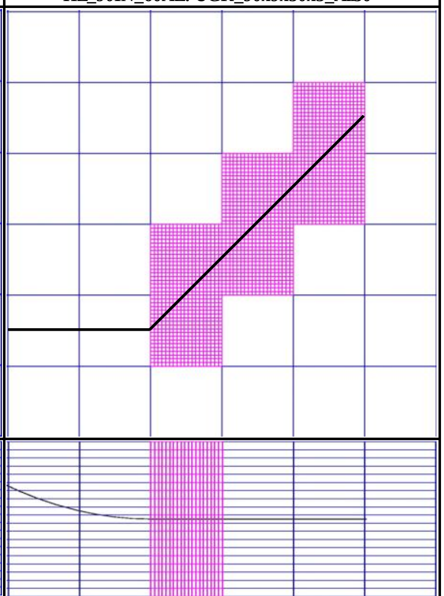

HZ_90IN_45AZ: LGR_19x1_Az45

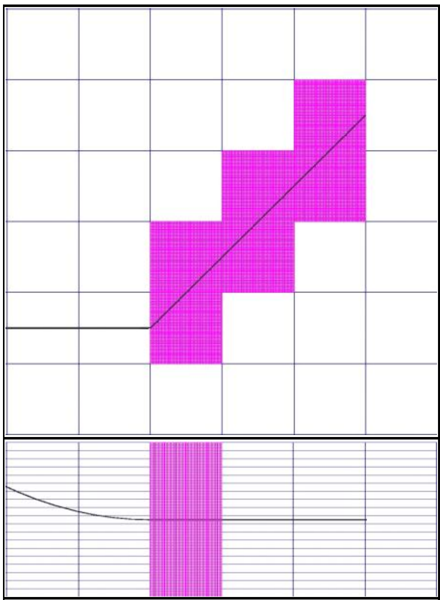
HZ_90IN_45AZ: LGR_57x3_Az45

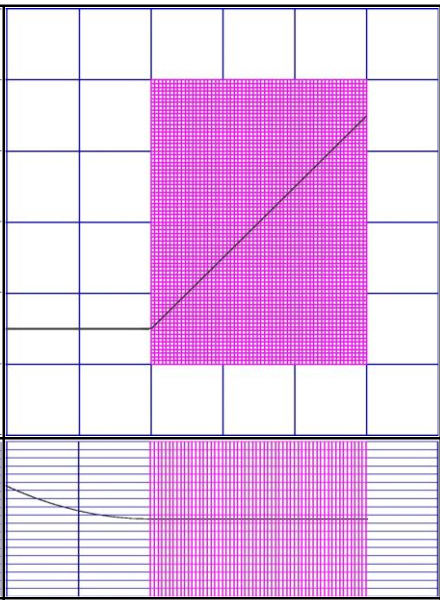
HZ_90IN_45AZ: LGR_57x3_4x3

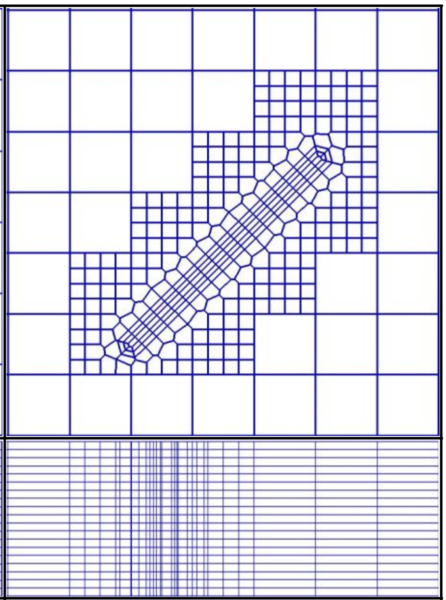
HZ_90IN_45AZ: UGR_50x5x50x1_Az45

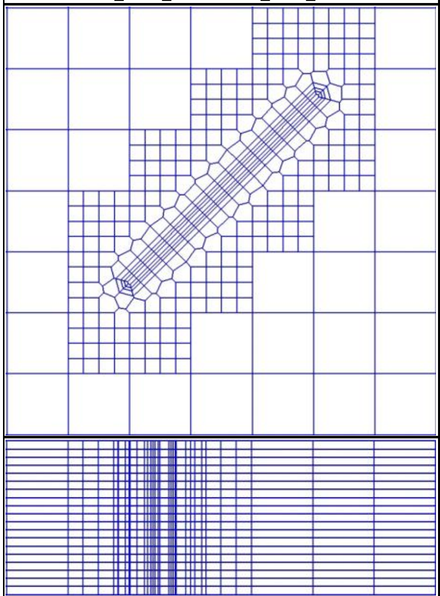
HZ_90IN_45AZ: UGR_50x7x50x1_Az45+

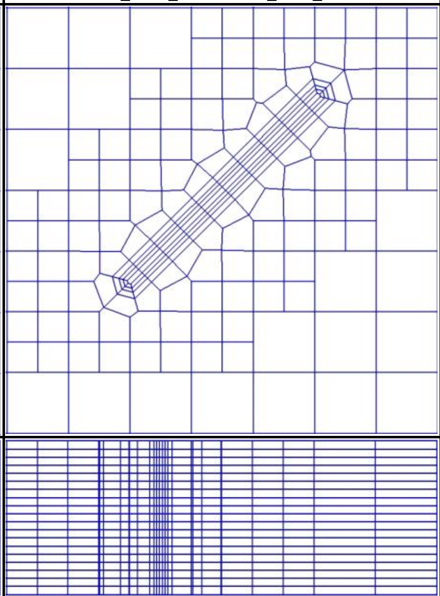
HZ_90IN_45AZ: UGR_63x7x100x1_Az45+

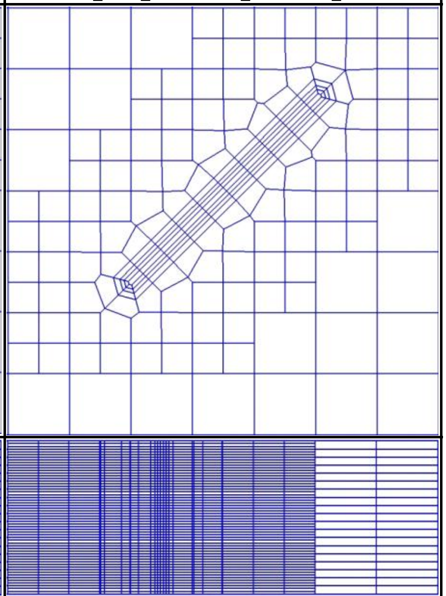
HZ_90IN_45AZ: UGR_63x7x100x3_Az45+

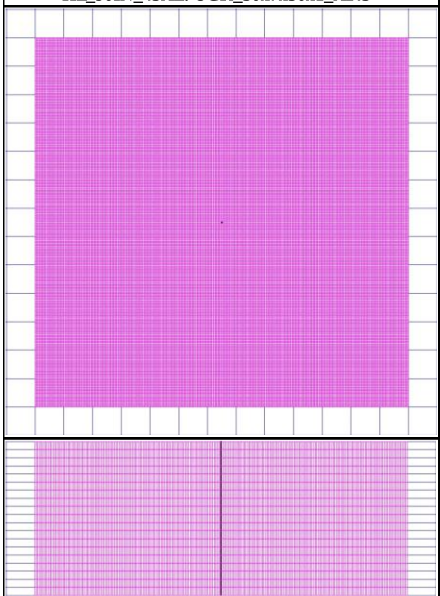
VERT_FP: LGR_19x1_13x13

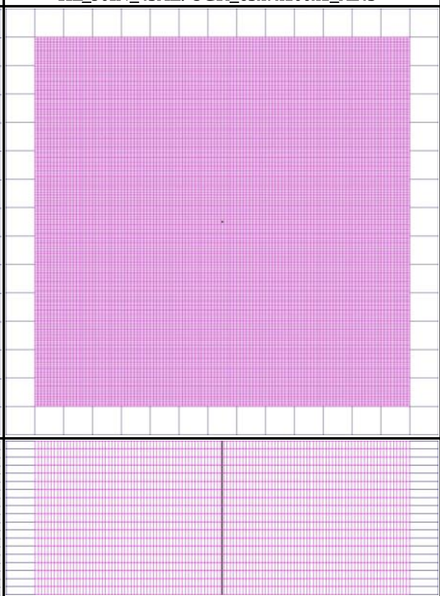
VERT_FP: LGR_9x19x1_13x13

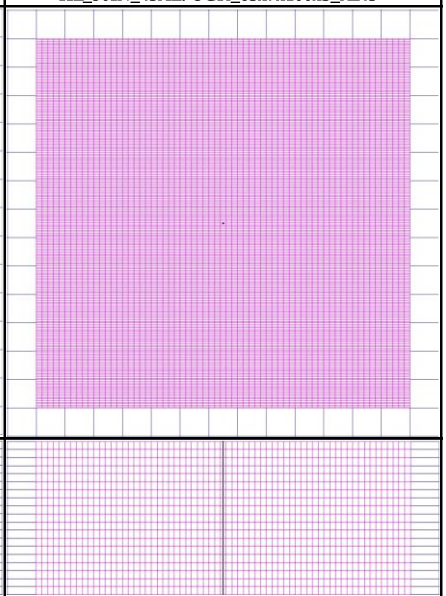
VERT_FP: LGR_5x19x1_13x13

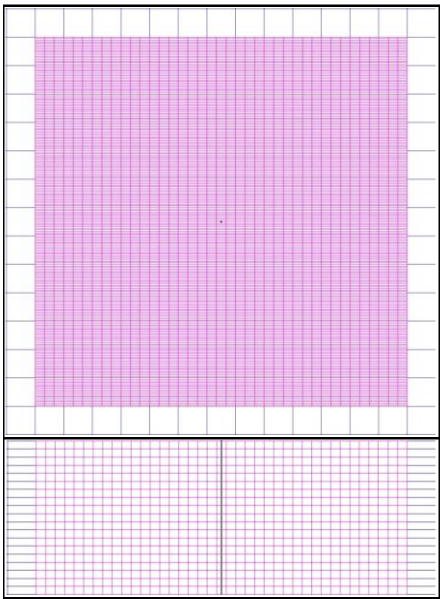
VERT_FP: LGR_3x19x1_13x13

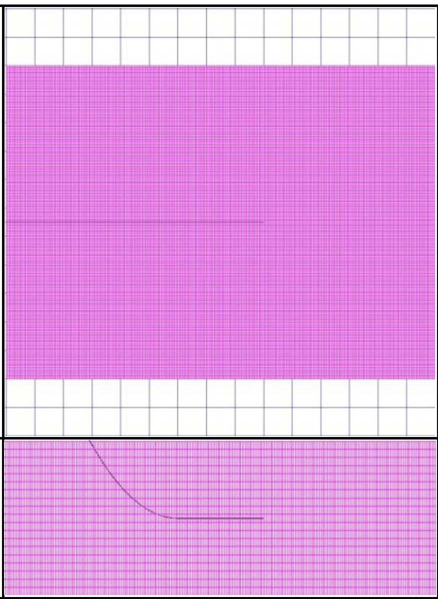
HZ_90IN_90AZ: LGR_19x1_15x11

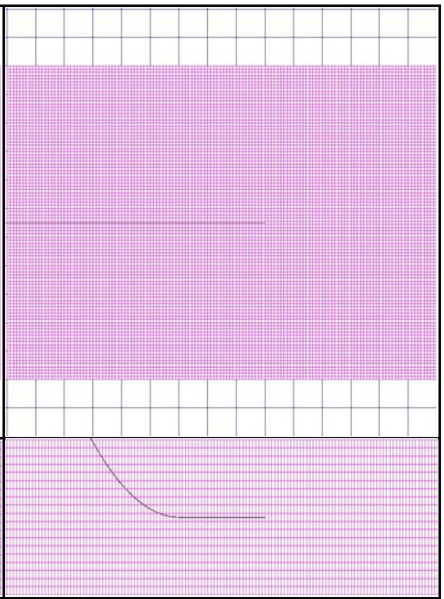
HZ_90IN_90AZ: LGR_9x1_15x11

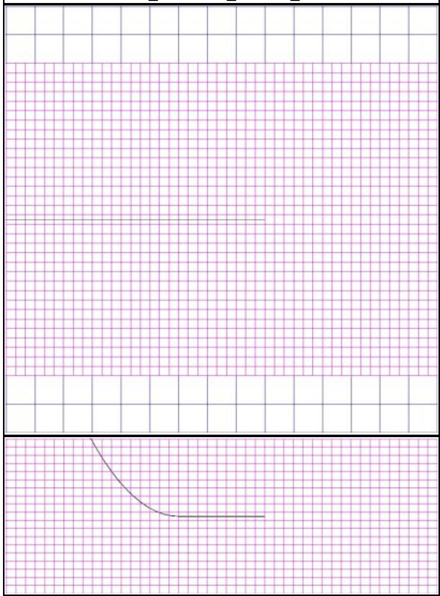
HZ_90IN_90AZ: LGR_3x1_15x11

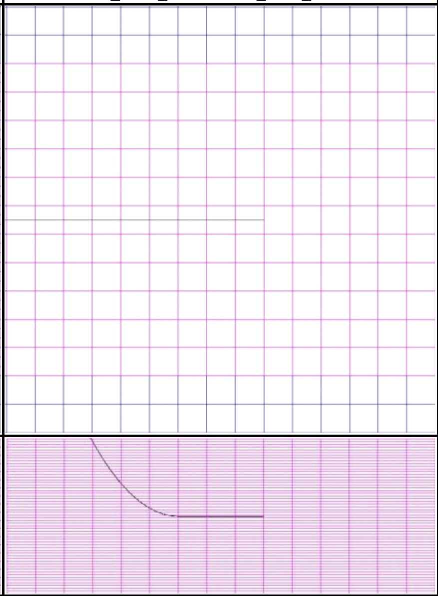
HZ_90IN_90AZ: LGR_1x3_15x11

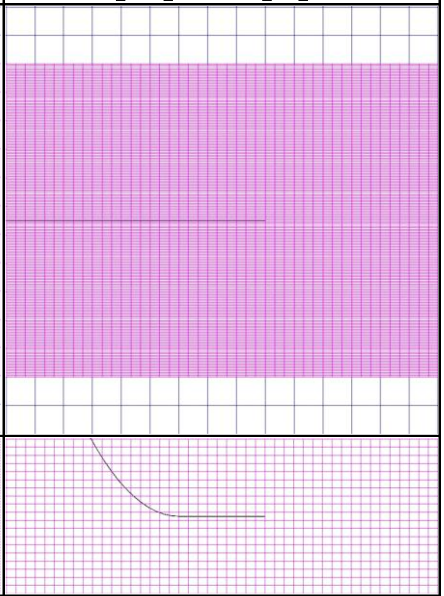
HZ_90IN_90AZ: LGR_3x19x1_15x11

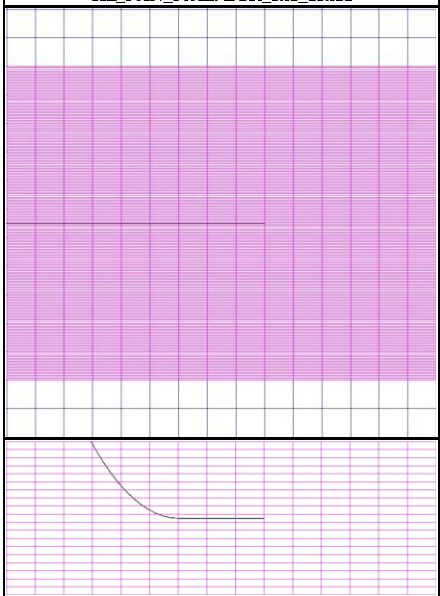
HZ_90IN_90AZ: LGR_1x19x1_15x11

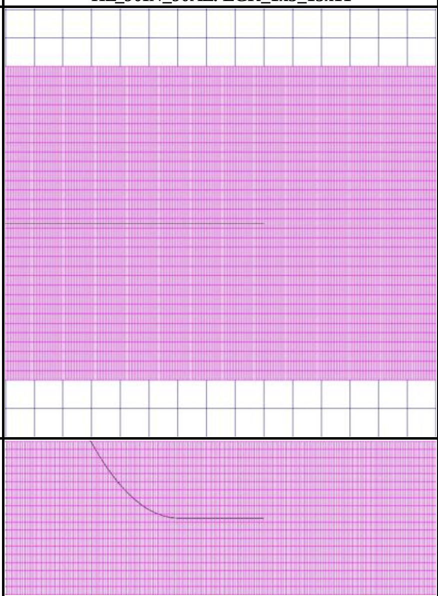
HZ_90IN_90AZ: LGR_19x3x1_15x11

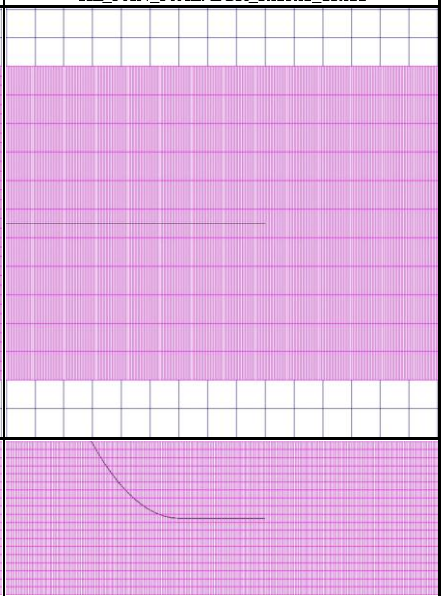
HZ_90IN_90AZ: LGR_19x1x1_15x11

Appendix E: Simulation Results

Fully Penetrating Vertical Well (VERT_FP)

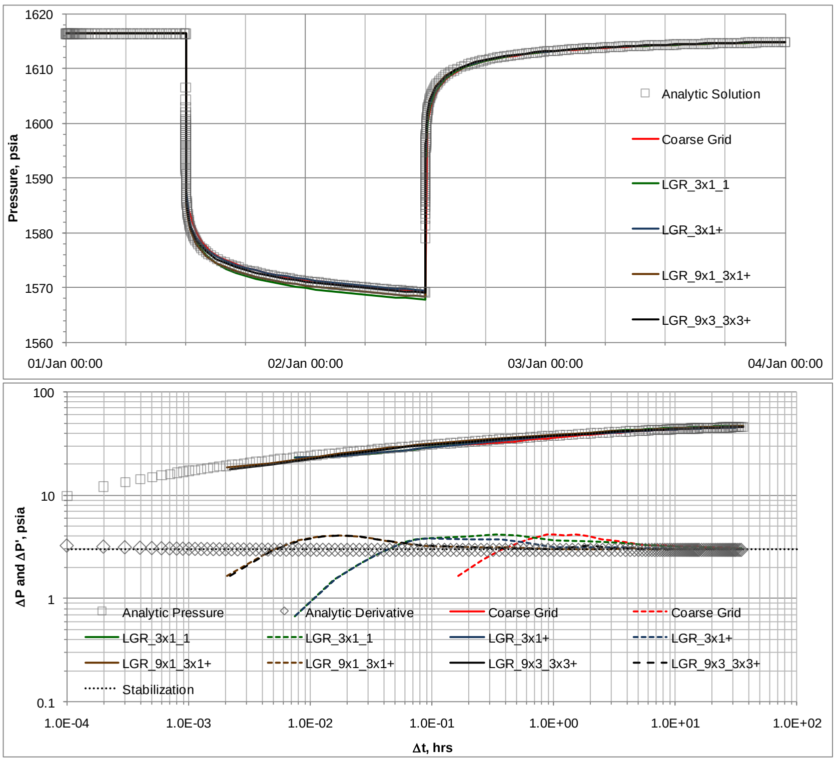

Figure E-1: Results of simulation for VERT_FP using Cartesian refinement.

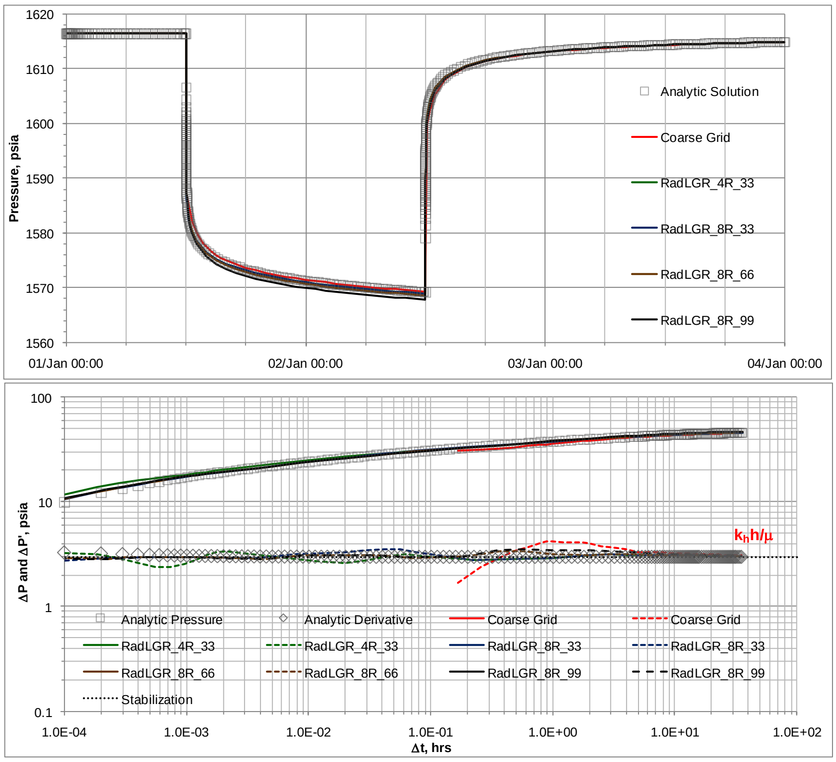

Figure E-2: Results of simulation for VERT_FP using radial refinement.

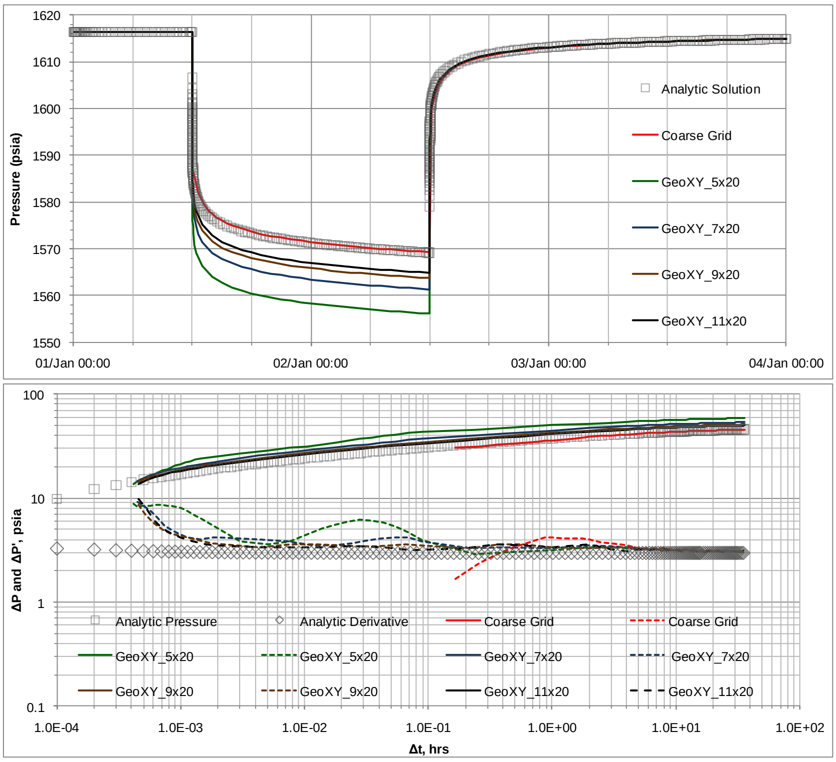

Figure E-3: Results of simulation for VERT_FP using geometric series refinement.

Partially Penetrating Vertical Well (VERT_PP)

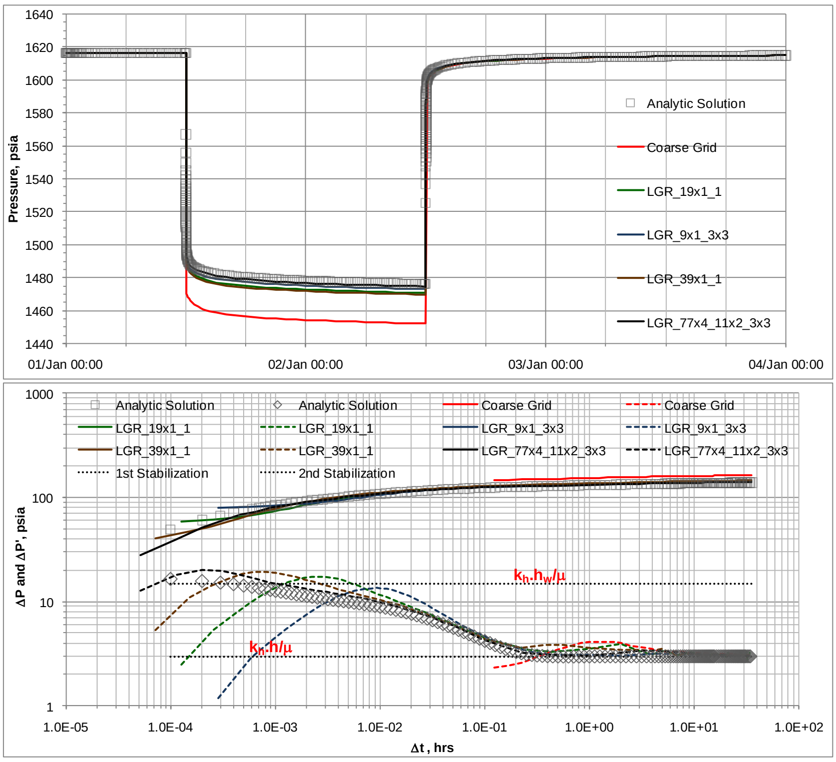

Figure E-4: Results of simulation for VERT_PP using Cartesian refinement.

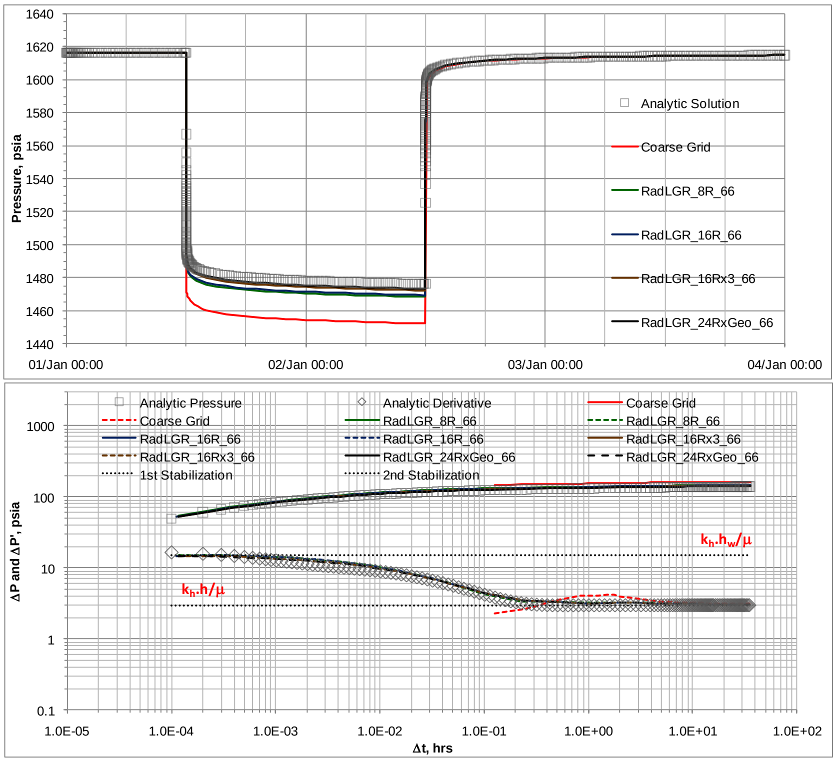

Figure E-5: Results of simulation for VERT_PP using radial refinement.

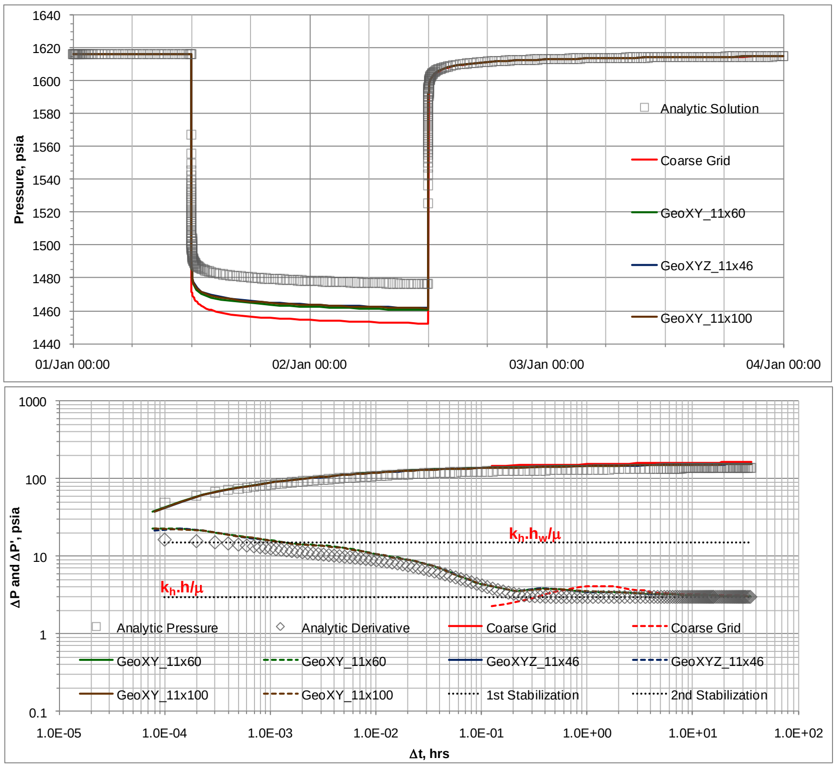

Figure E-6: Results of simulation for VERT_PP using geometric series refinement.

Horizontal Well Aligned with Grid (HZ_90IN_90AZ)

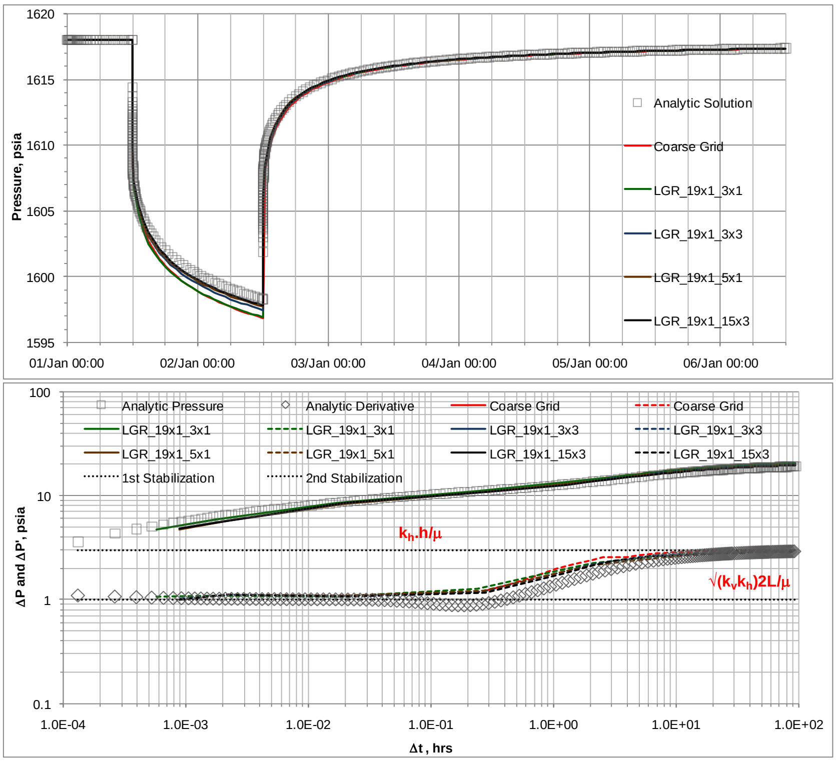

Figure E-7: Primary results of simulation for HZ_90IN_90AZ using Cartesian refinement.

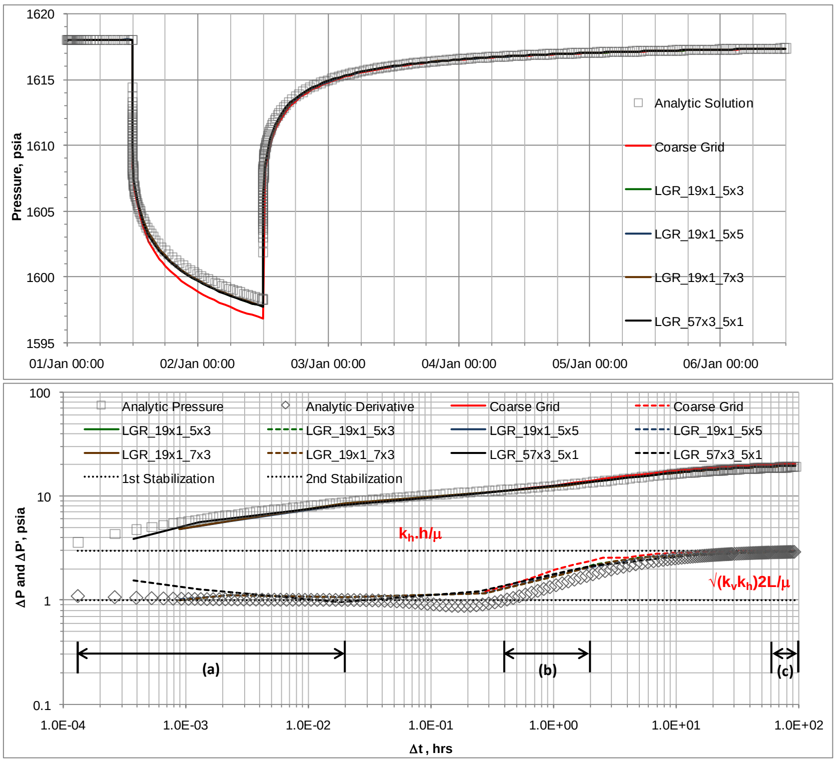

Figure E-8: Additional results of simulation for HZ_90IN_90AZ using Cartesian refinement.

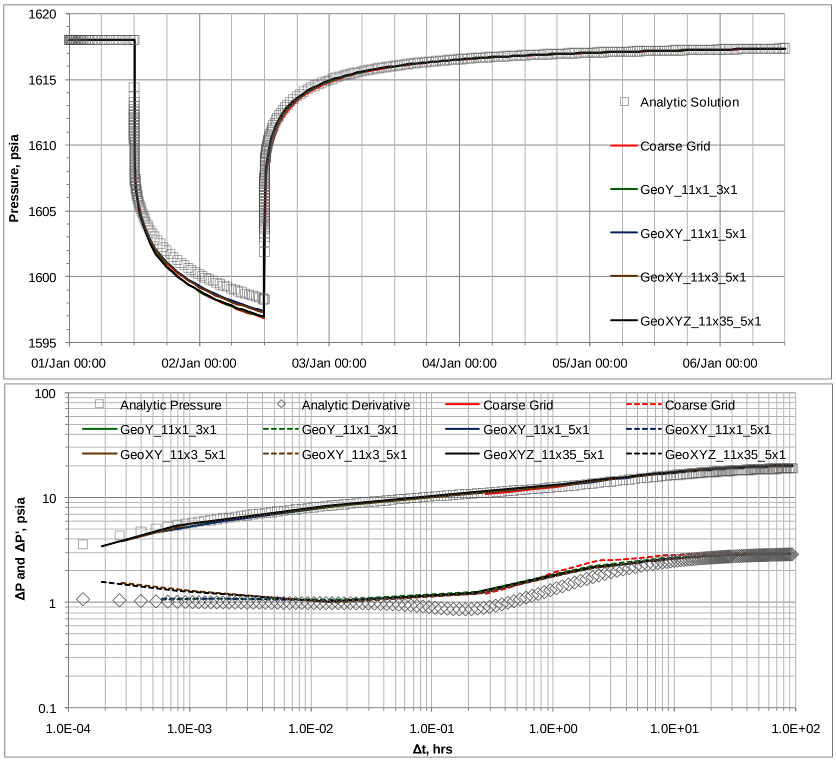

Figure E-9: Results of simulation for HZ_90IN_90AZ using geometric series refinement.

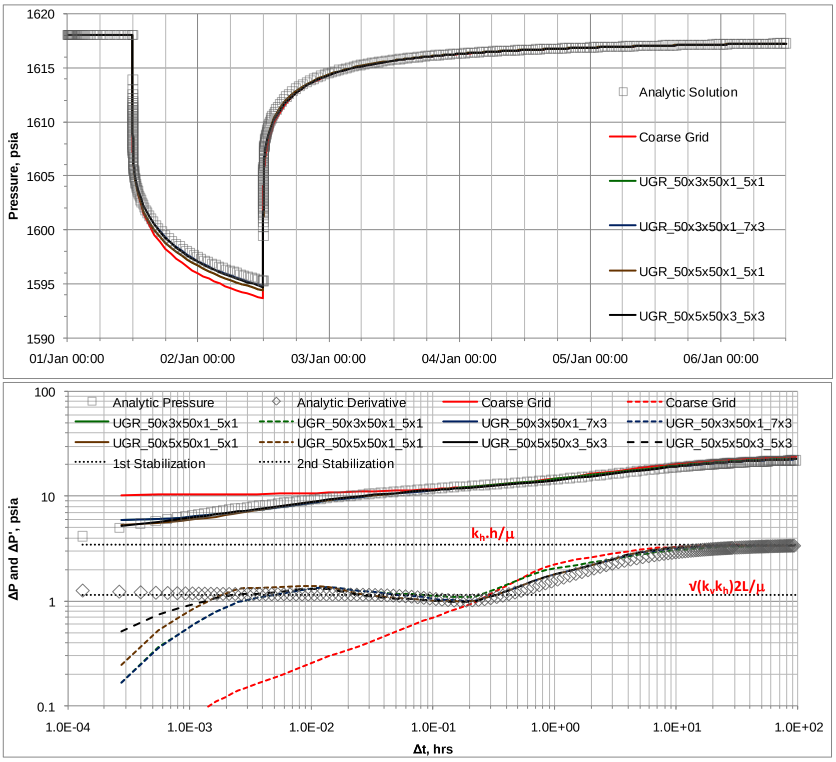

Figure E-10: Primary results of simulation for HZ_90IN_90AZ using unstructured refinement.

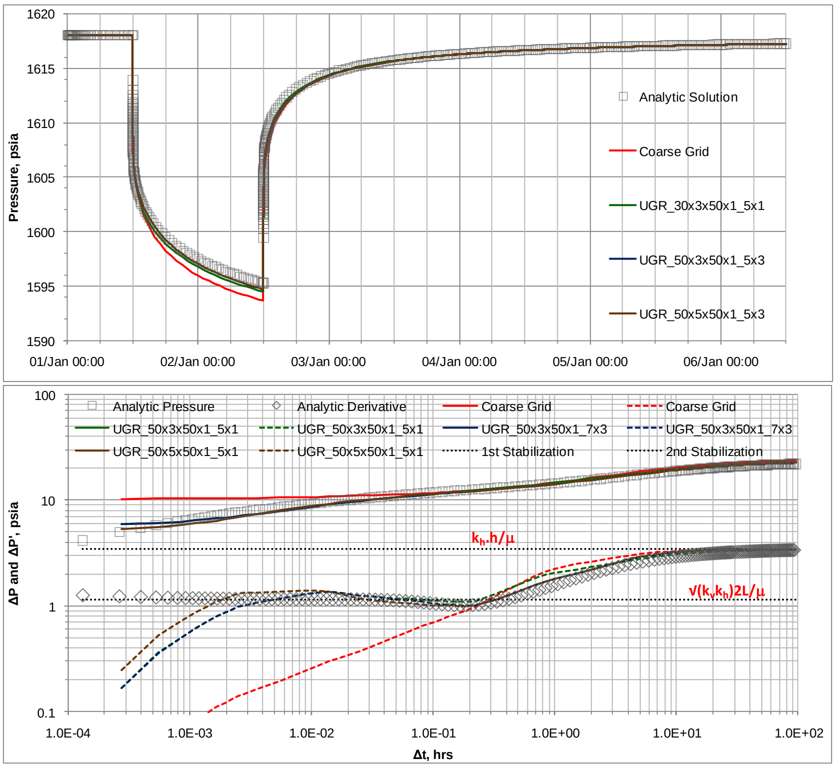

Figure E-11: Additional results of simulation for HZ_90IN_90AZ using unstructured refinement.

Deviated Well, Apparent Dip 30º and Apparent Rotation 0º (W_30IN_90AZ)

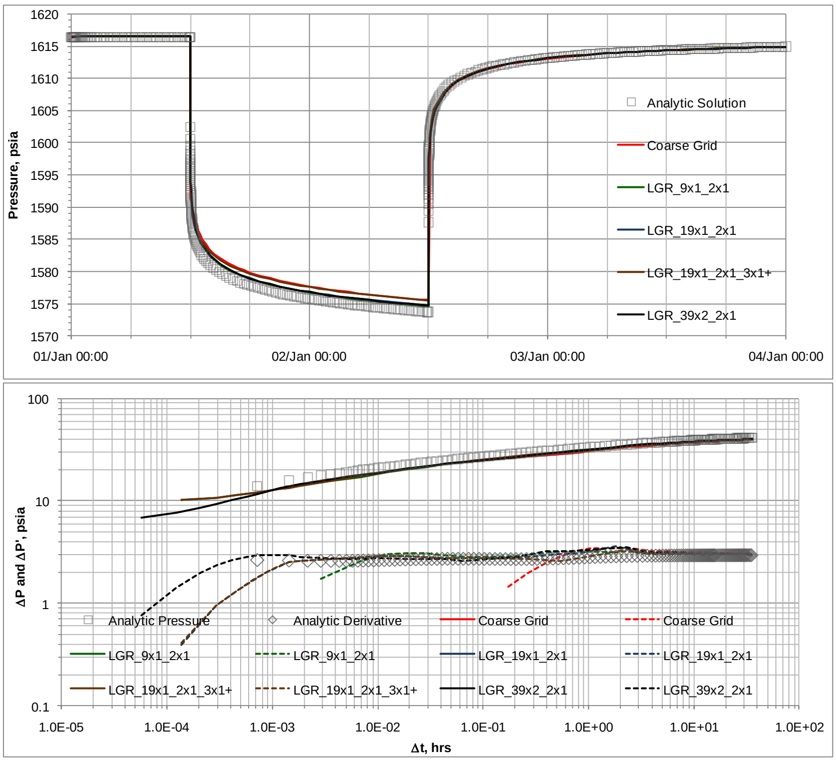

Figure E-12: Results of simulation for W_30IN_90AZ using Cartesian refinement.

Deviated Well, Apparent Dip 30º and Apparent Rotation 30º (W_34IN_60AZ)

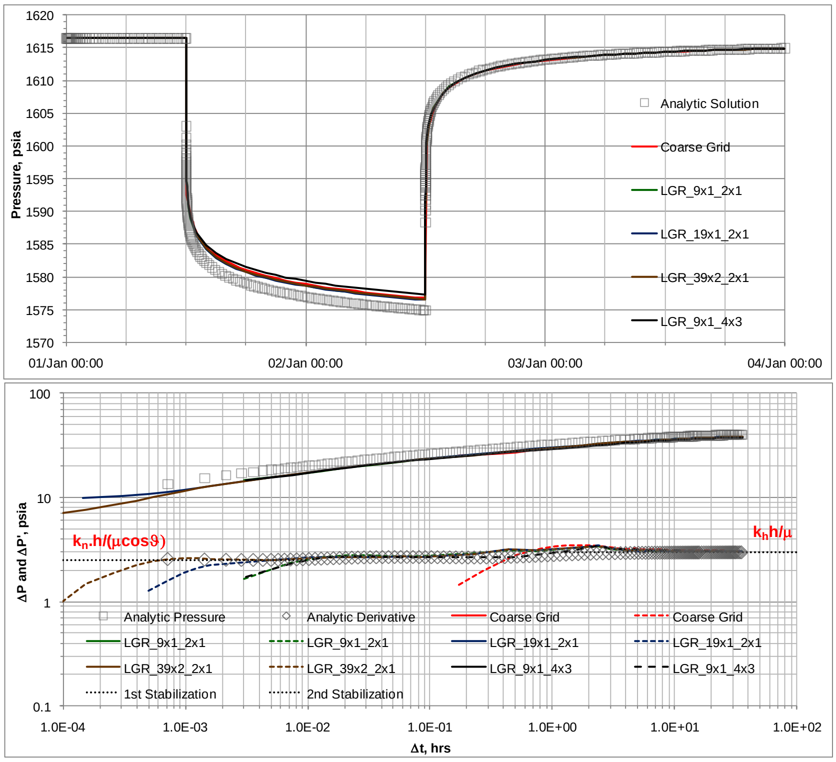

Figure E-13: Results of simulation for W_34IN_60AZ using Cartesian refinement.

Deviated Well, Apparent Dip 30º and Apparent Rotation 45º (W_39IN_45AZ)

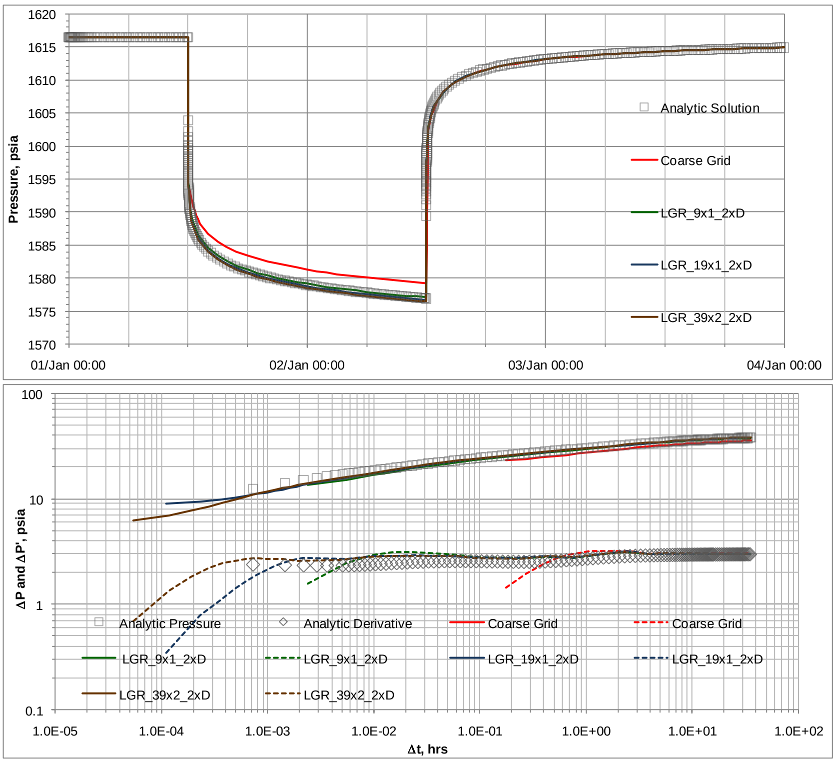

Figure E-14: Results of simulation for W_39IN_45AZ using Cartesian refinement.

Horizontal Well, Apparent Dip 90º and Apparent Rotation 30º (HZ_90IN_60AZ)

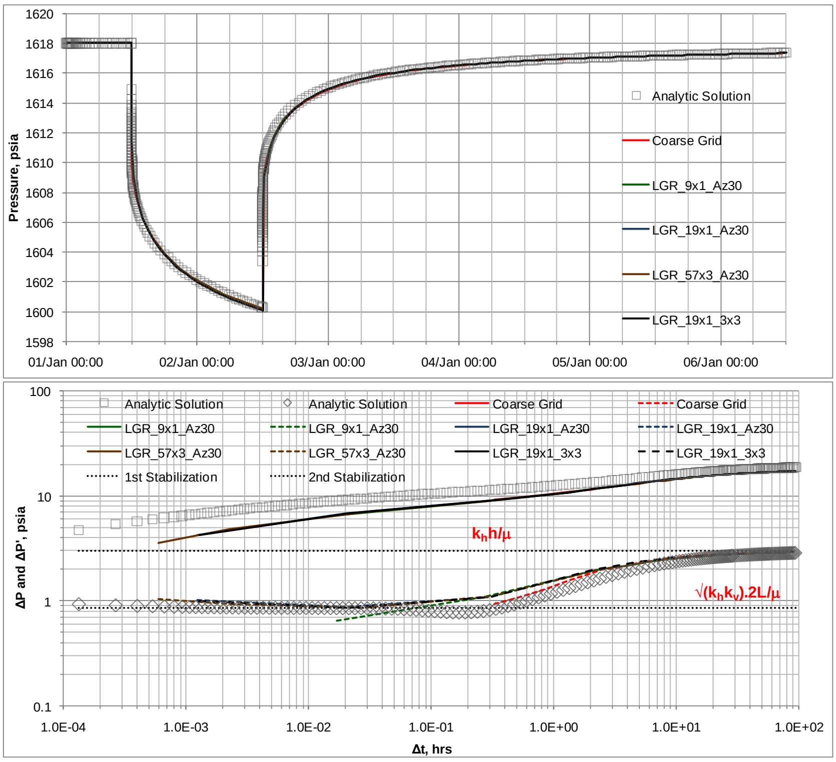

Figure E-15: Results of simulation for HZ_90IN_60AZ using Cartesian refinement.

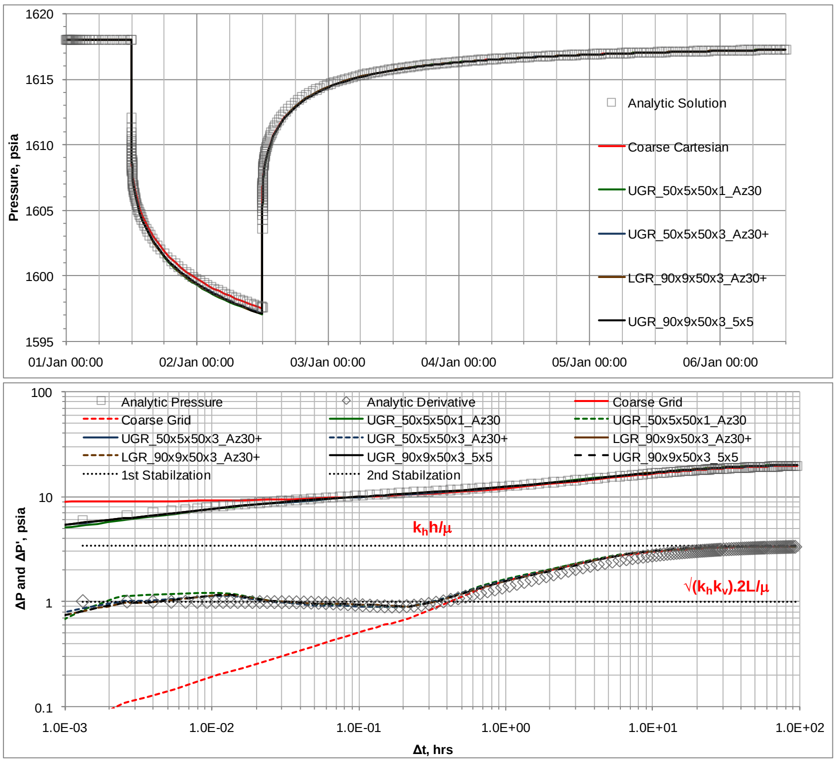

Figure E-16: Results of simulation for HZ_90IN_60AZ using unstructured refinement.

Horizontal Well, Apparent Dip 90º and Apparent Rotation 45º (HZ_90IN_45AZ)

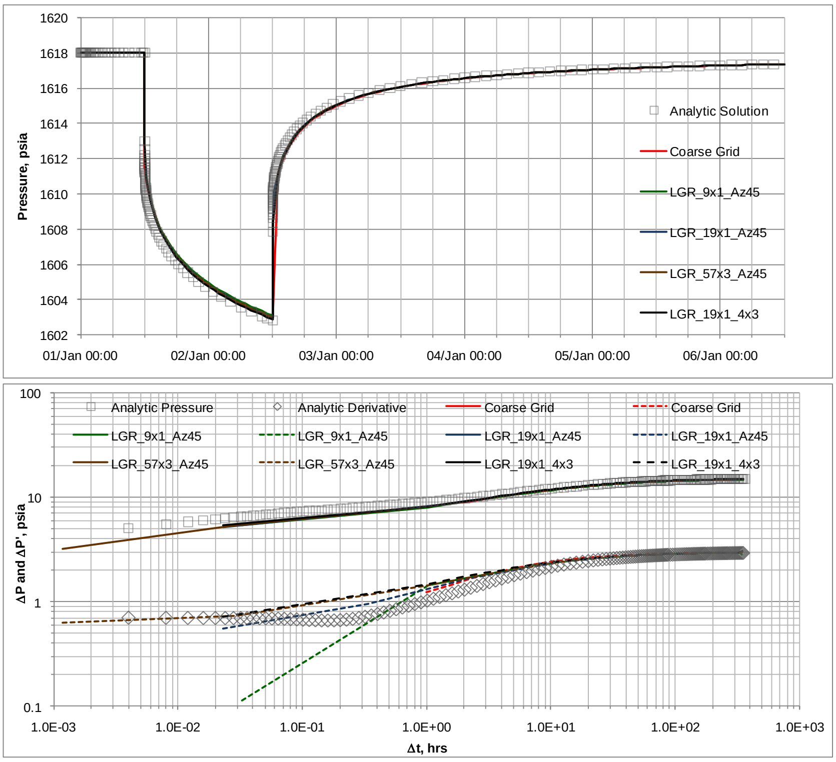

Figure E-17: Results of simulation for HZ_90IN_45AZ using Cartesian refinement.

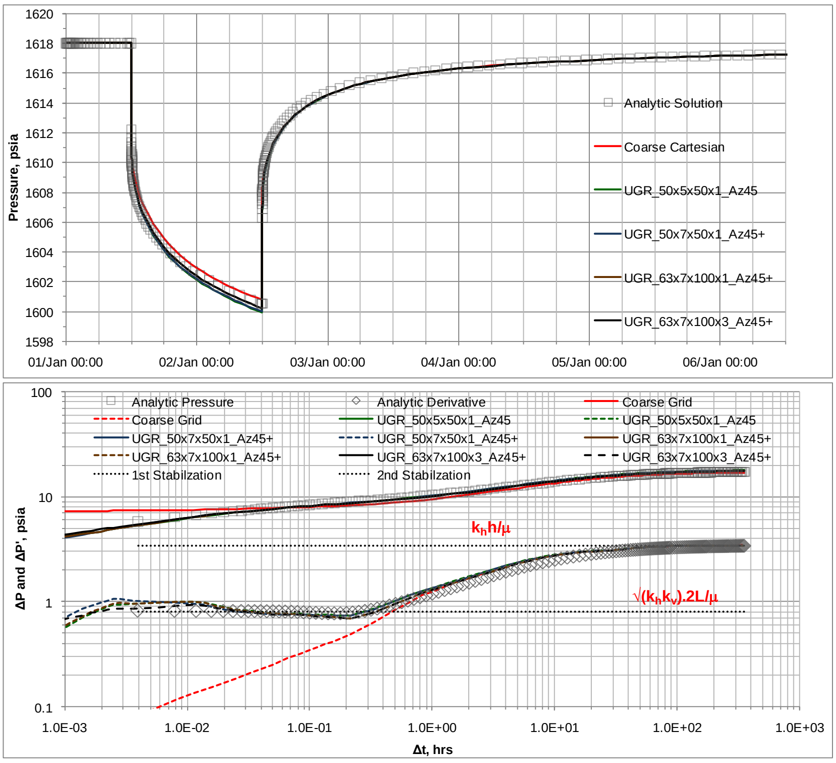

Figure E-18: Results of simulation for HZ_90IN_45AZ using unstructured refinement.

Aspect Ratio Sensitivity Cases

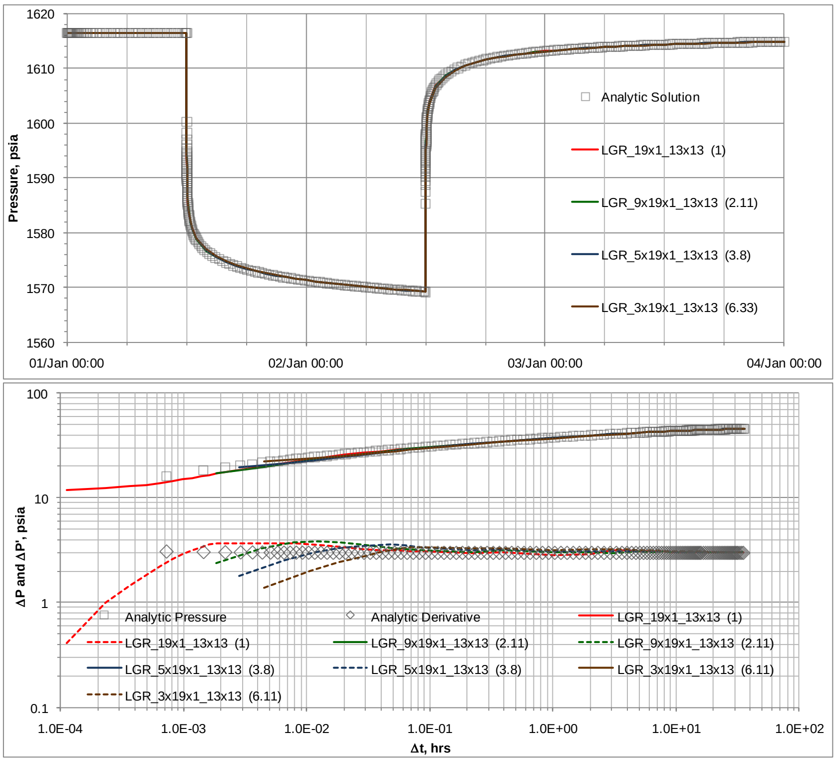

Figure E-19: Results of simulation for VERT_FP to test DX/(DY=DZ) aspect ratios. The associated aspect ratios are shown in parenthesis.

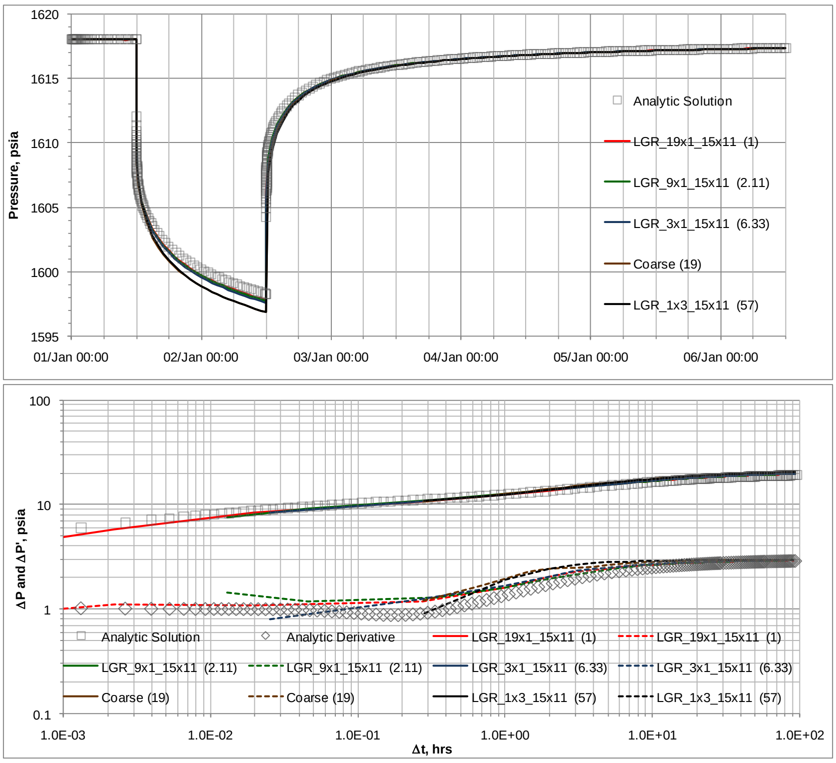

Figure E-20: Results of simulation for HZ_90IN_90AZ to test (DX=DY)/DZ aspect ratios. The associated aspect ratios are shown in parenthesis.

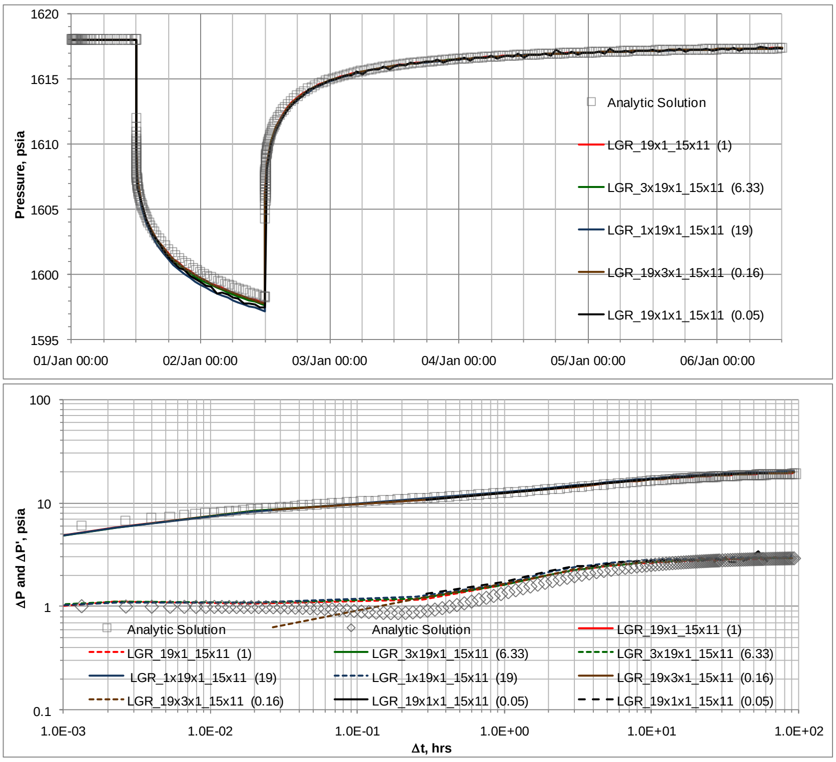

Figure E-21: Results of simulation for HZ_90IN_90AZ to test DX/DY aspect ratios. The associated aspect ratios are shown in parenthesis.

5-Point versus 9-Point Flux Sensitivity Cases

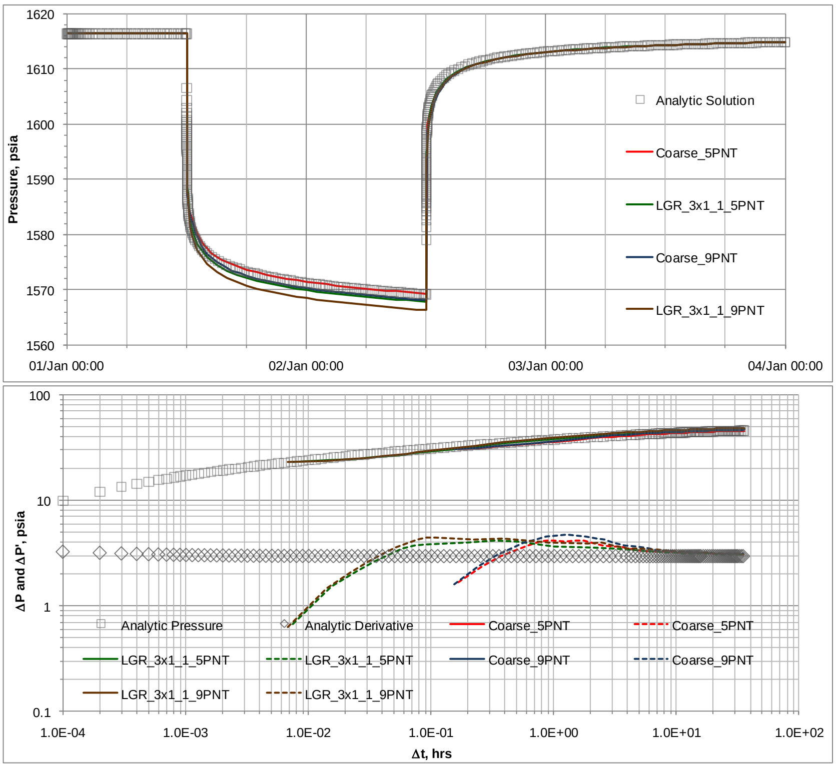

Figure E-22: Results of simulation for VERT_FP to test flux schemes.

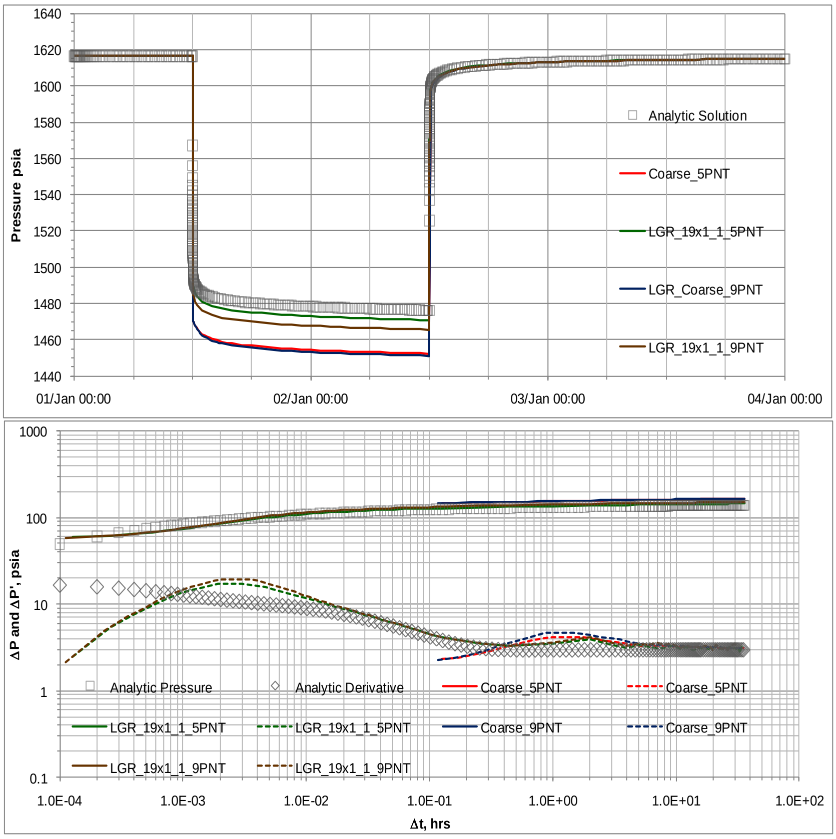

Figure E-23: Results of simulation for VERT_PP to test flux schemes.

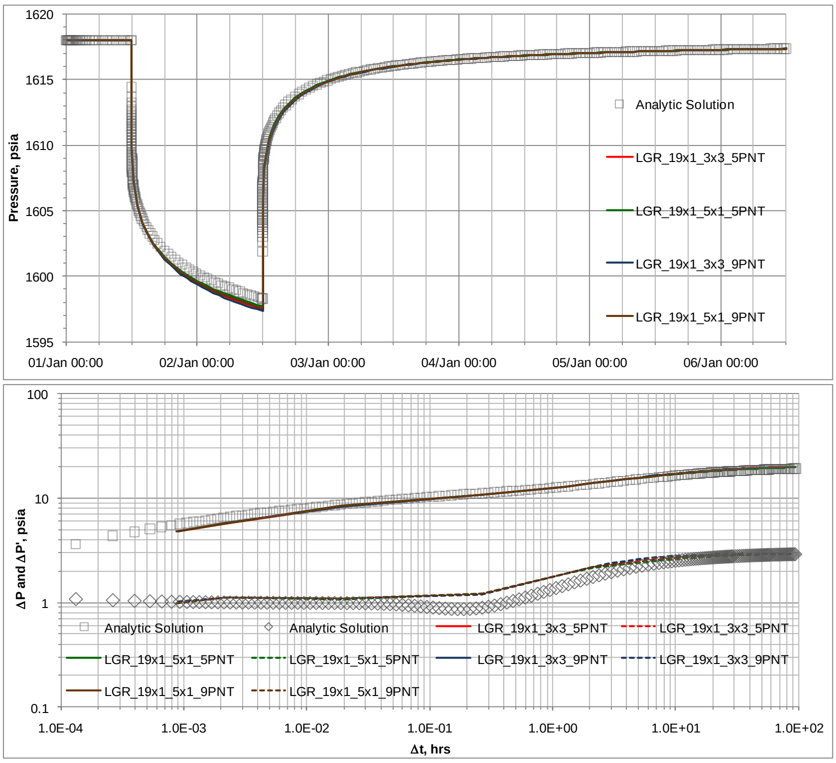

Figure E-24: Results of simulation for HZ_90IN_90AZ to test flux schemes.

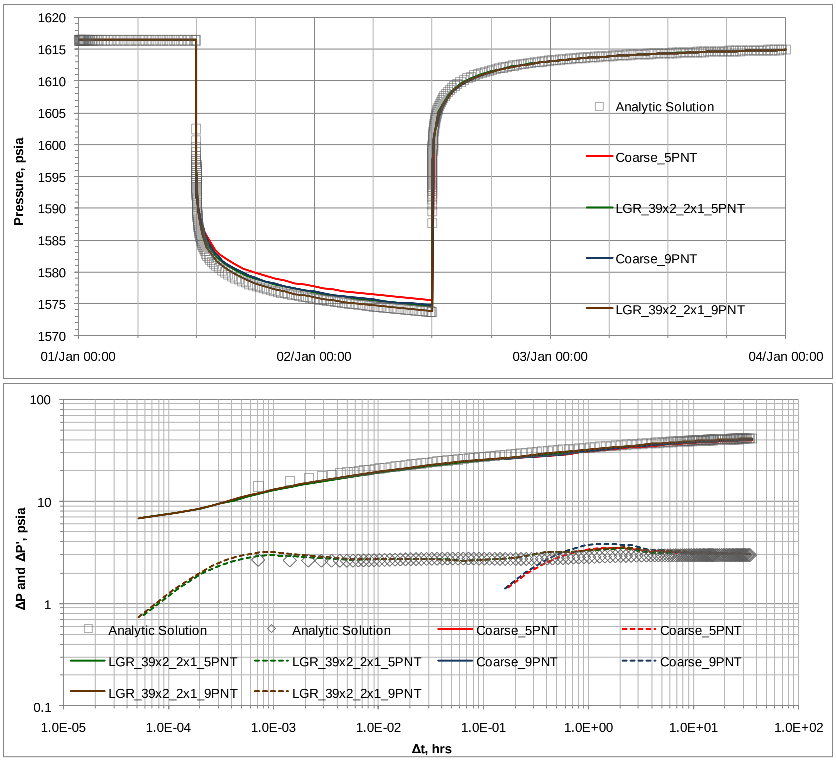

Figure E-25: Results of simulation for W_30IN_90AZ to test flux schemes.

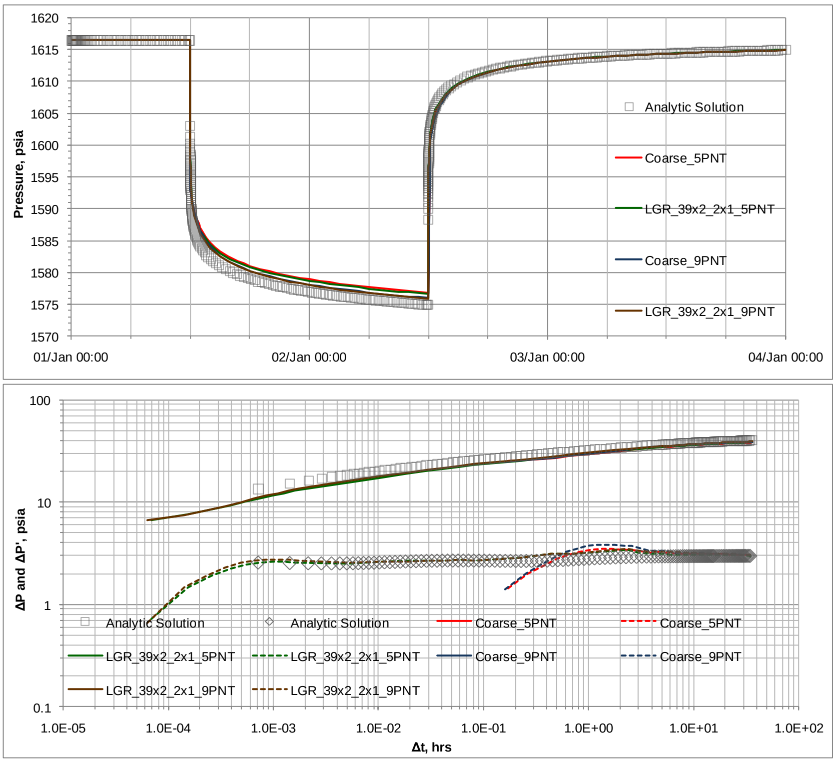

Figure E-26: Results of simulation for W_34IN_60AZ to test flux schemes.

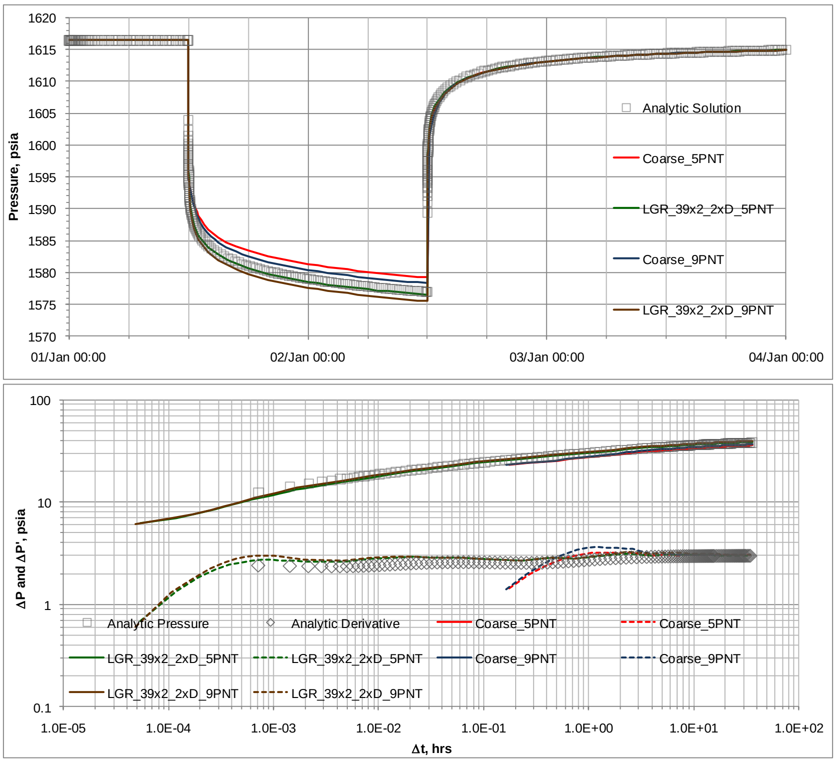

Figure E-27: Results of simulation for W_39IN_45AZ to test flux schemes.

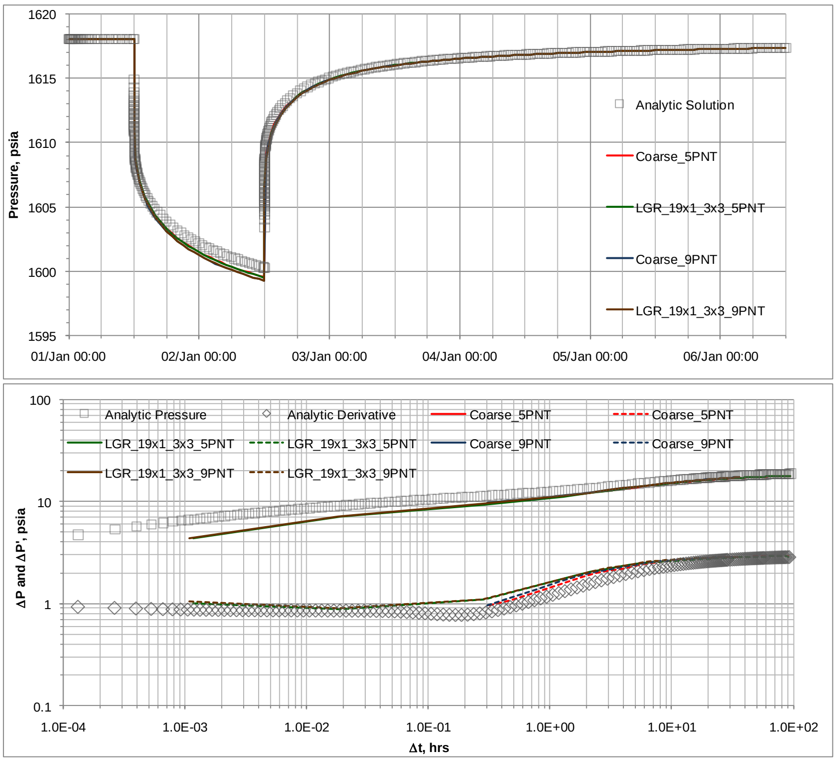

Figure E-28: Results of simulation for HZ_90IN_60AZ to test flux schemes

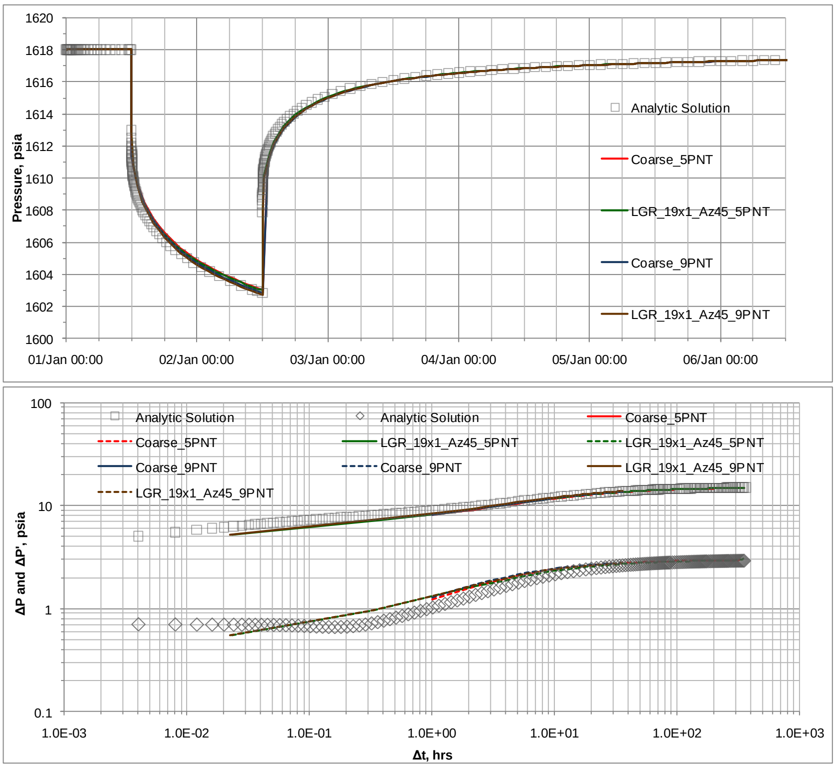

Figure E-29: Results of simulation for HZ_90IN_45AZ to test flux schemes

Appendix F: Pressure Transient Analyses

Fully Penetrating Vertical Well (VERT_FP)

		Values					Errors				
		C	$k_h h$	k_h	S_t	P_i	C	$k_h h$	k_h	S_t	P_i
		bbl/psi	mD-ft	mD	-	psia	%	%	%	-	%
	VERT_FP (ANALYTIC)	0.000113	28000.000	140.000	0.000	1616.430	0.000	0.000	0.000	0.000	0.000
Coarse Grid	Coarse	0.3	27400.000	137.000	-0.150	1616.460	265386.726	-2.143	-2.143	-0.150	0.002
	RMS Error, Absolute	**0.300**	**600.000**	**3.000**	**0.150**	**0.030**					
	RMS Error, Relative (%)	**265387**	**2.14**	**2.14**	**-**	**0.002**					
Cartesian Refinement	LGR_3x1_1	0.11	27400.000	137.000	0.090	1616.460	97245.133	-2.143	-2.143	0.090	0.002
	LGR_3x1+	0.07	28000.000	140.000	-0.040	1616.440	61846.903	0.000	0.000	-0.040	0.001
	LGR_9x1_3x1+	0.008	28000.000	140.000	0.150	1616.440	6979.646	0.000	0.000	0.150	0.001
	LGR_9x3_3x3	0.008	28000.000	140.000	0.025	1616.440	6979.646	0.000	0.000	0.025	0.001
	RMS Error, Absolute	**0.065**	**300.000**	**1.500**	**0.091**	**0.017**					
	RMS Error, Relative (%)	**57834**	**1.07**	**1.07**	**-**	**0.001**					
Radial Refinement	Rad_4R_33	0.00012	28000.000	140.000	0.050	1616.430	6.195	0.000	0.000	0.050	0.000
	Rad_8R_33	0.0001	28000.000	140.000	0.050	1616.430	-11.504	0.000	0.000	0.050	0.000
	Rad_8R_66	0.00005	27600.000	138.000	0.000	1616.460	-55.752	-1.429	-1.429	0.000	0.002
	Rad_8R_99	0.00005	27300.000	136.500	0.040	1616.460	-55.752	-2.500	-2.500	0.040	0.002
	RMS Error, Absolute	**0.000045**	**403**	**2.02**	**0.041**	**0.021**					
	RMS Error, Relative (%)	**40**	**1.44**	**1.44**	**-**	**0.001**					

Table F-1: Summary of the interpretation results for VERT_FP well model complete with root mean squared error calculations expressed in absolute and relative terms.

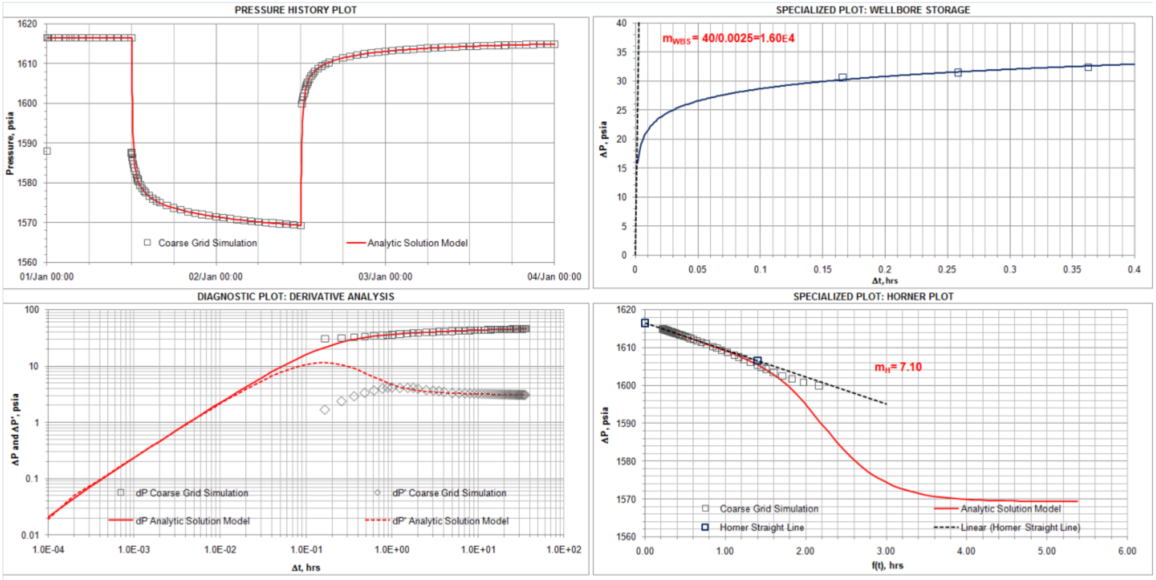

	MODEL PARAMETERS				
	C	$k_h h$	k_h	S_t	P_i
	bbl/psi	mD-ft	mD	-	psia
Actual Values	0.000113	28000	140	0	1616.43
Derivative Analysis	0.3	27400	137	-0.15	1616.46
Specialized Analysis	0.00447	27000	135	-0.27	1616.47
Difference	%	%	%	-	%
Actual vs Derivative	265387	-2.14	-2.14	-0.15	0.00
Actual vs Specialized	3856	-3.57	-1.46	-0.27	0.00
Derivative vs Specialized	-99	-1.46	-1.46	-0.12	0.00

Figure F-1: Analysis of well VERT_FP, coarse grid

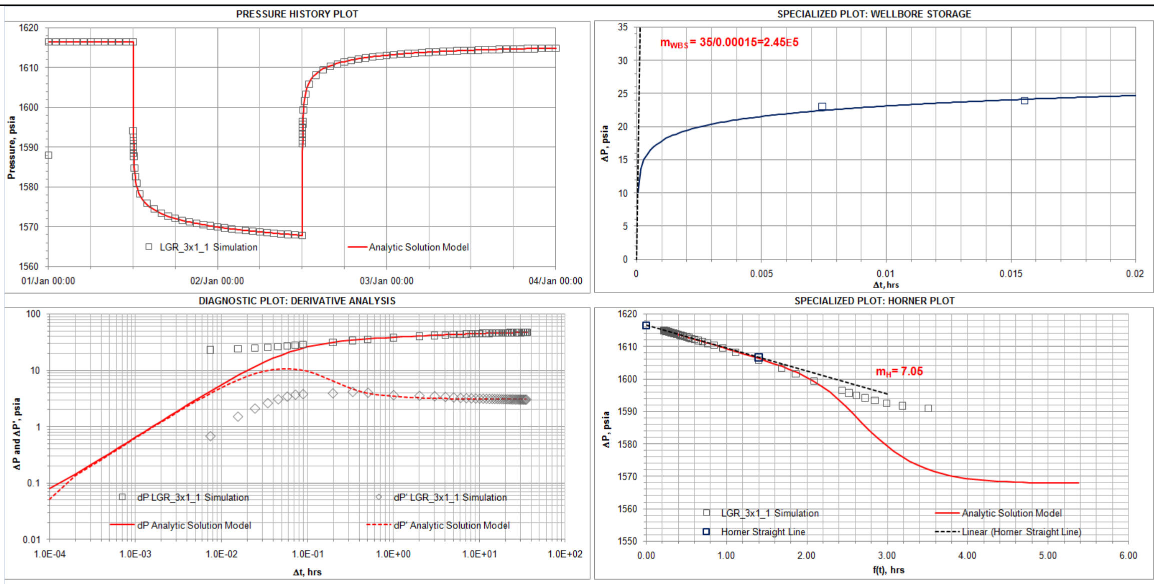

	C	$k_h h$	k_h	S_t	P_i
MODEL PARAMETERS					
	bbl/psi	mD-ft	mD	-	psia
Actual Values	0.000113	28000	140	0	1616.43
Derivative Analysis	0.11	27400	137	0.09	1616.46
Specialized Analysis	0.00029	27200	136	0.02	1616.47
Difference	%	%	%	-	%
Actual vs Derivative	97245	-2.14	-2.14	0.09	0.00
Actual vs Specialized	157	-2.86	-0.73	0.02	0.00
Derivative vs Specialized	-100	-0.73	-0.73	-0.07	0.00

Figure F-2: Analysis of well VERT_FP, LGR_3x1_1

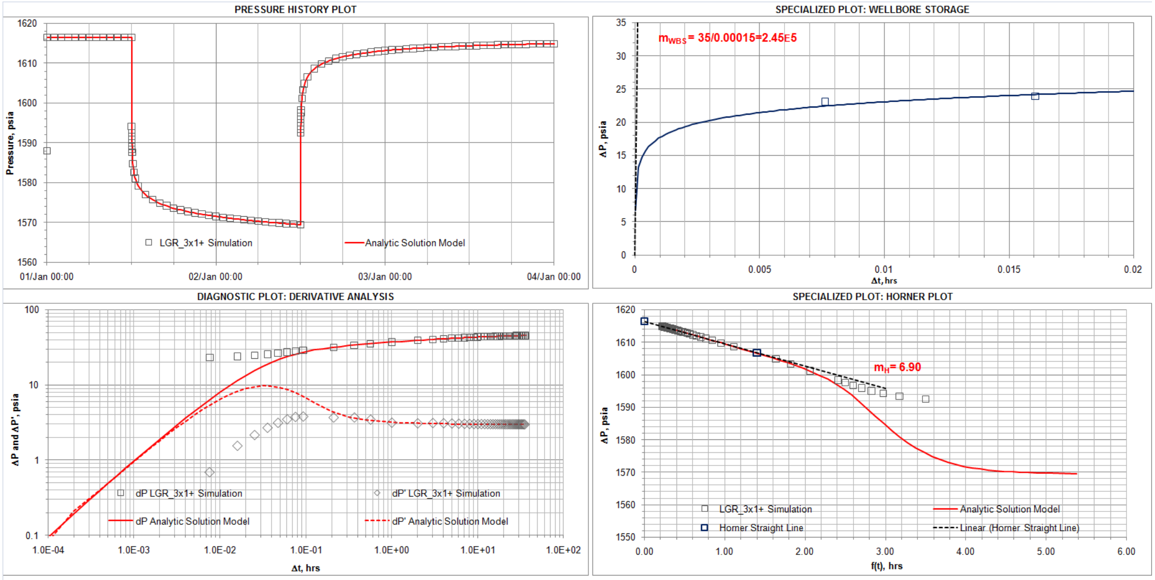

	C	$k_h h$	k_h	S_t	P_i
MODEL PARAMETERS					
	bbl/psi	mD-ft	mD	-	psia
Actual Values	0.000113	28000	140	0	1616.43
Derivative Analysis	0.07	28000	140	-0.04	1616.44
Specialized Analysis	0.00029	27800	139	-0.10	1616.45
Difference	%	%	%	-	%
Actual vs Derivative	61847	0.00	0.00	-0.04	0.00
Actual vs Specialized	157	-0.71	-0.71	-0.10	0.00
Derivative vs Specialized	-100	-0.71	-0.71	-0.06	0.00

Figure F-3: Analysis of well VERT_FP, LGR_3x1+

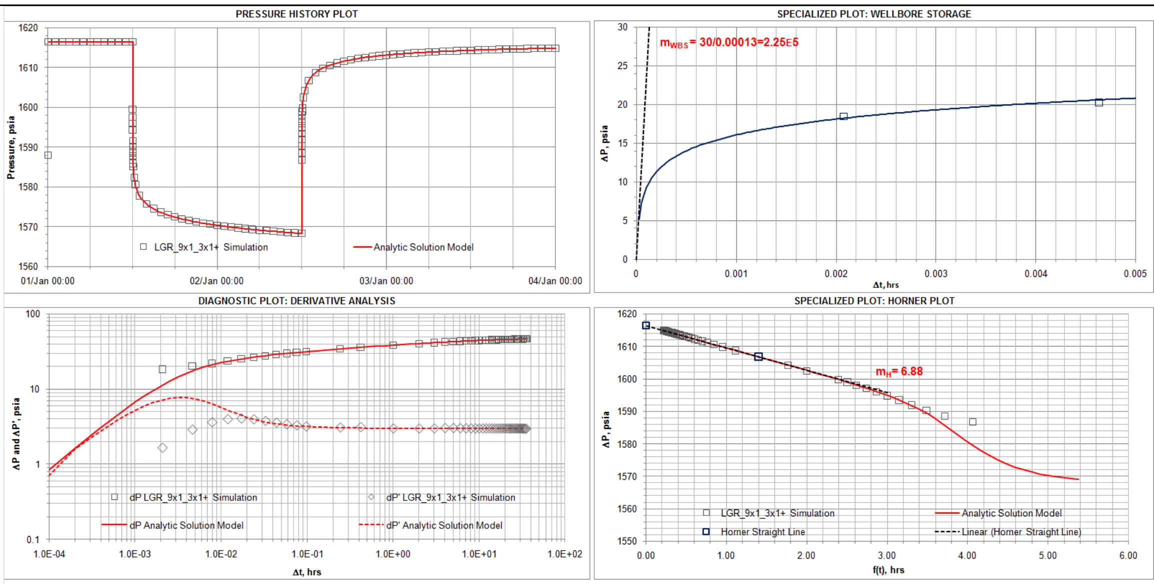

	MODEL PARAMETERS				
	C	$k_h h$	k_h	S_t	P_i
	bbl/psi	mD-ft	mD	-	psia
Actual Values	0.000113	28000	140	0	1616.43
Derivative Analysis	0.008	28000	140	0.15	1616.44
Specialized Analysis	0.00032	27900	139.5	0.12	1616.44
Difference	%	%	%	-	%
Actual vs Derivative	6980	0.00	0.00	0.15	0.00
Actual vs Specialized	183	-0.36	-0.36	0.12	0.00
Derivative vs Specialized	-96	-0.36	-0.36	-0.03	0.00

Figure F-4: Analysis of well VERT_FP, LGR_9x1_3x1+

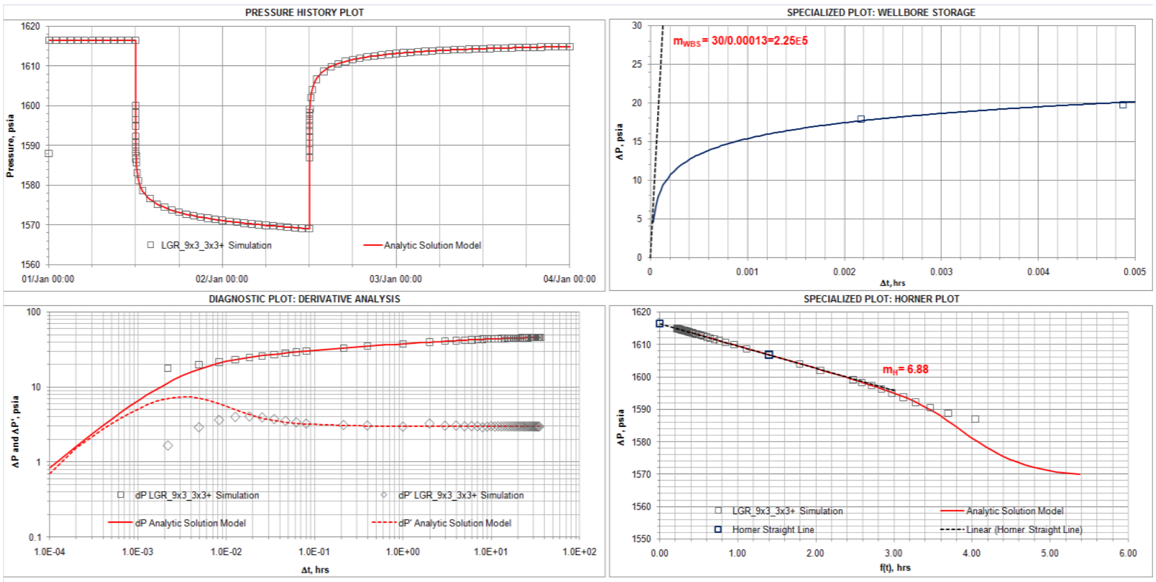

	MODEL PARAMETERS				
	C	$k_h h$	k_h	S_t	P_i
	bbl/psi	mD-ft	mD	-	psia
Actual Values	0.000113	28000	140	0	1616.43
Derivative Analysis	0.008	28000	140	0.025	1616.44
Specialized Analysis	0.00032	27900	139.5	0.00	1616.44
Difference	%	%	%	-	%
Actual vs Derivative	6980	0.00	0.00	0.03	0.00
Actual vs Specialized	183	-0.36	-0.36	0.00	0.00
Derivative vs Specialized	-96	-0.36	-0.36	-0.03	0.00

Figure F-5: Analysis of well VERT_FP, LGR_9x3_3x3

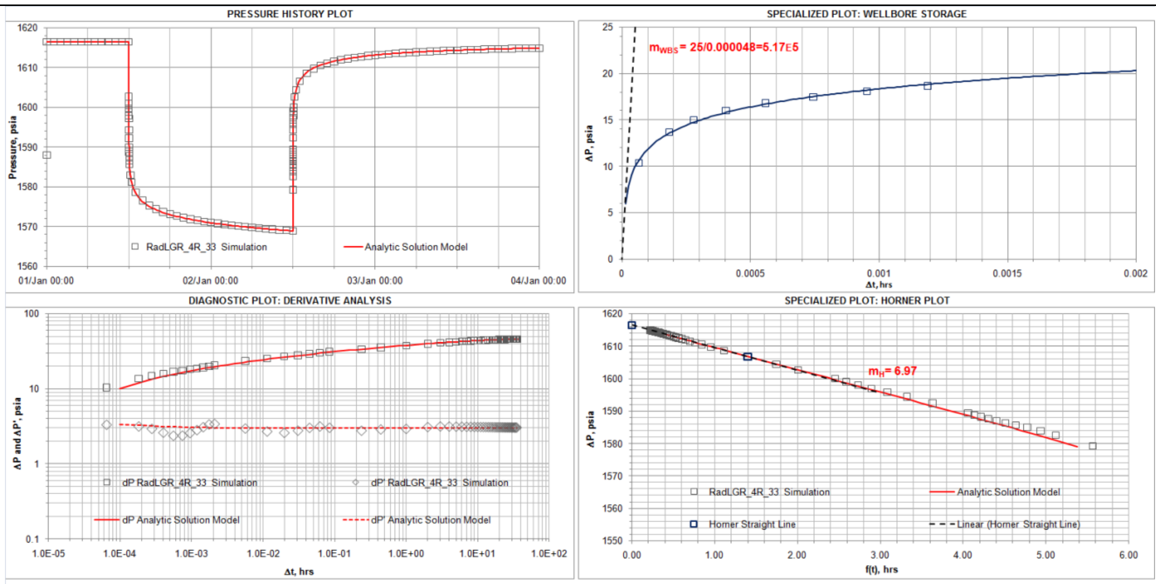

	MODEL PARAMETERS				
	C	k_hh	k_h	S_t	P_i
	bbl/psi	mD-ft	mD	-	psia
Actual Values	0.00011	28000	140	0	1616.43
Derivative Analysis	0.00012	28000	140	0.05	1616.43
Specialized Analysis	0.00014	27500	137.5	-0.08	1616.46
Difference	%	%	%	-	%
Actual vs Derivative	9	0.00	0.00	0.05	0.00
Actual vs Specialized	27	-1.79	-1.79	-0.08	0.00
Derivative vs Specialized	17	-1.79	-1.79	-0.13	0.00

Figure F-6: Analysis of well VERT_FP, RadLGR_4R_33

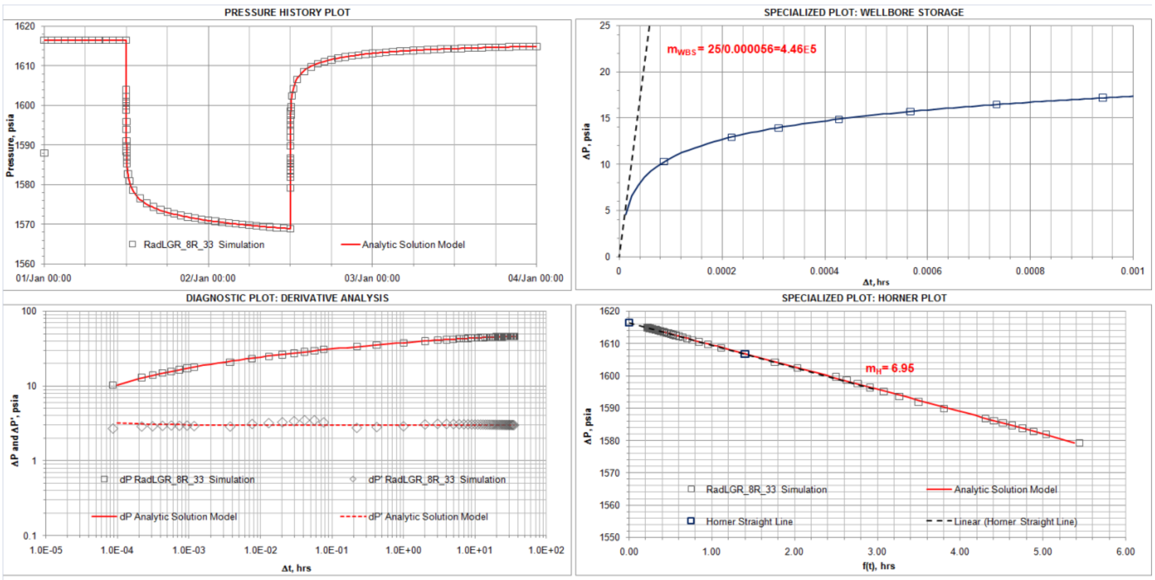

	MODEL PARAMETERS				
	C	k_hh	k_h	S_t	P_i
	bbl/psi	mD-ft	mD	-	psia
Actual Values	0.00011	28000	140	0	1616.43
Derivative Analysis	0.0001	28000	140	0.05	1616.43
Specialized Analysis	0.00016	27600	138	-0.06	1616.45
Difference	%	%	%	-	%
Actual vs Derivative	-9	0.00	0.00	0.05	0.00
Actual vs Specialized	45	-1.43	-1.43	-0.06	0.00
Derivative vs Specialized	60	-1.43	-1.43	-0.11	0.00

Figure F-7: Analysis of well VERT_FP, RadLGR_8R_33

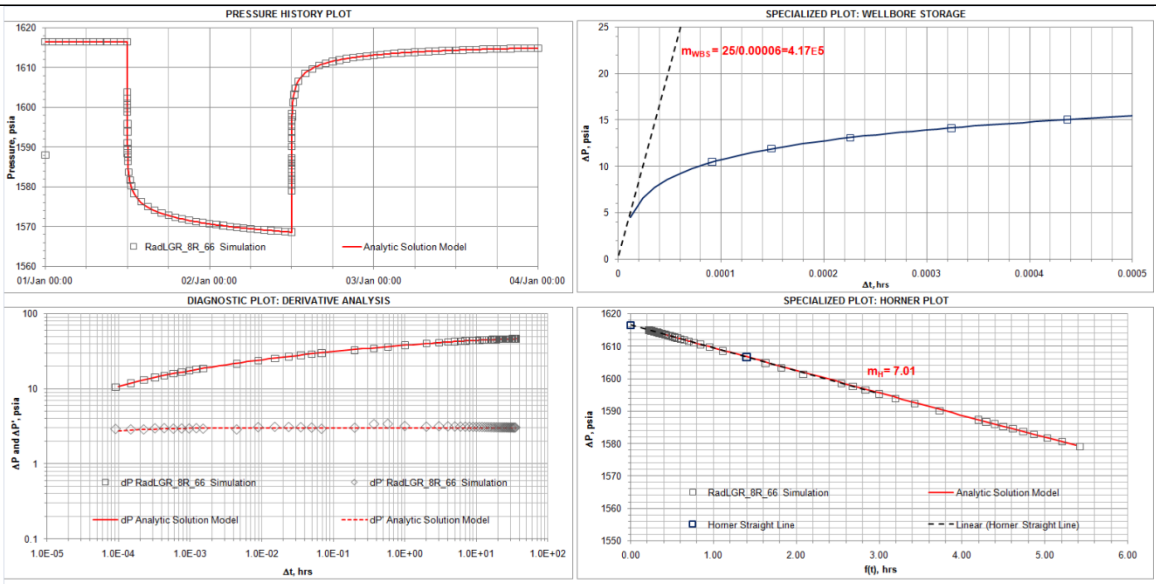

	MODEL PARAMETERS				
	C	$k_h h$	k_h	S_t	P_i
	bbl/psi	mD-ft	mD	-	psia
Actual Values	0.00011	28000	140	0	1616.43
Derivative Analysis	0.00005	27600	138	0	1616.46
Specialized Analysis	0.00017	27300	136.5	-0.07	1616.46
Difference	%	%	%	-	%
Actual vs Derivative	-55	-1.43	-1.43	0.00	0.00
Actual vs Specialized	55	-2.50	-1.09	-0.07	0.00
Derivative vs Specialized	240	-1.09	-1.09	-0.07	0.00

Figure F-8: Analysis of well VERT_FP, RadLGR_8R_66

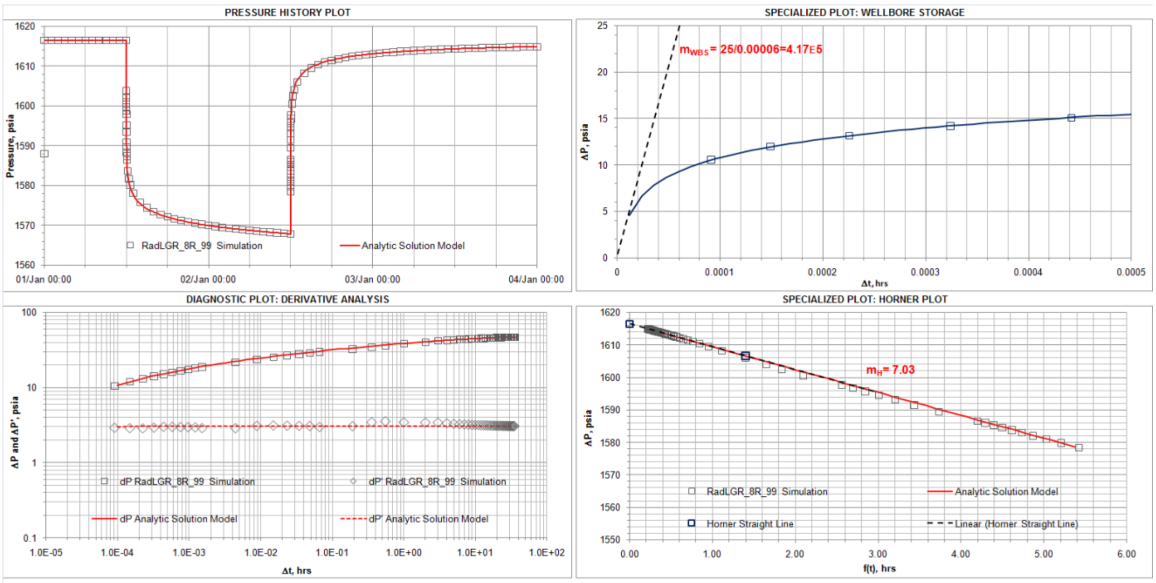

	MODEL PARAMETERS				
	C	$k_h h$	k_h	S_t	P_i
	bbl/psi	mD-ft	mD	-	psia
Actual Values	0.00011	28000	140	0	1616.43
Derivative Analysis	0.00005	27300	136.5	0.04	1616.46
Specialized Analysis	0.00017	27300	136.5	0.04	1616.46
Difference	%	%	%	-	%
Actual vs Derivative	-55	-2.50	-2.50	0.04	0.00
Actual vs Specialized	55	-2.50	0.00	0.04	0.00
Derivative vs Specialized	240	0.00	0.00	0.00	0.00

Figure F-9: Analysis of well VERT_FP, RadLGR_8R_99

Partially Penetrating Vertical Well (VERT_PP)

		Values						Errors					
		C	$k_h h$	k_h	k_v/k_h	S_t	P_i	C	$k_h h$	k_h	k_v/k_h	S_t	P_i
		bbl/psi	mD-ft	mD	-	-	psia	%	%	%	%	-	%
	VERT_PP (ANALYTIC)	0.000023	28000	140	1.000	15.60	1616.43	0.000	0.000	0.000	0.000	0.000	0.000
Coarse Grid	Coarse	0.065	27000	135	-	18.70	1616.47	282508.696	-3.571	-3.571	-	3.100	0.002
	RMS Error, Absolute	**0.065**	**1000**	**5.00**	**-**	**3.10**	**0.040**						
	RMS Error, Relative (%)	**282509**	**3.57**	**3.57**	**-**	**19.87**	**0.0025**						
Cartesian Refinement	LGR_19x1_1	0.00047	27000	135	0.800	15.70	1616.48	1943.478	-3.571	-3.571	-20.000	0.100	0.003
	LGR_9x1_3x3	0.001	27600	138	0.820	15.80	1616.45	4247.826	-1.429	-1.429	-18.000	0.200	0.001
	LGR_39x1_1	0.0002	27400	137	0.710	16.20	1616.46	769.565	-2.143	-2.143	-29.000	0.600	0.002
	LGR_77x4_11x2_3x3	0.00009	27500	138	0.980	15.50	1616.46	291.304	-1.786	-1.786	-2.000	-0.100	0.002
	RMS Error, Absolute	**0.00055**	**665**	**3.33**	**0.20**	**0.32**	**0.034**						
	RMS Error, Relative (%)	**2372**	**2.38**	**2.38**	**19.81**	**2.08**	**0.002**						
Radial Refinement	RadLGR_8R_66	0.00004	27400	137	1.000	16.40	1616.46	73.913	-2.143	-2.143	0.000	0.800	0.002
	RadLGR_16R_66	0.000022	27400	137	0.800	16.10	1616.46	-4.348	-2.143	-2.143	-20.000	0.500	0.002
	RadLGR_16Rx3_66	0.00002	27500	138	0.880	15.90	1616.46	-13.043	-1.786	-1.786	-12.000	0.300	0.002
	RadLGR_16RxGeo_66	0.00002	27400	137	0.870	15.60	1616.46	-13.043	-2.143	-2.143	-13.000	0.000	0.002
	RMS Error, Absolute	**0.000009**	**577**	**2.88**	**0.134**	**0.495**	**0.030**						
	RMS Error, Relative (%)	**38**	**2.06**	**2.06**	**13.35**	**3.17**	**0.002**						

Table F-2: Summary of the interpretation results for VERT_PP well model complete with root mean squared error calculations expressed in absolute and relative terms.

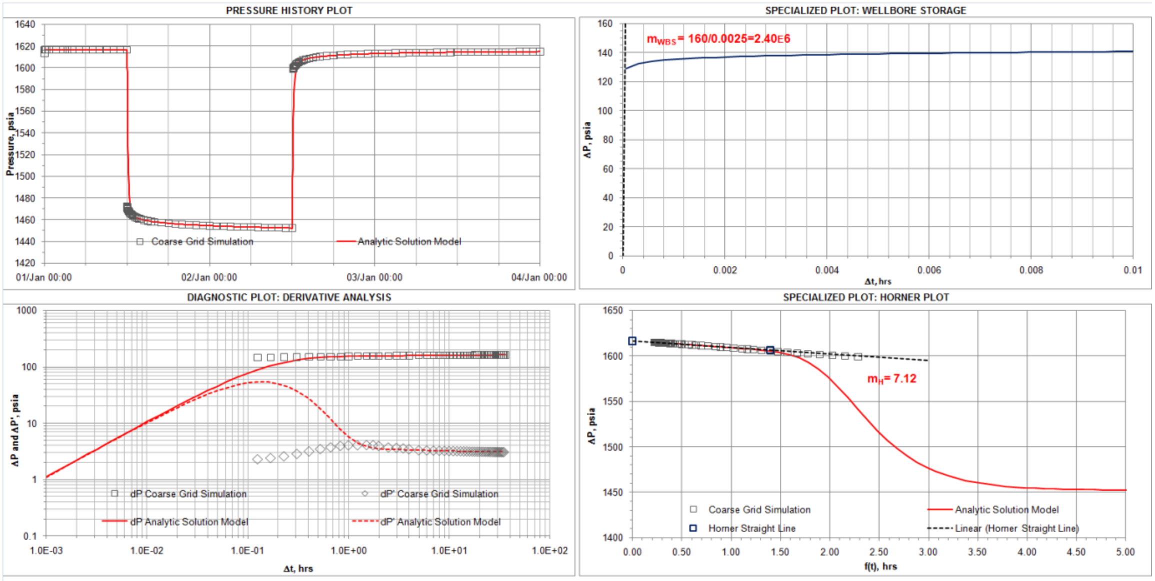

	MODEL PARAMETERS					
	C	$k_h h$	k_h	k_v/k_h	S_t	P_i
	bbl/psi	mD-ft	mD	-	-	psia
Actual Values	0.000023	28000	140	1	15.6	1616.43
Derivative Analysis	0.065	27000	135	-	18.7	1616.47
Specialized Analysis	0.00003	26900	134.5	-	18.6	1616.47
Difference	%	%	%	%	-	%
Actual vs Derivative	282509	-3.57	-3.57	-	3.10	0.00
Actual vs Specialized	30	-3.93	-0.37	-	3.00	0.00
Derivative vs Specialized	-100	-0.37	-0.37	-	-0.10	0.00

Figure F-10: Analysis of well VERT_PP, coarse grid

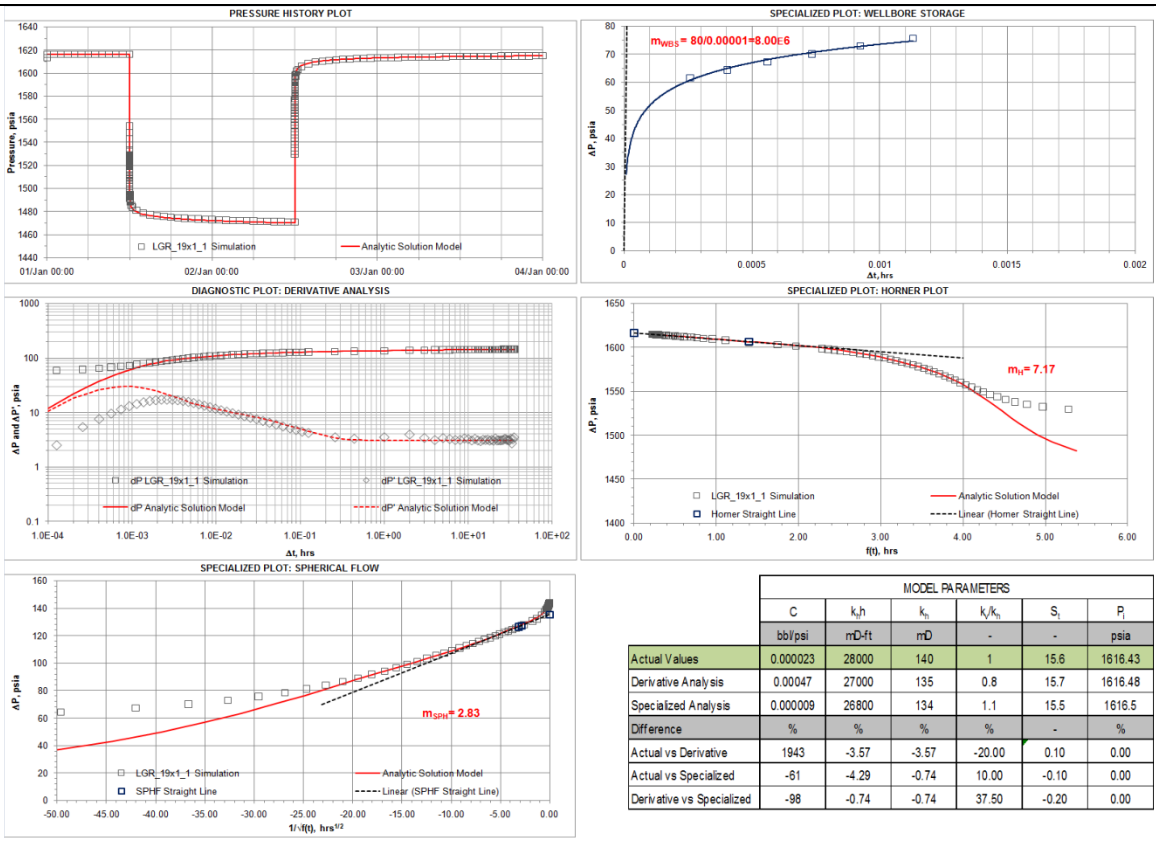

MODEL PARAMETERS	C	$k_h h$	k_h	k_v/k_h	S_t	P_i
	bbl/psi	mD-ft	mD	-	-	psia
Actual Values	0.000023	28000	140	1	15.6	1616.43
Derivative Analysis	0.00047	27000	135	0.8	15.7	1616.48
Specialized Analysis	0.000009	26800	134	1.1	15.5	1616.5
Difference	%	%	%	%	-	%
Actual vs Derivative	1943	-3.57	-3.57	-20.00	0.10	0.00
Actual vs Specialized	-61	-4.29	-0.74	10.00	-0.10	0.00
Derivative vs Specialized	-98	-0.74	-0.74	37.50	-0.20	0.00

Figure F-11: Analysis of well VERT_PP, LGR_19x1_1

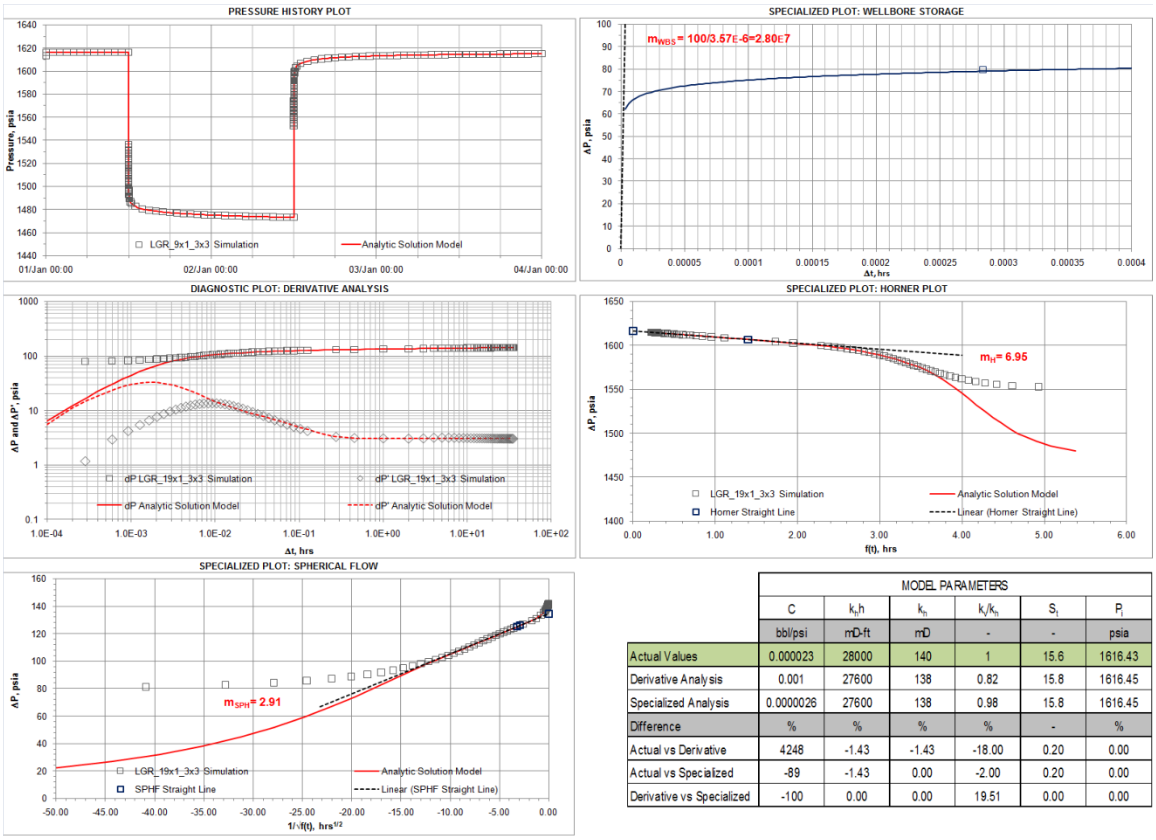

MODEL PARAMETERS	C	$k_h h$	k_h	k_v/k_h	S_t	P_i
	bbl/psi	mD-ft	mD	-	-	psia
Actual Values	0.000023	28000	140	1	15.6	1616.43
Derivative Analysis	0.001	27600	138	0.82	15.8	1616.45
Specialized Analysis	0.0000026	27600	138	0.98	15.8	1616.45
Difference	%	%	%	%	-	%
Actual vs Derivative	4248	-1.43	-1.43	-18.00	0.20	0.00
Actual vs Specialized	-89	-1.43	0.00	-2.00	0.20	0.00
Derivative vs Specialized	-100	0.00	0.00	19.51	0.00	0.00

Figure F-12: Analysis of well VERT_PP, LGR_9x1_3x3

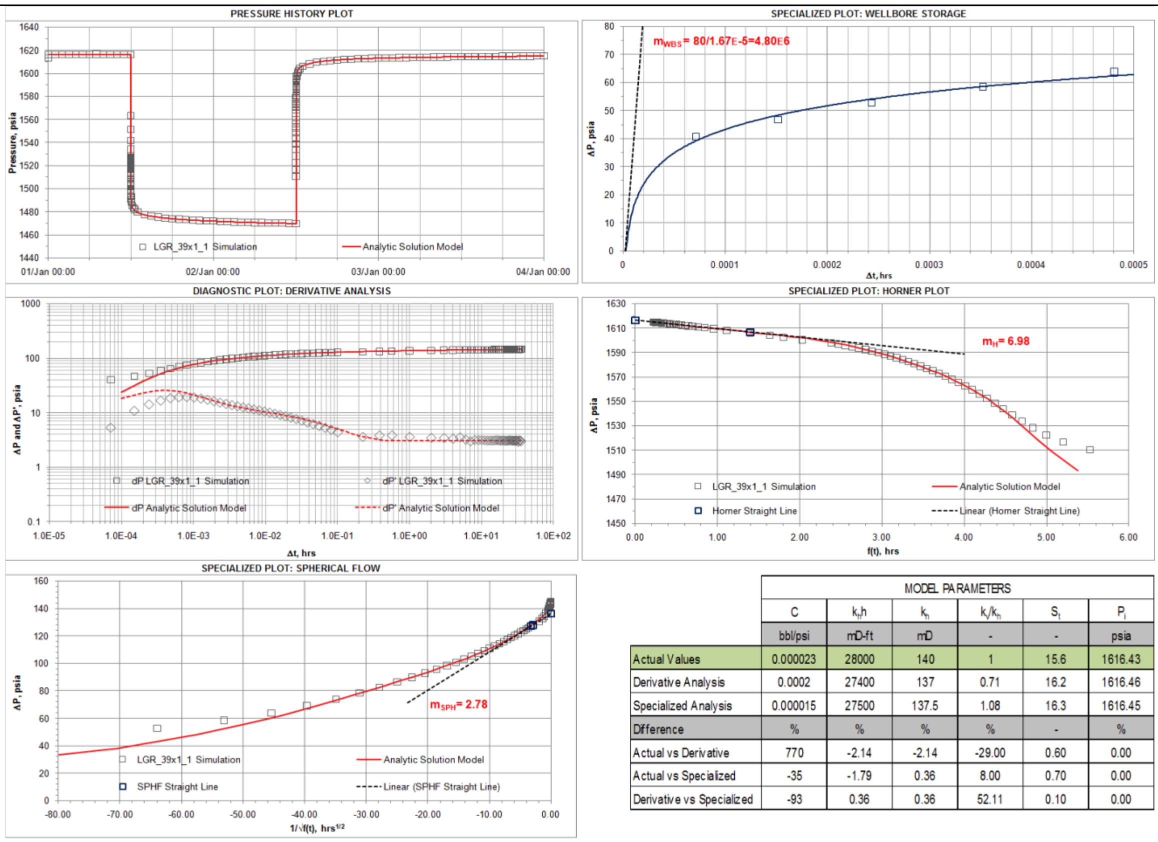

MODEL PARAMETERS	C	$k_h h$	k_h	k_v/k_h	S_t	P_i
	bbl/psi	mD-ft	mD	-	-	psia
Actual Values	0.000023	28000	140	1	15.6	1616.43
Derivative Analysis	0.0002	27400	137	0.71	16.2	1616.46
Specialized Analysis	0.000015	27500	137.5	1.08	16.3	1616.45
Difference	%	%	%	%	-	%
Actual vs Derivative	770	-2.14	-2.14	-29.00	0.60	0.00
Actual vs Specialized	-35	-1.79	0.36	8.00	0.70	0.00
Derivative vs Specialized	-93	0.36	0.36	52.11	0.10	0.00

Figure F-13: Analysis of well VERT_PP, LGR_39x1_1

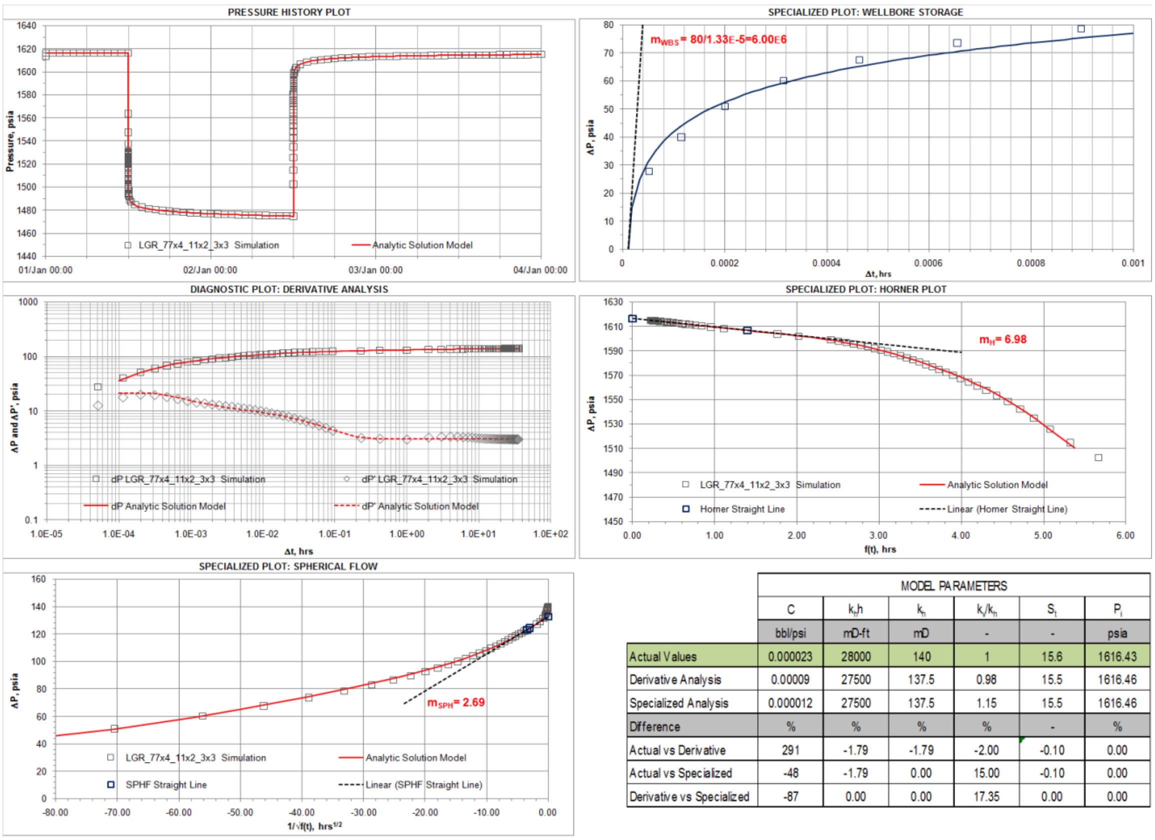

MODEL PARAMETERS	C	$k_h h$	k_h	k_v/k_h	S_t	P_i
	bbl/psi	mD-ft	mD	-	-	psia
Actual Values	0.000023	28000	140	1	15.6	1616.43
Derivative Analysis	0.00009	27500	137.5	0.98	15.5	1616.46
Specialized Analysis	0.000012	27500	137.5	1.15	15.5	1616.46
Difference	%	%	%	%	-	%
Actual vs Derivative	291	-1.79	-1.79	-2.00	-0.10	0.00
Actual vs Specialized	-48	-1.79	0.00	15.00	-0.10	0.00
Derivative vs Specialized	-87	0.00	0.00	17.35	0.00	0.00

Figure F-14: Analysis of well VERT_PP, LGR_77x4_11x2_3x3

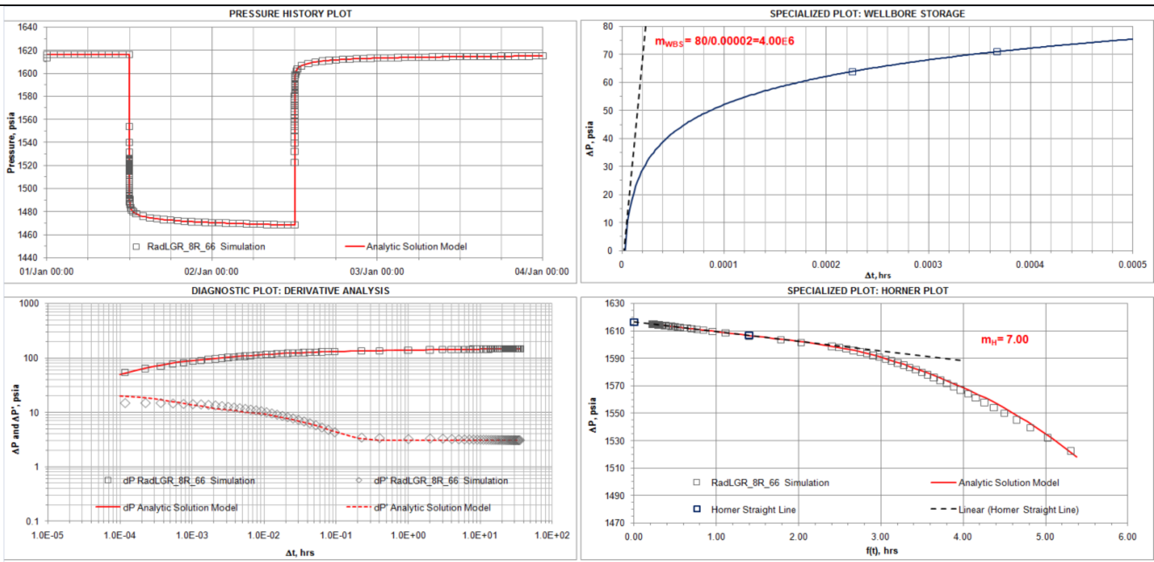

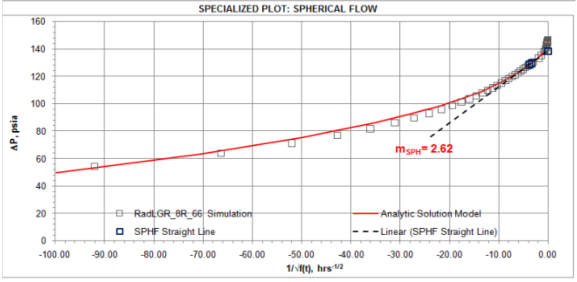

	MODEL PARAMETERS					
	C	$k_h h$	k_h	k_v/k_h	S_t	P_i
	bbl/psi	mD-ft	mD	-	-	psia
Actual Values	0.000023	28000	140	1	15.6	1616.43
Derivative Analysis	0.00004	27400	137	1	16.4	1616.46
Specialized Analysis	0.000018	27400	137	1.23	16.5	1616.46
Difference	%	%	%	%	-	%
Actual vs Derivative	74	-2.14	-2.14	0.00	0.80	0.00
Actual vs Specialized	-22	-2.14	-2.14	23.00	0.90	0.00
Derivative vs Specialized	-55	0.00	0.00	23.00	0.10	0.00

Figure F-15: Analysis of well VERT_PP, RadLGR_8R_66

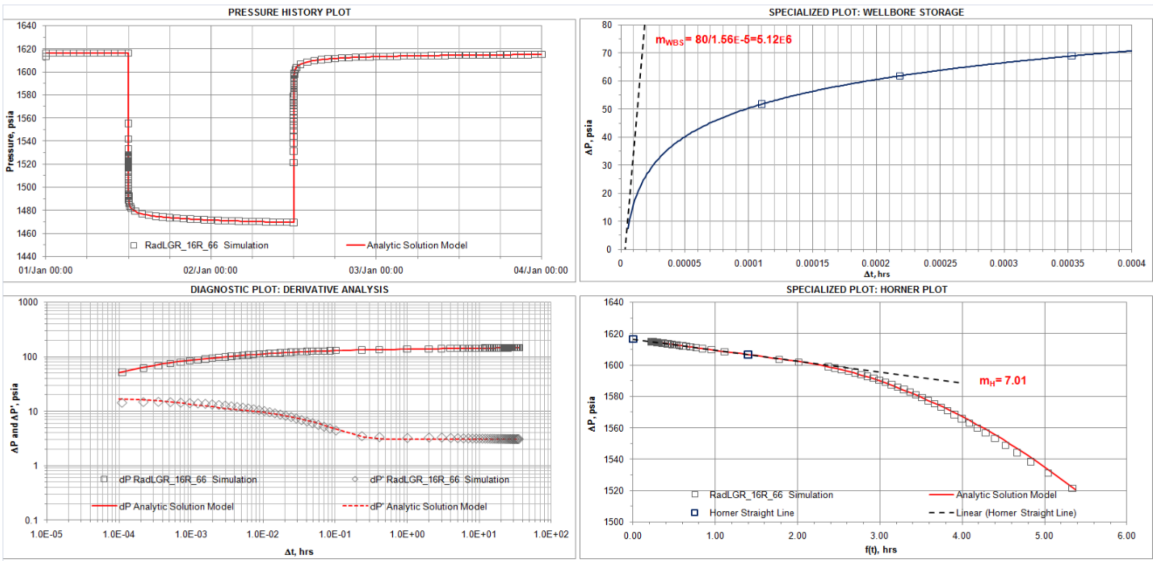

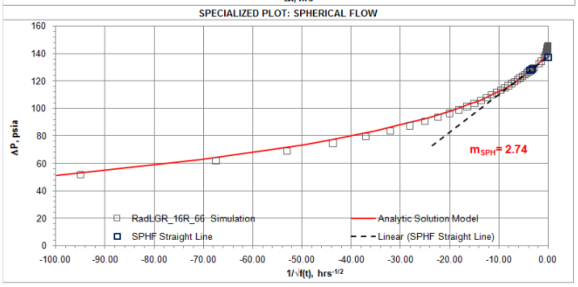

	MODEL PARAMETERS					
	C	$k_h h$	k_h	k_v/k_h	S_t	P_i
	bbl/psi	mD-ft	mD	-	-	psia
Actual Values	0.000023	28000	140	1	15.6	1616.43
Derivative Analysis	0.000022	27400	137	0.8	16.1	1616.46
Specialized Analysis	0.000014	27300	136.5	1.13	16.2	1616.46
Difference	%	%	%	%	-	%
Actual vs Derivative	-4	-2.14	-2.14	-20.00	0.50	0.00
Actual vs Specialized	-39	-2.50	-0.36	13.00	0.60	0.00
Derivative vs Specialized	-36	-0.36	-0.36	41.25	0.10	0.00

Figure F-16: Analysis of well VERT_PP, RadLGR_16R_66

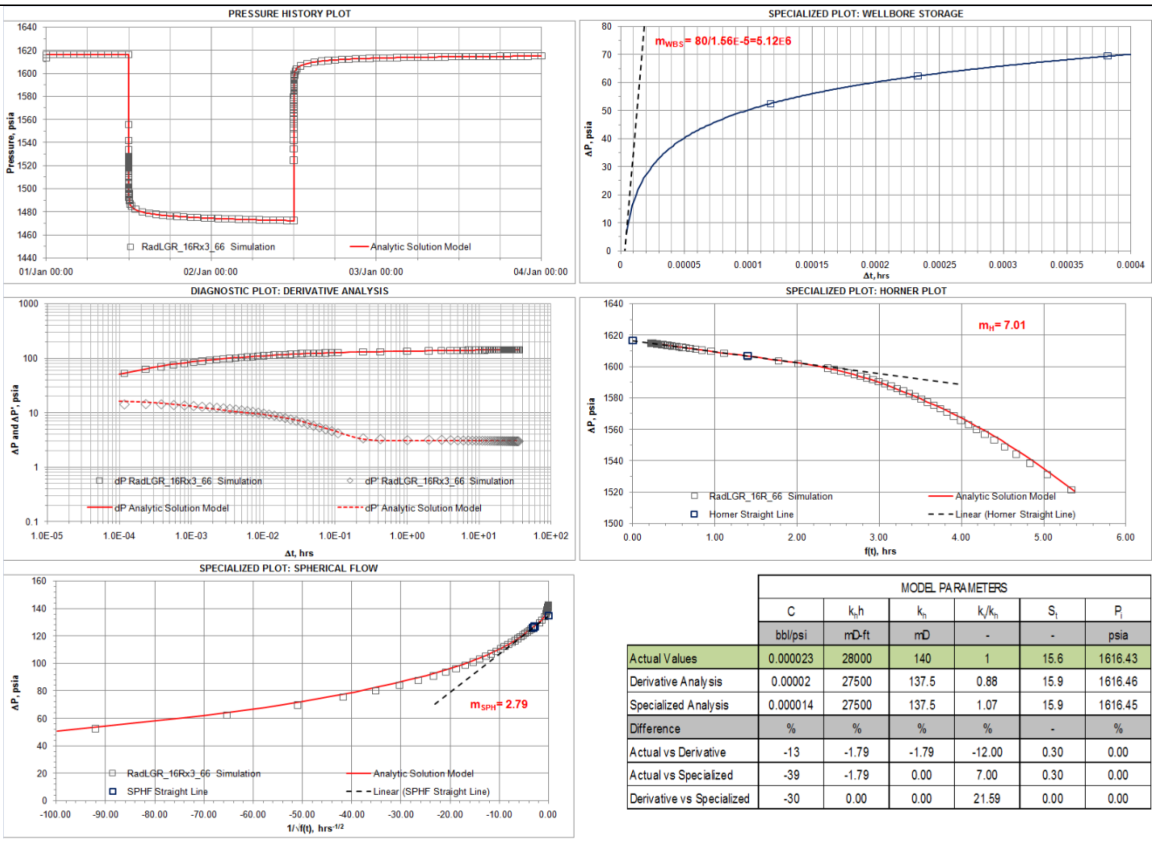

MODEL PARAMETERS	C	$k_h h$	k_h	k_v/k_h	S_t	P_i
	bbl/psi	mD-ft	mD	-	-	psia
Actual Values	0.000023	28000	140	1	15.6	1616.43
Derivative Analysis	0.00002	27500	137.5	0.88	15.9	1616.46
Specialized Analysis	0.000014	27500	137.5	1.07	15.9	1616.45
Difference	%	%	%	%	-	%
Actual vs Derivative	-13	-1.79	-1.79	-12.00	0.30	0.00
Actual vs Specialized	-39	-1.79	0.00	7.00	0.30	0.00
Derivative vs Specialized	-30	0.00	0.00	21.59	0.00	0.00

Figure F-17: Analysis of well VERT_PP, RadLGR_16Rx3_66

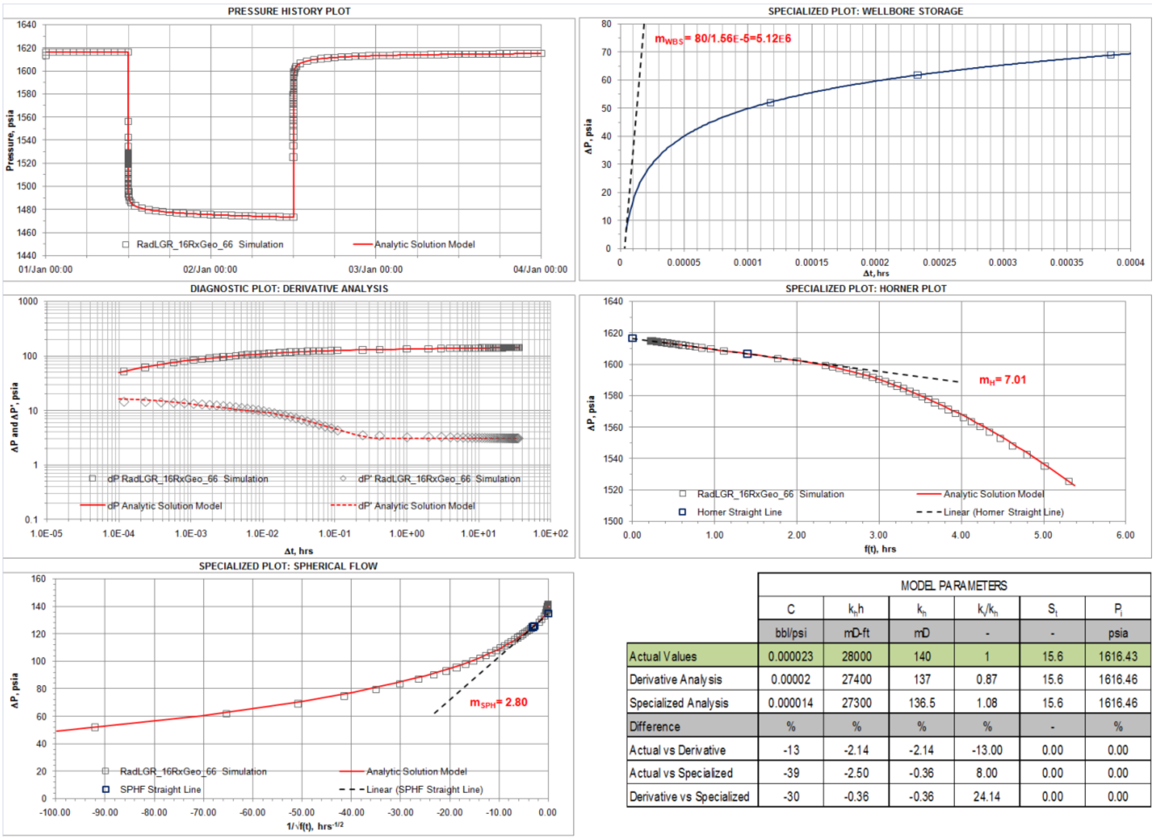

MODEL PARAMETERS	C	$k_h h$	k_h	k_v/k_h	S_t	P_i
	bbl/psi	mD-ft	mD	-	-	psia
Actual Values	0.000023	28000	140	1	15.6	1616.43
Derivative Analysis	0.00002	27400	137	0.87	15.6	1616.46
Specialized Analysis	0.000014	27300	136.5	1.08	15.6	1616.46
Difference	%	%	%	%	-	%
Actual vs Derivative	-13	-2.14	-2.14	-13.00	0.00	0.00
Actual vs Specialized	-39	-2.50	-0.36	8.00	0.00	0.00
Derivative vs Specialized	-30	-0.36	-0.36	24.14	0.00	0.00

Figure F-18: Analysis of well VERT_PP, RadLGR_24RxGeo_66

Horizontal Well Aligned With Grid (HZ_90IN_90AZ)

		Values							Errors						
		C	$k_h h$	k_h	L	k_v/k_h	S_t	P_i	C	$k_h h$	k_h	L	k_v/k_h	S_t	P_i
		bbl/psi	mD-ft	mD	ft	-	-	psia	%	%	%	%	%	-	%
	HZ_90IN_90AZ (ANALYTIC)	0.00034	28000	140.0	300	1.00	-4.65	1618.02	0.000	0.000	0.000	0.000	0.000	0.000	0.000
Coarse Grid	Coarse	0.05	27500	137.5	190	1.82	-4.44	1618.03	14605.882	-1.786	-1.786	-36.667	82.000	0.210	0.001
	RMS Error, Absolute	**0.050**	**500**	**2.50**	**110**	**0.82**	**0.21**	**0.010**							
	RMS Error, Relative (%)	**14606**	**1.79**	**1.79**	**37**	**82**	**4.52**	**0.001**							
Cartesian Refinement	LGR_19x1_3x1	0.0006	27600	138.00	213	1.60	-4.50	1618.03	76.471	-1.429	-1.429	-29.000	60.000	0.150	0.001
	LGR_19x1_3x3	0.0006	28300	141.50	215	1.50	-4.47	1618.01	76.471	1.071	1.071	-28.333	50.000	0.180	-0.001
	LGR_19x1_5x1	0.0006	28000	140.00	243	1.24	-4.55	1618.02	76.471	0.000	0.000	-19.167	24.000	0.100	0.000
	LGR_19x1_15x3	0.0006	28500	142.50	234	1.38	-4.50	1618.01	76.471	1.786	1.786	-22.000	38.000	0.150	-0.001
	RMS Error, Absolute	**0.00026**	**354**	**1.77**	**75**	**0.45**	**0.15**	**0.009**							
	RMS Error, Relative (%)	**76**	**1.26**	**1.26**	**25**	**45**	**3.18**	**0.001**							
Unstructured Refinement	UGR_50x3x50x1_5x1	0.0005	28000	140.00	235	1.21	-4.510	1618.02	47.059	0.000	0.000	-21.667	21.000	0.140	0.000
	UGR_50x3x50x1_7x3	0.003	27500	137.50	250	1.50	-4.620	1618.01	782.353	-1.786	-1.786	-16.667	50.000	0.030	-0.001
	UGR_50x5x50x1_5x1	0.002	27500	137.50	245	1.40	-4.420	1618.01	488.235	-1.786	-1.786	-18.333	40.000	0.230	-0.001
	UGR_50x5x50x3_5x3	0.0009	27500	137.50	255	1.45	-4.610	1618.01	164.706	-1.786	-1.786	-15.000	45.000	0.040	-0.001
	RMS Error, Absolute	**0.00159**	**433**	**2.17**	**54**	**0.41**	**0.137**	**0.009**							
	RMS Error, Relative (%)	**469**	**1.55**	**1.55**	**18**	**41**	**2.94**	**0.001**							

Table F-3: Summary of the interpretation results for HZ_90IN_90AZ well model complete with root mean squared error calculations expressed in absolute and relative terms.

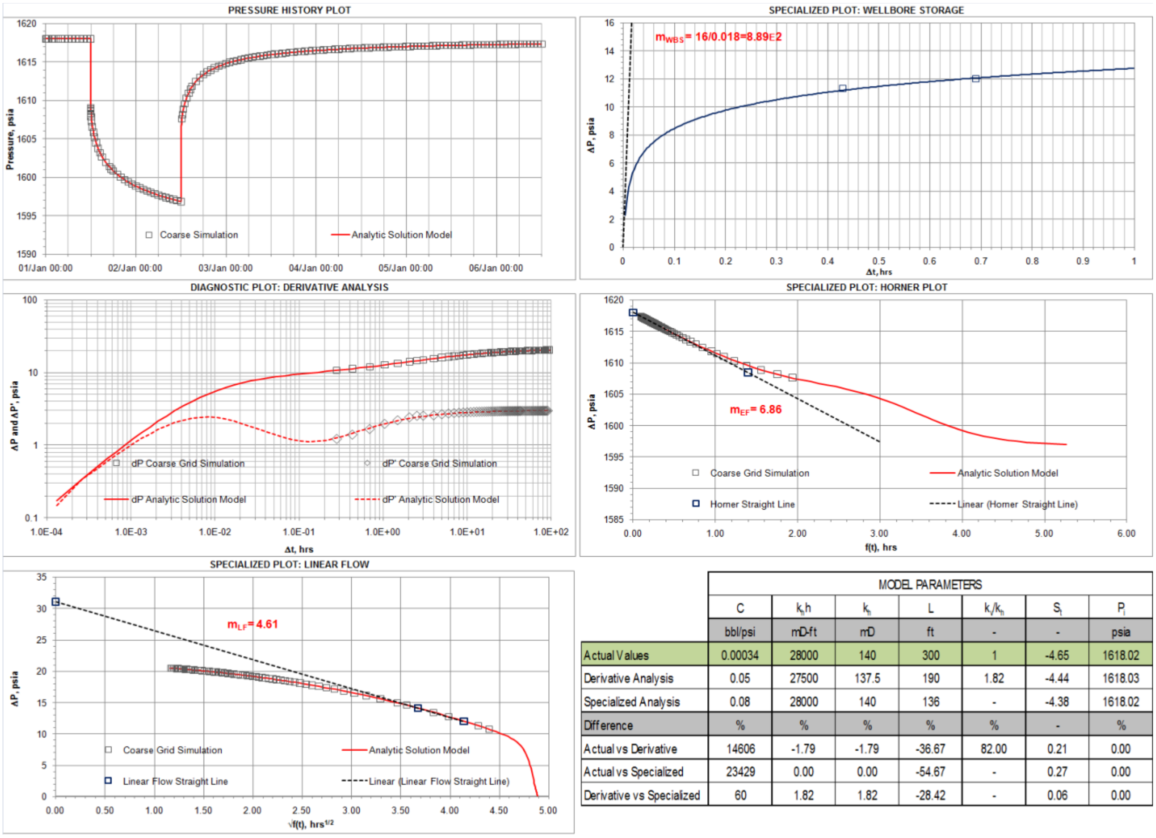

	MODEL PARAMETERS						
	C	$k_h h$	k_h	L	k_v/k_h	S_t	P_i
	bbl/psi	mD-ft	mD	ft	-	-	psia
Actual Values	0.00034	28000	140	300	1	-4.65	1618.02
Derivative Analysis	0.05	27500	137.5	190	1.82	-4.44	1618.03
Specialized Analysis	0.08	28000	140	136	-	-4.38	1618.02
Difference	%	%	%	%	%	-	%
Actual vs Derivative	14606	-1.79	-1.79	-36.67	82.00	0.21	0.00
Actual vs Specialized	23429	0.00	0.00	-54.67	-	0.27	0.00
Derivative vs Specialized	60	1.82	1.82	-28.42	-	0.06	0.00

Figure F-19: Analysis of well HZ_90IN_90AZ, coarse grid

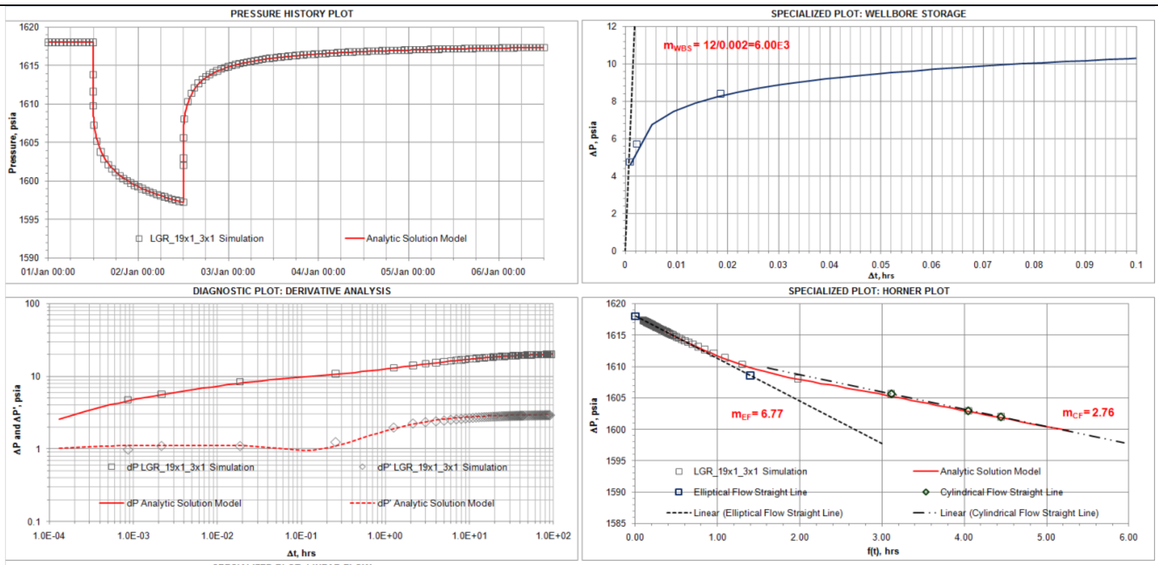

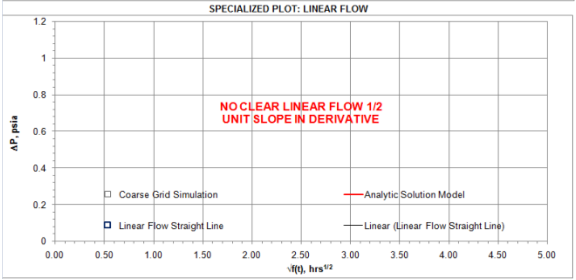

	MODEL PARAMETERS						
	C	$k_h h$	k_h	L	k_v/k_h	S_t	P_i
	bbl/psi	mD-ft	mD	ft	-	-	psia
Actual Values	0.00034	28000	140	300	1	-4.65	1618.02
Derivative Analysis	0.0006	27600	138	213	1.6	-4.5	1618.03
Specialized Analysis	0.012	28300	141.5	-	[0.66]	-4.41	1618.01
Difference	%	%	%	%	%	-	%
Actual vs Derivative	76	-1.43	-1.43	-29.00	60.00	0.15	0.00
Actual vs Specialized	3429	1.07	1.07	-	[-34.00]	0.24	0.00
Derivative vs Specialized	1900	2.54	2.54	-	[-58.75]	0.09	0.00

[] Terms in brackets have used a value drawn from the actual model parameters to complete the analysis, where it was not possible to obtain that value solely from the analysis of the simulation data.

Figure F-20: Analysis of well HZ_90IN_90AZ, LGR_19x1_3x1

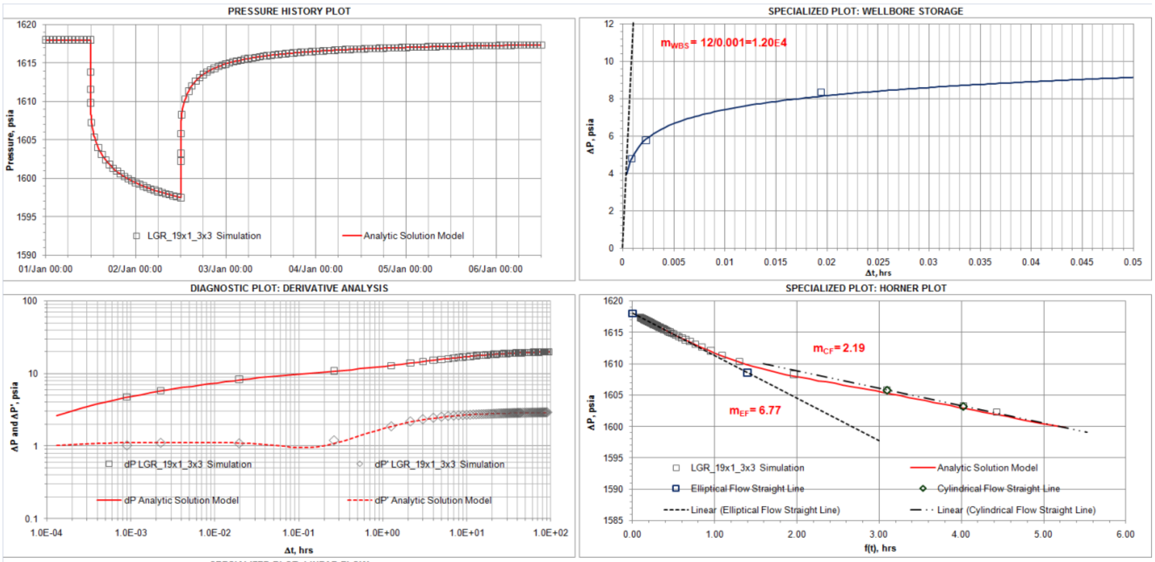

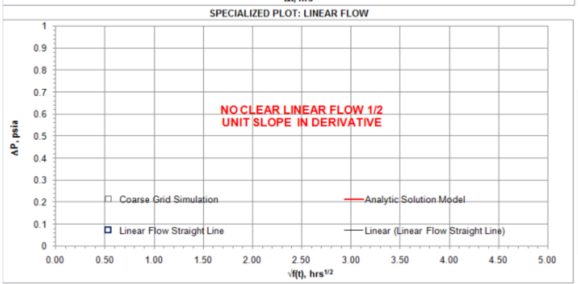

	MODEL PARAMETERS						
	C	$k_h h$	k_h	L	k_v/k_h	S_t	P_i
	bbl/psi	mD-ft	mD	ft	-	-	psia
Actual Values	0.00034	28000	140	300	1	-4.65	1618.02
Derivative Analysis	0.0006	28300	141.5	215	1.5	-4.47	1618.01
Specialized Analysis	0.0059	28300	141.5	-	[1.06]	-4.45	1618.01
Difference	%	%	%	%	%	-	%
Actual vs Derivative	76	1.07	1.07	-28.33	50.00	0.18	0.00
Actual vs Specialized	1635	1.07	1.07	-	[6.00]	0.20	0.00
Derivative vs Specialized	883	0.00	0.00	-	[-29.33]	0.02	0.00

[] Terms in brackets have used a value drawn from the actual model parameters to complete the analysis, where it was not possible to obtain that value solely from the analysis of the simulation data.

Figure F-21: Analysis of well HZ_90IN_90AZ, LGR_19x1_3x3

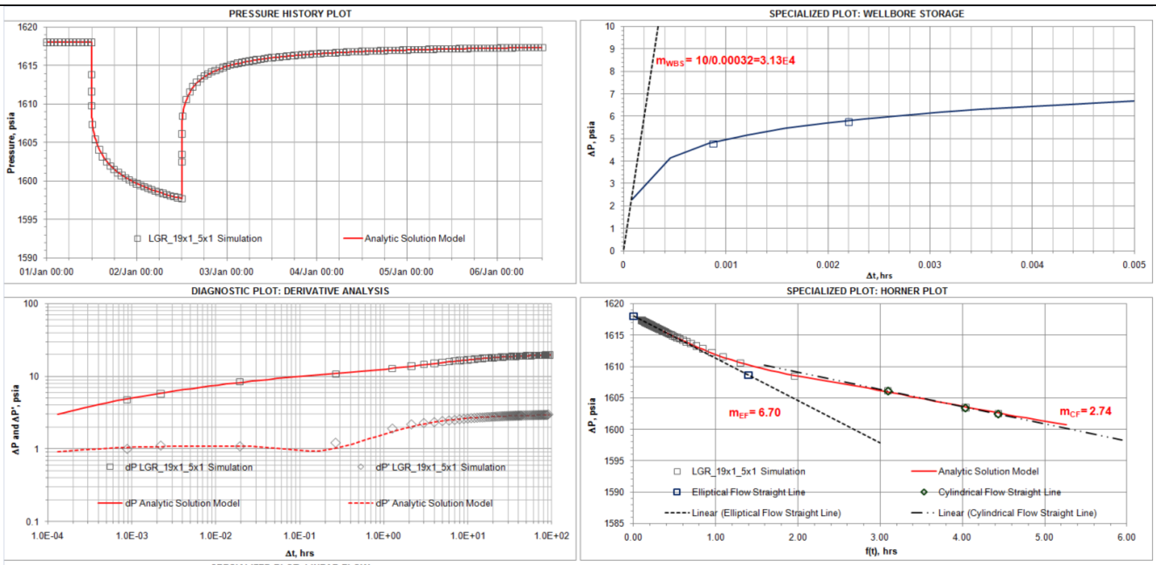

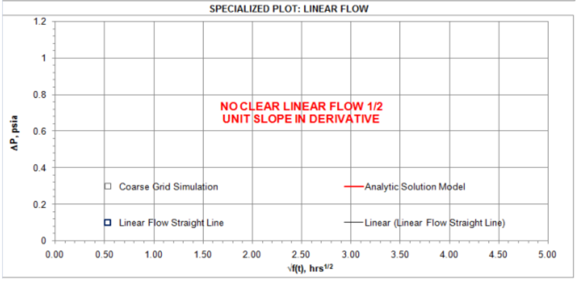

	C	$k_h h$	k_h	L	k_v/k_h	S_t	P_i
MODEL PARAMETERS	bbl/psi	mD-ft	mD	ft	-	-	psia
Actual Values	0.00034	28000	140	300	1	-4.65	1618.02
Derivative Analysis	0.0006	28000	140	242.5	1.24	-4.55	1618.02
Specialized Analysis	0.0023	28600	143	-	[0.67]	-4.46	1618.01
Difference	%	%	%	%	%	-	%
Actual vs Derivative	76	0.00	0.00	-19.17	24.00	0.10	0.00
Actual vs Specialized	576	2.14	2.14	-	[-33.00]	0.19	0.00
Derivative vs Specialized	283	2.14	2.14	-	[-46.00]	0.09	0.00

[] Terms in brackets have used a value drawn from the actual model parameters to complete the analysis, where it was not possible to obtain that value solely from the analysis of the simulation data.

Figure F-22: Analysis of well HZ_90IN_90AZ, LGR_19x1_5x1

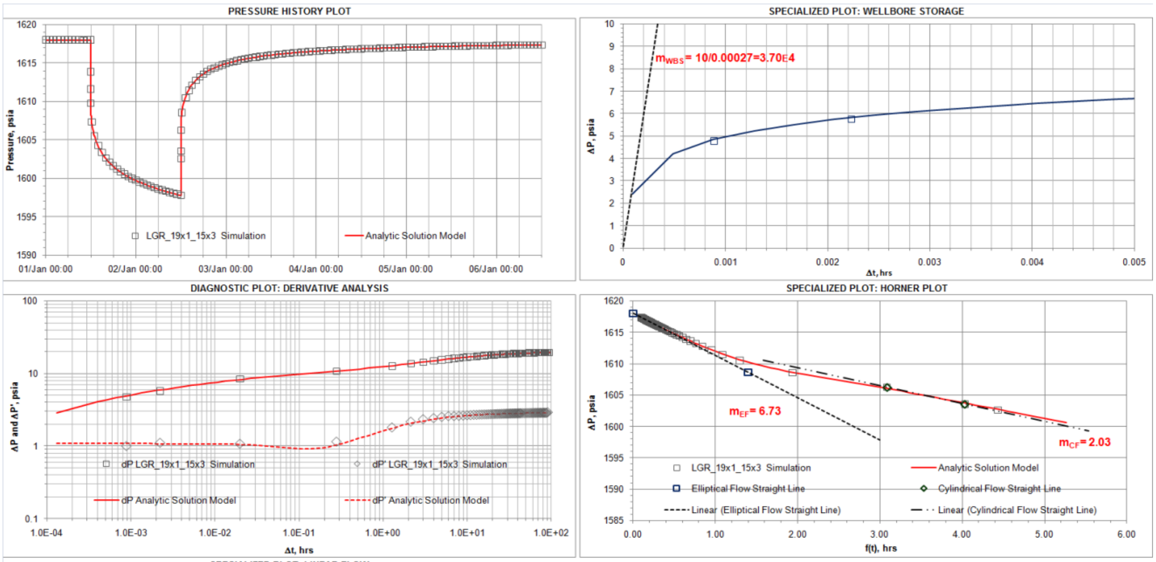

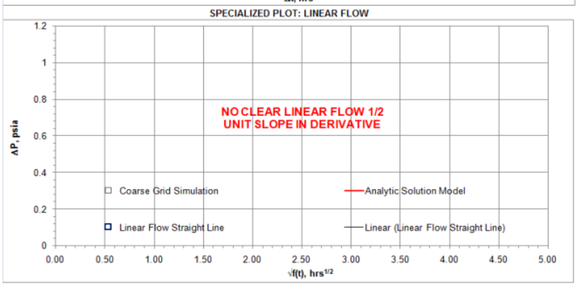

	C	$k_h h$	k_h	L	k_v/k_h	S_t	P_i
MODEL PARAMETERS	bbl/psi	mD-ft	mD	ft	-	-	psia
Actual Values	0.00034	28000	140	300	1	-4.65	1618.02
Derivative Analysis	0.0006	28500	142.5	234	1.38	-4.5	1618.01
Specialized Analysis	0.0019	28500	142.5	-	[1.22]	-4.49	1618.02
Difference	%	%	%	%	%	-	%
Actual vs Derivative	76	1.79	1.79	-22.00	38.00	0.15	0.00
Actual vs Specialized	459	1.79	1.79	-	[22.00]	0.16	0.00
Derivative vs Specialized	217	0.00	0.00	-	[-12.00]	0.01	0.00

[] Terms in brackets have used a value drawn from the actual model parameters to complete the analysis, where it was not possible to obtain that value solely from the analysis of the simulation data.

Figure F-23: Analysis of well HZ_90IN_90AZ, LGR_19x1_15x3

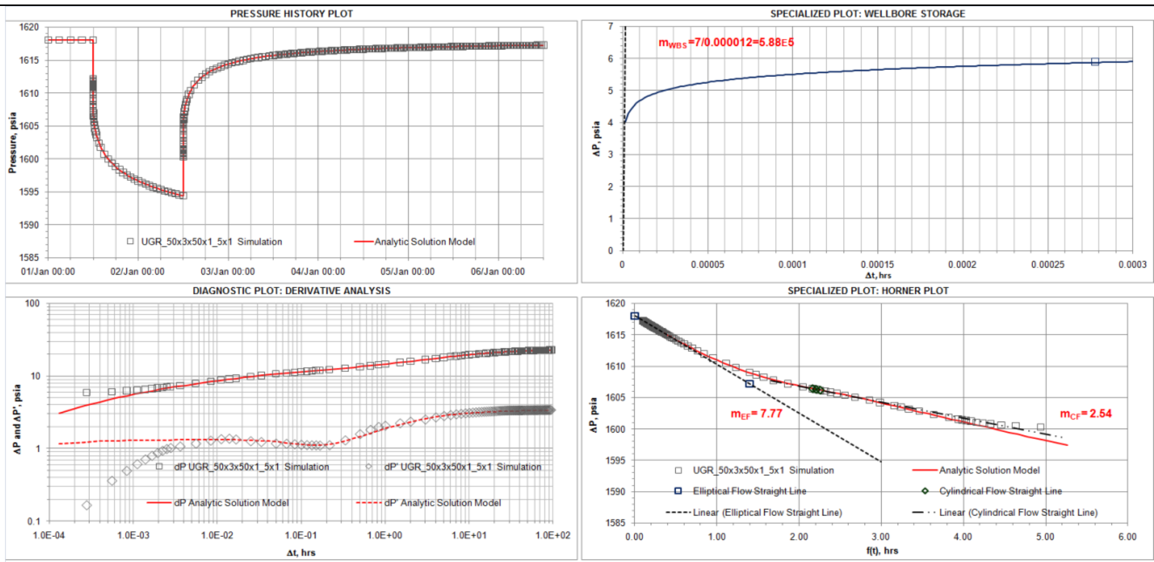

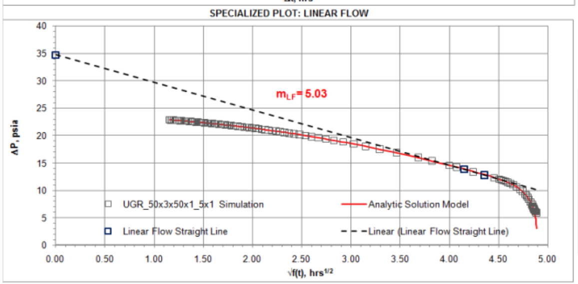

	MODEL PARAMETERS						
	C	$k_h h$	k_h	L	k_v/k_h	S_t	P_i
	bbl/psi	mD-ft	mD	ft	-	-	psia
Actual Values	0.00034	28000	140	300	1	-4.65	1618.02
Derivative Analysis	0.0005	28000	140	235	1.21	-4.51	1618.02
Specialized Analysis	0.00014	28400	142	286	1.15	-4.45	1618.01
Difference	%	%	%	%	%	-	%
Actual vs Derivative	47	0.00	0.00	-21.67	21.00	0.14	0.00
Actual vs Specialized	-58.82	1.43	1.43	-4.67	15.00	0.20	0.00
Derivative vs Specialized	-72.00	1.43	1.43	21.70	-4.96	0.06	0.00

Figure F-24: Analysis of well HZ_90IN_90AZ, UGR_50x3x50x1_5x1

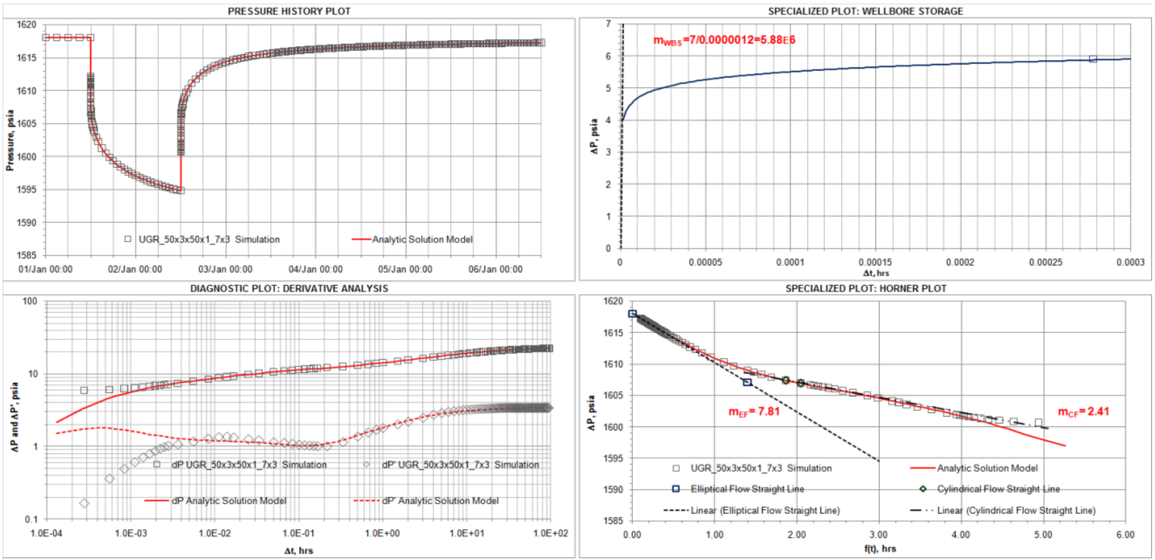

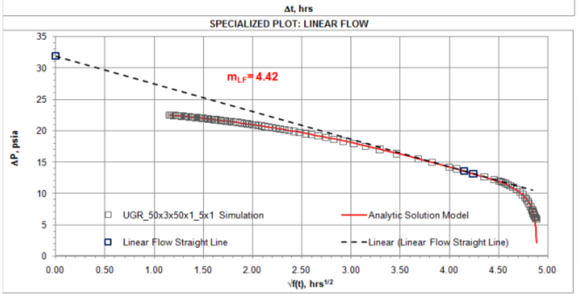

	MODEL PARAMETERS						
	C	$k_h h$	k_h	L	k_v/k_h	S_t	P_i
	bbl/psi	mD-ft	mD	ft	-	-	psia
Actual Values	0.00034	28000	140	300	1	-4.65	1618.02
Derivative Analysis	0.003	27500	137.5	250	1.5	-4.62	1618.01
Specialized Analysis	0.000014	28300	141.5	326	0.99	-4.52	1618.01
Difference	%	%	%	%	%	-	%
Actual vs Derivative	782	-1.79	-1.79	-16.67	50.00	0.03	0.00
Actual vs Specialized	-95.88	1.07	1.07	8.67	-1.00	0.13	0.00
Derivative vs Specialized	-99.53	2.91	2.91	30.40	-34.00	0.10	0.00

Figure F-25: Analysis of well HZ_90IN_90AZ, UGR_50x3x50x1_7x3

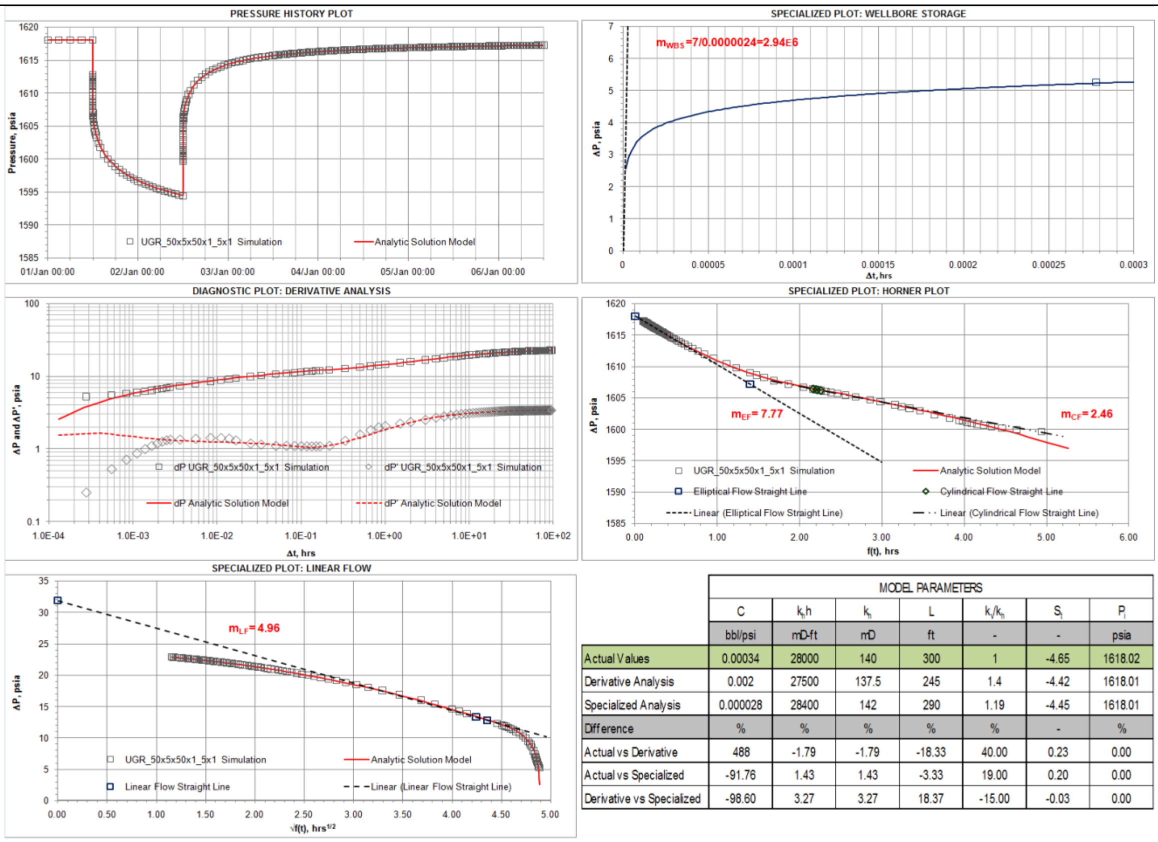

	MODEL PARAMETERS						
	C	$k_h h$	k_h	L	k_v/k_h	S_t	P_i
	bbl/psi	mD-ft	mD	ft	-	-	psia
Actual Values	0.00034	28000	140	300	1	-4.65	1618.02
Derivative Analysis	0.002	27500	137.5	245	1.4	-4.42	1618.01
Specialized Analysis	0.000028	28400	142	290	1.19	-4.45	1618.01
Difference	%	%	%	%	%	-	%
Actual vs Derivative	488	-1.79	-1.79	-18.33	40.00	0.23	0.00
Actual vs Specialized	-91.76	1.43	1.43	-3.33	19.00	0.20	0.00
Derivative vs Specialized	-98.60	3.27	3.27	18.37	-15.00	-0.03	0.00

Figure F-26: Analysis of well HZ_90IN_90AZ, UGR_50x5x50x1_5x1

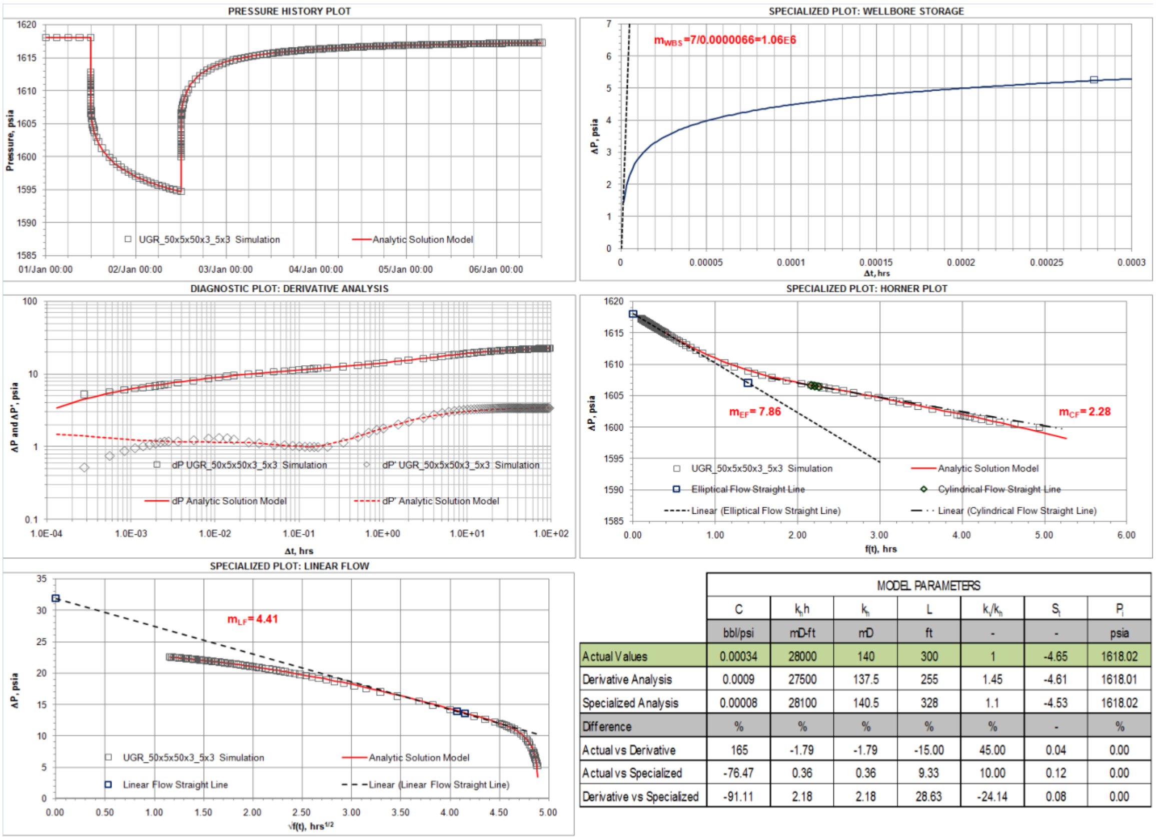

	MODEL PARAMETERS						
	C	$k_h h$	k_h	L	k_v/k_h	S_t	P_i
	bbl/psi	mD-ft	mD	ft	-	-	psia
Actual Values	0.00034	28000	140	300	1	-4.65	1618.02
Derivative Analysis	0.0009	27500	137.5	255	1.45	-4.61	1618.01
Specialized Analysis	0.00008	28100	140.5	328	1.1	-4.53	1618.02
Difference	%	%	%	%	%	-	%
Actual vs Derivative	165	-1.79	-1.79	-15.00	45.00	0.04	0.00
Actual vs Specialized	-76.47	0.36	0.36	9.33	10.00	0.12	0.00
Derivative vs Specialized	-91.11	2.18	2.18	28.63	-24.14	0.08	0.00

Figure F-27: Analysis of well HZ_90IN_90AZ, UGR_50x5x50x3_5x3

Horizontal Well, Apparent Dip 90º and Apparent Rotation 30º (HZ_90IN_60AZ)

		Values							Errors						
		C	$k_h h$	k_h	L	k_v/k_h	S_t	P_i	C	$k_h h$	k_h	L	k_v/k_h	S_t	P_i
		bbl/psi	mD-ft	mD	ft	-	-	psia	%	%	%	%	%	-	%
	HZ_90IN_60AZ (ANALYTIC)	0.00039	28000	140.0	346	1.00	-5.00	1618.02	0.000	0.000	0.000	0.000	0.000	0.000	0.000
Coarse Grid	Coarse	0.080	28300	141.5	280	1.69	-4.93	1618.02	20412.821	1.071	1.071	-19.075	69.000	0.070	0.000
	RMS Error, Absolute	**0.080**	**300**	**1.50**	**66**	**0.69**	**0.07**	**0.00**							
	RMS Error, Relative (%)	**20413**	**1.07**	**1.07**	**19**	**69**	**1.40**	**0.00**							
Cartesian Refinement	LGR_9x1_Az30	0.008	28000	140	225	1.40	-4.71	1618.03	1951.282	0.000	0.000	-34.971	40.000	0.290	0.001
	LGR_19x1_Az30	0.0032	28000	140	278	1.60	-4.96	1618.02	720.513	0.000	0.000	-19.653	60.000	0.040	0.000
	LGR_57x3_Az30+	0.0018	28000	140	278	1.50	-4.78	1618.02	361.538	0.000	0.000	-19.653	50.000	0.220	0.000
	LGR_19x1_3x3	0.0033	28000	140	270	1.79	-4.94	1618.02	746.154	0.000	0.000	-21.965	79.000	0.060	0.000
	RMS Error, Absolute	**0.0044**	**0.00**	**0.00**	**43**	**0.59**	**0.22**	**0.005**							
	RMS Error, Relative (%)	**1130**	**0.00**	**0.00**	**13**	**59**	**4.48**	**0.000**							
Unstructured Refinement	UGR_50x5x50x1_Az30	0.003	27000	135	300	1.40	-5.00	1618.01	669.231	-3.571	-3.571	-13.295	40.000	0.000	-0.001
	UGR_50x5x50x3_Az30+	0.001	27000	135	312	1.39	-5.02	1618.01	156.410	-3.571	-3.571	-9.827	39.000	-0.020	-0.001
	UGR_90x9x50x3_Az30+	0.0025	26800	134	310	1.48	-5.02	1618.05	541.026	-4.286	-4.286	-10.405	48.000	-0.020	0.002
	UGR_90x9x50x3_5x5	0.001	26800	134	310	1.51	-5.03	1618.01	156.410	-4.286	-4.286	-10.405	51.000	-0.030	-0.001
	RMS Error, Absolute	**0.0018**	**1105**	**5.52**	**9**	**0.45**	**0.368**	**0.017**							
	RMS Error, Relative (%)	**455**	**3.94**	**3.94**	**3**	**45**	**7.35**	**0.001**							

Table F-4: Summary of the interpretation results for HZ_90IN_90AZ well model complete with root mean squared error calculations expressed in absolute and relative terms.

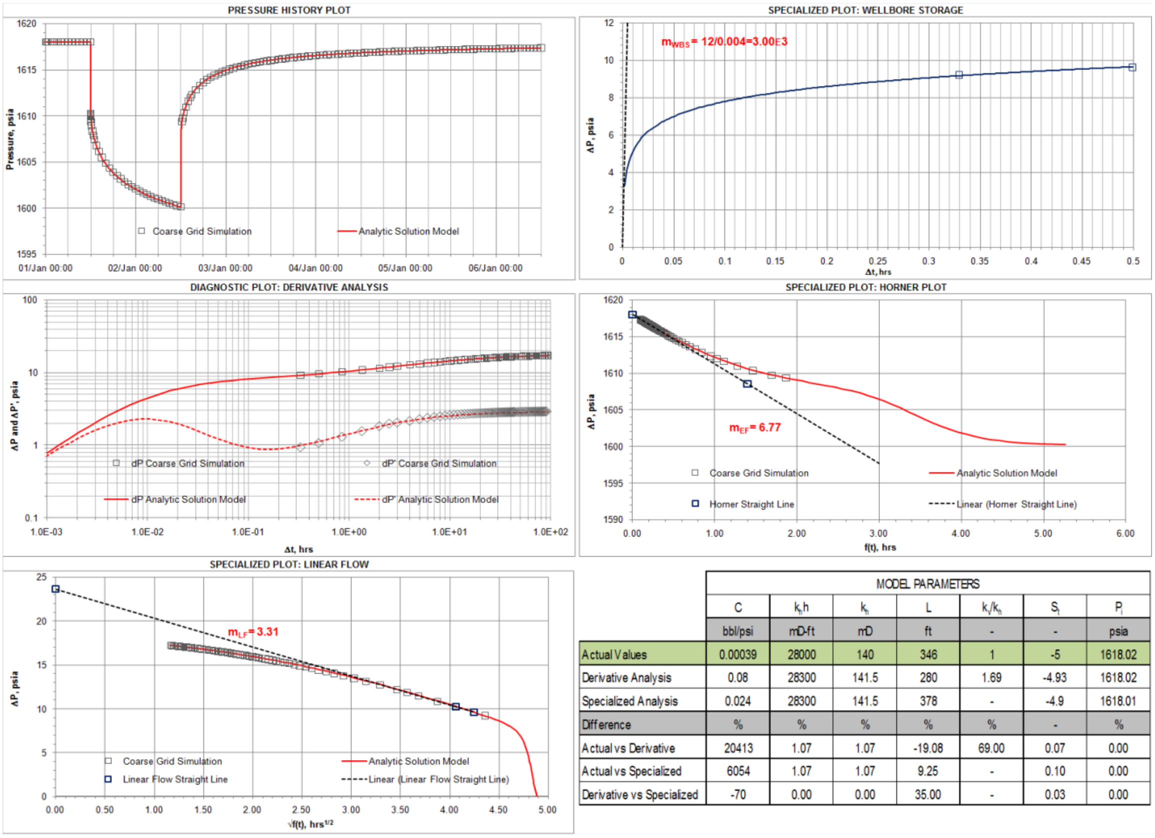

	MODEL PARAMETERS						
	C	$k_h h$	k_h	L	k_v/k_h	S_t	P_i
	bbl/psi	mD-ft	mD	ft	-	-	psia
Actual Values	0.00039	28000	140	346	1	-5	1618.02
Derivative Analysis	0.08	28300	141.5	280	1.69	-4.93	1618.02
Specialized Analysis	0.024	28300	141.5	378	-	-4.9	1618.01
Difference	%	%	%	%	%	-	%
Actual vs Derivative	20413	1.07	1.07	-19.08	69.00	0.07	0.00
Actual vs Specialized	6054	1.07	1.07	9.25	-	0.10	0.00
Derivative vs Specialized	-70	0.00	0.00	35.00	-	0.03	0.00

Figure F-28: Analysis of well HZ_90IN_60AZ, coarse grid

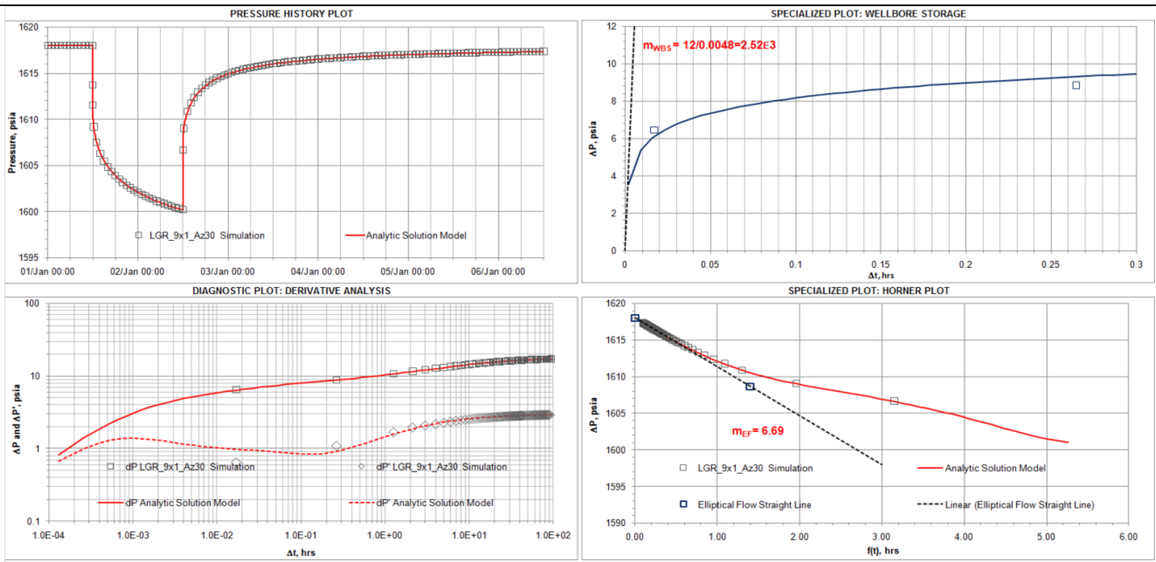

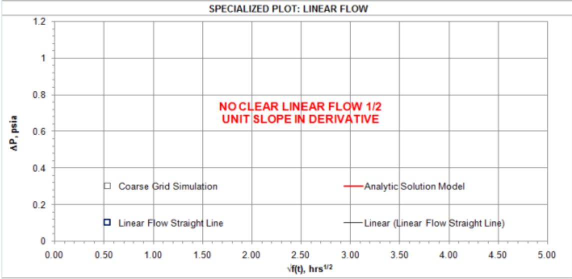

	MODEL PARAMETERS						
	C	$k_h h$	k_h	L	k_v/k_h	S_t	P_i
	bbl/psi	mD-ft	mD	ft	-	-	psia
Actual Values	0.00039	28000	140	346	1	-5	1618.02
Derivative Analysis	0.008	28000	140	225	1.4	-4.71	1618.03
Specialized Analysis	0.028	28700	143.5	-	-	-4.88	1618.01
Difference	%	%	%	%	%	-	%
Actual vs Derivative	1951	0.00	0.00	-34.97	40.00	0.29	0.00
Actual vs Specialized	7079	2.50	2.50	-	-	0.12	0.00
Derivative vs Specialized	250	2.50	2.50	-	-	-0.17	0.00

Figure F-29: Analysis of well HZ_90IN_60AZ, LGR_9x1_Az30

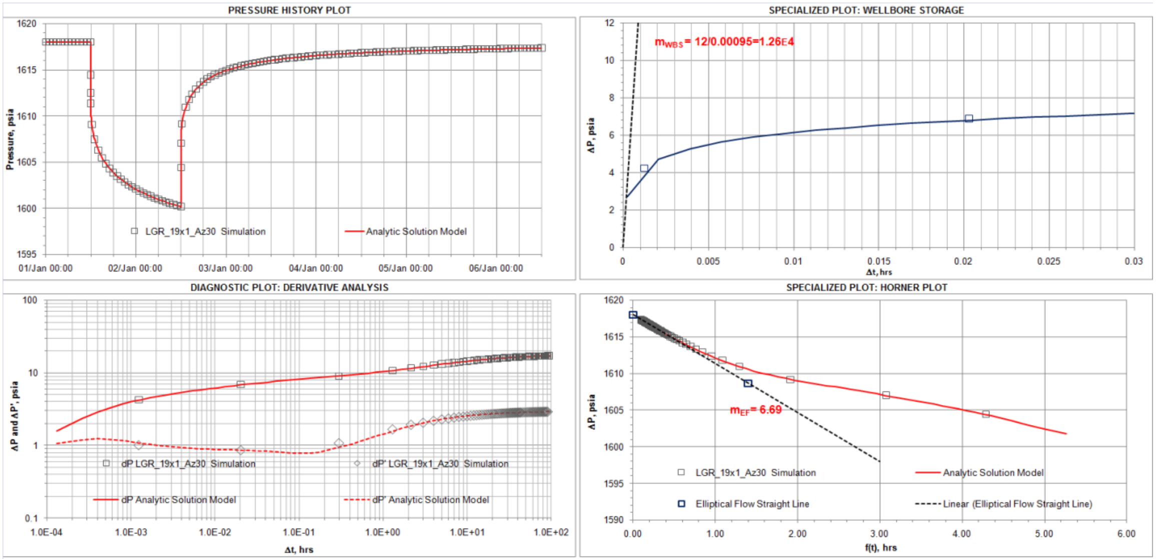

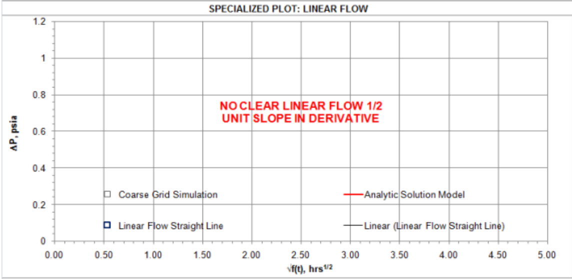

	MODEL PARAMETERS						
	C	$k_h h$	k_h	L	k_v/k_h	S_t	P_i
	bbl/psi	mD-ft	mD	ft	-	-	psia
Actual Values	0.00039	28000	140	346	1	-5	1618.02
Derivative Analysis	0.0032	28000	140	278	1.6	-4.96	1618.02
Specialized Analysis	0.0057	28700	143.5	-	-	-4.88	1618.01
Difference	%	%	%	%	%	-	%
Actual vs Derivative	721	0.00	0.00	-19.65	60.00	0.04	0.00
Actual vs Specialized	1362	2.50	2.50	-	-	0.12	0.00
Derivative vs Specialized	78	2.50	2.50	-	-	0.08	0.00

Figure F-30: Analysis of well HZ_90IN_60AZ, LGR_19x1_Az30

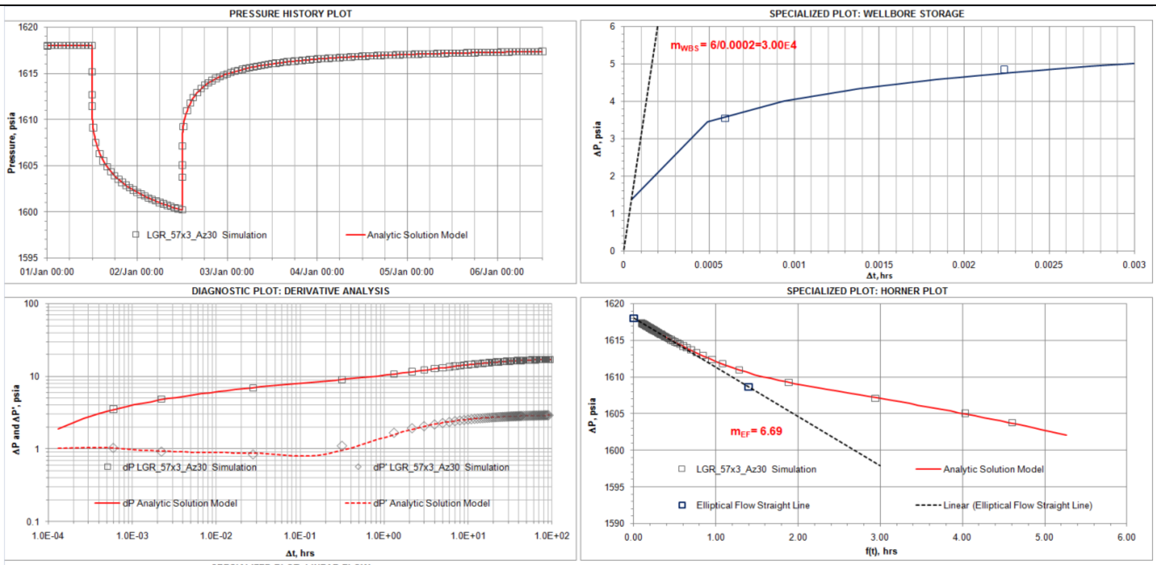

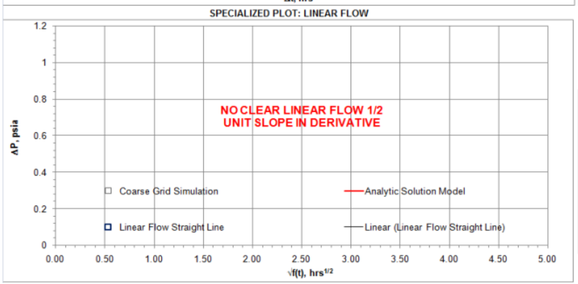

MODEL PARAMETERS	C	$k_h h$	k_h	L	k_v/k_h	S_t	P_i
	bbl/psi	mD-ft	mD	ft	-	-	psia
Actual Values	0.00039	28000	140	346	1	-5	1618.02
Derivative Analysis	0.0018	28000	140	278	1.5	-4.78	1618.02
Specialized Analysis	0.0024	28600	143	-	-	-4.89	1618.01
Difference	%	%	%	%	%	-	%
Actual vs Derivative	362	0.00	0.00	-19.65	50.00	0.22	0.00
Actual vs Specialized	515	2.14	2.14	-	-	0.11	0.00
Derivative vs Specialized	33	2.14	2.14	-	-	-0.11	0.00

Figure F-31: Analysis of well HZ_90IN_60AZ, LGR_57x3_Az30+

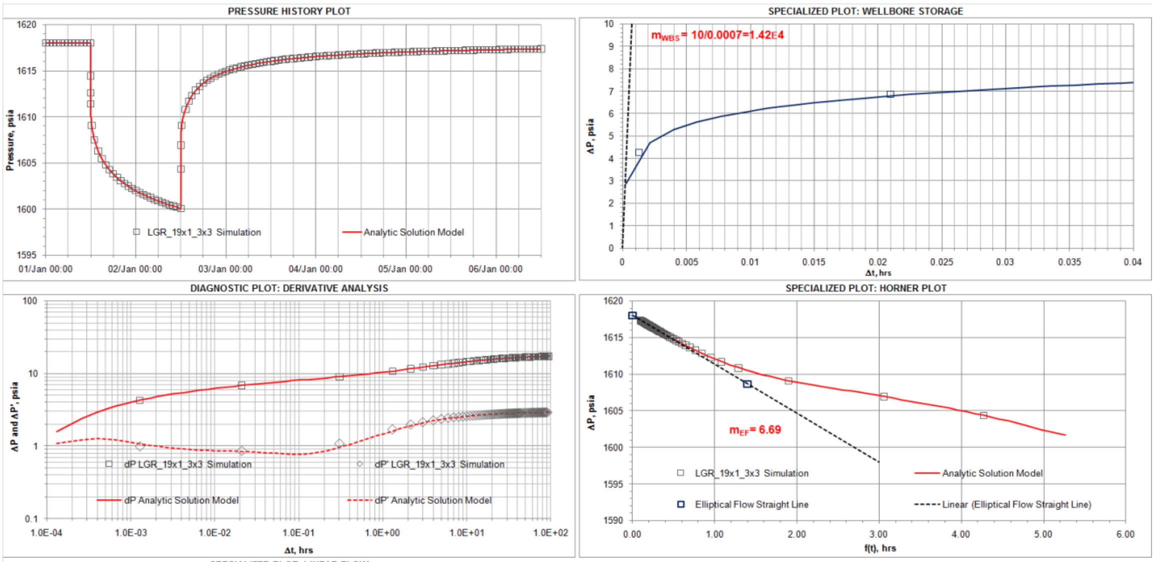

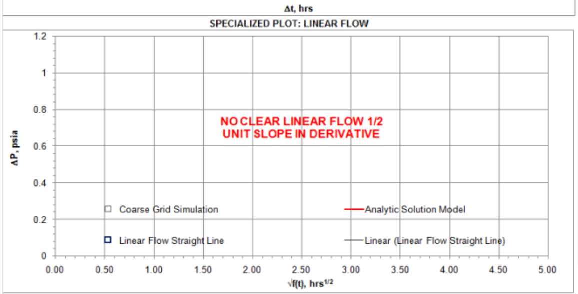

MODEL PARAMETERS	C	$k_h h$	k_h	L	k_v/k_h	S_t	P_i
	bbl/psi	mD-ft	mD	ft	-	-	psia
Actual Values	0.00039	28000	140	346	1	-5	1618.02
Derivative Analysis	0.0033	28000	140	270	1.79	-4.94	1618.02
Specialized Analysis	0.005	28600	143	-	-	-4.89	1618.01
Difference	%	%	%	%	%	-	%
Actual vs Derivative	746	0.00	0.00	-21.97	79.00	0.06	0.00
Actual vs Specialized	1182	2.14	2.14	-	-	0.11	0.00
Derivative vs Specialized	52	2.14	2.14	-	-	0.05	0.00

Figure F-32: Analysis of well HZ_90IN_60AZ, LGR_19x1_3x3

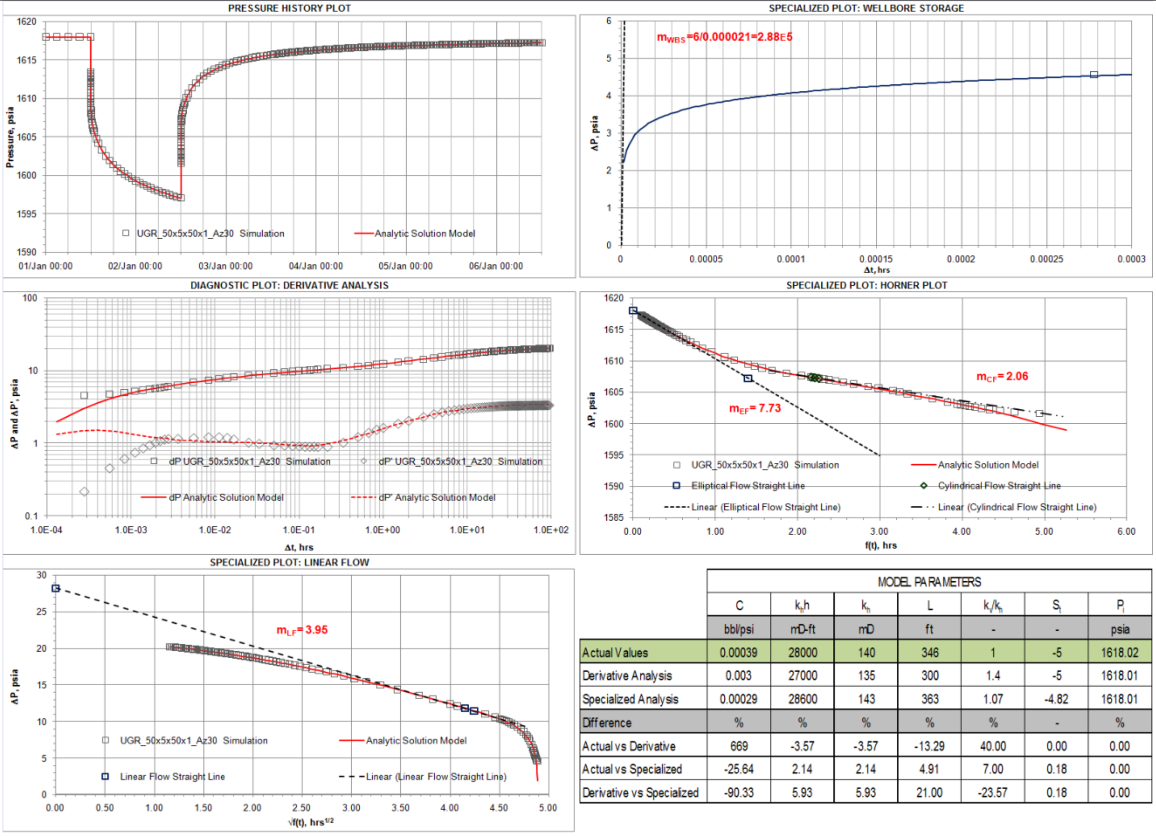

MODEL PARAMETERS							
	C	$k_h h$	k_h	L	k_v/k_h	S_t	P_i
	bbl/psi	mD-ft	mD	ft	-	-	psia
Actual Values	0.00039	28000	140	346	1	-5	1618.02
Derivative Analysis	0.003	27000	135	300	1.4	-5	1618.01
Specialized Analysis	0.00029	28600	143	363	1.07	-4.82	1618.01
Difference	%	%	%	%	%	-	%
Actual vs Derivative	669	-3.57	-3.57	-13.29	40.00	0.00	0.00
Actual vs Specialized	-25.64	2.14	2.14	4.91	7.00	0.18	0.00
Derivative vs Specialized	-90.33	5.93	5.93	21.00	-23.57	0.18	0.00

Figure F-33: Analysis of well HZ_90IN_60AZ, UGR_50x5x50x1_Az30

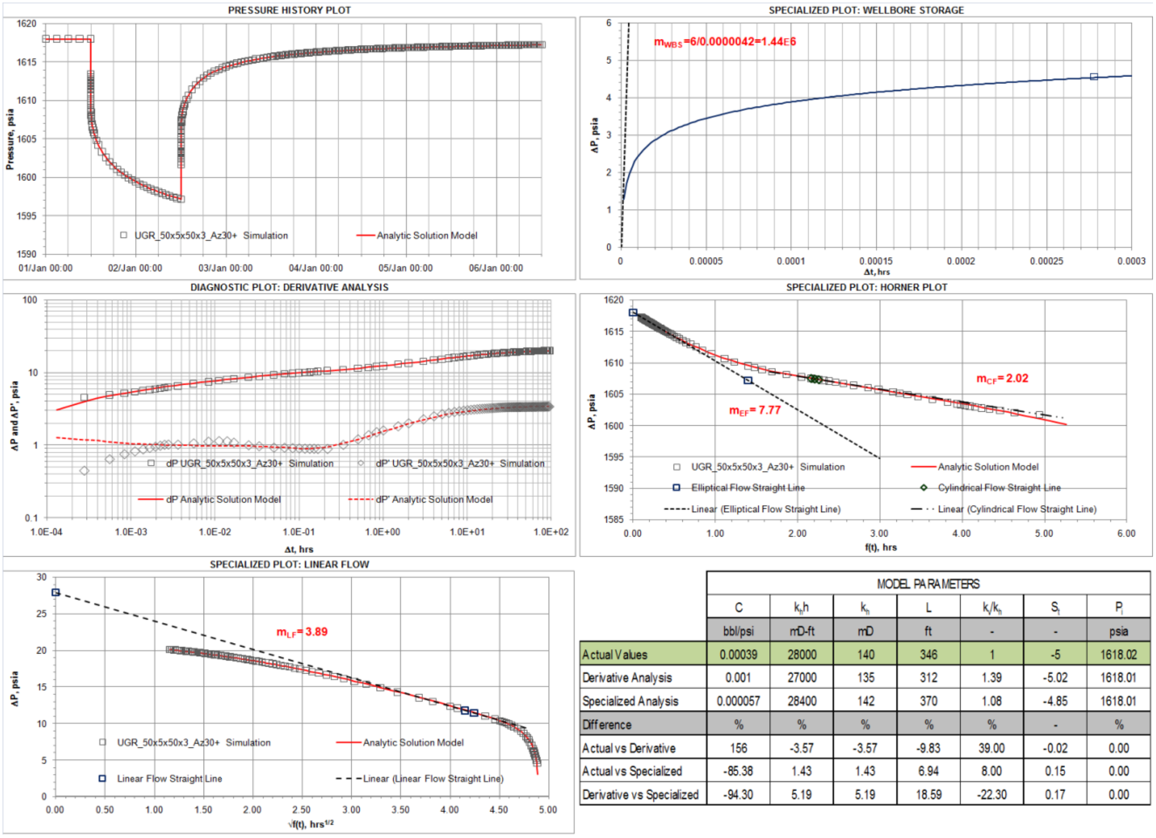

MODEL PARAMETERS							
	C	$k_h h$	k_h	L	k_v/k_h	S_t	P_i
	bbl/psi	mD-ft	mD	ft	-	-	psia
Actual Values	0.00039	28000	140	346	1	-5	1618.02
Derivative Analysis	0.001	27000	135	312	1.39	-5.02	1618.01
Specialized Analysis	0.000057	28400	142	370	1.08	-4.85	1618.01
Difference	%	%	%	%	%	-	%
Actual vs Derivative	156	-3.57	-3.57	-9.83	39.00	-0.02	0.00
Actual vs Specialized	-85.38	1.43	1.43	6.94	8.00	0.15	0.00
Derivative vs Specialized	-94.30	5.19	5.19	18.59	-22.30	0.17	0.00

Figure F-34: Analysis of well HZ_90IN_60AZ, UGR_50x5x50x3_Az30+

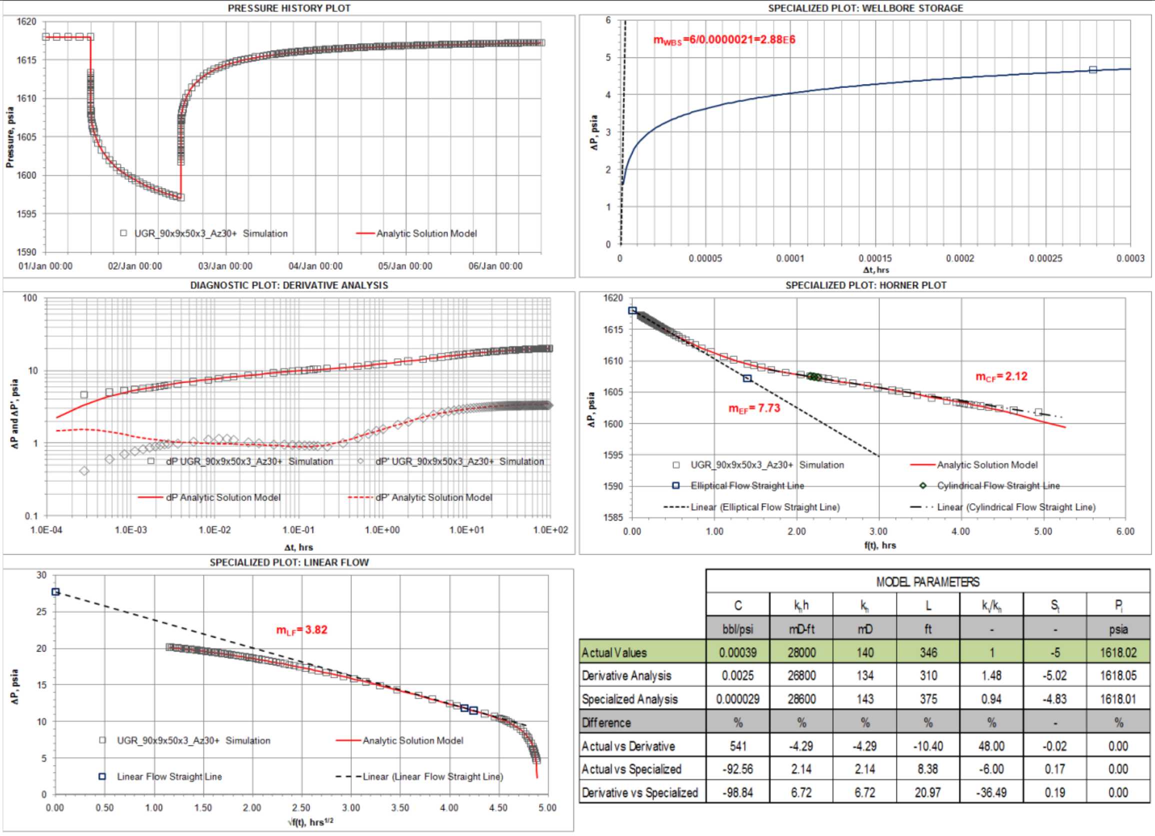

	MODEL PARAMETERS						
	C	k_hh	k_h	L	k_v/k_h	S_t	P_i
	bbl/psi	mD-ft	mD	ft	-	-	psia
Actual Values	0.00039	28000	140	346	1	-5	1618.02
Derivative Analysis	0.0025	26800	134	310	1.48	-5.02	1618.05
Specialized Analysis	0.000029	28600	143	375	0.94	-4.83	1618.01
Difference	%	%	%	%	%	-	%
Actual vs Derivative	541	-4.29	-4.29	-10.40	48.00	-0.02	0.00
Actual vs Specialized	-92.56	2.14	2.14	8.38	-6.00	0.17	0.00
Derivative vs Specialized	-98.84	6.72	6.72	20.97	-36.49	0.19	0.00

Figure F-35: Analysis of well HZ_90IN_60AZ, UGR_90x9x50x3_Az30+

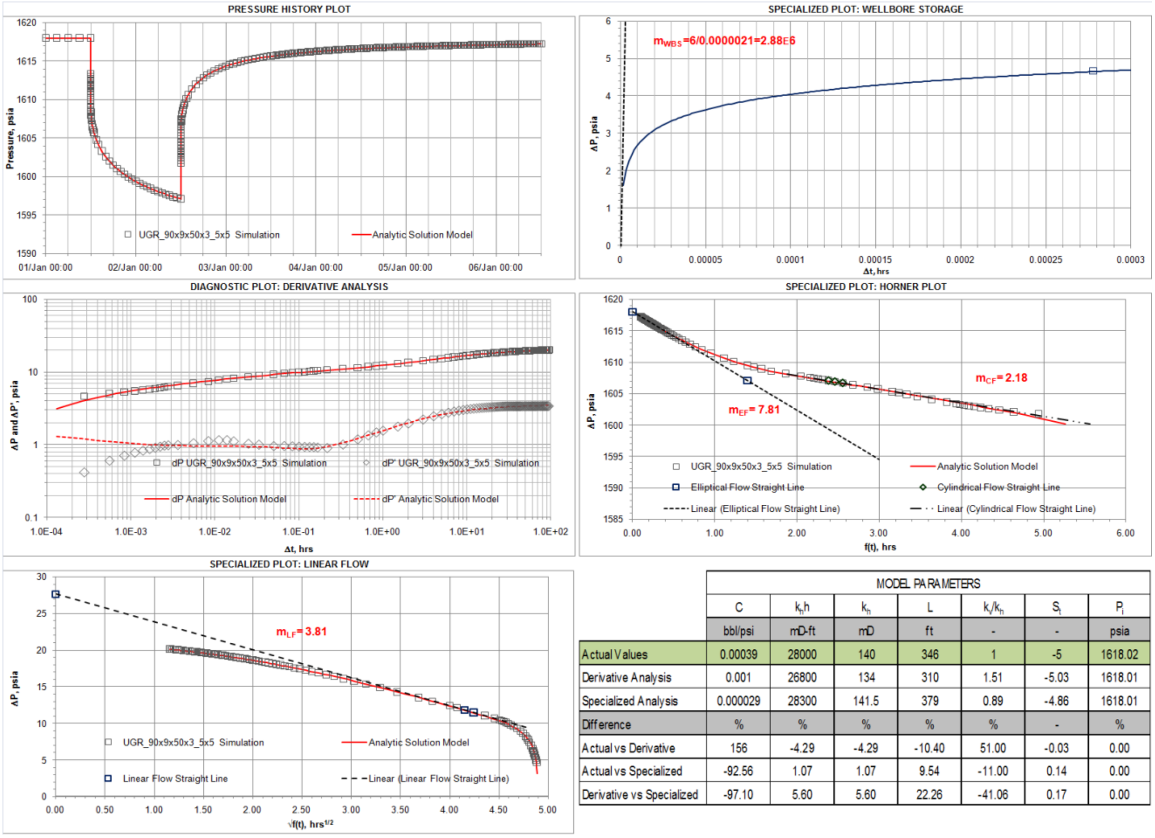

	MODEL PARAMETERS						
	C	k_hh	k_h	L	k_v/k_h	S_t	P_i
	bbl/psi	mD-ft	mD	ft	-	-	psia
Actual Values	0.00039	28000	140	346	1	-5	1618.02
Derivative Analysis	0.001	26800	134	310	1.51	-5.03	1618.01
Specialized Analysis	0.000029	28300	141.5	379	0.89	-4.86	1618.01
Difference	%	%	%	%	%	-	%
Actual vs Derivative	156	-4.29	-4.29	-10.40	51.00	-0.03	0.00
Actual vs Specialized	-92.56	1.07	1.07	9.54	-11.00	0.14	0.00
Derivative vs Specialized	-97.10	5.60	5.60	22.26	-41.06	0.17	0.00

Figure F-36: Analysis of well HZ_90IN_60AZ, UGR_90x9x50x3_5x5

Appendix G: Peculiarities of Working with Unstructured Refinement

The simulation of unstructured grids introduced several peculiarities related to software functionality. Numerical modelling using unstructured refinement was run using a different software (see *Software* in the main body of the report), which was unable to support the dead-oil fluid model and was not compatible with the time-stepping output from the pre-processor.

An equivalent live-oil fluid model was generated by modification of the stock tank oil density such that reservoir fluid density and reservoir pressure were maintained constant between simulations under both static and dynamic conditions. The live-oil's saturation pressure (bubble point) was set well below the simulated bottomhole flowing pressure to ensure fluid remained single-phase in the reservoir at all times.

Since unstructured grids could only be successfully exported and run using time-steps which were whole number multiples of a day, and given that accurate description of the pressure transients required time steps in the order of seconds, it was necessary to transform the model parameters, using the dimensionless pressure and dimensionless time variables given in Appendix C. This involved a modification of parameters by a factor of 86400 – dictated by the transformation of second equivalent time-steps into days and resulted in very low rates from very low permeability rock over extremely large time-steps. Finally, prior to analysis, the time-stamp of data output from the simulator was modified back in accordance with all other simulations.

Furthermore, due to rounding of the oil rate in the simulator, 0.01736 STBD rounded to 0.02 STBD, this had to be reflected in the rate input to the pressure transient interpretations – an increase from 1500 STBD to 1728.1 STBD.

Appendix H: Simulator Performance Vectors

Fully Penetrating Vertical Well (VERT_FP)

Model	Simulator	Active Cells #	LGR Cells #	NNC #	TCPU (s)	Time Steps #	Linear It. #	Non Lin. It. #	Cost (ms/cell-step)	Normalised Cost -	Iteration Ratio
VERT_FP											
Coarse	ECLIPSE	204020	0	0	143	108	108	108	6.49	1.00	1.00
LGR_3x1_1	ECLIPSE	204200	180	240	179	96	130	130	9.13	1.41	1.20
LGR_3x1+	ECLIPSE	204920	900	840	178	96	135	129	9.05	1.39	1.25
LGR_3x1_3x3	ECLIPSE	205640	1620	720	180	96	137	129	9.12	1.40	1.27
LGR_9x1_3x1+	ECLIPSE	206360	2340	1440	202	100	195	140	9.79	1.51	1.81
LGR_9x3_3x3+	ECLIPSE	211040	7020	4320	208	99	192	137	9.96	1.53	1.78
GeoXY_5x20	ECLIPSE	204520	500	400	398	132	677	250	14.74	2.27	6.27
GeoXY_7x20	ECLIPSE	205000	980	560	397	123	808	220	15.74	2.43	7.48
GeoXY_9x20	ECLIPSE	205640	1620	720	482	116	1225	197	20.21	3.11	11.34
GeoXY_11x20	ECLIPSE	206440	2420	880	590	115	1612	197	24.85	3.83	14.93
RadLGR_4R_33	ECLIPSE	204100	80	0	292	111	330	190	12.89	1.99	3.06
RadLGR_8R_33	ECLIPSE	204180	160	0	315	110	519	188	14.03	2.16	4.81
RadLGR_8R_66	ECLIPSE	204180	160	0	308	111	497	189	13.59	2.09	4.60
RadLGR_8R_99	ECLIPSE	204180	160	0	309	112	490	192	13.51	2.08	4.54

Table H-1: Summary of simulator performance vectors for the VERT_FP well model

Partially Penetrating Vertical Well (VERT_PP)

Model	Simulator	Active Cells #	LGR Cells #	NNC #	TCPU (s)	Time Steps #	Linear It. #	Non Lin. It. #	Cost (ms/cell-step)	Normalised Cost -	Iteration Ratio
VERT_PP											
Coarse	ECLIPSE	204020	0	0	154	110	110	110	6.86	1.00	1.00
LGR_19x1_1	ECLIPSE	211240	7220	1520	489	159	618	309	14.56	2.12	2.00
LGR_9x1_3x3	ECLIPSE	218600	14580	2160	410	144	390	259	13.02	1.90	1.51
LGR_39x1_1	ECLIPSE	234440	30420	3120	621	156	848	306	16.98	2.47	2.77
LGR_39x2_1	ECLIPSE	264860	60840	6240	724	152	894	293	17.98	2.62	3.05
LGR_77x1_11x1+	ECLIPSE	332280	128260	8800	1112	153	1123	299	21.87	3.19	3.76
LGR_77x4_11x2_3x3	ECLIPSE	341960	137940	10560	1159	153	1122	299	22.15	3.23	3.75
RadLGR_8R_33	ECLIPSE	204180	160	0	462	152	757	307	14.89	2.17	2.47
RadLGR_8R_66	ECLIPSE	204180	160	0	456	149	695	297	14.99	2.18	2.34
RadLGR_16R_66	ECLIPSE	204340	320	0	497	151	885	308	16.11	2.35	2.87
RadLGR_16Rx3_66	ECLIPSE	204980	960	240	594	148	1402	297	19.58	2.85	4.72
RadLGR_24RxGeo_66	ECLIPSE	205124	1104	136	729	148	1897	304	24.01	3.50	6.24
GeoXY_11x60	ECLIPSE	211280	7260	2640	909	156	2404	307	27.58	4.02	7.83
GeoXY_11x100	ECLIPSE	216120	12100	4400	1150	155	3072	304	34.33	5.00	10.11
GeoXYZ_11x46	ECLIPSE	209586	5566	2024	1088	155	3022	303	33.49	4.88	9.97

Table H-2: Summary of simulator performance vectors for the VERT_PP well model

Horizontal Well Aligned With Grid (HZ_90IN_90AZ)

Model	Simulator	Active Cells #	LGR Cells #	NNC #	TCPU (s)	Time Steps #	Linear It. #	Non Lin. It. #	Cost (ms/cell-step)	Normalised Cost -	Iteration Ratio
HZ_90IN_90AZ											
Coarse		193819	0	0	214	155	155	155	7.12	1.00	1.00
LGR_19x1_3x1	ECLIPSE	214396	20577	2888	289	142	321	152	9.49	1.33	2.11
LGR_19x1_3x3	ECLIPSE	255550	61731	4332	320	142	298	152	8.82	1.24	1.96
LGR_19x1_5x1	ECLIPSE	228114	34295	4332	273	142	309	152	8.43	1.18	2.03
LGR_57x3_5x1	ECLIPSE	1119784	925965	38988	2601	142	749	153	16.36	2.30	4.90
LGR_19x1_5x3	ECLIPSE	296704	102885	5776	400	142	317	152	9.49	1.33	2.09
LGR_19x1_5x5	ECLIPSE	365294	171475	7720	507	142	290	152	9.77	1.37	1.91
LGR_19x1_7x3	ECLIPSE	337858	144039	7220	470	142	317	152	9.80	1.38	2.09
LGR_19x1_15x3	ECLIPSE	502474	308655	12996	781	142	317	152	10.95	1.54	2.09
GeoY_11x1_3x1	ECLIPSE	200716	6897	1672	232	142	362	152	8.14	1.14	2.38
GeoXY_11x1_5x1	ECLIPSE	205314	11495	2508	246	142	372	152	8.44	1.18	2.45
GeoXY_11x1_7x1	ECLIPSE	193819	11913	2584	245	142	372	152	8.90	1.25	2.45
GeoXY_11x3_5x1	ECLIPSE	228304	34485	7524	356	143	632	155	10.90	1.53	4.08
GeoXY_11x5_5x1	ECLIPSE	251294	57475	12540	480	142	846	153	13.45	1.89	5.53
GeoXYZ_11x35_5x1	ECLIPSE	214994	21175	4620	505	143	1259	155	16.43	2.31	8.12
Coarse	INTERSECT	193819	0	0	1121	260	659	260	22.25	1.00	2.53
UGR_50x3x50x1_5x1	INTERSECT	196023	2204	-	1123	260	701	260	22.03	0.99	2.70
UGR_30x3x50x1_5x1	INTERSECT	196099	2280	-	1053	260	747	260	20.65	0.93	2.87
UGR_50x3x50x1_5x3	INTERSECT	198341	4522	-	1078	260	699	260	20.90	0.94	2.69
UGR_50x3x50x1_7x3	INTERSECT	200051	6232	-	1059	260	697	260	20.36	0.92	2.68
UGR_50x5x50x1_5x1	INTERSECT	196593	2774	-	1121	260	715	260	21.93	0.99	2.75
UGR_50x5x50x1_5x3	INTERSECT	198911	5092	-	1082	260	716	260	20.92	0.94	2.75
UGR_50x5x50x3_5x3	INTERSECT	209665	15846	-	1152	260	906	260	21.13	0.95	3.48

Table H-3: Summary of simulator performance vectors for the HZ_90IN_90AZ well model

Deviated Well, Apparent Dip 30º and Apparent Rotation 0º (W_30IN_90AZ)

		Active Cells	LGR Cells	NNC	TCPU	Time Steps	Linear It.	Non Lin. It.	Cost	Normalised Cost	Iteration Ratio
Model	Simulator	#	#	#	(s)	#	#	#	(ms/cell-step)	-	
W_30IN_90AZ											
Coarse	ECLIPSE	204020	0	0	140	104	104	104	6.60	1.00	1.00
LGR_9x1_2x1	ECLIPSE	207260	3240	1080	190	97	177	130	9.45	1.43	1.36
LGR_19x1_2x1	ECLIPSE	218460	14440	2280	318	107	369	169	13.60	2.06	2.18
LGR_19x1_2x1_3x1+	ECLIPSE	219000	14980	2940	320	106	365	167	13.78	2.09	2.19
LGR_19x1_2x1_3x1_3x3	ECLIPSE	219180	15160	3040	308	106	365	167	13.26	2.01	2.19
LGR_39x2_2x1	ECLIPSE	325700	121680	9360	645	109	647	177	18.17	2.75	3.66
LGR_9x1_3x3	ECLIPSE	218600	14580	2160	206	97	192	131	9.72	1.47	1.47
LGR_9x1_4x3	ECLIPSE	223460	19440	2520	207	96	180	128	9.65	1.46	1.41

Table H-4: Summary of simulator performance vectors for the W_30IN_90AZ well model

Deviated Well, Apparent Dip 30º and Apparent Rotation 30º (W_34IN_60AZ)

		Active Cells	LGR Cells	NNC	TCPU	Time Steps	Linear It.	Non Lin. It.	Cost	Normalised Cost	Iteration Ratio
Model	Simulator	#	#	#	(s)	#	#	#	(ms/cell-step)	-	
W_34IN_60AZ											
Coarse	ECLIPSE	204020	0	0	134	104	104	104	6.32	1.00	1.00
LGR_9x1_2x1	ECLIPSE	207260	3240	1080	187	97	190	130	9.30	1.47	1.46
LGR_19x1_2x1	ECLIPSE	218460	14440	2280	274	104	369	159	12.06	1.91	2.32
LGR_19x1_2x1_3x1+	ECLIPSE	219000	14980	2940	280	104	376	160	12.29	1.95	2.35
LGR_19x1_2x1_3x1_3x3	ECLIPSE	219180	15160	3040	267	102	354	153	11.94	1.89	2.31
LGR_39x2_2x1	ECLIPSE	325700	121680	9360	628	107	655	170	18.02	2.85	3.85
LGR_9x1_3x3	ECLIPSE	218600	14580	2160	199	95	187	125	9.58	1.52	1.50
LGR_9x1_4x3	ECLIPSE	223460	19440	2520	205	95	183	125	9.66	1.53	1.46

Table H-5: Summary of simulator performance vectors for the W_34IN_90AZ well model

Deviated Well, Apparent Dip 30º and Apparent Rotation 45º (W_39IN_45AZ)

		Active Cells	LGR Cells	NNC	TCPU	Time Steps	Linear It.	Non Lin. It.	Cost	Normalised Cost	Iteration Ratio
Model	Simulator	#	#	#	(s)	#	#	#	(ms/cell-step)	-	
W_39IN_45AZ											
Coarse	ECLIPSE	204020	0	0	137	104	104	104	6.46	1.00	1.00
LGR_9x1_2xD	ECLIPSE	207260	3240	1440	205	99	228	135	9.99	1.55	1.69
LGR_19x1_2xD	ECLIPSE	218460	14440	3040	353	115	504	196	14.05	2.18	2.57
LGR_39x2_2xD	ECLIPSE	325700	121680	12480	774	115	842	196	20.66	3.20	4.30

Table H-6: Summary of simulator performance vectors for the W_39IN_45AZ well model

Horizontal Well, Apparent Dip 90º and Apparent Rotation 30º (HZ_90IN_60AZ)

		Active Cells	LGR Cells	NNC	TCPU	Time Steps	Linear It.	Non Lin. It.	Cost	Normalised Cost	Iteration Ratio
Model	Simulator	#	#	#	(s)	#	#	#	(ms/cell-step)	-	
HZ_90IN_60AZ											
Coarse	ECLIPSE	193819	0	0	191	152	153	152	6.48	1.00	1.01
LGR_9x1_Az30	ECLIPSE	201514	7695	2394	198	139	205	142	7.07	1.09	1.44
LGR_19x1_Az30	ECLIPSE	228114	34295	5054	271	141	305	148	8.43	1.30	2.06
LGR_57x3_Az30	ECLIPSE	1119784	925965	45486	2870	142	773	152	18.05	2.78	5.09
LGR_19x1_Az30+	ECLIPSE	241832	48013	5415	295	141	313	148	8.65	1.33	2.11
LGR_19x1_3x3	ECLIPSE	255550	61731	4332	318	141	293	148	8.83	1.36	1.98
Coarse	INTERSECT	193819	0	-	962	260	656	260	19.09	1.00	2.52
UGR_50x5x50x1_Az30	INTERSECT	198056	4237	-	1108	260	753	260	21.52	1.13	2.90
UGR_50x5x50x3_Az30+	INTERSECT	211356	17537	-	1106	260	757	260	20.13	1.05	2.91
UGR_90x9x50x3_Az30+	INTERSECT	213522	19703	-	1205	260	757	260	21.71	1.14	2.91
UGR_90x9x50x3_5x5	INTERSECT	221559	27740	-	1223	260	757	260	21.23	1.11	2.91

Table H-7: Summary of simulator performance vectors for the HZ_90IN_60AZ well model

Horizontal Well, Apparent Dip 90º and Apparent Rotation 45º (HZ_90IN_45AZ)

Model	Simulator	Active Cells #	LGR Cells #	NNC #	TCPU (s)	Time Steps #	Linear It. #	Non Lin. It. #	Cost (ms/cell-step)	Normalised Cost -	Iteration Ratio
HZ_90IN_45AZ											
Coarse	ECLIPSE	193819	0	0	475	412	411	411	5.95	1.00	1.00
LGR_9x1_Az45	ECLIPSE	203053	9234	2736	533	402	537	404	6.53	1.10	1.33
LGR_19x1_Az45	ECLIPSE	234973	41154	5776	696	403	760	406	7.35	1.24	1.87
LGR_57x3_Az45	ECLIPSE	1304977	1111158	51984	6862	403	1452	408	13.05	2.19	3.56
LGR_19x1_Az45+	ECLIPSE	262409	68590	6498	807	402	764	404	7.65	1.29	1.89
LGR_19x1_4x3	ECLIPSE	276127	82308	5054	853	402	711	404	7.68	1.29	1.76
Coarse	INTERSECT	193819	0	-	895	228	559	228	20.25	1.00	2.45
UGR_50x5x50x1_Az45	INTERSECT	199690	5871	-	950	228	763	228	20.87	1.03	3.35
UGR_50x7x50x1_Az45+	INTERSECT	201001	7182	-	956	228	771	228	20.86	1.03	3.38
UGR_63x7x100x1_Az45+	INTERSECT	197125	3306	-	921	228	769	228	20.49	1.01	3.37
UGR_63x7x100x3_Az45+	INTERSECT	204877	11058	-	955	228	781	228	20.44	1.01	3.43

Table H-8: Summary of simulator performance vectors for the HZ_90IN_45AZ well model

Aspect Ratio Sensitivity Cases

Model	Simulator	Active Cells #	LGR Cells #	NNC #	TCPU (s)	Time Steps #	Linear It. #	Non Lin. It. #	Cost (ms/cell-step)	Normalised Cost -	Iteration Ratio
VERT_FP											
LGR_19x1_13x13	ECLIPSE	1342990	1159171	18772	3391	114	367	193	22.15	3.41	1.90
LGR_9x19x1_13x13	ECLIPSE	742900	549081	13832	1049	99	180	136	14.26	2.20	1.32
LGR_5x19x1_13x13	ECLIPSE	498864	305045	11856	648	97	156	131	13.39	2.06	1.19
LGR_3x19x1_13x13	ECLIPSE	376846	183027	10868	443	95	141	126	12.37	1.91	1.12
HZ_90IN_90AZ											
Coarse	ECLIPSE	193819	0	0	196	157	157	157	6.44	1.00	1.00
LGR_19x1_15x11	ECLIPSE	1325554	1131735	18772	2328	142	313	152	12.37	1.92	2.06
LGR_9x1_15x11	ECLIPSE	447754	253935	8892	652	140	211	145	10.40	1.61	1.46
LGR_3x1_15x11	ECLIPSE	222034	28215	2964	226	139	151	142	7.32	1.14	1.06
LGR_1x3_15x11	ECLIPSE	203224	9405	2964	201	138	141	139	7.17	1.11	1.01
LGR_9x19x1_15x11	ECLIPSE	729904	536085	13072	1199	142	271	152	11.57	1.80	1.78
LGR_5x19x1_15x11	ECLIPSE	491644	297825	10792	762	142	257	152	10.91	1.69	1.69
LGR_3x19x1_15x11	ECLIPSE	372514	178695	9652	522	142	247	152	9.87	1.53	1.63
LGR_1x19x1_15x11	ECLIPSE	253384	59565	8512	314	142	234	152	8.73	1.35	1.54
LGR_19x9x1_15x11	ECLIPSE	729904	536085	14592	1059	139	213	142	10.44	1.62	1.50
LGR_19x5x1_15x11	ECLIPSE	491644	297825	12920	648	139	184	142	9.48	1.47	1.30
LGR_19x3x1_15x11	ECLIPSE	372514	178695	12084	458	139	172	142	8.85	1.37	1.21
LGR_19x1x1_15x11	ECLIPSE	253384	59565	11248	274	138	167	139	7.84	1.22	1.20

Table H-9: Summary of simulator performance vectors for the HZ_90IN_45AZ well model

5-Point Versus 9-Point Flux Sensitivity Cases

Model	Simulator	Active Cells #	LGR Cells #	NNC #	TCPU (s)	Time Steps #	Linear It. #	Non Lin. It. #	Cost (ms/cell-step)	Normalised Cost -	Iteration Ratio
VERT_FP											
Coarse	ECLIPSE	204020	0	400000	311	108	108	108	14.11	1.00	1.00
LGR_3x1_1	ECLIPSE	204200	180	400240	419	101	154	143	20.32	1.44	1.08
VERT_PP	ECLIPSE										
Coarse	ECLIPSE	204020	0	400000	347	113	113	113	15.05	1.00	1.00
LGR_19x1_1	ECLIPSE	211240	7220	401520	1041	158	630	302	31.19	2.07	2.09
HZ_90IN_90AZ	ECLIPSE										
Coarse	ECLIPSE	193819	0	380000	383	155	155	155	12.75	1.00	1.00
LGR_19x1_3x3	ECLIPSE	255550	61731	384332	629	142	299	152	17.33	1.36	1.97
LGR_19x1_5x1	ECLIPSE	228114	34295	384332	552	142	317	152	17.04	1.34	2.09
W_30IN_90AZ	ECLIPSE										
Coarse	ECLIPSE	204020	0	400000	303	107	107	107	13.88	1.00	1.00
LGR_39x2_2x1	ECLIPSE	325700	121680	409360	1148	110	678	181	32.04	2.31	3.75
W_34IN_60AZ	ECLIPSE										
Coarse	ECLIPSE	204020	0	400000	317	107	107	107	14.52	1.00	1.00
LGR_39x2_2x1	ECLIPSE	325700	121680	409360	1210	108	705	174	34.40	2.37	4.05
W_39IN_45AZ	ECLIPSE										
Coarse	ECLIPSE	204020	0	400000	314	106	106	106	14.52	1.00	1.00
LGR_39x2_2xD	ECLIPSE	325700	121680	412480	1438	118	878	206	37.42	2.58	4.26
HZ_90IN_60AZ	ECLIPSE										
Coarse	ECLIPSE	193819	0	380000	375	153	154	153	12.65	1.00	1.01
LGR_19x1_3x3	ECLIPSE	255550	61731	384332	582	141	297	148	16.15	1.28	2.01
HZ_90IN_45AZ	ECLIPSE										
Coarse	ECLIPSE	193819	0	380000	859	412	411	411	10.76	1.00	1.00
LGR_19x1_Az45	ECLIPSE	234973	41154	385776	1253	403	785	406	13.23	1.23	1.93

Table H-10: Summary of simulator performance vectors for the 9-point flux scheme simulations